Université catholique de Louvain
Faculté des Sciences
Département de Physique
Center for Particle Physics and Phenomenology

Measurements of photon induced processes in CMS and forward proton detection at the LHC

Xavier Rouby
Promoteur: Prof. K. Piotrzkowski

Thèse présentée en vue de l'obtention
du grade de Docteur en Sciences

September 2008

Prélude à trois temps

Cet ouvrage est l'accomplissement de cinq années de travail. Une tranche de vie. Une somme de rencontres et d'expériences, tant professionnelles qu'humaines.

Il est également le fruit de la collaboration avec nombreuses personnes, qui y ont, *chacune*, apporté leur contribution, grande ou petite. Sans les échanges d'idées, les conseils, les avis, les discussions et les coups de mains, il est évident que je ne serais pas parvenu à réaliser une grande partie de ce travail.
Ces quelques lignes leur sont dédiées...

Tout d'abord, je souhaite remercier mon promoteur, Krzysztof Piotrzkowski. Ses idées audacieuses sont à la base du travail présenté ici. Merci pour les nombreuses opportunités qu'il m'a proposées, la grande liberté qu'il m'a accordée et les responsabilités qu'il m'a laissé prendre en toute confiance. Son intuition physique, ses commentaires précis et ses critiques avisées ont contribué à améliorer régulièrement la qualité des résultats produits, aux fils des ans.

Ensuite, je tiens à remercier trois personnes qui ont particulièrement joué un rôle dans l'avancement de ma recherche, au jour le jour: Otilia Militaru, Jérôme de Favereau et Séverine Ovyn.

Merci à Otilia, pour sa disponibilité, son acharnement et son éternelle bonne humeur. Ensemble, nous avons pu effectuer certains développements techniques et participer à des projets ambitieux, à propos des détecteurs au silicium. Son expérience dans le domaine a été très enrichissante et indispensable.

Ami depuis le premier jour à Louvain-la-Neuve, merci à Jérôme. Toujours plein de projets en tête, nous avons à deux réalisé un des travaux dont je suis le plus fier, baptisé "*Hector, the simulator*". Tout ceci au fil de nombreuses heures de discussions, lors d'innombrables moments passés devant un café et une barre de chocolat ou lors de journées entières de programmation. Notre complémentarité a été très motivante et fructueuse.

Enfin, il est des défis insurmontables sans encouragements, pression et tenacité. Merci à Séverine pour cette collaboration exceptionnelle, en toute spontanéité, franchise et efficacité. La complémentarité de nos approches et de nos méthodes, et ce sens des responsabilités, nous ont permis, en quelques mois, d'abattre quelques montagnes cachées dans la forêt obscure du *trigger*, et bien au-delà ...

Merci à Jonathan Hollar pour la collaboration fructueuse dans la simulation et l'analyse des événements contenant exclusivement deux muons, malgré la distance qui sépare Louvain-la-Neuve du CERN. Merci aussi à Gaëtan Pierre pour sa participation au projet des détecteurs sans-bord, le temps d'un mémoire de licence. Cette période, agrémentée de questions précises et d'une permanente bonne humeur, a été très intéressante et enrichissante.

Je tiens également à remercier tous les membres du jury qui ont lu ce document et contribué à en améliorer la qualité par leurs nombreux commentaires. En particulier merci à Monika Grothe et à Vincent Lemaître, pour le suivi du travail et les conseils récurrents, ainsi que les diverses opportunités et prises de responsabilités qu'ils m'ont proposées.

Lors de ces années de travail, j'ai pu recevoir de l'aide de beaucoup de personnes de ce lieu étrange que l'on nomme le *cyclotron*. Les développements techniques, liés aux différents environnements de mesure, ont bénéficié énormément de l'expérience inégalable et de la grande disponibilité de Luc Bonnet et Bernard de Callataÿ; la confection des pièces a été effectuée avec grands soins par Dominique Hougardy, Pierre Nemeger et les autres membres de l'atelier de mécanique. L'informatique a joué un rôle permanent durant ces cinq ans. Un très grand merci pour l'infrastructure mise à disposition par Thomas Keutgen, Fabrice Charlier, Fabian Boldrin et Pavel Demin. Un clin d'oeil aussi à Christophe Delaere pour la *hotline C++* permanente... Enfin, merci à tout le personnel administratif de FYNU-CP3, et en particulier à Ginette Tabordon.

La physique expérimentale, dans les *hautes énergies*, nécessite de rencontrer de nombreuses personnes pour en partager les connaissances, l'expérience et le savoir-faire. Les développements liés aux détecteurs au silicium ont été effectués en collaboration directe avec Blanca Perea Solano, Jaakko Haerkoenen, Tapio Niinikoski, Panja Luukka et le Cryolab du CERN. Je leur suis reconnaissant pour les échanges fructueux et le travail accompli ensemble. Merci également au groupe Trigger de CMS, dont Sridhara Dasu et Christos Leonidopoulos, pour leurs commentaires avisés.

Ce texte, beaucoup plus long que prévu initialement, a été lu et corrigé par de nombreuses personnes. En particulier, un très grand merci à Muriel Vander Donckt, Keith Hamilton et Laura Irvine pour leur travail de longue haleine.

Une pensée également à ces nombreux professeurs, motivants et motivés, qui m'ont appris à apprécier la saveur inégalable des sciences et des mathématiques. En particulier, merci à Eric Dartevelle et Stéphane Canard.

Je tiens à remercier énormément ma famille, et surtout mes parents pour les encouragements, les questions franches et les aides multiples et diverses, tout au cours de ces années, et depuis toujours. C'est de leur caractère que j'ai hérité. La conclusion de ce travail est quelque part l'aboutissement de 28 ans d'apprentissage dont ils sont en grande partie responsables. Merci beaucoup.

Enfin, merci à toi, qui es là depuis le premier jour de cette thèse. Tu étais là lors des hauts et des bas. Avec une grande patience, tu m'as laissé prendre du temps, des soirées, des nuits, à m'occuper de mon travail. De nombreuses heures sur notre temps, sur *ton* temps. Tu m'as encouragé en permanence. Pour y arriver. Merci à toi, Bernie.

Contents

Foreword

Photon induced processes have been studied in the past in various colliders, but at relatively low energy. The very high luminosity and collision energy at the Large Hadron Collider open widely a window on unexplored regions of the land of photon interactions.

Those interactions are favoured by very clean experimental signatures and good theoretical description. Some processes are very well known theoretically: for instance, the exclusive production of same-flavour lepton pairs have a theoretical uncertainty on their cross-section below 1%. Applications like the measurement of the absolute luminosity are then achievable with a great precision.

In case of an elastic emission of a photon, the interacting proton is scattered away with some energy loss. It escapes in the beampipe with the beam protons and leaves the central detector without being detected. In order to use this important signature, near-beam detectors can be used. Such detectors are located in the forward regions, a few millimetres away from the beam position, to detect the scattered protons.

Using such near-beam detector data to identify and measure photon interactions require some prerequisites: (i) to have a radiation hard detector, using a technology with the smallest insensitive edge, in order to have the sensor active area as close as possible to the beam; (ii) to be able to predict the path of the scattered proton along the beamline, in order to optimise the position and characteristics of the near-beam detectors.

In the present thesis, some existing technologies for edgeless detectors are reviewed with a long discussion on results on silicon microstrip detectors etched with a laser or a plasma are discussed.

The simulation of the transport of particles in the beamline is a second main subject of the document. Results of such simulations provide crucial inputs for (i) the characterisation of the near-beam detectors, and (ii) the reconstruction of the final state proton kinematics.

Finally, the exclusive two-photon production of a pair of leptons is analysed in the last part of this work. This process is particularly important as it is a standard candle used as a reference process when studying other photon interaction. The comparatively large number of exclusively produced muon pairs allows to study these events from the LHC start-up. Several applications are then possible, from detector alignment to the absolute luminosity measurement.

This document is divided into four main sections: the first three parts introduce the theoretical (part I), hardware (part II) and software (part III) concepts on which the analysis (part IV) relies.

The first part describes the physics background behind the main subjects of this dissertation, namely the high energy photon interactions and the concept of collider luminosity. The theory of photon-photon and photon-proton interactions is described and some cross-sections are given after reasonable detector acceptance cuts. Luminosity is defined and several techniques are presented for its measurement.

The second part deals with the experimental aspects, introducing the LHC accelerator, giving details on each part of the CMS detector and on forward instrumentation. Some R&D on silicon edgeless sensors, providing possible technologies for near-beam detectors, is further developed at the end of this section.

The third part introduces the software framework in CMS and gives an insight into online selection and generic reconstruction. A simulation program called HECTOR has been developed for the transport of particles in beamline and in particular of forward protons scattered in γ interactions. This software is exhaustively addressed in this section.

Finally, an analysis of exclusive dimuon production at CMS is discussed in the last part, as well as possible applications of these selected events. In particular, emphasis is put on luminosity measurement at the LHC with dimuons. Using a similar selection procedure, the photoproduction of Upsilon mesons is also studied.

Part I

Introduction and motivation

Chapter 1

Photon interactions at the LHC

Photon-induced collisions, namely γp and $\gamma\gamma$, constitute a testing ground for physics within and beyond the Standard Model. Their study at the LHC *is a natural extension of their measurements at* LEP, TEVATRON, RHIC *and* HERA. *The high relative luminosity and the significant cross-sections lead to a considerable event rate of high-energy processes, above the electroweak scale. These processes are theoretically well-understood. According to the Equivalent Photon Approximation, one can factorise a photon exchange and a photon interaction with a parton or another photon. Clean experimental signatures, i.e. forward rapidity gaps and very forward proton detection, allow for tagging photon interactions.*

1.1 Potential of $\gamma\gamma$ and γp interactions at the LHC

The major focus of this document concerns some aspects of the photon interactions at the Large Hadron Collider (LHC) [1, 2, 3]. The LHC is a powerful collider located at CERN in Geneva. It will accelerate two proton beams and collide them at 14 TeV, reaching unprecedented centre-of-mass energies. The LHC intensity of collisions, or *luminosity* $\mathcal{L}$, will grow from about 10^{27} to 10^{34} cm^{-2}s^{-1}.

One drawback of such hadron colliders in general is the uncertainty on the initial state, as the momentum fraction of the interacting partons (gluons or quarks) is unknown. Another difficulty is the high multiplicity of tracks, due to gluon radiation, the multiple parton interactions and the hadronisation of the proton remnants in forward directions. Moreover, for a luminosity $\mathcal{L}$ around 10^{33} cm^{-2}s^{-1} and above, multiple proton-proton collisions per bunch crossing are highly probable. This leads to a relatively large *occupancy* of the detector channels even at low luminosities.

Photon interactions are a class of events with cleaner topologies than processes involving strong interactions. No colour flow is associated to the photon exchange, leading to lower particle multiplicities. Moreover, if the photon emission is *elastic*, i.e. if the proton remains intact, it can be possible to experimentally constrain the initial state. The probability that the emitting proton remains intact is high for a relatively low photon *virtuality* Q^2, defined as follows:

$$(p_2 - p_1)^2 = q^2 = -Q^2, \tag{1.1}$$

where p_1 and p_2 are the $4-$momenta of the protons, before and after the γ emission, respectively, and q is the $4-$momentum transfer. The emitted photon interacts either with a proton or with another photon (Fig. 1.1). The effective $\gamma\gamma$ and γp luminosities are significant, resulting in considerable rates of produced events. Even if these luminosities are lower than the pp ones ($\mathcal{O}(10^{-3})$ and $\mathcal{O}(10^{-2})$, respectively [2]), the large cross-section values maintain the event rates such that an interesting physics programme can be carried out.

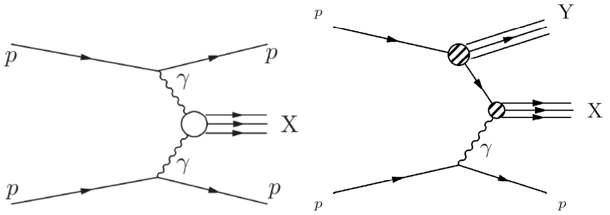

Figure 1.1: Examples of Feynman diagrams for the $\gamma\gamma$ and γp interactions. The photon is emitted by a proton, which is scattered in a forward direction. Photon-photon collision (left) happens when both incoming protons emit a photon, yielding a central system X and two forward protons in the final state. In case of γp process (right), this photon interacts with a parton and creates a system X. The photon-parton interaction breaks one interacting proton into a Y remnant.

1.1.1 Interactions between two photons

As both interacting protons could remain intact in $\gamma\gamma$ events, this class of events provides very clean event topologies. This is seen for instance in the case of exclusive pair production of leptons (e^+e^-, $\mu^+\mu^-$) [4,5], gauge bosons (W^+W^-, Z^0Z^0) [6], or Super-Symmetric (SUSY) particles [7,8]. These are called *exclusive* productions as only a given set of particles is produced (for instance, two charged fermions) and nothing else.

The exclusive production of pairs of light charged leptons, $\gamma\gamma \to \ell^+\ell^-$, is discussed in detail in Chapter 8. This theoretically well-understood process can be used for luminosity measurement [5, 9, 10, 11] or the calibration of the Very Forward Detectors (VFD) [12, 13].

The triple and quartic gauge coupling measurements are sensitive to physics beyond the Standard Model (SM). Quartic Gauge Couplings, for $\gamma\gamma W^+W^-$ and $\gamma\gamma Z^0Z^0$ have been studied and constrained previously at LEP [16]. The current limits could be improved upon in a very short time at the LHC, even at low luminosity [6].

The exclusive production of charged supersymmetric particles is also possible, although the corresponding cross-sections are small. For a few particular SUSY models, preliminary studies show that realistic SUSY analyses at the LHC are possible in $\gamma\gamma$ interactions [8]. However, this will require a large integrated luminosity and sophisticated methods for background rejection.

Photon-photon fusion will also allow generic searches for new heavy charged particles produced in pairs. Heavy Dirac-Schwinger magnetic monopoles m are favoured by some models in photon-photon fusion: $\gamma\gamma \to m\bar{m}$. According to the models, the LHC would be very adequate for their production, with high cross-section and large masses [14]. The current experimental mass threshold is set at 370 GeV (95% CL) by CDF [15]. Their detection would rely on either two long-living final state monopoles or two photons in the final state ($\gamma\gamma \to m\bar{m} \to \gamma\gamma$).

The cross-section values are determined by the charge, mass and spin of the produced particles (TAB. 1.1). Photon-photon interactions have been largely studied in e^+e^- colliders, like LEP [16].

Process $\gamma\gamma \to X$	$\boldsymbol{\sigma}_{\textbf{prod}}$ (fb)		**Generator**	
$\mu^+\mu^-$	74.7	$\times 10^3$	LPAIR	$p_T > 2.5$ GeV
e^+e^-	10.4	$\times 10^3$	"	$p_T > 5.5$ GeV
W^+W^-	108.5		MG/ME	-
f^+f^-	4.064		"	$m_f = 100$ GeV
$\tilde{f}^+\tilde{f}^-$	0.680		"	$m_{\tilde{f}} = 100$ GeV
$H \to b\bar{b}$	0.154		"	$m_H = 120$ GeV
$m\bar{m}$	~ 5	$\times 10^3$	-	$m_m = 1000$ GeV

Table 1.1: Typical values for the leading order of the cross-sections of some $\gamma\gamma$ processes, $\sigma_{pp(\gamma\gamma\to X)pp}$, for lepton pairs $\ell = e, \mu$, gauge boson pairs W, Higgs boson H, supersymmetric fermions f and scalars $\tilde{f}$ and Dirac magnetic monopoles m [1, 5, 15].

1.1.2 Photoproduction

The γq and γg interactions are deep inelastic interactions referred to as *photoproduction*. Midway from pp to $\gamma\gamma$, photoproduction yields events with a high cross-section (TAB. 1.2).

Interesting processes are, for instance, the associated photoproduction of W and Higgs bosons for studying the scalar sector [17]. Similarly, photoproduction of a W and a t quark is very valuable, as it probes the $|V_{tb}|$ element of the Cabibbo-Kobayashi-Maskawa (CKM) matrix, via the $\gamma b \to Wt$ process [17,18].

The anomalous production of a top quark through γut and γct vertices, i.e. via Flavour Changing Neutral Currents (FCNC[1]), can be better constrained [19] with respect to the current experimental limits on the couplings [20].

The photoproduction of a $t\bar{t}$ pair is also interesting, thanks to its large cross-section. These events could be used to measure parameters like the t charge or mass [1,3]. In general, studies of γp interactions at the LHC will be complementary to the studies done in Deep Inelastic Scattering in ep colliders [21,22,23].

Process	$\boldsymbol{\sigma_{\text{prod}}}$ **(fb)**	**Generator**	
$\gamma q \to WHq'$	23.0	MG/ME	$m_H = 115$ GeV
$\gamma q \to WHq'$	17.5	〃	$m_H = 170$ GeV
$\gamma q/g \to WX$	> 90	〃	-
$\gamma g \to t\bar{t}$	1.54	〃	-
$\gamma q \to Wt$	1.01	〃	-
$\gamma q \to t$	$(368\ k^2_{tu\gamma} + 122\ k^2_{tc\gamma}) \times 10^3$	CompHEP	-

Table 1.2: Typical values of the leading-order cross-sections for photoproduction (photon-quark and photon-gluon), $\sigma_{pp(\gamma p \to X)pY}$ [1, 17, 19]. The effective couplings $k_{tq\gamma}$ are real and positive: the best upper experimental limit on $k^2_{tu\gamma}$ is 0.14 [20], while $k^2_{tc\gamma}$ has never been probed. All these values assume $p_T^{\text{jet}} > 10$ GeV, $|\eta^{\text{jet}}| < 5$, $\Delta R(jet_1, jet_2) > 0.3$.

1.1.3 Diffractive photoproduction

The *diffractive photoproduction* is a class of γp interactions involving colourless soft QCD interactions. It provides interesting physics, like for the photoproduction of heavy quarks and vector mesons [5, 24, 25]. However, meson masses being relatively small, they restrict the kinematics of their decay products to a range very close to the lower limits of detector acceptance and trigger selection thresholds. In practice, only the heaviest ones, namely the bottomonium states (i.e. $b\bar{b}$ bound states), like the upsilon Υ(1S), Υ(2S) and Υ(3S) resonances, can be observed in LHC experiments. The observation of the $\gamma p \to \Upsilon p \to \mu^+\mu^- p$ process in CMS is discussed in Chapter 10.

The analysis of the hadronic decay of a diffractive photoproduction of a Z^0 benefits from the low detector occupancy, as the hadronic activity is not polluted by remnants of the proton collision [26].

---

[1] Flavour Changing Neutral Currents (FCNC) are forbidden in SM at tree level, although they appear in many of its extensions.

This class of events (Tab. 1.3) probes the diffractive structure function of the protons, as the photon flux is well-understood. Moreover, the cross-section measurements will extend the range of current measurements to the LHC energies. Diffractive photoproduction $\gamma I\!P \to X$ is not theoretically well-understood due to the limitations to the limited applicability of perturbative methods to diffractive processes. These limitations depend on the energy scale of the produced system X. Diffractive photoproduction has already been studied in many previous experiments [27].

Process	$\boldsymbol{\sigma_{\mathrm{prod}}}$ **(pb)**	**Generator**
$\gamma p \to \Upsilon p \to \mu^+\mu^- p$	12 (1S)	Phiti
$\gamma p \to \Upsilon p \to \mu^+\mu^- p$	39 (1S), 13 (2S), 10 (3S)	Starlight
$\gamma p \to Z^0 p$	69	-

Table 1.3: Typical values for diffractive photoproduction γp cross-sections, at pp level $\sigma_{pp(\gamma I\!P \to X)pp}$ [5, 26]. The cross-section values for Υ states include the corresponding branching ratio $BR(\Upsilon \to \mu^+\mu^-)$ into a muon pair.

Photon-induced processes can be theoretically divided into two steps: (1) the emission of a photon by an incoming proton and (2) the interaction of the photon with another photon or with a proton. This approximation, involving an incoming *equivalent photon flux*, is explained in the next section, as well as corrections due to the rescattering effects.

1.2 Theoretical description: EPA, proton dissociation, rescattering effects

The electromagnetic field of the colliding hadrons (protons or heavy ions) at the LHC can be seen as an incoming photon flux, distributed with some density $dN(x, Q^2)$. The photon emission characterises its energy E_γ (or its energy fraction $x = E_\gamma/E$, where E is the hadron energy), virtuality Q^2 and polarisation. The *equivalent photon approximation* (EPA) [28] factorises the dependence on photon virtuality Q^2 from the cross-section of the photon-induced process (σ_γ or $\sigma_{\gamma p}$) to the equivalent photon flux dN. Subsequently, the hadron-hadron collision is written:

$$d\sigma_{pp} = \sigma_{\gamma p}(x, s)\ dN(x, Q^2) \qquad \text{for } \gamma p \text{ interactions} \qquad (1.2)$$

$$d\sigma_{pp} = \sigma_{\gamma\gamma}(x_1, x_2, s)\ dN(x_1, Q_1^2)\ dN(x_2, Q_2^2) \qquad \text{for } \gamma\gamma \text{ interactions} \qquad (1.3)$$

where $s = 4E_1E_2$ is the squared centre of mass system (c.m.s) energy of the hadron collision.

The EPA considers the interacting photon as real and with no polarisation. It is valid as long as this cross-section is not too dependent on Q^2. A dynamical cut-off Λ_γ fixes the validity of the approximation: the photon-level cross-section σ_γ should be insensitive to Q^2 while $Q^2 < \Lambda_\gamma$, and should drop quickly if Q^2 is larger. For instance, the EPA is not valid in cases where there is a production of light particles (e.g., $\gamma\gamma \to e^+e^-$).

Flux from a point-like hadron

Assuming quasi-real photons ($Q^2/E_\gamma^2 \ll 1$), the photon flux from an incoming point-like proton with an energy E and a mass m_p can be written

$$dN(x,Q^2) = \frac{\alpha}{\pi}\,\frac{dQ^2}{Q^2}\,\frac{dx}{x}\left[(1-x)\left(1-\frac{Q^2_{\text{min}}}{Q^2}\right)+\frac{x^2}{2}\right], \tag{1.4}$$

where α is the fine-structure constant and where the minimum photon virtuality is fixed from kinematics to

$$Q^2_{\text{min}} \approx m_p^2\,\frac{x^2}{1-x}. \tag{1.5}$$

Flux from a non point-like hadron

If the photon flux originates in a nucleon which is not considered as point-like, the electric and magnetic form factors should be taken into account in Eq. 1.4. These factors are defined via the matrix element of the electromagnetic current [29]:

$$\langle N(P')|j_\mu^{\text{em}}|N(P)\rangle = \bar{N}(P')\big[\gamma_\mu F_1(Q^2) - i\frac{\sigma_{\mu\nu}q^\nu}{2m_N}F_2(Q^2)\big]N(P), \tag{1.6}$$

where P and P' are the $4-$momentum of the nucleon of mass m_N before and after photon emission; F_1 and F_2 are the Dirac and Pauli form factors, respectively; $\sigma_{\mu\nu} = \gamma_\mu\gamma_\nu - \gamma_\nu\gamma_\mu$; $q = P - P'$ and $Q^2 = -q^2 > 0$ as before. The Sachs form factors are expressed in terms of F_1 and F_2 electromagnetic functions:

$$G_E(Q^2) = F_1(Q^2) - \frac{Q^2}{4m_N}F_2(Q^2) \tag{1.7}$$

$$G_M(Q^2) = F_1(Q^2) + F_2(Q^2). \tag{1.8}$$

At $Q^2 = 0$, these functions correspond to the total charge and to the magnetic momentum μ_p of the proton, respectively:

$$G_E(0) = 1 \tag{1.9}$$

$$G_M(0) = \mu_p = 2.79. \tag{1.10}$$

In the usual *dipole approximation*, the dependence on Q^2 of the form factors is explicit (Fig. 1.2):

$$G_E(Q^2) = \frac{G_M(Q^2)}{\mu_p} = \left(1+\frac{Q^2}{0.71\ \text{GeV}^2}\right)^{-2}. \tag{1.11}$$

In the EPA, the photon flux from a proton can then be written in terms of the form factors:

$$dN(x,Q^2) = \frac{\alpha}{\pi}\,\frac{dQ^2}{Q^2}\,\frac{dx}{x}\left[(1-x)\left(1-\frac{Q^2_{\min}}{Q^2}\right)\,F_E + \frac{x^2}{2}\,F_M\right], \tag{1.12}$$

where the functions F_E and F_M are defined as follows:

$$F_E = \frac{4m_N^2 G_E^2 + Q^2 G_M^2}{4m_N^2 + Q^2} \tag{1.13}$$

$$F_M = G_M^2. \tag{1.14}$$

In this case, the dynamical cut-off Λ_γ constraining the validity of the approximation arises from the proton form factors.

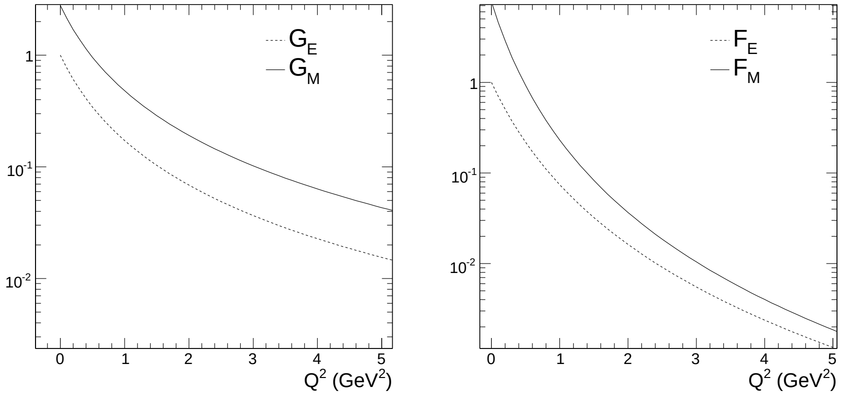

Figure 1.2: Dependence of the proton electromagnetic form factors on the photon virtuality Q^2. The Q^2 dependence is steep for the Sachs form factors G_E and G_M (left) and the F_E and F_M functions, as introduced in Eq. 1.12.

Proton dissociation

This description also applies when the photon emission is not elastic, i.e. when the proton *dissociates* into a heavier system. This dissociative system of mass m_Y usually has a large Lorentz boost in the forward directions. Eq. 1.12 should be changed by introducing structure functions instead of F_E and F_M. The minimum photon virtuality also becomes:

$$Q^2_{\min} \approx \left[m_Y^2 \frac{1}{1-x} - m_p^2\right] x. \tag{1.15}$$

Photon-photon interaction could then lead to three types of topologies : elastic, semi-elastic or fully inelastic. In elastic processes both protons are scattered elastically after photon exchange. In semi-elastic processes, one of the scattered proton dissociates. Fully inelastic processes have both protons dissociated in the final state.

Process cross-section and integrated photon flux

In photoproduction, the pp interaction cross-section is given by the convolution of the γp interaction cross-section $\sigma_{\gamma p}$ with the relative, Q^2-integrated, luminosity spectrum f_γ:

$$\sigma_{pp(\gamma p\to X)pY}(s) = \int_{s_{\min}/s}^{1} dx\ f_\gamma(x)\ \sigma_{\gamma p\to X}(x,s). \tag{1.16}$$

The f_γ spectrum is the integral of the photon flux over Q^2 and the integral bounds are given by kinematic limits or experimental constraints:

$$f_\gamma(x) = \int_{Q^2_{\min}}^{Q^2_{\max}} dN(x,Q^2)dQ^2. \tag{1.17}$$

Similarly, for $\gamma\gamma$ interactions, the process cross-section is factorised from the photon-photon subprocess by a relative luminosity:

$$\sigma_{pp(\gamma\gamma\to X)pp}(s) = \int_{W_{\min}}^{\sqrt{s}} dW\ \frac{\mathrm{dL}_{\gamma\gamma}}{dW}(W,s)\ \sigma_{\gamma\gamma\to X}(W)\ , \tag{1.18}$$

where W is the $\gamma\gamma$ c.m.s energy and the relative luminosity $\frac{\mathrm{dL}_{\gamma\gamma}}{dW}$ encompasses the integrated flux of each photon:

$$\frac{dL_{\gamma\gamma}}{dW}(W,s) = \int_{W^2/s}^{1} 2W\ f_\gamma(x)\ f_\gamma\left(\frac{W^2}{xs}\right)\ \frac{dx}{xs}. \tag{1.19}$$

The spectrum is peaked at low photon energy (Fig. 1.3), such that W is usually much smaller than the total pp centre of mass energy; it remains significant for energies up to 1 TeV. The photon virtuality is usually small in the elastic case, $\langle Q^2\rangle \approx 0.01\ \mathrm{GeV}^2$.

Rescattering effects

The *rescattering effects* correspond to secondary (strong) interactions occurring between the two incoming protons, independently from the photon interaction. The rescattering could lead to the creation of soft particles in the hemisphere where the proton exits, and have a non-negligible impact on the experimental signature. The rescattering effects can be described by the effective impact parameter d of the pp interaction with a γ exchange, where a small d can lead to important rescattering effects. The closer the protons (low d), the stronger

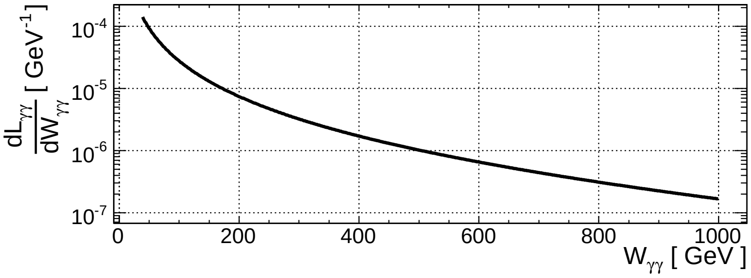

Figure 1.3: Expected relative luminosity for the $\gamma\gamma$ interactions at the LHC, as a function of the centre of mass energy of the $\gamma\gamma$ system, $W_{\gamma\gamma}$. This effective luminosity includes the emission spectrum for both photons (Eq. 1.19). Adapted from [1].

they can feel each other. Interactions with low Q^2 can be interpreted in terms of a large impact parameter d:

$$d \sim 1/|Q|.$$

Photon-induced processes are thus usually safe in terms of rescatterings, as the average virtuality is small. The experimental implication of these rescattering effects and the low values of Q^2 for photon-induced processes are discussed below in terms of the *survival factor* $\widehat{S}^2$.

1.3 Experimental approach: tagging $\gamma\gamma$ and γp events at low luminosity

In hadron colliders, as the photon interactions are less probable than the strong ones, it is necessary to use some remarkable signatures to *tag* them. The event measurement relies on a set of detectors. The extension of detector coverage is usually expressed in terms of the *pseudorapidity* η, which relates to the polar angle θ as follows:

$$\eta = -\ln\Big(\tan\frac{\theta}{2}\Big). \tag{1.20}$$

The higher the pseudorapidity, the more forward the particle. Conversely, particles with a small η are said to be *central*. In order to be observed by one of the detectors, it is required that particles enter its η coverage. Moreover, if the detector has a solenoidal magnetic field, the *transverse momentum* $p_T = \sqrt{p_x^2 + p_y^2}$ should be high enough ($\mathcal{O}$[GeV]) to reach at least the inner tracking system.

The spatial coverage of the central detector is incomplete, independently from its technology: the opening by which the beams enter and exit the detector are leaks where final state particles can escape without being measured. In particular, when a proton emits a photon, it is scattered with such a small angle that it exits the central detector by the beampipe. Thus, independently of the event final state in the central detector, two experimental signatures arise for photon interactions [2]:

- When an interacting proton exits the central detector without being detected, the energy deposit in this forward region is low, compared to an event where the proton is destroyed and where the proton remnant is seen by the calorimeters. Subsequently, for photon interactions, at least one of the two forward regions of the central detector has a significant lack of energy. In particular, for γp events, looking at the minimum of the energies measured in each forward region allows the distinction between γ-induced interactions and usual pp ones. The region devoid of particles defines a forward *large rapidity gap* (LRG). Applying a selection cut on this quantity rejects usual pp backgrounds (Fig. 1.4).
- After the elastic emission of a photon, the emitting proton is scattered and exits the central detector along with beam protons. It will be transported in the beamline with the beam protons. However, as its energy $E = E_p - E_\gamma$ is lower than the beam energy, its trajectory decouples from the beam path into the very forward region. Along its path in the beam line, the magnetic elements deflect it much further away than the beam envelope limit, as the effect of the magnetic field depends on the particle momentum. Consequently, in the very forward region, this leading proton can be safely detected with near-beam detectors (Fig. 1.5). Moreover, its *very forward detection* does not only allow the event to be tagged, but also provides some information on the scattered proton energy, which constraints the initial state.

Following the literature [2], a *double tag* is assigned to events where two leading protons have been identified, as expected for elastic two-photon interactions. The relative luminosity distribution given by the EPA can be constrained by the VFD acceptance. This gives the range of photon-photon c.m.s energies accessible by the LHC very forward detectors (Fig. 1.6). Similarly, *single tagged* events are events which have been reconstructed with only one proton tag corresponding either to γp processes or to $\gamma\gamma$ events with one undetected proton.

Proton dissociation

With the photon virtuality Q^2 being generally low:

$$Q^2 \lesssim 0.1 \text{ GeV}^2, \tag{1.21}$$

the rescattering effects are suppressed [48] and the probability that the emitting proton does not dissociate remains high. Moreover, since the typical centre-of-mass energy W in $\gamma\gamma$ and γp interaction is small compared to the nominal

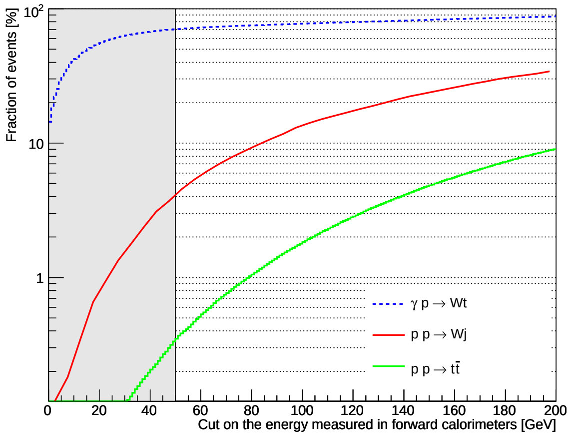

Figure 1.4: Tagging photon-induced interactions by using the very low activity in one forward region of the central detector. Energy distribution of the gap side for $\gamma p \rightarrow Wt$ events and for $pp \rightarrow Wj$ and $pp \rightarrow t\bar{t}$ events (semi-leptonic topologies). The rapidity gap side corresponds to the forward region with the minimal total energy deposit (here *forward* means $3 \leq |\eta| \leq 5$). As an illustration a selection cut of 50 GeV would preserve most (97%) of the $\gamma p \rightarrow Wt$ signal while rejecting a large fraction ($> 95\%$) of the pp semi-leptonic backgrounds [18].

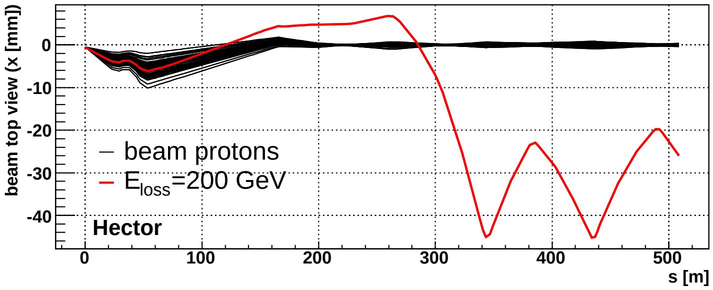

Figure 1.5: Tagging photon-induced interactions by the observation of a scattered proton in very forward detector. Simulated path of a proton which did not dissociate after the emission of a 200 GeV photon at the IP5 (thick line) and with respect to beam protons (thin dark lines), using Hector for the simulation [13]. Forward near-beam detectors could tag such a photon-induced interaction by detecting this leading proton without being too close to the beam.

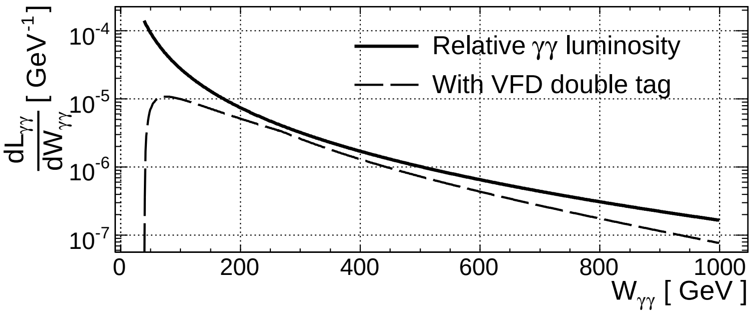

Figure 1.6: Expected relative luminosity for the $\gamma\gamma$ interactions at the LHC, as a function of the centre of mass energy of the $\gamma\gamma$ system, $W_{\gamma\gamma}$. Full line is total luminosity. The effective luminosity (dashed line) includes the effect of the acceptance of very forward detectors (VFDs), located at 220 m and 420 m away from the interaction point at the LHC. Adapted from [1].

beam proton energy, even if the emitting proton dissociates, the boost of the remnant increases the chance that the dissociative product is not seen by the central detector (Fig. 1.7). Possible forward near-beam detectors can however help in measuring the dissociative system.

The forward detection is completely different whether the proton dissociates or not, but both cases are similar in the central detector, which sees very little activity in the hemisphere where the emitting proton escapes. In general, the rapidity gap is hence preserved in the case of proton dissociation. A corresponding constraint on the detector activity in forward regions is then possible for the selection of these events.

Event pile-up

The discussion thus far holds in ideal collision conditions, when no *event pile-up* (i.e. extra simultaneous *pp* collisions occurring at the same bunch crossing) is present. This point is crucial as the tagging depends either on a lack of regional detector activity or on a detection of leading scattered protons, far away from the interaction point. These *zero-conditions* are very sensitive to event pile-up as any additional, simultaneous interaction, could either leave some hits in the empty region (filling in the rapidity gap), or throw a particle directly in the VFD, faking a photon-induced interaction. Dealing with low luminosity and taking benefit from the complementarity of all detector parts is crucial for a proper tagging. Solutions at higher luminosities are outlined at the end of the next section.

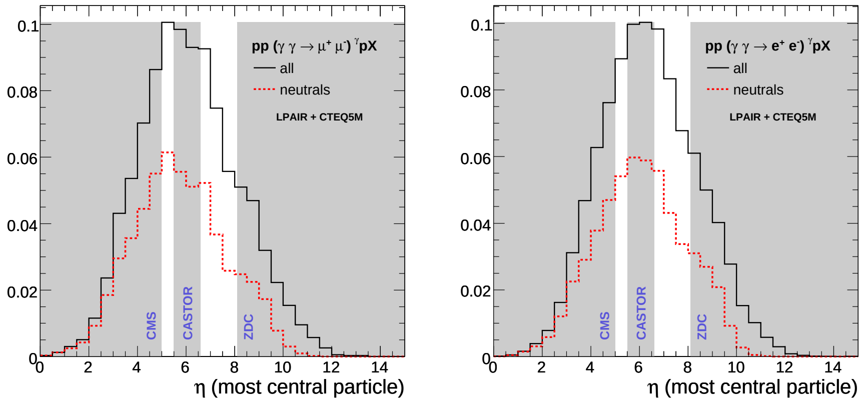

Figure 1.7: η distribution of the most central particle of a proton dissociative system, for a singly-dissociated $pp(\gamma\gamma \to \mu^+\mu^-)pX$ (left) and $pp(\gamma\gamma \to e^+e^-)pX$ (right) events – using CTEQ5M fragmentation functions. The shaded areas correspond to the acceptance of the central detector CMS ($|\eta| < 5$) and two possible extensions, respectively, such as the CASTOR ($5.5 < |\eta| < 6.6$) and the ZDC calorimeters ($|\eta_{neutrals}| > 8.1$). The plots are normalised to unity.

1.4 Diffraction as background for photon physics

Diffraction is another class of interactions at the LHC where at least one proton survives. Unlike photon interactions, which are electromagnetic processes, diffraction is driven by the strong interaction [43]. Diffractive events are characterised by the exchange of a colourless composite object: the *pomeron* ($I\!\!P$). The pomeron is usually interpreted as a set of gluons carrying altogether the same quantum numbers as the vacuum – the simplest picture of a $I\!\!P$ is a gluon pair. Diffractive events are low energy strong interactions. Subsequently the perturbative approach is not always valid, making calculations more difficult. Similarly to photon interactions, there is no net colour flow when a pomeron is exchanged, leading to a large gap in rapidity in the detector. This corresponds experimentally to a *large rapidity gap*.

Interactions involving pomeron exchanges are *Single-Diffractive*, *Double Diffractive*, *Double Pomeron Exchange* (DPE) and *Single+Double Diffractive* events (Fig. 1.8). Elastic interactions are pomeron driven. *Central Exclusive Processes* (CEP) refer to $pp \to p \oplus X \oplus p$ events, where the central final state X is well-separated from the forward scattered protons by large rapidity gaps (symbolised here by $\oplus$). CEP corresponds to $\gamma\gamma$ or exclusive double diffractive events. Diffractive photoproduction can be seen as a $\gamma I\!\!P$ interaction.

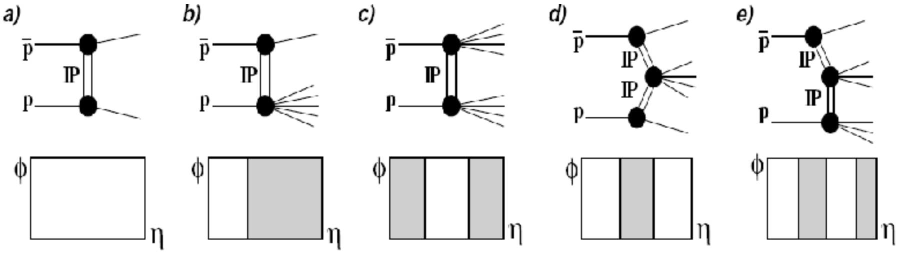

Elastic

Single-Diffractive (SD)

Double-Diffractive (DD)

Double Pomeron Exchange (DPE)

Single+Double Diffractive (SDD)

Figure 1.8: Examples of diffractive events [44]

The $4-$momentum transfer squared[2] t in a pomeron exchange is generally larger than that in a photon exchange. For low $|q^2|$, the yield of photons is then enhanced while the pomeron, being composite, does not experience this low $|t|$ effect. Higher $|t|$ on average means that the scattering occurs at smaller impact parameter d in diffraction. These effects can generate secondary particles populating the rapidity gaps, which can possibly destroy the LRG experimental signature. The *Survival Factor* $\widehat{S}^2$ expresses the probability that the rapidity gap outlives rescatterings. A major outcome of the different momentum transfer ranges for photon- and pomeron- interactions is the fact that $\widehat{S}^2$ drops drastically for diffractive events. In practice, this strongly constrains the observability of the central exclusive production like $pp \to p \oplus H \oplus p$ with $\widehat{S}^2_{I\!PI\!P\to H} \simeq 0.02$. On the contrary, as $\gamma\gamma$ interactions deal with two large impact parameters, they are preserved from rescattering ($pp \to p \oplus H \oplus p$ with $\widehat{S}^2_{\gamma\gamma\to H} \simeq 0.86$) [48, 49, 50].

As their cross-sections are large[3], a significant amount of diffractive proton (i.e. protons scattered by diffraction) are seen by the forward detectors. For luminosities $\mathcal{L}$ above 1×10^{33} cm^{-2}s^{-1}, when the event pile-up becomes non-negligible, possible diffractive events could arise as backgrounds in photon-induced process analyses. This will happen for usual dissociative events producing a similar final state as the one of interest, simultaneously of a diffractive event with at least one proton tagged in very forward regions. As a consequence, handling the pile-up diffractive events tagged by the VFDs properly is a major concern when studying photon physics at high luminosity at the LHC. A possibility to reduce this issue is to check that all observed particles come from the same point in space, or *vertex*. Vertexing will include tracker information for centrally produced final state particles. For the scattered protons, very forward timing detectors, synchronised on the LHC clock, can produce a

---

[2] The $4-$momentum transfer squared t and q^2 refer to the same quantity: $t = q^2 = -Q^2$, where Q^2 is the virtuality, even though t is usually used for pomeron exchange and q^2 for photon exchange.

[3] Excluding elastic scattering, diffractive processes are expected to contribute about 25% of the total pp cross-section at the LHC [21].

time-of-flight measurement. When knowing the position of the timing detector in the beamline, the time measurement gives an estimate of the vertex longitudinal position[4] in the interaction region [78]. Matching this time-of-flight measurement with the track information should provide reliable vertex identification, assuming that the VFD time resolution is good enough (Chapter 4). This vertex identification discriminates the final state particles to consider for analyses in the case of pile-up events.

---

[4] The luminous region in the CMS interaction point is about 30 cm in z coordinate.

Chapter 2

Luminosity

Most of measurements at the LHC are based on counting experiments. The process cross-section is obtained by dividing the event rate by an experimental parameter, called luminosity. This parameter is thus crucial, as it relates the observations to the theoretical predictions. Luminosity is monitored via relative and absolute methods, detailed in this chapter. Integrated luminosity represents the amount of accumulated data over time. Determining precise luminosity is challenging, but remains essential for a proper experimental estimation of process cross-sections.

2.1 Definition of luminosity

The LHC experiments aim amongst other things to measure process cross-sections, which requires counting the number of corresponding events. The rate of events R is given by the product of the process cross-section σ and of the *luminosity* $\mathcal{L}$ delivered by the collider:

$$R = \mathcal{L} \times \sigma \tag{2.1}$$

The luminosity is the rate of interactions per units of cross-section ($\mathrm{cm}^{-2}\mathrm{s}^{-1}$ or $\mathrm{fb}^{-1}\mathrm{s}^{-1}$). The cross-section is computed process by process, from the corresponding Feynman diagrams like in Tab. 1.1, 1.2 and 1.3. On the contrary, the luminosity is process-independent and is completely determined by the colliding beam properties. It can vary from run to run, or even during a physical run, as the bunches are depopulated by the collisions. These variations affect the total number of events counted by the experiments.

A constant monitoring of the luminosity is thus of the highest importance. In practice, the limited phase space coverage and detection efficiencies affect the event counting. Still, they can be factorised out and absorbed by the cross-section term. This lets the luminosity depend exclusively on beam parameters.

Its expression for head-on colliding bunches is [64]:

$$\mathcal{L} = f \; \frac{\sum_k N_1^k N_2^k}{4\pi \; \sigma_x^* \; \sigma_y^*}, \tag{2.2}$$

where f is the beam revolution frequency, N_1^k and N_2^k the number of particles in the colliding bunches k, and the Gaussian deviations σ_x^* and σ_y^* represent the horizontal and vertical bunch widths at the IP. As long as the accelerated particles are in a relativistic regime, the beamline length defines the revolution frequency, that is subsequently fixed as long as the beam path does not change. On the other hand, the other parameters are tunable in order to fulfil luminosity goals. The number of particles N_i^k per bunch or the number of bunches k_B themselves can be increased. If these numbers get too large, the interactions between particles of the same bunch or of neighbouring bunches could be non-negligible, creating instabilities or particle losses. Similarly, high densities of bunches in the beamline could lead to multiple unwanted interaction regions. The application of a crossing angle prevents such undesirable collision points, at the price of the collision being no longer head-on anymore. The beam transverse dimensions at the IP σ_x^* and σ_y^* can also be reduced for a larger luminosity.

In a multi-bunch machine, it is highly important to monitor the luminosity bunch per bunch. If the beam filling evolves in time, bunches could be different within a given *train* (i.e., the set of bunches making a beam). This results in different pile-up conditions. Monitoring the bunch per bunch luminosity provides accelerator operators and physicists with important information.

As a rule of thumb, it is convenient to remember the unit conversion:

$$\mathcal{L} = 10^{33}\ \text{cm}^{-2}\text{s}^{-1} = 1\ \text{nb}^{-1}\text{s}^{-1} = 10^{-6}\ \text{fb}^{-1}\text{s}^{-1}.$$

The accumulation of data over time is quantified by the *integrated luminosity* L. This is the ultimate parameter to optimise for physics, as it provides the link between the total number of observed events and the predicted corresponding cross-section. Achieving a high luminosity is a major concern in modern accelerator. Recently, the HERA accelerator (DESY, Hamburg) has gathered $L = 779.9\ \text{pb}^{-1}$ at closedown, while its initial goal was 1 fb^{-1} [67]. Similarly, the luminosity of TEVATRON (at Fermilab, Chicago) will hardly reach 6 fb^{-1} by the end of 2009, while 3 fb^{-1} per year were expected after 2005 [68].

Several methods are available for the evaluation of the instantaneous luminosity $\mathcal{L}$. Absolute measurements provide the actual value for a given run but are usually slow. They can not provide the luminosity at the time scale of a bunch crossing (offline methods). These are used to calibrate the much faster relative methods, which continuously monitor the collision conditions (online methods).

- **Absolute** measurements rely on the observation of beam parameters (EQ. 2.2), or on some theoretically well-known physics processes.

- **Relative** monitoring requires very fast and reproducible measurements, covering the wide range of values achieved by the collider.

The rest of this chapter gives a deeper insight in the methods of estimating luminosity.

2.2 Absolute measurement from beam parameters

Luminosity can be fully characterised by collider parameters. Eq. 2.2 can be rewritten in accelerator terms:

$$\mathcal{L} = f \, \frac{\gamma k_B N_p^2}{4\pi \epsilon_n \beta^*} \, F \tag{2.3}$$

where γ is the Lorentz factor, f the revolution frequency, k_B the number of bunches and N_p the number of particle per bunch. In this formula, all bunches are assumed to be identical. The *normalised transverse emittance* ϵ_n corresponds to the area occupied by particles in the phase space. It is conserved along the beamline. The betatron function β^* is the lateral extent of the beam at the IP. The product $\epsilon_n \beta^*$ describes the beam focussing at the IP. The geometric reduction factor F, due to the crossing angle between colliding beams, is expressed by:

$$F = \left[1 + \left(\frac{\sigma_z}{\sigma_{x,y}} \tan \frac{\Phi}{2} \right)^2 \right]^{-\frac{1}{2}}. \tag{2.4}$$

It depends on the crossing angle Φ and the ratio of longitudinal extension of the bunches σ_z over their transverse width (being σ_x or σ_y depending if Φ is in the horizontal or vertical plane). The frequency f, the γ factor and the number of bunches k_B are adequately known during operation. The number of particles per bunch N_p is also well-measured with AC couplings or transformers measuring the beam current. The bunch dimensions are more difficult to obtain, in particular for the transverse directions σ_x^* and σ_y^*.

For low intensity beams, the insertion of a sensing wire in the beam path allows an estimation of the beam transverse size. The thin wire is moved and its interactions with the beam produce the signal. However, this measurement is destructive and can spoil the beam vacuum. Another method, developed by Van der Meer at the ISR [69] is based on the transverse displacement of one beam with respect to the other. If the relative luminosity is monitored with dedicated online instruments as well as the precise beam mutual positions, the absolute luminosity can be inferred from the evolution of the measured relative luminosity while scanning the beam position in the transverse plane:

$$\frac{\mathcal{L}}{\mathcal{L}_0} = \exp\left(- \left(\frac{\delta x}{2\sigma_x} \right)^2 - \left(\frac{\delta y}{2\sigma_y} \right)^2 \right), \tag{2.5}$$

$\delta_x(\sigma_x)$	$\delta_y(\sigma_y)$	$\mathcal{L}/\mathcal{L}_0$
0.1	0.1	0.995
0.2	0	0.990
0.2	0.2	0.980
0.3	0.3	0.956
0.4	0	0.961
0.4	0.4	0.923
0.5	0.5	0.882

Table 2.1: Required precision on the beam displacement for a luminosity calibration with a van der Meer scan. The displacements δ_x and δ_y are expressed in terms of the corresponding bunch width σ_x and σ_y.

where δx and δy are the beam displacements.

Tab. 2.1 collects some results on the required precision on beam displacement, to achieve a given accuracy. The beam displacements δ_x and δ_y are expressed in terms of the transverse beam sizes (σ_x and σ_y). For instance, a 1% determination requires a position resolution at the order of 0.2 σ in one direction and a perfect positioning in the other direction. But the bunch-by-bunch current should be also very well-known, to keep this precision. This is actually a major difference between the DC current of the ISR and the pulsed beams of the LHC. Direct currents are easily measured precisely, while a very good knowledge of the beam current at the bunch level is more difficult to achieve.

This method can not provide a precise measurement for modern colliders with bunched beams. Typical accuracy is about 10%.

2.3 Luminosity measurement with the central detector

2.3.1 Offline normalisation from physics

A calibration of relative methods can be done offline, directly from data taking: using electroweak physics ($\gamma\gamma \to \ell^+\ell^-$ or the inclusive production of heavy gauge bosons W and Z). The idea is to use a well-known process as a "standard candle" to normalise the luminosity, simply by computing the ratio between the predicted cross-section and the observed rate. The studied process should have: (1) a large cross-section in order to gather enough signal to reduce statistical errors in a very short time; (2) a clean signature for easy identification and selection, if possible using physical objects measured with low systematic bias; (3) a small theoretical uncertainty on its cross-section.

In general, leptons are good candidates for the signature, either from $\gamma\gamma \to \ell^+\ell^-$, $W^\pm \to \ell^\pm\nu_\ell$ or $Z \to \ell^+\ell^-$. For the gauge bosons, calculations up to NNLO lead to a theoretical uncertainty of about 4%. Most of the uncertainty comes from the strong coupling $\alpha_S(m_Z)$ and from the parton distribution functions in the proton. Any well-known and experimentally easy to detect process could serve in principle for estimating the luminosity if its *visible cross-section* (i.e. after all acceptance cuts) is high enough.

2.3.2 Online monitoring

An obvious way to monitor the luminosity is to measure the global event rate and see its evolution in time. This online monitoring, based on the observation of almost all events, can not rely on too large detection areas as the detector occupancy would be too large. Consequently, small area detectors, or larger but segmented ones will measure relative activity from bunch to bunch. Theoretical (like the one on the cross-section) and systematic uncertainties prevent us from using this raw data as an absolute measurement of luminosity. For instance the real detector acceptance is difficult to estimate. The measurement is subsequently not anymore an event rate estimate but an observation of the flow of particles. These monitoring methods thus require an *a posteriori* calibration from offline absolute measurements. However, the bunch-by-bunch monitoring abilities, using either dedicated instruments or some parts of the central detectors, make them very important for the LHC experiments. Detectors used for the luminosity monitoring are also expected to remain stable in operation.

2.4 Luminosity measurement with the forward detectors

The luminosity can be evaluated using the forward detectors for the measurement of elastic scattering events. When the data on the inelastic component is available, the *optical theorem* can be used. This will be used by the TOTEM experiment at the LHC. The Coulomb scattering allows a luminosity measurement based on the rate of elastic events only, as performed by the ATLAS experiment. Both methods require a delicate counting of the number of events at very small t values and dedicated LHC runs with special optics. Moreover, the luminosity calibration is performed at low luminosity and has to be carefully transferred to high luminosity runs.

2.4.1 Determination using the Optical Theorem

The observation of the number of elastic N_{el} and inelastic N_{inel} events, also provides an original way to evaluate both the total cross-section at a collider, and a reference for the calibration of luminosity monitors. These evaluations are based on the number of particle collisions at the interaction point.

$$\mathcal{L}\sigma_{\text{tot}} = N_{\text{el}} + N_{\text{inel}}, \tag{2.6}$$

and on the Optical Theorem (Eq. 2.7):

$$Im\big[f(\theta = 0)\big] = \frac{q}{4\pi}\sigma_{\text{tot}}, \tag{2.7}$$

where $f(\theta)$ is the elastic scattering amplitude, q is the c.m.s. momentum and σ_{tot} is the total cross-section. Using the definition of the ρ factor, $\rho = \frac{\mathcal{R}e[f(0)]}{\mathcal{I}m[f(0)]}$ and $\frac{d\sigma_{\text{el}}}{d\Omega}\Big|_{\theta=0} = |f(0)|^2$, one gets:

$$\frac{d\sigma_{\text{el}}}{d\Omega}\bigg|_{\theta=0} = \frac{1+\rho^2}{16\pi^2}\; q^2\sigma^2_{\text{tot}} \tag{2.8}$$

and subsequently:

$$\mathcal{L}\sigma^2_{\text{tot}} = \frac{16\pi}{(1+\rho^2)}\left(\frac{dN_{\text{el}}}{dt}\right)_{t=0}, \tag{2.9}$$

where t the momentum transfer during the pp interaction.
The combination of equations (2.6) and (2.9) lead to the evaluation of the total cross-section σ_{tot}:

$$\sigma_{\text{tot}} = \frac{16\pi}{(1+\rho^2)}\,\frac{(dN_{\text{el}}/dt)_{t=0}}{(N_{\text{el}}+N_{\text{inel}})} \tag{2.10}$$

and of the luminosity

$$\mathcal{L} = \frac{(1+\rho^2)}{16\pi}\,\frac{(N_{\text{el}}+N_{\text{inel}})^2}{(dN_{\text{el}}\;/dt)_{t=0}}. \tag{2.11}$$

This method has been used in the past at other colliders like S$p\bar{p}$S and Tevatron. Even if it looks promising (e.g., 2% at S$p\bar{p}$S), the measurement is in practice very delicate. The ρ factor is not well-known. The best experimental estimate comes from the COMPETE collaboration [62] with $\rho = 0.1361 \pm 0.0015^{+0.0058}_{-0.0025}$. The observation of all elastic and inelastic events requires a detector coverage very close to the beamline, with all the constraints that arise from their location.

Dedicated runs with favourable operation modes of the collider could be desirable for the N_{el} and N_{inel} observations. Even for perfect instruments (i.e. with 100% detection efficiency), the coverage can not be complete for the whole (θ, ϕ) plane, as both beams should enter and leave the detection zone. Consequently, the factor $\left(\frac{dN_{\text{el}}}{dt}\right)_{t=0}$ is obtained through the extrapolation to small angles of the $\frac{dN_{\text{el}}}{dt}$ measurement.

This extrapolation is subject to uncertainties that limit the power of the method. This is precisely what happened at the Tevatron, with contradicting luminosity estimates between E710/E811 and CDF experiments, due to a discrepancy of 2.6 standard deviation in their measurements of the total $p\bar{p}$ cross-section [58].

Using this method, the TOTEM experiment expect to reach a precision on luminosity measurement of about 7%, and ultimately below 3% [59].

2.4.2 Coulomb scattering

The total cross-section can also be obtained without using detectors for inelastic events. This measurement [63, 60] relies on Coulomb scattering (Eq. 2.12):

$$\frac{1}{\mathcal{L}}\frac{dN_{\mathrm{el}}}{dt}\Big|_{t\simeq 0} \approx \pi\Big(-\frac{2\alpha G_E^2(t)}{|t|} + \frac{\sigma_{\mathrm{tot}}}{4\pi}|i+\rho|e^{-b|t|/2}\Big)^2. \quad (2.12)$$

The first term is the Coulomb scattering amplitude, expressed by the fine-structure constant α and the Sachs electromagnetic form factor $G_E(t)$. The second part is the strong interaction (*nuclear*) term, which depends on total cross-section σ_{tot}, the ρ parameter and nuclear slope b. The number of elastic events is measured as a function of the squared transfer momentum $|t|$. This gives an estimate on the luminosity if the scattering functions are known. The theoretically well-known Coulomb component dominates for low $|t|$. However, accessing the region of interest in $|t|$ for this measurement could require runs with dedicated accelerator optics, with no crossing angle. Fitting the observed distribution could provide σ_{tot}, $\mathcal{L}$ and b simultaneously, but with a large correlation. Using proposed forward detectors, the ATLAS experiment expects to achieve a precision on luminosity measurement below 3% [61].

Summary

Luminosity determination at the LHC is very important but delicate, as many measurements rely on its value. Moreover, a good precision is desirable but challenging as recently seen at Tevatron. The pulsed structure of the interacting beams requires a bunch-per-bunch monitoring of luminosity and current. For the estimation from beam parameters, the size of the colliding bunches is needed. Moreover, a good determination of the bunch shape and intensity is challenging for hadron colliders like the LHC. Several methods are available, based for example on dedicated detectors or on physics processes. Any well-predicted process, with large cross-section and easy experimental signature is a good candidate for luminosity measurement. In general, a big interest is present in any novel approach for the luminosity measurement. Using exclusive dimuons for the determination of the integrated luminosity in CMS is detailed in Chapter 9.

Part II

From hardware...: particle accelerators and detectors

Chapter 3

The Large Hadron Collider

The Large Hadron Collider is a two-ring accelerator and collider located at CERN *in Geneva. It operates two beams of protons and is designed to collide them with challenging centre-of-mass energy ($\sqrt{s_{pp}} = 14$ TeV) and luminosities (in several phases, up to $\mathcal{L} = 10^{34}$ cm^{-2}s^{-1}). The total pp hadronic cross-section is more than 110 mb and the expected accumulation of data, expressed in terms of the integrated luminosity L, should reach $\mathcal{O}(100)$ fb^{-1} per year at $\mathcal{L} = 10^{34}$ cm^{-2}s^{-1}. High luminosity leads to a large level of event pile-up, with on average around 25 pp collisions per bunch crossing. The* LHC *relies on a thousand of magnets and very large cryogenic and vacuum systems. Five experiments, namely* ATLAS, ALICE, CMS, TOTEM *and* LHC*b, share its four interaction points.*

3.1 The collider and its acceleration chain

The Large Hadron Collider (LHC) is a 27 km long, circular accelerator. It is located in the LEP tunnel, 100 m underground, at CERN [64, 65]. It will accelerate and collide two beams of 7 TeV protons[1], reaching an unprecedented *pp* c.m.s energy of $\sqrt{s_{pp}} = 14$ TeV. With this energy, the protons are highly relativistic: $\gamma = 7461$ and $1 - \beta = 8.98 \times 10^{-9}$. The LHC will provide high statistics thanks to its large *pp* total hadronic cross-section and luminosity $\mathcal{L}$. Design parameters will be achieved after several phases: the luminosity will increase from 10^{27} to 10^{34} cm^{-2}s^{-1} and the *pp* collision energy will step at 0.9, 10 and 14 TeV. A precise theoretical determination of the total cross-section σ_{tot} is difficult, mainly due to the diffractive component: 125 ± 25 mb [66]. One of the best experimental estimates of the total expected *pp* cross-section is given by the COMPETE collaboration [62]:

$$\sigma_{\text{tot}}(\text{LHC}) = 111.5 \pm 1.2(\text{stat})^{+4.1}_{-2.1}(\text{syst})\ \text{mb}. \tag{3.1}$$

---

[1] A program of collisions of heavy ions, like $^{208}\text{Pb}^{82+}$, is also foreseen, but not described in this document.

Acceleration chain

The LHC relies on a chain of several subsystems from the source to the final acceleration step [65]. The protons originate in a 92 keV duoplasmatron source, fed with H_2 gas, yielding a 300 mA beam current (FIG. 3.1 and TAB. 3.1). The protons from this source are collected as an input to a linear accelerator (LINAC2), which increases their energy up to 50 MeV. This linac supplies the Proton Synchrotron Booster (PSB) with protons for an increase in energy up to 1.4 GeV. All protons are then accelerated by the Proton Synchrotron (PS, up to 25 GeV) and subsequently by the Super Proton Synchrotron (SPS, up to 450 GeV). The PS also builds up the proton bunches, with a 24.95 ns separation and less than 4 ns time extension. Finally, the SPS injects both beams into the LHC pipes.

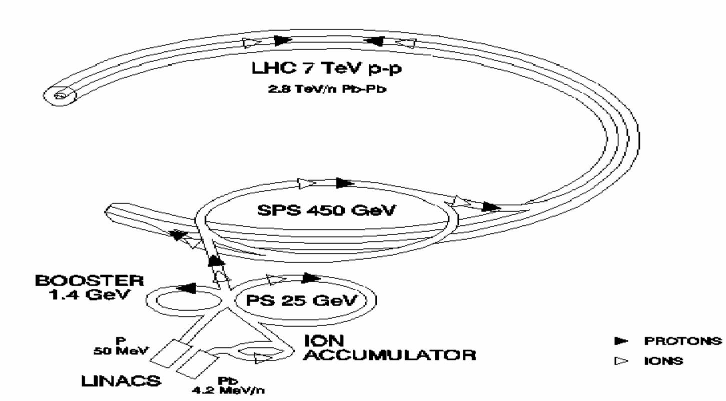

Figure 3.1: LHC acceleration chain. Protons from the H_2 source are driven by linear accelerators (LINACS), then enter into successive circular accelerators (the booster, the PS and the SPS). They are finally injected in bunches into the LHC storage ring, where they reach their maximal energy [65].

Name	Size (km)	E_{out} (GeV)	
LINAC2	.	0.05	source
PSB	.	1.4	
PS	0.6	25	bunch build up
SPS	6	450	
LHC	26.659	7000	collision

Table 3.1: Acceleration stages from source to collision. Typical sizes and output energy are given for each subsystem [65].

The final accelerator itself lies in the circular, 27 km long, LEP tunnel. It consists of two beams, counter-circulating in separate vacuum chambers which are horizontally spaced by 194 mm. The beam pipes fuse into a single piece, only at about 100 m next to each interaction point (IP). The convention is to name *beam 1* (*beam 2*) the beam travelling clockwise (counterclockwise, respectively).

These two pulsed beams are driven up to 7 TeV, thanks to 8 resonant cavities. The electrical field of these radio frequency (RF) cavities oscillates at 400.8 MHz to achieve a 0.5 MeV/turn energy kick. At top energy, the field strength reaches ~ 5.5 MV/m. The beams are steered by 1232 cryogenic dipole magnets with a field of $B = 8.33$ T and of 0.6 mm deviation per m. These dipoles are operated at around 3 K to maintain a superconducting state. Their particular shape allows them to steer both counter-circulating beams at the same time by sharing the field inside a common structure.

The total stored energy is $E = 362$ MJ in circulating beams and $E \approx 600$ MJ in the magnet system. The whole beam pipe is kept under an Ultra High Vacuum. This is needed to avoid beam proton interactions with residual gas in the pipe, ensuring a long beam lifetime. The equivalent hydrogen gas density is required to be less than 10^{15} H_2/m^3 in order to maintain the luminosity[2]. In the interaction regions around the experiments, this density should drop to 10^{13} H_2/m^3 to minimise the background events. This corresponds to a value at the order of 10^{-9} Pa [64].

Beam structure

Both beams are sampled in bunches of protons. Depending on the luminosity goal, the number of bunches can vary, but this number should always comply with the LHC 40.08 MHz clock. The clock rhythm creates 3564 slots for bunches, repeated every 24.95 ns. Not all slots are used, leaving some collision-free latencies to experiments for activities like online calibration, subdetector synchronisation or electronics front-end reset. The pattern of the *bunch train* at full luminosity is:

$$2-3-4 \;\oplus\; 3-3-4 \;\oplus\; 3-3-4 \;\oplus\; 3-3-4,$$

where the digits refer to the number of consecutive sets of 72 bunches. At least 8 bunch slots are empty after 72 filled ones. The small gaps, "$-$″, correspond to 38 empty slots and the larger ones, "$\oplus$", to 39 empty slots. Finally, the missing set of 72 bunches at the beginning of the train is also taken into account, as well as the foreseen 8 empty slots. In summary, 119 empty slots separate the end of one train to the beginning of the next one, which is 2.975 μs. A high luminosity bunch train thus corresponds to $k_B = 2808$ bunches, in either beam, with 25 ns separation and 1.15×10^{11} proton per bunch. During lower phase,

---

[2] The luminosity decay time corresponding to the residual gas should be at the order of 100 h.

collisions of 936 × 936 bunches with less protons will happen with a latency three times longer.

3.2 Eight octants for five experiments

The two LHC symmetrical rings are divided into eight octants (Fig. 3.2). The first and the fifth octants host the two high luminosity interaction points (up to 10^{34} cm^{-2}s^{-1}): the ATLAS experiment is located at the IP1, and CMS at the IP5. These two general purpose detectors will use the full power of the LHC. Those two interaction points feature the same beam characteristics, except for their crossing planes: ATLAS has been attributed a vertical plane while beams will collide horizontally in CMS (Fig. 3.3).

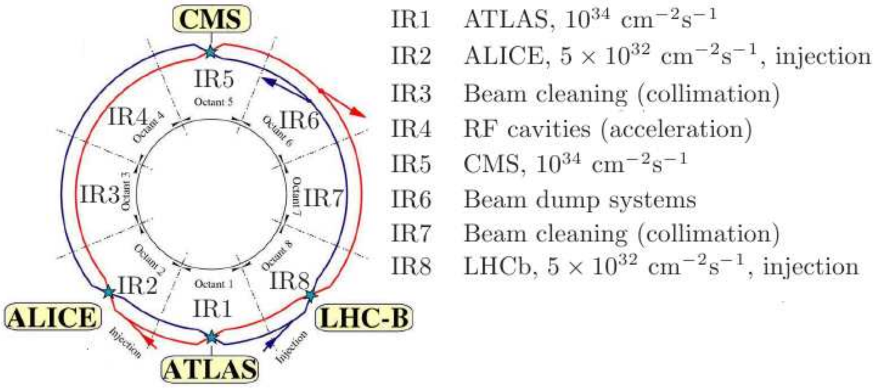

IR1	ATLAS, 10^{34} cm^{-2}s^{-1}
IR2	ALICE, 5×10^{32} cm^{-2}s^{-1}, injection
IR3	Beam cleaning (collimation)
IR4	RF cavities (acceleration)
IR5	CMS, 10^{34} cm^{-2}s^{-1}
IR6	Beam dump systems
IR7	Beam cleaning (collimation)
IR8	LHCb, 5×10^{32} cm^{-2}s^{-1}, injection

Figure 3.2: Division of the two LHC rings into octants, and experiment locations. Beam 1 is rotating clockwise (red) and beam 2 counterclockwise (blue). Adapted from [64].

The other two large experiments, ALICE and LHCb, are located in octants 2 and 8, respectively. These two experiments are specialised, and their corresponding luminosity reaches $\mathcal{L} = 5 \times 10^{32}$cm^{-2}s^{-1}. There are no beam crossings, thus no collisions in other octants. Instead, octants 3 and 7 host collimation systems meant for beam cleaning. The two independent accelerating RF systems are located in the fourth octant, and the beam dump system is in the interaction region 6. TOTEM, a fifth experiment, which is smaller both in size of its community and in the number of collecting channels, shares the IP5 with CMS. It covers only a limited region of large pseudorapidities to study the elastic and diffractive interactions, and shares a large physics programme with CMS.

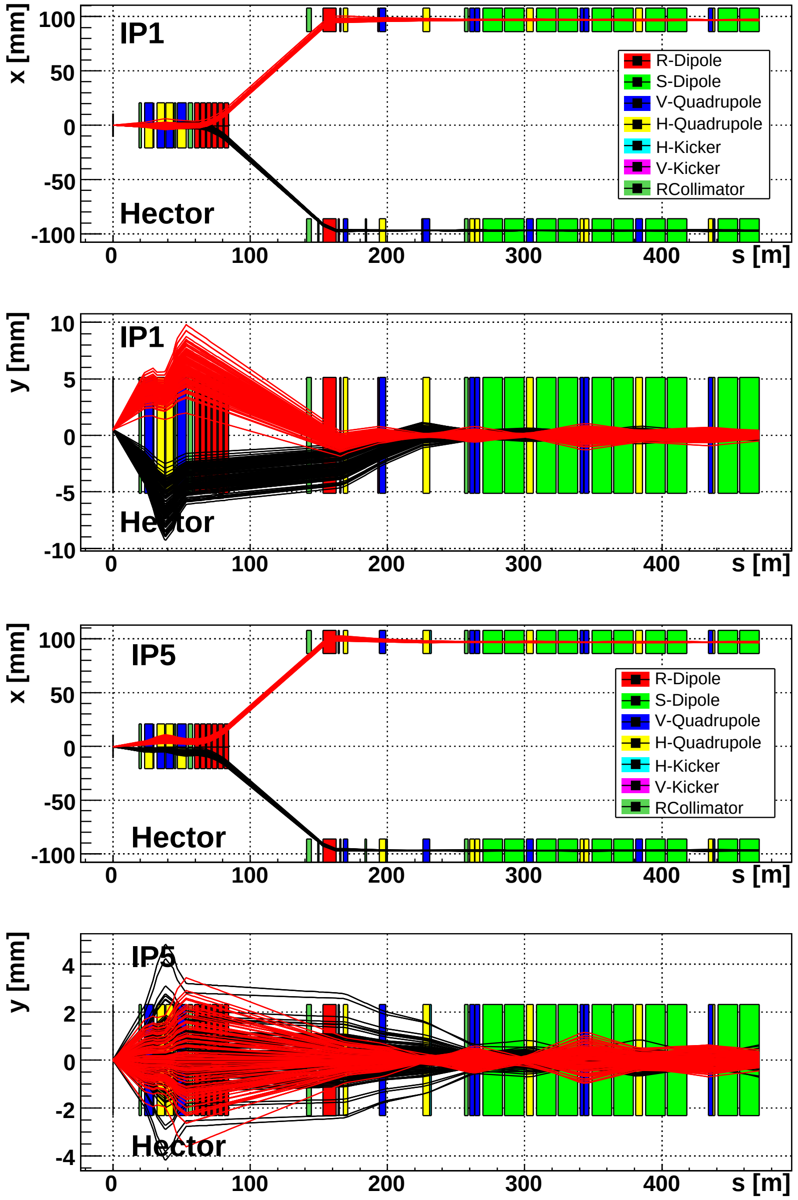

Figure 3.3: Similarities and differences in the beam optics near the high luminosity interaction points. Top and side views of both LHC beams around the IP5 (*top two graphs*) and the IP1 (*bottom two graphs*). The IP is located[4] at $s = 0$ m. Beam 2 (red) flows from the right to the left and is seen before its passage at the IP. Beam 1 (black) is seen downstream, passing from the left to the right after the crossing. In this graph, the bending effect of the sector magnets has been switched off, thus rectifying the beam path to a straight line after 250 m. The difference between the IP1 and IP5 is clearly seen, as the crossing planes are perpendicular to each other. Simulations with Hector [13].

3.3 Luminosity evolution

Different luminosity scenarios are foreseen[5] for the nominal 14 TeV centre-of-mass energy: mostly $\mathcal{L} = 10^{32}$, 2×10^{33} and 10^{34} cm^{-2}s^{-1}. These scenarios (Tab. 3.2) will be achieved by adjusting two parameters: the beam focus at the interaction point (expressed in terms of the β^* function) and the beam current (sampled by the number of particle bunches building up the beams).
Coming back to Eq. 2.3:

$$\mathcal{L} = f\ \frac{\gamma k_B N_p^2}{4\pi\epsilon_n\beta^*}\ F \tag{3.2}$$

At 7 TeV, protons have a relativistic γ equal to 7461. The tunnel circumference, covered at the speed of light, fixes the revolution frequency to 11.245 kHz. The transverse normalised emittance ϵ_n is lower bounded by the injection stages and is expected to be 3.75 μmrad.

For instance, the highest luminosity value is obtained with 2808 bunches of 1.15×10^{11} protons with the β function at the IP of 0.55 m. Finally, a 285 μrad crossing angle is applied between incoming beams, leading to a luminosity geometric reduction of $F = 0.836$ (Eq. 2.4). The crossing angle is required, as both beams share the same pipe during about 140 m. Given the number of bunches and their 25 ns time separation, head-to-head collisions in a common beam pipe would imply 34 extra collision points. A crossing angle is subsequently applied in order to avoid all parasitic collisions, but this geometrically decreases the luminosity[6]. The luminosity is expected to be known with a precision of 5 %, which is assumed to be achieved after 1 fb^{-1} of collected data. Before reaching this integrated luminosity, the expected precision is approximately 10 % [71].

The LHC luminosity [64] is not constant during a run, as the beam current decreases and the emittance deteriorates. Several effects cause the luminosity to vanish, but the main contributors are the collisions themselves. The corresponding time scale τ_{nuclear} is easily obtained from the total cross-section and the initial luminosity (where k_{IP} is the number of high luminosity interaction points):

$$\tau_{\text{nuclear}} = \frac{N_{\text{tot},0}}{\mathcal{L}\ \sigma_{tot}\ k_{\text{IP}}}. \tag{3.3}$$

For $\mathcal{L} = 10^{34}$ cm^{-2}s^{-1} and $\sigma_{\text{tot}} = 10^{-25}$ cm^{-2}, this time amounts to 45 h. Other effects play a role in the luminosity decrease and are characterised by a corresponding lifetime, like the intrabeam scattering (IBS) and the interaction with residual gas. While the IBS, the radio frequency cavity noise and the beam-beam interactions tend to increase the beam emittance, the synchrotron emissions compensate it slightly, leading to a $\tau_\epsilon \approx 80$ h. The beam lifetime

---

[5] LHC *ultimate* operation drives the luminosity up to 2.5×10^{34} cm^{-2}s^{-1}, with 2808 bunches of 1.7×10^{11} protons.

[6] Consequently, increasing the time separation to 75 ns decreases the number of parasitic collision points and allows for a smaller crossing angle, i.e. a smaller geometric suppression.

associated to the vacuum quality is $\tau_{\text{res gas}} \approx 100$ h. In summary, the net expected luminosity lifetime in a run is:

$$\tau_L \approx 15 \text{ h}. \tag{3.4}$$

The ultimate quantity to maximise is the integrated luminosity $L = \int_0^T \mathcal{L}\, dt$. The injections ($T_{\text{inj}} \approx 16$ min), magnetic field ramping phases ($T_{\text{ramp}} \approx 20$ min for increase or decrease) and accelerator checks take some time. This specific amount of time is called the *turnaround time* ($T_{\text{turn}} \approx 70$ min), during which no physical events are acquired. The physical run duration should thus be optimised accordingly. If it is too short, the contribution of the turnaround is too large. If the run lasts too long, the luminosity drop is too large for an efficient data taking. At the end of a run lasting T_{run}, the integrated luminosity is

$$L_{\text{run}} = \mathcal{L}_0\ \tau_L\ \left(1 - e^{-T_{\text{run}}/\tau_L}\right), \tag{3.5}$$

which leads to a total integrated luminosity per year (assuming 200 working days of 24 hours) of:

$$L_{\text{year}} = \frac{200 \times 24}{T_{\text{turn}}[h] + T_{\text{run}}[h]} L_{\text{run}}. \tag{3.6}$$

From Eq. 3.6, the optimal run time can be computed as a function of the actual turnaround time. In the optimistic scenario, T_{turn} is estimated to be 1.2 h, leading to an optimal run time T_{run} of 5.5 h. In the pessimistic scenario, the optimal run time T_{run} is 12 h with a T_{turn} at 7 h. At $\mathcal{L}_0 = 10^{34}$ cm^{-2}s^{-1}, the yearly integrated luminosity is expected to be between 80 fb^{-1} and 120 fb^{-1}.

3.4 Event pile-up concerns

A given mid-range luminosity can be achieved in various ways. For instance, a small number of big bunches (i.e. with a lot of protons) or a large number of thinner ones. However, high density bunch collisions have a high probability for simultaneous collisions (called *event pile-up*), making data selection and analysis more difficult (Tab. 3.2).

The number n of interactions in a given bunch crossing is distributed according to Poisson statistics

$$p(n; \mu) = \mu^n \frac{e^{-\mu}}{n!}\ , \tag{3.7}$$

where μ is the mean number. Neglecting the elastic collisions, the total LHC cross-section should reduce to approximately 80 mb. From the bunch train, the effective bunch crossing frequency f_{BX} is $(2808/3564) \times 40$ MHz. Subsequently, at $\mathcal{L} = 10^{34}$ cm^{-2}s^{-1}, the average number of interactions per bunch crossing is

$$\mu = \frac{\sigma \mathcal{L}}{f_{BX}} \approx 25. \tag{3.8}$$

Luminosity scenario				**Pileup**
$\mathcal{L}$ (cm^{-2}s^{-1})	$k_B \times k_B$	I_b (p/beam)	β^* (m)	
1.6×10^{27}	1×1	1×10^{10}	18	0.011
3.8×10^{29}	43×43	3×10^{10}	18	0.05
6.1×10^{30}	43×43	4×10^{10}	2	0.76
5.6×10^{31}	156×156	9×10^{10}	4	1.9
1.1×10^{32}	156×156	9×10^{10}	2	3.9
2×10^{33}	936×936			12
2×10^{33}	2808×2808			4.4
1×10^{34}	2808×2808	1.15×10^{11}	5.5	22
2.5×10^{34}	2808×2808	1.70×10^{11}	5.5	

Table 3.2: Pile-up events with respect to the luminosity scenario. Each scenario of luminosity $\mathcal{L}$ is detailed in terms of the number of colliding bunches k_B, the beam current I_b and the value of the betatron function at the IP β^*.

It is interesting to see that, depending on the number of bunches k_B, the event pile-up is different at a given luminosity. Indeed, from Eq. 3.8 and 2.3, the average number of interactions per bunch crossing becomes:

$$\mu(k_B) = \frac{\gamma f}{4\pi\epsilon_b\beta^*} \; \frac{k_{max}}{T_{LHC}} N_p^2(k_B)F(k_B), \tag{3.9}$$

where $k_{max} = 3564$ is the maximal number of bunch slots and $1/T_{LHC} =$ 40.08 MHz the LHC bunch crossing rate.

When the number of bunches is smaller, the number of parasitic interaction points is smaller for head-on collisions. The crossing angle and the corresponding luminosity reduction factor F can be set accordingly, making the k_B dependence of F explicit but not straightforward. To a first approximation, moving from 2808 to 936 bunches allows the crossing angle to be divided by 3. From Eq. 2.4, F increases from 0.836 to 0.977. Taking this into account, a given luminosity can be obtained by adapting the particle density in the bunches with respect to their number (i.e. by fixing the beam total current): $k_B N_p^2 F = Const$. Hence,

$$\frac{N_p(\mathcal{L} = \mathcal{L}_0; k_B = 936)}{N_p(\mathcal{L} = \mathcal{L}_0; k_B = 2808)} \approx 1.60 \tag{3.10}$$

and

$$\frac{\mu(\mathcal{L} = \mathcal{L}_0; k_B = 936)}{\mu(\mathcal{L} = \mathcal{L}_0; k_B = 2808)} = \frac{2808}{936} = 3. \tag{3.11}$$

Multiple proton collisions can happen at a given bunch crossing. When looking at a particular event, the pile-up events correspond to the collisions that have occurred at the same bunch crossing. All these events are almost simultaneous and their final states mix in the central detector. However, due to the extension of the bunches, these events are neither exactly simultaneous nor are they originating from a common point. These two characteristics should be employed to discriminate the final state particles from those from the "spectator" pile-up events.

Chapter 4

Detectors around the IP5

The instrumentation around the fifth interaction point of the LHC *consists in the central* CMS *detector and in the forward of detectors of both the* CMS *and* TOTEM *experiments, located along the beamline. The central detector is made of an inner tracking system with pixels and microstrip sensors, a high resolution electromagnetic calorimeter, a hadronic calorimeter with a large η coverage and a high performance muon system. The forward detectors, starting from the* IP*, are the* TOTEM *telescopes, the possible* CASTOR *calorimeters, the* ZDC *calorimeters at a zero θ angle, the* TOTEM *roman pots and the possible forward proton taggers of* FP420*. In addition, dedicated instruments will provide input for the luminosity determination at this* IP*.*

4.1 CMS coordinate system

This chapter and the rest of the document will focus on the *Compact Muon Solenoid* (CMS) experiment, located at the fifth IP of the LHC. The centre of the CMS detector fixes the origin[1] of the Cartesian coordinate system [70]:

- The x axis is horizontal, pointing South to the LHC centre.
- The y axis is vertical, pointing upwards.
- The z axis is horizontal, pointing West.

Some ambiguities should be removed on angular variables:

- The sign of the pseudorapidity η is equal to the sign of z.
- The polar angle θ is measured with respect to the z axis: $\theta = 0$ is $+z$ axis, $\theta = \pi$ is $-z$ axis.

---

[1] The actual position of the interaction point is $(x, y) = (-500, 0)$ in the transverse plane, in μm.

- The azimuthal angle $\phi = \arctan(\frac{y}{x})$ is measured in the (x, y) plane: $\phi = 0$ is $+x$ axis, $\phi = \pi/2$ is $+y$ axis.

Available detectors

The instrumentation around the IP5 can be divided into two categories: the components of the central CMS detector and the forward detectors of both the CMS and TOTEM experiments. Most of the forward instrumentation is located outside of the CMS volume, along the two LHC beamlines. These instruments have complementary uses: (1) the observation of the particle position, trajectory and origin (i.e., *vertexing*) and (2) the determination of their energy. Timing detectors, synchronised with the LHC clock, could provide a time-of-flight estimate, also used for vertexing as the distance of these detectors to the IP is known. In addition, a set of sensors monitor the LHC beam parameters (luminosity, position, etc).

Many calorimeters mentioned in this chapter are tungsten/quartz detectors (Tab. 4.1). Tungsten has the following properties: $\lambda_I = 10.0$ cm, $X_0 = 0.365$ cm and has a density of 18.5 g/cm^2. It gives the smallest possible shower size, thus is suitable for small detectors. Fused silica quartz (amorphous SiO_2) is very radiation hard and has a fast signal generation. Incident high-energy particles shower in the tungsten absorber and produce relativistic charged particles that emit a Čerenkov light in the quartz plane. This light is collected and transported to light avalanche photodiodes (APD) or photomultiplier tubes (PMT).

4.2 The Central Detector

The CMS detector (Fig. 4.1) has the classical layered structure of central detectors in high energy physics: an inner tracker, an electromagnetic (EM) calorimeter, a hadronic (HAD) calorimeter and a muon system (from the interaction point to the outermost layer). All are embedded in an 4 T magnetic field.

The detector components obey two types of geometries: CMS volume is made of coaxial *barrels* closed by one vertical *endcap* on each side. The difference between the barrel region and the endcaps is not only geometric. The orientation and intensity variations of the magnetic field in the endcap disks are different than in the barrel region, as the endcaps close the field lines. These lines are parallel to the beam axis in the barrel; they are vertical in the endcap disks and converge towards the disk centre, making a non-uniform field within endcap detectors. This implies a set of different technologies for a same subdetector depending on its location in the detector volume. Subsequently, the detection features (sensitivity, noise, resolution measurement) of each subdetectors will vary from the barrel to the endcaps. The central detector as a whole is a 21.6 m long cylinder, of radius 7.3 m and weighs $12,500$ tons (Fig. 4.1).

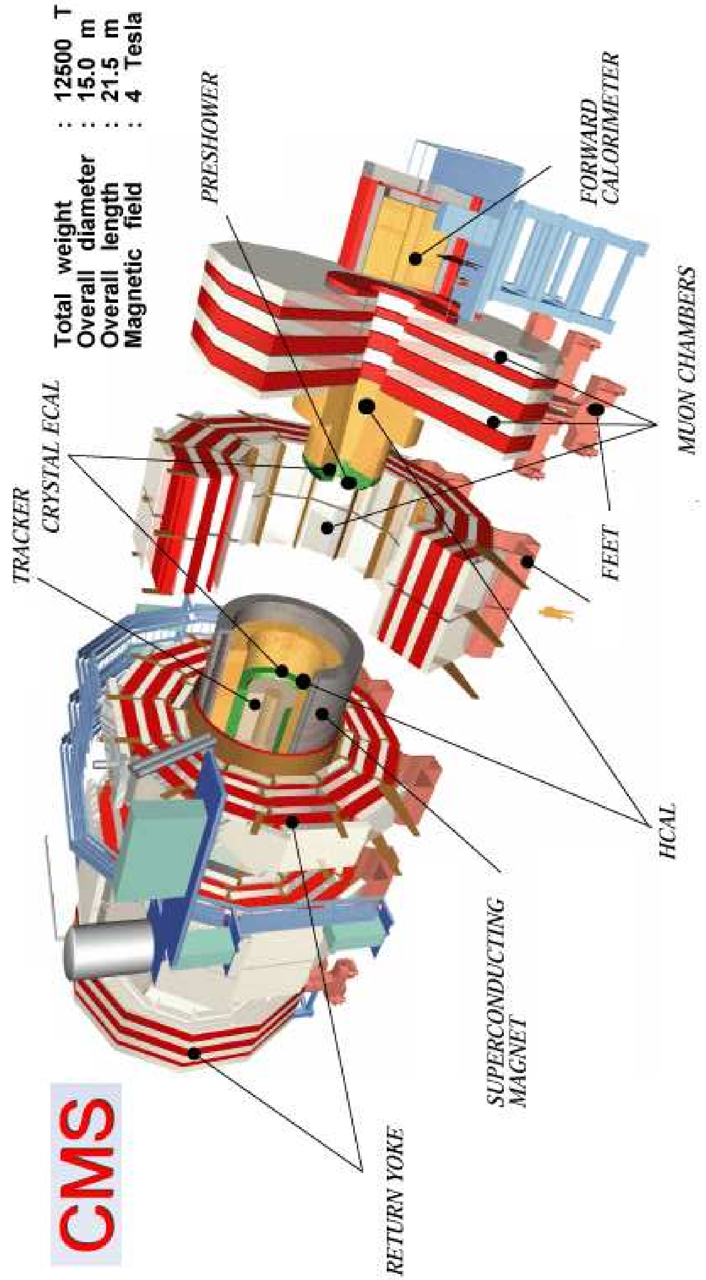

Figure 4.1: Exploded view of the central detector of the Compact Muon Solenoid experiment.

CMS central detector

Name	**Type**	**Particle**	**$|\eta|$ coverage**	**Technology**
TRACKER	track	charged	$[0 - 2.5]$	
* Pixels			$[0 - 2.5]$	Si pixels
* SST			$[0 - 2.5]$	Si strips
ECAL	calo	$e^{\pm}/\gamma$/jets	$[0 - 3.0]$	PbWO_4
* EB			$[0 - 1.479]$	
* EE			$[1.479 - 3.0]$	
* ES			$[1.653 - 2.06]$	Pb-Si strips
HCAL	calo	jets	$[0 - 3.0]$	Cu + scint
* HB			$[0 - 1.4]$	
* HO			$[0 - 1.26]$*	
* HE			$[1.3 - 3.0]$	
MUON	track	$\mu^{\pm}$	$[0 - 2.4]$	
* MB			$[0 - 1.2]$	DT +RPC
* ME			$[1.0 - 2.4]$*	CSC +RPC

Forward detectors

Name	**Type**	**Particle**	**$|\eta|$ coverage**	**Technology**	**s (m)**
TOTEM T1	track	charged	$[3.1 - 4.7]$	CSC	7.5
HCAL HF	calo	all	$[3.0 - 5.0]$	steel + quartz	11.2
TOTEM T2	track	charged	$[5.3 - 6.7]$	GEM	14
CASTOR	calo	all	$[5.0 - 6.6]$	W + quartz	16
ZDC	calo	$(n/\gamma/\pi^0)$	$[8.1 - \infty[$	W + quartz	140
	-	all	$[9.3 - \infty[$	-	-
TOTEM RP	track	charged	$0.02 < \xi < 0.2$	edgeless Si	
* RP at 220					$[216 - 220]$
FP420		p	$0.002 < \xi < 0.02$		$[420 - 428]$
* Si pixels	track			Si 3D	
* QUARTIC	timing	-		quartz Čerenkov	-
* GASTOF	-	-		gas Čerenkov	-

Table 4.1: Detectors available around the IP5 from the interaction point, outwards.

4.2.1 The Tracker

The CMS Tracker is the largest silicon detector ever built. It is composed of a central pixel detector surrounded by a large volume of planar microstrip sensors. These subdivisions are due to both the particle flow at a given distance from the interaction point and the subsequent radiation levels. For instance, at $r =$ 10 cm, a flux of the order of 10^7 particles per second per cm^2 is expected. Pixel detectors are better suited to such environments. At larger distances, silicon microstrips are used in order to keep the number of channels low, compared to an "all-pixel" detector solution. Like other CMS subdetectors, the tracker components are categorised into barrel and endcap geometries (Fig. 4.2). The tracker is designed to ensure a high quality momentum resolution ($\Delta p_T/p_T = 0.15 \times p_T$ [TeV]).

In spite of a smaller volume (0.9 m^3 vs 20 m^3), the pixels have far more channels than the strip detectors (66 millions of pixels vs 9.6 millions). The tracker dominates, by far, the total number of channels of the whole experiment. An important parameter is hence the *occupancy*, being the percentage of activated channels per bunch crossing. This should be kept as low as possible in order to have bearable event data sizes.

The large number of particles flowing through the tracker causes irradiation damages, which has been intensively studied. Not only particles flowing from the IP are destructive, but also, after activation of the calorimeters, the huge flux of neutrons coming backwards are damaging. In order to slow down the impact of the radiation damages, the tracker is operated at -20^oC.

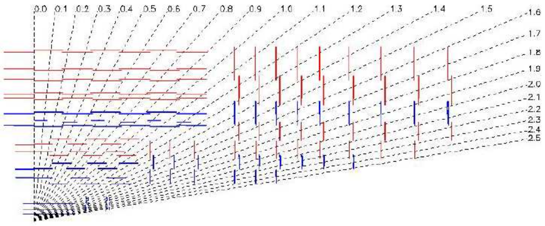

Figure 4.2: Projection of the tracker, showing the pixel modules, the microstrip inner and outer barrels (TIB and TOB), inner disks (TID) and endcaps TEC [70]. Dashed lines are iso-η curves. The plot is limited to $\eta > 0$ and $\phi > 0$.

Pixel detector The pixel fine granularity positions the vertex of the events, allowing identification of displaced secondary vertices for tagging B hadrons, for instance. Although radiation hard, they will endure such doses that it is already foreseen to regularly replace them. Three layers of pixels make the barrel (TPB for Tracker Pixel Barrel), in the [$r = 44,\ 73,\ 102$ mm] $\otimes$ [-265 mm $\leq z \leq$ 265 mm] region, for a total of 768 modules. Both Tracker Pixel Endcaps (TPE) consist of a pair a layers at $[60 \text{ mm} \leq r \leq 150\text{mm}] \otimes [|z| = 345 \text{ and } 465 \text{ mm}]$ assembled from 672 modules.

In total, 66 millions of $100 \times 150\ \mu\text{m}^2$ pixels are read-out by approximately 16,000 chips and covering almost 1 m^2. The expected occupancy is 10^{-4} per pixel per *pp* bunch crossing. As the pixels are embedded into a strong magnetic field, the pixel modules are tilted in order to benefit from the Lorentz angle (i.e. for an optimal incidence angle of the particle with respect to the detector). The spatial resolution of the pixels is 10 μm in $r - \phi$ and 20 μm in z.

Silicon Strip Tracker The silicon Microstrip Detector is made of 15,400 modules and covers approximately 200 m^2. Its outer radius was constrained by the high magnetic field intensity and the constraints on the charged particle curvature for a good charged particle identification.

It is not possible in practice to fill this volume with pixels as the number of output channels would be too large[2] to handle. Subsequently, using a smart assembly of 1D detectors is a good compromise between a fine position resolution and a comparatively low number of channels. The sensors are either single- or double-sided (*stereo* back-to-back modules, tilted by 100 μrad, for a coupled $r - \phi/r - z$ measurement), and have a thickness of 320 or 500 μm. As the signal generation in these silicon sensors is too slow (~ 50 ns peaking time) to take part to the Level-1 trigger decision, the analogue levels are sampled and fed to the analogue pipeline of the front-end electronics (APV25) before being possibly read-out by CMS and further processed.

The Silicon Strip Tracker (SST) is divided into a barrel ($0.20 \text{ m} \leq r \leq 1.1 \text{ m}$) and two endcaps ($1.2 \text{ m} \leq |z| \leq 2.8 \text{ m}$). The Tracker Inner Barrel (TIB) is made of 2 stereo and 2 single-sided layers. It covers up to $|z| = 0.65$ m with 320 μm thick sensors with a strip pitch ranging between 80 and 120 μm. The Tracker Outer Barrel (TOB), further from the IP, experiences a milder radiation level. This allows for the use of 500 μm thick sensors with longer strips and a larger pitch (in $[120\ \mu\text{m}; 180\ \mu\text{m}]$), arranged in 2 double- and 4 single-sided layers. Due to larger pitches, TOB module resolution is $35 - 52\ \mu$m in $r - \phi$ and 530 μm in z. TIB achieves a resolution in $r - \phi$ in $[23\ \mu\text{m}; 34\ \mu\text{m}]$ and $\delta z = 230\ \mu\text{m}$. Both endcaps are made of Tracker Inner Disks (TID) and a Tracker End Cap (TEC), with strips pointing toward the beam axis, that have variable pitches. The TID consists of 3 rings (2 stereo + 1 single rings) with 320 μm sensors. Each TEC is made with a set of 9 disks (in which 3 are double-sided), made with $3 \times 320\ \mu$m and $6 \times 500\ \mu$m thick sensors.

---

[2] The *zero suppression* and digitisation of the tracker data happen in the CMS Counting Room, in a neighbouring cavern. This means that each channel should then be output from CMS and transported to these acquisition boards (FED). The *multiplexing*, i.e. the serialisation of several channels into one stream (now reducing by a factor 128x2x2), would not suffice the need for decreasing the channel numbers if the whole volume was made of pixels. The number of optical fibres outputting the tracker data would then be unbearable. This proves by absurdity that an all-pixel tracker was not possible in CMS, assuming a zero-suppression outside the CMS volume.

4.2.2 ECAL

Located just behind the tracker[3], the inner (*electromagnetic*) calorimeter [73] (ECAL) is dedicated to the measurement of electrons, positrons and photons. It is made of $75,848$ lead tungstate scintillating crystals ($PbWO_4$), assembled into 2×18 supermodules in the barrel region EB (with $1,700$ crystals each) and 2×2 "Dees"[4] (with $3,662$ crystals each, divided into *supercrystals* of 25 crystals) in the endcap regions (EE). Its overall shape is a 6.4 m long cylinder with a 2.6 m radius, operated at 18^oC. One expects doses of $\sim 10^{12}$ and $\sim 10^{14}$ charged hadrons in the barrel and endcaps, respectively.

The $PbWO_4$ crystals are dense ($\rho = 8.3$ g/cm^3, $X_0 = 0.89$ cm and $R_M = 2.2$ cm), fast (80 % of the scintillation light within 25 ns) and radiation tolerant (~ 3 kGy are expected in the barrel). However, their light yield is only 4.5 photoelectrons per MeV (around 420 nm). The effect of radiations is a temporary loss of transparency. No damage is made to the scintillation mechanism, but colour centres appear and decrease the light transmittance. As the crystals recover in the absence of radiation, a monitoring of their response will be performed with laser light injection during the empty slots of the bunch trains. The balance between damage and recovery leads to a saturation of the radiation effects, albeit the attenuation length is greater than three times the crystal length. The temperature dependence of their behaviour is considerable: -1.9 %/^oC at 18^oC. This imposes a temperature stabilisation within 0.05^oC, around 18^oC.

The ECAL resolution is targeted to be $5\ \%/\sqrt{E} + 0.5\ \%$ above 100 GeV, in order to have an excellent mass resolution for a light Higgs boson decaying into two photons: $H \to \gamma\gamma$.

EB The ECAL barrel extent is $0 \leq |\eta| \leq 1.479$. It is split into two halves. Each half is segmented into 18 ϕ -sections and 85 η -sections. The crystals correspond to $\Delta\eta \times \Delta\phi = 0.0174 \times 0.0174$, and their 230 mm length is a 25.8 X_0 depth. Their arrangement is quasi projective (i.e. they point almost to the IP) to minimise the cracks. EB starts at a radius of 1.29 m. A set of 5×5 crystals give a barrel tower. The scintillation light is acquired by Avalanche Photo Diodes (APD) in the barrel, with a gain of about 50 at 18^oC and a quantum efficiency around 75 %. Two APDs are glued to each crystal.

EE The ECAL endcaps complement the coverage up to $|\eta| \leq 3$ (Fig. 4.3). The crystals only differ in shape, leading to a 24.7 X_0 deep endcap. Due to the strong and varying magnetic field, the read-out must be different: Vacuum Photo Triods (VPT) are used. These are 1-stage photomultipliers with lower gains ($\lesssim 10.2$) and quantum efficiencies (~ 22 %) than the APDs.

---

[3] Actually, a thermal screen makes the separation between the cold tracker(-20^oC) and the warm ECAL ($+18^oC$).

[4] The name of these supporting structure refers to its shape, similar to the 'D' character.

ES Each endcap is partially covered by a preshower, extending from $|\eta| = 1.653$ to $|\eta| = 2.6$. The goal of the preshowers is to clearly distinguish π^0 from photons. Their high granularity also improves the EE abilities. ES is a sampling calorimeter and consists in two layers of lead and silicon microstrips. The two lead disks ($2\ X_0 + 3\ X_0$) are used as a radiator whilst the 320 μm silicon sensors (32-microstrips, 1.9 mm pitch) sample the showers into a total of $\sim 137,000$ channels. Moreover, ES contains a paraffin layer to moderate the flux of neutrons coming from the calorimeters and irradiating the tracker from the back.

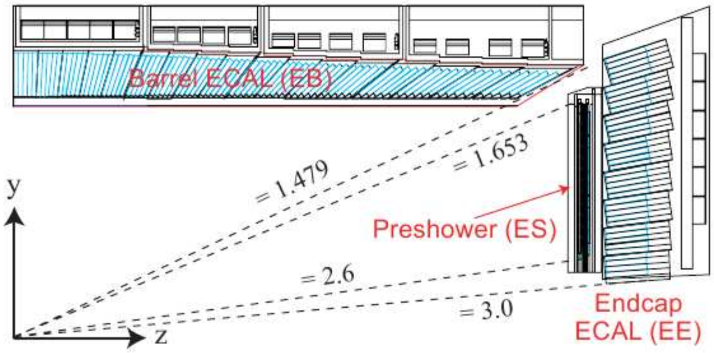

Figure 4.3: Projection of the ECAL, showing the $\eta-$coverage for positive z and ϕ of the barrel EB, the endcap EE and the preshower ES [70].

4.2.3 HCAL

The hadronic calorimeter (HCAL) is located downstream the ECAL. It is subdivided into four geometrically separate parts: the barrel HB, the outer barrel HO, the endcaps HE and the forward detectors HF. The η coverage of these parts is listed in Tab. 4.2. As the HF differs substantially from the other subdetectors, it will be detailed separately thereinafter. HB, HO and HE (Fig. 4.4) are scintillation-based calorimeters, differing by the absorber. The scintillation light is collected by Wavelength Shifting Fibres (WSF), subsequently gathered into bundles of all the layers matching the same projection in $\eta - \phi$, called *calorimetric towers*. The light from each tower is detected by the pixels of a high gain (~ 2000) multichannel Hybrid Photo Diode (HPD).

HB The HCAL barrel consists in two halves, each subdivided into 18×20^o wedges in ϕ. The absorber is mostly[5] brass (70 % Cu and 30 % Zi) with

---

[5] As the HCAL components have a large variety of geometries and characteristics, refer to [70] for details.

	$\lvert\eta\rvert$ **coverage**	**Absorber /**	**Collector/**	**Acquisition**	**Light origin**
HB	[0.0 ; 1.4]	brass /	WSF	/ HPD	scintillation
HO	[0.0 ; 1.26]*	steel /	WSF	/ HPD	scintillation
HE	[1.3 ; 3.0]	brass /	WSF	/ HPD	scintillation
HF	[3.0 ; 5.0]	steel /	quartz	/ PMT	Čerenkov

Table 4.2: Coverage in pseudorapidity $\lvert\eta\rvert$ of the hadronic calorimeter HCAL subdetectors (the incomplete $\phi -$ coverage of HO is denoted by *). The corresponding absorbers and collectors, as well as the physical process of signal generation are detailed.

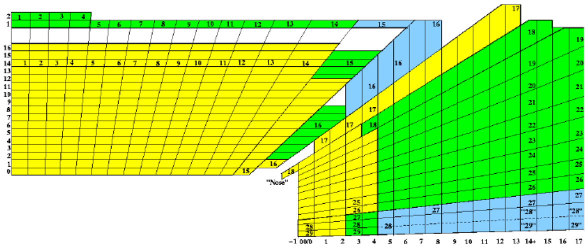

Figure 4.4: Schematic projection of HB, HO and HE for $z > 0$ and $\phi > 0$ [70].

a thickness of at least 50.5 mm. Seventeen active plastic scintillating plates (1×9 mm$+ 16 \times 3.7$ mm) are interleaved between the absorbers, corresponding to $\Delta\eta \times \Delta\phi = 0.087 \times 0.087$. This leads to 2×32 HB towers. The HB resolution is ~ 100 %$/\sqrt{E}$ with detection planes parallel to the beam pipe.

HO Covering almost the same region as the HB (Tab. 4.2), the outer barrel calorimeter HO is located behind the solenoid. It is subdivided in z into 5 rings with a 2.54 m radius, and 12 sectors in ϕ. It is made of 1 or 2 layers of 10 mm scintillator planes, depending on the pseudorapidity (2 layers for $\lvert\eta\rvert < 1.305$ and only 1 above 1.305). However, HO coverage is not complete in ϕ, due to the 12×75 mm holes for services. Altogether with HB, HO lead to an hadronic calorimetry thickness of 11 λ_I.

HE The two hadronic endcap calorimeters (HE) have a petal structure perpendicular to the beam pipe, with some overlap with the HB. Its $18 -$ fold segmentation provides a coverage ranging from 5^o to 20^o in ϕ, as η increases. Each HE is made of 19 scintillator planes (3.7 mm thick) interspersed in 78 mm brass absorbers. HE has 2304 towers. Its resolution is estimated to ~ 150 %$/\sqrt{E}$.

HF The two forward hadron calorimeters (HF), located at 11.2 m from the IP, complement HCAL coverage in pseudorapidity from 3 to 5. HF is a sampling calorimeter made of 8 slices of steel and of scintillating quartz fibres embedded into a matrix (Fig. 4.5). The Čerenkov light is collected by 2×900 channels, with $\Delta\eta \times \Delta\phi = 0.175 \times 0.175$ towers, for a full 2π azimuthal coverage and 13 towers in η, read-out by one 8-stage photomultiplier tube (PMT) per tower. The absorber length, 1.65 m, corresponds to 8.3 λ_I. The iron core is grooved in every 2.5 mm for the insertion of 300 μm fibres. They are parallel to the beam axis (non projective geometry).

No ECAL component faces HF, only TOTEM T1 forward tracking detector. Hence, the distinction between electromagnetic and hadronic hits is based on three fibre lengths segmenting the calorimeter longitudinally: (i) the so-called *electromagnetic* fibres are 1.65 m long and 93.75 X_0 deep[6], (ii) the *hadronic* fibres are 1.43 m long, with 81.25 X_0 and finally (iii) the *tail catcher* fibres have only 17.05 X_0 with 30 cm. As the shower must penetrate 22 cm (135 cm) before reaching the hadronic (tail catcher, respectively) fibres, it has a modest resolution of $200\ \%/\sqrt{E} + 10\ \%$. A good jet identification is required to reject superimposed particles coming from simultaneous (minimum bias) events, faking other jets.

The quartz fibres were selected for several reasons: (i) the extremely high radiation environment, reaching ~ 1 GRad at $|\eta| = 5$ after 10 years of the LHC operation; (ii) their insensitivity to low-energy neutrons; (iii) their very fast signal generation (~ 3 ns), as HF should take part in the global calorimetric trigger; and (iv) the relative compactness of the detector.

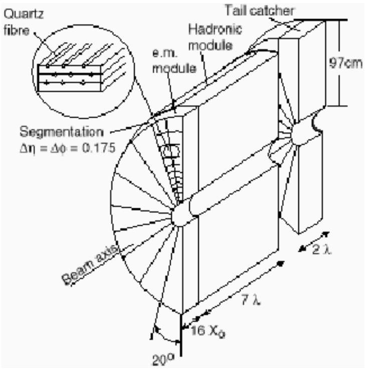

Figure 4.5: Schematic view of one half of the CMS HF. This detector consists of quartz fibres inserted into a iron bulk. The segmentation is visible in ϕ, with the 9 slices at 20^o; and in z, with the three components (electromagnetic, hadronic, tail catcher).

---

[6] The steel is characterised by the following numbers: $\lambda_I = 17.4$ cm, $X_0 = 1.9$ cm, density= 7.5 g/cm^3.

4.2.4 Superconducting Magnet

Even if it has no sensitive area, the superconducting solenoid of the CMS experiment [74] is a major part of the apparatus as it provides a magnetic field as high as 4 T. This field is central for particle identification and measurement, in particular for the $\mu^{\pm}$. The solenoid is designed to provide a resolution of $\Delta p/p \approx 0.1$ for a muon below 1 TeV. It is provided by a $19,500$ A current. The central coil, with an inner diameter of 5.9 m, has 2168 turns. The superconducting state is kept with indirect cooling based on liquid Helium. The critical current is $55,600$ A for a 5 T field and at 4.2 K. The total amount of energy stored in the solenoid is 2.7 GJ. CMS owns the largest and the most powerful superconducting magnet ever built.

4.2.5 Muon Chambers

As the very name of the experiment specifies it, the muon measurement is a central part of CMS, due to its unique signature. It offers many possibilities for calibration and analysis. The Muon System relies on the combination of three types of gaseous detectors. The reconstruction also involves data from the inner tracker. Like other subdetectors, the muon system is divided into a barrel geometry (MB) and two endcaps (ME), as depicted in FIG. 4.6. It covers $25,000$ m^2 with about $1,000,000$ channels. While drift tubes (DT) are deployed only in the barrel region (low neutron induced background) and cathode strip chambers (CSC) in the endcaps (higher neutron induced background, large muon rates and intense transverse magnetic field), resistive plate chambers (RPC) complement the measurement in all the muon system thanks to their high rate ability and time resolution.

An important issue for the muon system is its alignment, both internally and with respect to the inner tracker. The misalignment originates in imperfect assembly, temperature instabilities or deformations related to the magnetic field. It is important to monitor the alignment, as the measurement of muons is based on the combination on data from muon chambers and from the tracker. While for high p_T muons the momentum measurement depends on the bending power of the magnet and is limited by the multiple scattering in the material in front of the first muon station, low p_T muons are observed with a much better resolution by the tracker.

MB The muon barrel expands in pseudorapidities up to $|\eta| = 0.8$. It consists in 4 stations[7], interleaved with the iron yokes, and organised in coaxial cylinders, for the $r-$ segmentation between 4.0 and 7.0 m. These layers are chopped into 5 wheels ($z-$ segmentation). Each wheel is further divided into $12 \times (\Delta\phi = 30^o)$ sectors.

The MB is equipped with aluminium drift tubes and resistive plate chambers. The drift tubes are characterised by a 20 mm drift length and a single point

---

[7] These layers are denoted MB1, MB2, MB3 and MB4.

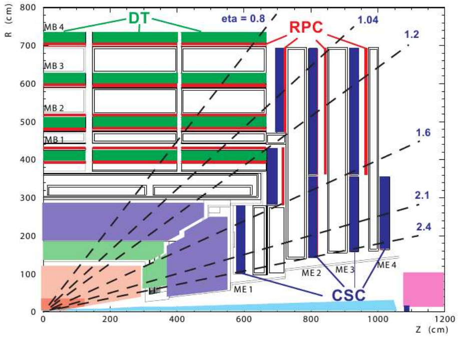

Figure 4.6: Layout of one quarter of the CMS muon system, for $\eta > 0$ and $z > 0$ [70]. Dashed lines represent iso $-\ \eta$ curves. Drift tube chambers are located in the barrel, cathod strip chambers in the endcaps. High rate resistive plate chamber are evenly located in the detector.

resolution of $\sim$ 200 μm. Each station provides a vector with resolution of 100 μm in position and 1 mrad in direction. In total, MB contains 250 DT chambers and 480 RPCs.

A sub-assembly of 4 drift tubes is called a *superlayer*. A set of 2 or 3 superlayers makes a DT *chamber*[8]. A 280 mm gap provides a lever arm inside a DT chamber. Each one of the stations (MB1, MB2, MB3, MB4) is a set of one DT and 1, 2 or 4 double-gap RPCs. A small n-induced background has driven the choice of drift tubes for the MB.

ME The Muon Endcaps consist in 2×234 trapezoidal CSCs, supplemented by 2×216 RPC detectors. There are 4 disks ($z -$ segmentation), perpendicular to the beam, per endcap. Each disk is divided in two rings ($\eta -$ segmentation) and a ring in 36 $\phi -$ sectors.A higher neutron-induced background than in barrel implied the choice of Cathode Strip Chambers. CSC are multiwire proportional chambers with cathodes segmented into strips. They consist of 7 cathode strip planes interspersed by 6 gas gaps with anode wires. The strips and the wires are roughly perpendicular. Each CSC provides 6 (r, ϕ, z) points. During a first stage, CMS ME will be also equipped with RPCs up to $|\eta| = 1.6$. The extension up to $|\eta| = 2.1$ will follow. The RPC detectors are double gap (2 mm width) bakelite chambers operated in avalanche mode. The strip length is either 85 or 130 cm.

---

[8] A DT chamber is composed of 8 to 12 drift tubes.

4.3 The Forward Detectors

The numerous detectors in the forward region around the interaction point provide the largest η coverage ever achieved in particle collider experiments. FIG. 4.7 summarises the detector locations.

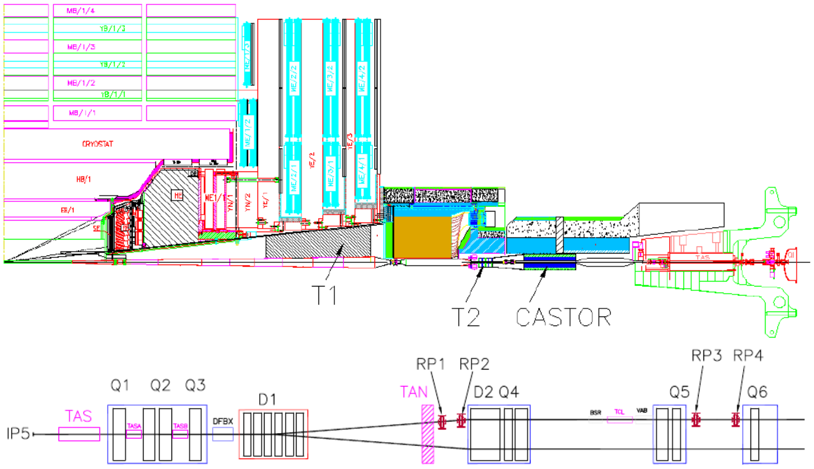

Figure 4.7: Location of the forward detectors around CMS [55]. Upper figure shows the first 20 m downstream the IP5. The CMS central detector is visible, as well as TOTEM T1 and T2 telescopes, and the CASTOR calorimeter. The figure in the bottom shows the LHC beamline on one side of the IP5, with the dipoles (D1, D2), the quadrupoles (from Q1 to Q6) and TOTEM roman pots (from RP1 to RP4).

4.3.1 TOTEM

The TOTEM experiment[9] [55] aims at measuring forward scattered protons and products of inelastic interactions. This could serve for the determination of the total cross-section σ_{tot} of pp interactions and the LHC luminosity $\mathcal{L}$. A large physics programme is also foreseen in common with the CMS experiment [21], while the LHC is operated below 5×10^{33} cm^{-2}s^{-1}. It shares the IP5 with CMS. TOTEM detectors are split into three different stations called T1, T2 and RP. They differ in position, acceptance and technology, but their use as tracking detectors. T1 and T2 forward telescopes cover the $[3.1 - 6.5]$ η-range for both elastic and inelastic scatterings. They also provide the trigger for TOTEM.

---

[9] Even if its physics program evolved, TOTEM stood first for TOTal cross-section and Elastic scattering Measurement.

Two sets of roman pots measure protons with a momentum loss $\xi = \Delta p/p$ in $[0.02; 0.2]$. T1, T2 and RPs are located symmetrically on both sides of CMS.

TOTEM T1

The two T1 forward telescopes are housed inside the CMS magnet endcaps, in front of the HF, with each subsystem attached to the beam pipe, in the vacuum. They are located at 7.5 m from the IP and cover the $3.1 < |\eta| < 4.7$ range. Their sensors are Cathode Strip Chambers, similar to the CMS endcap muon chambers. Each T1 is 2.8 m long, with 5 CSC planes. One plane consists in 6 trapezoidal detectors, overlapping for a uniform ϕ coverage (FIG. 4.8). Each of these 43 mm thick trapezoidal detectors is made of the juxtaposition of two cathode strip planes with an anode wire plane in between, with 5.0 ± 0.1 mm between the planes. The cathodes are segmented in parallel 4 mm copper strips with 4.5 mm pitch, laying on a 0.7 mm honeycomb structure. The strips from one plane have a 60^o angle with respect to the other cathode plane. The anode in between is made of 30 μm goldplated tungsten wires, orientated at 120^o from the strip directions, with a pitch of 3 mm and attached to a fibre glass structure.

Altogether, T1 telescopes account for $24,000$ cathode strips and $12,000$ anode wires. During the low luminosity phase (usually assumed to last 3 years with $\mathcal{L} \leq 2{\times}10^{33}$ cm^{-2}s^{-1}), T1 detectors are safe in terms of radiation damages; they will, however, be removed before full LHC luminosity (1 kGy expected after 10 years). Finally, T1 was designed with the requirement to minimise the amount of material, to avoid decreasing HF resolution (T1 is 0.108 X_0 or 0.034 λ_I). The expected position resolution is $\sigma_x = 0.5$ mm and $\sigma_y = 0.9$ mm.

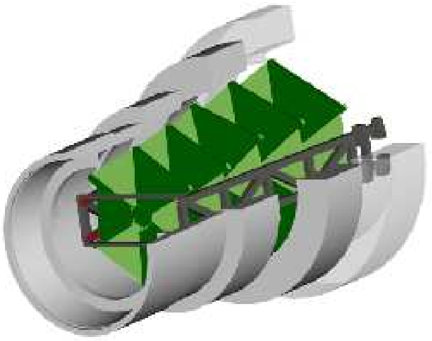

Figure 4.8: Schematic view of one half T1 telescope, with 6 CSC planes [55].

TOTEM T2

T2 telescopes consist in Gas Electron Multiplier (GEM) sensors, assembled into a cylinder with 10 aligned detector half planes with 512 annular strips (θ view) and 1024 radial strips (ϕ view), covering $5.3 < |\eta| < 6.7$ with a $\Delta\phi \times \Delta\eta = 0.06 \times 0.017\pi$ resolution [81]. The circular strips with 400 μm pitch are read-out by the same APV25 chips as the silicon strip tracker. They are located at 13.56 m from the IP, inside the plug of HF, in front of the CASTOR calorimeter, with a length of 400 mm and a diameter of 470 mm. T2 will accumulate about 100 kGy after 10 years of LHC operation.

T2 is made of triple holed D-shape GEM, reaching a gain of $\lesssim 10^5$, and a sensitive area extending from 35 to 135 cm. It has a sandwich structure: 1 drift-plane + 3 GEM + 1 read-out board, all interleaved with spacers. T2 is made of 10 planes. Half of the planes are meant for triggering. These forward telescopes have a similar read-out chips are for T1, and also same gas mixture. Final position resolution σ_{pos} is expected to be approximately 70 μm.

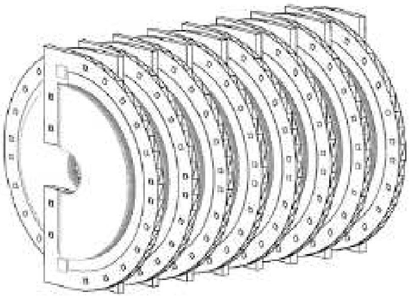

Figure 4.9: Schematic view of one half T2 telescope [55].

TOTEM RP

TOTEM roman pots (RP) are divided into two station pairs. One is located just after the beam separation and after the ZDC, at (147 m, 149.5 m). The other one is located at (216 m, 220 m). One station consists in 2 units made of 3 partially overlapping insertions, two vertical ones (from the top and the bottom) and a horizontal one (Fig. 4.10). At each insertion point, a *roman pot* (RP) containing 5 pairs of back-to-back edgeless silicon detectors [75] can be pushed in or pulled out of the beam pipe, thanks to the RP mechanics. The microstrips on silicon sensors have a 45^o angle with respect to the vertical axis, and a relative angle of 90^o, providing (x, y) coordinates. These detectors are movable in order to approach the beam at about $10\ \sigma_{\text{beam}} + 0.5$ mm ≈ 1.3 mm during collisions, while they should move back into their docking position during injection phases. The volume of the vacuum chamber is subsequently modified. A stepping motors is used for RP, applying a force at the order of ~ 1000 N. It achieves a position resolution of a few microns.

The read-out electronics are shared between analogue APV25 and digital VFAT chips (providing trigger signals, while APVs do not), which provide similar data output formats. For better measurements, the pots are directly inserted into the primary beam vacuum. Detected particles have to cross a dedicated thin window separating this primary beam vacuum to the detector vessel. During operation, a secondary vacuum is performed in the pot to minimise the thin window deformation. The expected working temperature is around 240 K. Both APV25 and VFAT rely on 0.25 μm technology, making them radiation hard for two years at low luminosity 10^{32} cm^{-2}s^{-1}, which is $\sim 10^{13}$ n$_{\rm eq}$/cm^2 or equivalently $\mathcal{O}$(few 100 kRad).

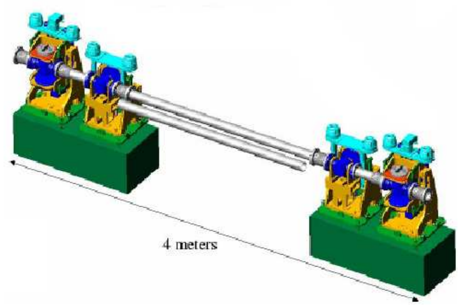

Figure 4.10: Schematic view of one TOTEM roman pot station [55].

Part of the physics programme of TOTEM is performed when dedicated LHC optical schemes are applied – the so-called[10] *high* β^*, with a reduced number of bunches (43), a low luminosity $\mathcal{L} = 10^{28}$ cm^{-2}s^{-1}, no beam crossing-angle, very small beam divergence at the IP (0.29 μrad) and $\beta^* \sim 1540$ m. This will allow, amongst other things, to measure precisely the total cross-section of LHC $\sigma_{\rm tot}$ in a very short time (*only a few days at* 10^{28} *cm*$^{-2}$*s*$^{-1}$ *with* $\beta^* = 1540$ [54]). TOTEM will also provide a luminosity measurement in nominal LHC optics, independently of any data from the central detector or from other luminosity monitoring apparatus (EQ. 2.11). TOTEM collaboration claims to reach an expected precision around 1 % [54], while other documents tend to be less optimistic [56], quoting $5-10$ %. In particular, this measurements suffer from the uncertainty on the ρ parameter and on the errors on the extrapolation of $dN_{\rm el}/dt$ to $t = 0$. Besides these measurements, TOTEM has a common physics programme with the CMS experiment, including photon interactions, low $- x$ physics, soft QCD [44, 57].

---

[10] There are actually two modes at high β^*. The first one has $k_1 = 43$ bunches, with $N_1 = 0.29 \times 10^{11}$protons per bunches, a normalised emittance $\epsilon_{n,1} = 1$ μm rad, leading to $\mathcal{L}_1 = 1.6 \times 10^{28}$ cm^{-2}s^{-1}. The second one has $k_2 = 156$ bunches, with $n_2 = 1.15 \times 10^{11}$ protons per bunches, $\epsilon_{n,2} = 3.75$ μm rad and $\mathcal{L}_2 = 2.4 \times 10^{29}$ cm^{-2}s^{-1}.

4.3.2 CASTOR

Located at 14.38 m from the IP5, the CASTOR sampling calorimeters[11] cover the same η region as TOTEM T2 detectors, from 5.2 to 6.6. Their technology relies on layers of tungsten absorber and quartz plates as active medium, for a Čerenkov radiation measurement. They have separate electromagnetic (2 read-out units) and hadronic (4 read-out units) sections, with respectively 26.8 X_0 and 3.2 λ_I characteristic lengths. Each electromagnetic read-out unit consists in 11 pairs of W-plate (3 mm) and Q-plate (1.5 mm), each pair accounting for 1.218 X_0 or 4.22×10^{-2} λ_I. The hadronic read-out units are made of 10 thicker pairs (W: 5 mm , Q: 2 mm) with a 7.96 $\times 10^{-2}$ λ_I depth per pair.

The plates are inclined at 45^o in order to reduce the light output from particles coming from the rear and to maximise the incoming particle light collection[12].

The whole structure holds onto the beam pipe, with a stainless steel skeleton. The tungsten/quartz materials have been chosen also because of the very high accumulated radiation dose of $\lesssim$ 100 MGy. Avalanche photodiodes APD perform the read-out of the light transmitted from the quartz plates.

The CASTOR calorimeters consist in a 0.65 m long octagonal cylinder (Fig. 4.11) with a 0.36 m diameter. It is segmented in 16 folds in ϕ. Both calorimeters are constructed and installed in two phases: first one in 2008 and second one in 2009 (if funded).

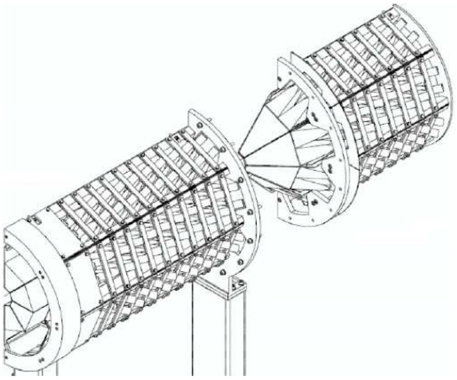

Figure 4.11: Schematic view of the CASTOR calorimeter [76].

---

[11] CASTOR stands for Centauros and Strange Object Research

[12] This angle should match the čerenkov light cone opening angle, evaluated around $46^o - 50^o$ for quartz [77].

4.3.3 ZDC

The *Zero Degree Calorimeters* (ZDC) are sampling calorimeters meant for the detection of neutrals, mainly n and γ, for $|\eta| > 8.1$. This Čerenkov detector also consists of Q/W, like CASTOR, and is located within the structure of the TAN element (neutral beam absorber), at 140 m from the IP5. As the charged particles are deviated by the D1 dipole series, that separate the incoming and outgoing beams into two distinct pipes, only the neutral particles can reach this calorimeter below $|\eta| = 9.3$. Above this threshold, all particles can be seen by the ZDC, since the deflection by the separation dipoles is not sufficient to kick them out of the path to ZDC. Like CASTOR, both ZDC's are segmented into separate electromagnetic (19 X_0) and hadronic (5.6 λ_I) sections. In addition to CASTOR, ZDC is a good complement to CMS HCAL for the estimation of the missing energy $\not{E}_{\mathrm{T}}$.

4.3.4 FP420

FP420 is a common R&D project for both ATLAS and CMS, studying the addition of forward proton detectors located[13] between 420 and 428 m, from the corresponding IP [12].

FP420 detectors are co-moving with the beampipe to protect the sensors during injection phases, in contrast with the roman pot approach where only detectors are displaced. Two bellows allow a parallel displacement of the structure a few centimetres away in a docking position [12]. Moreover, as seen in FIG. 4.12, if a proton has less energy than the beam ones, its path shifts outwards at 220 m with respect to the other beam pipe, while at 420 m, this shift goes inwards. Hence the roman pot solution would have been practically impossible. The co-moving pipe is called *Hamburg pipe*, in reference to similar setup at HERA.

The detectors are assembled into several *pockets*. Each pocket contains a set of several Si 3D planes for the position measurement, and one Čerenkov detector for some timing information. The Si 3D sensors are made of a n bulk filled-in with towers of p implants. Typical distance between towers is 50 μm. As the collection distance is very small, even if the signal is quite small, the signal-to-noise ratio keeps high in spite of the radiation damage. This can be easily understood when the damage effects is thought in terms of the decrease of the charge carrier mean free path in the silicon bulk [12]. In order to reduce the insensitive border, these detectors have n^+ implants covering the border, called *active edge*.

Depending on the pocket, the Čerenkov timing detector active medium is either gaseous (GASTOF [78]) or solid (Quartic [12]), read-out by a Constant Fraction Discriminator, with a timing resolution below 10 ps. The measurement of the arrival time of the detected proton gives its time-of-flight from the

---

[13] the so-called *cold region* of the beamline, where the pipes and surrounding materials are kept at 1.8 K.

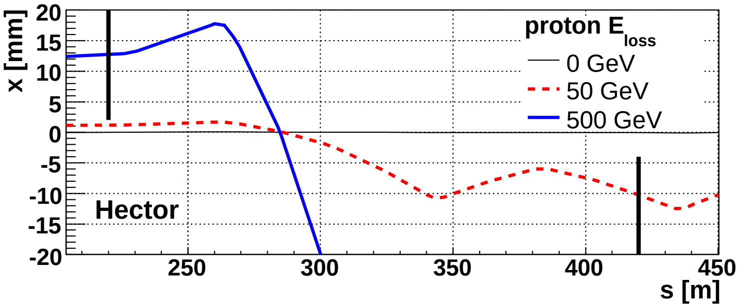

Figure 4.12: Proton position at 220 m and 420 m. When proton experience some energy loss, its path goes outwards at 220 m, compared to the second beam pipe, while at 420 m, it goes in the direction of the second beam pipe. Simulation with HECTOR [13].

vertex to the detector. Measuring the p timing gives an estimate of the z coordinate of the vertex. At high luminosity, when event the pile-up is large, this z estimate is discriminant to reject backgrounds with forward protons coming from diffractive pile-up events. Assuming timing detectors located at a distance L from nominal IP, and a vertex displaced by a distance z, the time difference between the arrival of both protons in each forward timing detector is given by:

$$\Delta t = \frac{L+z}{c} - \frac{L-z}{c} = \frac{2z}{c} \tag{4.1}$$

This approximation holds well as $\beta \approx 1$ for beam protons and as the path trajectory is in very good estimate L. Hence a detector resolution of 10 ps results in $\delta z = c\delta t/\sqrt{2} = 2.1$ mm. Finally, the FP420 stations could be equipped with very precise beam position monitors ($\mathcal{O}(\mu\text{m})$) [12].

The acceptance is directly complementary to the one of roman pots at 220 m, as the proton acceptance in the range $0.002 < \xi < 0.02$ is 100 %. A major advantage of these detectors, as for the ones at 220 m, is that from precise measurement of the proton momentum losses ξ_1 and ξ_2 (in case of double-tagged events), the mass M of the central system can be reconstructed with a very good presion. This uses the *Missing Mass Method* (EQ. 4.2), independently of the decay modes:

$$M^2 = \xi_1 \xi_2 s. \tag{4.2}$$

If this upgrade is approved by CMS, the installation of FP420 stations is expected in 2010.

4.4 Online luminosity monitors

As mentioned in Chapter 2, the observation of the on-going rate of events provides an online monitoring of the instantaneous luminosity, possibly bunch-to-bunch. In CMS, this method is applied on HF data or using a dedicated near-beam pixel telescope, the PLT. The design goal for luminosity measurement is to reach 1% of statistical errors on a particular bunch luminosity in about[14] 1 s, and that the absolute measurement is precise to 5% or better.

4.4.1 Hadron Forward calorimeter

Two methods are envisaged for the online luminosity monitoring with HF: the counting methods and the average E_T sum per bunch crossing. The number of collisions per bunch crossing is given by Eq. 3.7. This Poisson statistics allows for bunch crossing with no collisions, whose probability is

$$p(0, \mu) = e^{-\mu}. \tag{4.3}$$

When the luminosity is such that μ is small, $p(0, \mu)$ does not falls off too rapidly. In particular, from the noise level in HF it should be quite easy to distinguish between events without collisions from events with one or more. Putting together Eq. 3.8 and 4.3, the observation of the rate of bunch crossings without collisions provides a relative evaluation of the instantaneous luminosity:

$$\mu = -\ln p(0) = \frac{\sigma \mathcal{L}}{f_{BX}}. \tag{4.4}$$

This method, based on the HF occupancy, is called *Zero counting*. However, as the luminosity increases to reach the design value, so does μ. The probability for having no interaction subsequently vanishes[15]: $p(0; \mu) \to 0$. Fortunately, the segmentation of the forward calorimeter ($\Delta\phi \times \Delta\eta = 0.175 \times 0.175$) lead to 864 measurements with a small average value of sensed particles:

$$\mu\big(E_T > 0.1 \text{ GeV}, \Delta\phi \times \Delta\eta = 0.175 \times 0.175\big) \approx 1.$$

The Zero Counting can hence take place at the level of HF towers.

Besides these counting methods, HF data can also be used for luminosity monitoring by looking at the linear relationship between the total energy deposit in HF rings and the mean number of collisions per bunch crossing [53,70].

4.4.2 Pixel Luminosity Telescope

The 2×8 Pixel Luminosity Telescopes (i.e. the PLT detector), are altogether a CMS instrument for the determination of the relative instantaneous luminosity,

---

[14] One should remind that the revolution frequency is more than 11 kHz, so 1 s corresponds already to a large number of data per bunch.

[15] This effect is usually called *Zero starvation*.

bunch-by-bunch. At the same time, the PLT will provide the location of the IP centroid. The requirements for this instruments are to be fast, stable and precise. The telescopes are symmetrically placed around the IP5, and each one consists in 3 planes of 8×8 mm^2 sensors. These sensors are single crystal diamond (Chemical Vapour Deposition), 400 μm thick. The very wide band gap[16] in diamond structure is such that the noise level is kept to really low values, making this kind of sensors radiation hard, and having no need for cooling during operation. The sensors have been mounted as pixel detectors, using the CMS tracker pixel chip. All planes are located in $1.65 \text{ m} < |z| < 1.85 \text{ m}$, with 10 cm between the sensor planes. This small angle corresponds to $|\eta| = 4.3$. A measurement is a 2×3 fold coincidence. Using the counting from the PLT, the expectations for luminosity determination are approximately 1% (stat) for each bunch after 1 s.

Moreover, at a lower rate (few kHz), the PLT will provide CMS acquisition chain with some information on the position of the IP centroid, with an expected precision of 28 μm in the direction transverse to the beam and 520 μm in the beam direction [70]. The PLT have not yet been approved by the CMS collaboration.

4.4.3 BRAN

Using a Van der Meer scan (Eq. 2.5) for the calibration of luminosity monitors requires two type of instruments: (1) very precise beam position monitors, as the required positioning are really constrained, with respect to the bunch transverse sizes; (2) an independent luminosity monitor, to compare the measurements during the scan. For this purpose, a gas ionisation chamber is placed in the TAN collimator, at 140 m from the IP, in a vacancy just behind the ZDC, on both sides of the IP5. The BRAN detector is a sampling calorimeter, using 30 cm of copper as an absorber. This detector is actually placed near the maximum of the hadronic shower in TAN. It detects the shower originating from neutrons coming from the IP with $\mathcal{O}$(TeV) energy. This flux monitor provides individual bunch resolution, for instantaneous luminosity monitoring and for the measurement of the crossing angle. The gas chamber is about 10 cm$\times$10 cm and will have to deal with 170 MGy/year radiation levels [70].

---

[16] With a 5.5 eV wide band gap, diamond is considered as an insulator

Chapter 5

Edgeless silicon detectors

Very forward detectors, located further than 200 *m from the* IP*, are near-beam detectors measuring scattered protons with an energy lower than the beam one. Their distance to the beam determines their acceptance: the closer the detector, the wider its acceptance. Two constraints arise from this location: (1) the need for a very good radiation hardness, due to the large particle flux coming from diffraction and beam halo; (2) the need for minimising the width of the insensitive edge between the sensor active area and the detector physical border. Several designs of radiation hard edgeless detectors are reviewed. Some Research and Development on cold silicon edgeless detectors has been carried out in the framework of the* CERN RD39 *collaboration. It aimed at producing prototypes of such detectors by cutting silicon microstrip sensors through their sensitive area, with laser or plasma beams. The leakage current of such devices is very large but its effects can be controlled: (1) it decreases with a lower operating temperature ($\mathcal{O}(200\ \mathrm{K})$); (2) it affects only the closest strips to the detector cut edge. The results have been presented in two conferences [98, 99].*

5.1 Motivations

Very forward detectors (VFD) are meant for the measurement of scattered protons, escaping the central detector by the beam pipe along with beam protons. VFDs are located far from the IP (e.g., at 420 m) and very close to the outgoing beams in the transverse plane ($\mathcal{O}(1\ \mathrm{mm})$). Their distance s from the interaction point is the compromise between technical beamline constraints and the requirements for an optimal detector acceptance.

Final state protons scattered at a small angle and experiencing a small energy loss ($E_{\mathrm{loss}} \lesssim 1000$ GeV) at the IP follow closely the beam path. The proton path deviation is mostly driven by this energy loss (FIG. 1.5). The key principle of very forward detectors is to measure the proton lateral displacement.

Very large fluxes of particles coming from beam halos and from interactions at CMS themselves (mostly diffraction) prevent a long-term operation of forward detectors, if too close from the nominal beam position.

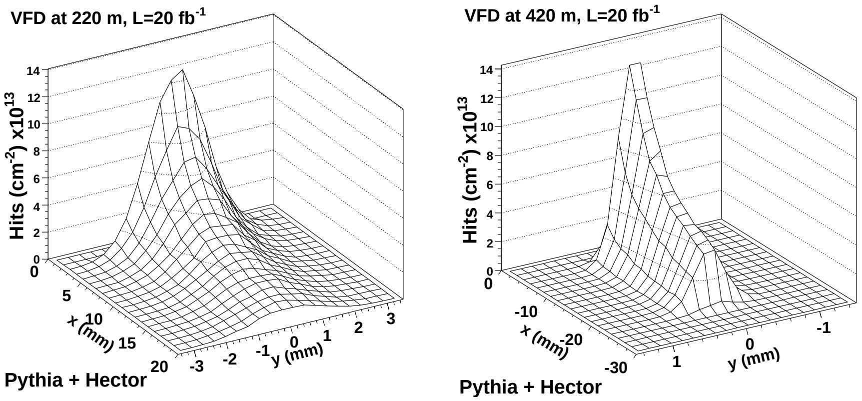

Figure 5.1: Proton fluences expected from $pp \to pX$ interactions, for very forward detectors located at 220 m (left) and 420 m (right). Detectors horizontal distance to the beam x is assumed to be 2 mm and 4 mm, respectively. The y coordinate is the vertical position of the detector. These fluences correspond to an integrated luminosity $L = 20$ fb^{-1}. Proton fluences can locally exceed 10^{14} hits per cm^2, but are highly non-uniform. Simulation with PYTHIA 6.2.10 [136] for the signal generation and HECTOR [13] for the leading proton transport.

FIG. 5.1 illustrates the proton fluence[1] expected from Single Diffractive (SD) events only. VFDs are assumed to be located at $s = 220$ m (left) and $s = 420$ m (right) from the IP. Their horizontal position to the beam is $x = 2$ mm and $x = 4$ mm, respectively. Fluences of 7 TeV protons can exceed locally 10^{14} hits per cm^2, but this is highly dependent on the x coordinate. However the model is possibly underestimating the SD contribution and a safety margin should be taken into account. Moreover, the effects of beam halos are not considered. Finally, an integrated luminosity L of 20 fb^{-1} is assumed, which is an estimate of one year of LHC running at low luminosity. Hence, radiation hardness to fluences above 10^{15} particles per cm^2 should be considered for the edgeless detector design, even if the dose is not expected to be uniformly distributed across the detector area.

For comparisons, a fluence of given particles (like protons, Φ_p) is usually converted into an equivalent fluence of 1 MeV neutrons Φ_{eq}, producing the same amount of damages in the silicon bulk:

$$\Phi_{\text{eq}} = k \times \Phi_p \tag{5.1}$$

where the *hardness factor* k is tabulated as a function of the particle energy [84].

---

[1] The fluence is the time integral of the flux.

It is observed that k decreases continuously with the proton energy and seems to reach a plateau at high energies. No data are available for protons with an energy above 9 GeV (with $k(E = 9\ \text{GeV}) = 0.5084$), so is assumed here, to fix the ideas, that:

$$k(E = 7\ \text{TeV}) \approx 0.5. \tag{5.2}$$

The requirements are then that the detectors must withstand an equivalent fluence Φ_{eq} at the order of $10^{15}\ \text{n}_{\text{eq}}/\text{cm}^2$, which is the same order of magnitude as for the SLHC. Radiation hardness at this level is currently only provided by silicon technologies.

The minimal distance of approach of the detectors to the beam is thus strongly constrained. Knowing the beam width σ_{beam} at detector position, the rule of thumb at the LHC is to keep the detectors at a distance of at least $1\ \text{mm} + 10 \times \sigma_{\text{beam}}$ [54]. The non-sensitive physical edge of VFDs subsequently restricts the detector acceptance. Fig. 5.2 illustrates the relation between the acceptance of some forward detector, in terms of proton energy loss E_{loss}, and the position of the edge of the sensitive area. In the current R&D, the goal is to reach an non-sensitive edge of approximately 100 μm.

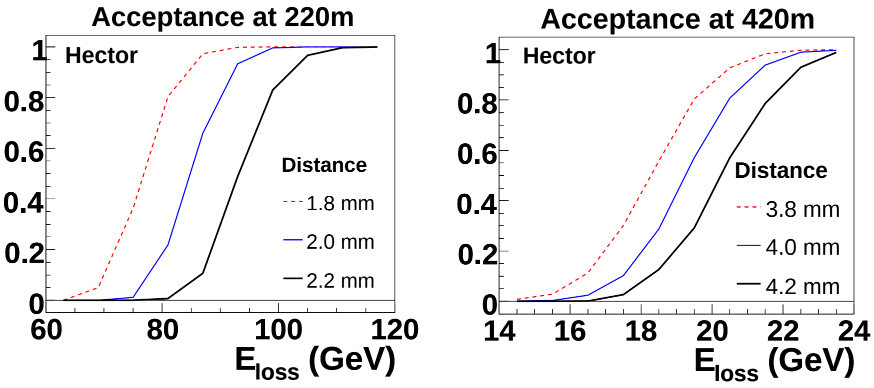

Figure 5.2: Dependence of the proton acceptance on E_{loss} as a function of the detector edge distance from the beam, for very forward tracking detectors located at 220 m (left) and 420 m (right), respectively. Simulation with Hector [13].

Most of the current designs of silicon microstrip detectors [85,86,87] have a large inactive border around the sensitive area. This border is due to the guard rings, bias rings and the margin left when sawing the sensor out of its wafer. This border typically extends from 300 μm to 500 μm from the physical edge to the sensitive area[2]. Sensors with a minimal inactive edge are called *edgeless* detectors.

---

[2] For safety margin, the border of the CMS tracker sensors is as large as 700 μm.

In the following, several approaches for the design of silicon edgeless detectors are discussed. A study of two particular technologies for the implementation of a prototype is presented. This study was performed in the framework of CERN RD39 collaboration [89]. This collaboration has been aiming for the development of super radiation-hard cryogenic silicon detectors for applications in LHC experiments and their future upgrades, as for the Super LHC (SLHC). Fluences between 10^{15} and 10^{16} $\mathrm{n_{eq}/cm^2}$ are considered. RD39 studies original modes and environments for the operation of such sensors, which are a low working temperature and a forward bias of the sensors. The initial key factor for joining to this collaboration was a common interest in operability of sensors at low temperatures in order to cope with the leakage current and the irradiation damages. The RD39 collaboration has also investigated the impact of cutting silicon pads (diode) with a laser. Cutting through existing structure is easy and straightforward, and offers a freedom in the edge shape. This simple process has been investigated for the production of radiation hard edgeless sensors, operated at low temperatures.

5.2 Impact of the radiation damages on silicon sensor performance

The Charge Collection Efficiency (CCE) is a key factor reflecting the actual detector performance. This parameter depends on the detector sensitive volume (depletion thickness times sensitive area) and on the presence of trapping levels due to radiation-induced defects, that decrease the signal collection. The CCE thus evolves with the accumulated dose.

The high level of radiations with hadrons strongly increases the absolute effective doping concentration ($|N_{\mathrm{eff}}|$) of the silicon bulk. A full depletion of the detector then requires a higher bias voltage. But at a fluence close to 10^{16} $\mathrm{n_{eq}/cm^2}$, thousands of volts would be needed to deplete completely a standard detector of 300 μm thickness, which leads to difficulties in practical operation.

In addition, radiation-induced defects imply the presence of parasitic levels in the gap between valence and conduction bands, in the energy level representation of semi-conductors. The new, unwanted, energy levels can trap free charge carriers created by the crossing of a charged particle.

At 10^{16} $\mathrm{n_{eq}/cm^2}$, free carriers can only drift 20 to 30 μm before being trapped inside the silicon bulk. Assuming an average drift velocity v_{th} of 10^7 cm/s and a level trapping cross-section σ_{trap}, the presence of these defects can be expressed into the *trapping* and *detrapping time constants*, τ_t and τ_d. The trapping time represents the typical time scale after which a free carrier fills a trapping level. Its evolution with respect to the radiation dose underwent by sensors motivates the need for new developments in radiation hard silicon technologies, meant for heavily irradiating environments. For an unaltered mean drift velocity, a sharp decrease of the trapping time leads to a corresponding decrease of the typical trapping distance. Assuming the concentration of traps N_t of 5×10^{16} cm^{-3} and the trapping cross-section of the value of 10^{-14} cm^2, the trapping time[3] is 0.2 ns (Eq. 5.3).

$$\tau_t = \frac{1}{\sigma_{\text{trap}} v_{\text{th}} N_t} \tag{5.3}$$

Subsequently, the effective charge collection distance d_{eff} could then be restricted to that of a 20 μm layer, regardless the depletion depth [94].

Both issues, the high value of the full depletion voltage V_d and the shortness of the effective charge collection distance d_{eff}, should be tackled in order to preserve CCE.

The modeling [91] shows that the electric field in irradiated silicon detectors can be modified by filling the deep defect levels created during irradiation. Due to the strong temperature dependence of the detrapping time (Eq. 5.4), it is possible to keep these levels filled, if the detector is operated at low temperatures:

$$\tau_d = \frac{\exp(-E_t/kT)}{\sigma_{\text{trap}}\ v_{\text{th}}\ N_C}, \tag{5.4}$$

where N_C is the electric state density in the conduction band and E_t is the trap energy level.

RD39 is developing radiation hard detectors using the current/charge injection operation mode. The current- or charge-injected diodes (CID) have an electric field controlled by the space charge limited current mode (SCLC) in such a way that the internal electric field is nearly uniform, almost independent of the fluence that the detector has to withstand.

Several approaches might be used to fill the deep levels: like using a light source (laser or LED) on $p/n/p$ structures or by operating $p/n/n^+$ structures in forward bias. In all cases, low temperature operation is needed, in order to freeze-out the trapping centres. Temperatures around 80 K are considered by the collaboration. In this operation mode, the partial recovery of the CCE of heavily irradiated sensors is called the *Lazarus effect* [92, 93].

Major advances in the development of radiation hard detectors, done by the collaboration, are related to the Lazarus effect and the charge or current injected devices.

As an illustration, Fig. 5.3 shows the C-TCT signal[4] of Magnetic Czochralski silicon (MCz-Si) sensors with 300 μm in thickness. The TCT technique provides the signal shape of one of the charge carrier type (electron or hole) which has to cross the whole detector width before being acquired. It relies on the generation of the signal on one surface of the sensor, with a laser. The upper curve (triangles) corresponds to the operation at 60 K of the non-irradiated sensor, with 200 V reverse bias, which defines the reference level for further comparisons. The circles are the signal of a CID detector made of MCz-Si measured at

---

[3] This mean value takes into account the fact that the trapping time is twice bigger for the holes than for the electrons.

[4] Cryogenic-Current Transient Technique: setup using the TCT technique at low temperature, built in the Cryolab at CERN.

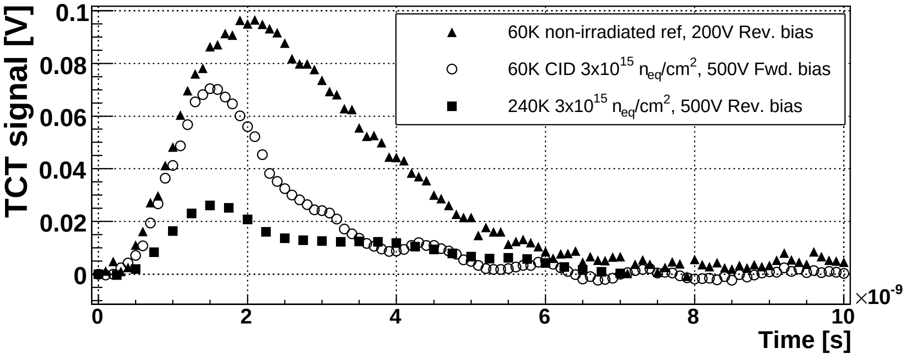

Figure 5.3: C-TCT signal of MCz-Si sensors before irradiation in reverse bias (200 V) at 60 K (triangles), after irradiation in reverse bias (500 V) at room temperature (squares), and after irradiation in forward bias (500 V) at 60 K (current-injection operation mode, circles) [99].

60 K with 500 V forward bias. This sample has been irradiated with 9 MeV protons to the effective fluence of $3 \times 10^{15} \mathrm{n_{eq}/cm^2}$. The same sensor operated at 240 K with 500 V reverse bias is the lower curve (squares).
Assuming that the reference detector produces 100% CCE and collects 24,000 electrons for 1 MIP (Minimum Ionising Particle), the CCE of CID is 45% and collects 10,800 electrons for 1 MIP whereas the same detector measured at 240 K shows 27% CCE. So, the CID CCE is almost twice as much. The 27% CCE is expected and is largely due to the fact that the detector is under depleted with 500 V bias which is a practical upper limit in large tracker system.
These measurements have been done by a 1060 nm infrared laser (IR) which simulates well MIPs [91]. Because the absorption coefficient of the IR depends strongly on the operation temperature, the calibration measurements with non-irradiated reference have been performed for both temperatures [89]. The amount of IR excitation during these measurements was equivalent to about 10 MIPs, with a laser trigger frequency of 10 Hz. The laser stability was observed to be better than 1% over 60 hours period of operation [99].

In summary, the RD39 collaboration has developed super radiation-hard silicon detectors, based on usual Float Zone or Magnetic Czochralski silicon sensors, able to cope with high particle fluences (3×10^{15} $\mathrm{n_{eq}/cm^2}$). These detectors are operated at low temperatures and in forward bias. This motivates the development of prototypes of radiation hard edgeless detectors, based on cut sensors operated at low temperature.

5.3 Palette of techniques for the design of edgeless sensors.

Reducing the dead border around the sensitive area of sensors is a active field in current R&D. Edgeless sensors are used in collider physics [75] or in medical research [88]. Several techniques for the fabrication of effectively edgeless sensors are presented in this section.

i **Mechanical cuts**. The simplest way to cut silicon detectors is to use diamond saw. This is the way the sensors are extracted from the silicon wafer during production. However, as the cut border is not smooth and due to the presence of many cracks, sawing through the active bulk of a sensor is not a good option as it will induce a high leakage current. Another mechanical method, used for the R&D for the TOTEM collaboration consists in, first, digging a straight line on the sensor backplane with a laser that melts the silicon; then the sensor is mechanically bent along this line until it breaks [95]. For such rough cutting processes, where the edge is not quite smooth, a subsequent chemical treatment of the border improves the detector behaviour.

ii **Laser cutting** [96, 97, 98]. The local energy deposition by a laser light could melt the silicon crystal. This provides a way to cut through the bulk of sensors, and at the same time the ability to adapt the geometry of the cut edge to the practical need. Curved cuts and even holed sensors can be produced this way, independently to the strip orientation and topologies. This cut process was first investigated as a mean to easily produce edgeless detectors, by cutting through the sensitive area of usual silicon microstrip sensors. Prototypes with straight cuts with three kinds of orientation with respect to the strip (parallel, angular and perpendicularly) were produced. The abrupt increase of leakage current, due to the fact that the sensitive area is affected, to the creation of defects along the cut border, and to the discontinuity of the bias and guard ring structures, is managed by operation of the sensors at low temperatures (i.e. below -20^o C). The corresponding results are presented in Section 5.4.3.

iii **Plasma *dry* etching** [99, 100, 101] Similarly to the laser cutting, a plasma can be used to cut through the silicon bulk, following a chosen pattern. The main advantage is in cleaner and sharper edges, less affecting the crystal structure around the cut. Similar tests as for laser-cut devices are presented in Section 5.4.4.

iv **3D pixels** [102, 12, 55]. The so-called 3D pixels consist of a bulk of silicon, pierced by an array of p and n implants. Oppositely to usual sensors where the free charge flow through the whole bulk width to reach the corresponding implant, in 3D pixels, the carriers travel a very short distance before being collected by an implant. This small distance lead to the possibility of reducing the insensitive border around the sensor. Moreover, the radiation hardness is improved as the collection distance is smaller. The sensor is quite insensitive to a *moderate* irradiation dose. TAB. 5.1 compares 3D and planar detectors.

	3D	**planar**
$V_{\text{depletion}}$ (V)	< 10	70
$d_{\text{collection}}$ (μm)	~ 50	300
$t_{\text{collection}}$ (ns)	~ 2	~ 20
insensitive edge (μm)	< 10	~ 300

Table 5.1: 3D vs planar silicon detector parameters, based on a 300 μm thick silicon bulk [55].

v **Dedicated designs**. Using a dedicated terminal structure, very close to the edge of silicon sensor helps in extending the depletion region, allowing for signal collection very close to the edge. Reference [106] proposes simulation results of $p^+/n/n^+$ devices with a n^+ terminating ring close to the edge, for the reduction of dead space, while preserving the leakage current at a reasonable level ($\mathcal{O}(1\ \text{nA})$). TOTEM experiment recently focused on sensors with two successive terminating structures, reaching sensitivity at 50 μm from the edge [107]. Sensors with *active edges*, i.e. with the backplane implant extending to one or several sides, are also interesting dedicated designs with an electrical field near the edge better controlled.

vi **Scintillating fibres for tracking**. This technology is for instance used in ALFA roman pots meant for luminosity monitoring for the ATLAS experiment [108], with plastic fibres. These forward detectors are located 240 m on each side of IP1. By overlapping several structures of plastic scintillating fibres, ALFA theoretically reaches a 14.4 μm spatial resolution. Radiation hardness is a concern for such technologies.

5.4 Testing laser- and plasma- etching processes

Some research and development (R&D) work has been done on laser-cut and plasma-cut silicon devices. This section reports on the various measurements performed during these studies, in the framework of CERN RD39 collaboration, mostly with O. Militaru (UCL). Measurements of plasma-cut devices were done with G. Pierre's support (UCL).

Silicon devices benefit from the large interest from technological industries and from the various uses and developments of silicon-based detectors in particle physics. All these developments have now reached a mature phase with mature fabrication processes and controlled sensor characteristics, even after ageing or irradiation. Many important developments are still being done by R&D collaborations like the large CERN RD50 (material engineering) or the smaller CERN RD39 (by varying the operation conditions). Therefore, the modification of existing silicon structures is one way amongst others of possible techniques for the development of edgeless sensors.

The possibility to build such sensors by cutting through the active area has been investigated. Such a method has already shown promising results for diode pads [96,97]. Operation of silicon microstrip sensors at low temperature results in a decrease of the leakage current. This property motivates studies of our particular edgeless designs, where the detector bulk has been affected by a harsh cutting process. The cut itself perturbs the crystal structure and implies local surface micro defects near the detector edge. Moreover, usual structures surrounding the active area, like bias rings and guard rings, are also affected by the cut. Altogether, this leads to a very large increase of the total leakage current, by ≈ 5 orders of magnitude (Fig. 5.6 and 5.10). Still, as explained thereinafter the operation temperature have beneficial effects on leakage current. Moreover, this large current only affects a limited number of strips. Before going into details for these devices, the available testing setup are being explained.

5.4.1 Probe Station

The manipulation of submillimeter structures requires precise and dedicated tools for current and voltage measurements at several points. A Karl-Süss PA200 *probe station* [109] was used for such measurements of the sensors. It combines needles for precise contacts and a microscope for a visual control of the probe positioning. The detector whose features are being measured is maintained on the holding structure – called the *chuck* – by a set of vacuum lines. This chuck has several other purposes, like a precise positioning of the tested structure (in X,Y,Z and θ_Z), its cooling (down to -40^oC) and possibly its bias via the detector backplane. A flow of cooled methanol and Peltier elements allow the control of the temperature, monitored via a Pt100 probe. A flux of dry air reduces the risk of condensation when cooled down.

The probe station is equipped by several instruments for the bias and the measurements: a Keithley 2410 sourcemeter [110] for the high voltage bias (up to 1100 V), an Agilent 6614C [111] for the low voltage (DC), an Agilent 4248A LCR-meter [112] for the capacity measurements and a Keithley 6514 [113] for the precise current measurements ($\sim 10^{-16}$ A). All these apparatuses are connected via a switching matrix. The probe station has been extensively discussed in [114,115,116].

5.4.2 Laser setup

The aim of the *laser setup* is to inject locally the energy of a pulsed laser onto a tested detector, in a protected environment, and to output an amplified and shaped signal. This system consists of a hermetically closed metallic cylinder, keeping the tested structure in vacuum and away from any external light source. The structure can be illuminated by a movable red laser, probing the strips separately. The operation temperature is achieved by a thermal contact to a cooling circuit, whose temperature is set through a controlled flux of cold dry air. The Yokogawa controller [120] monitors the temperature of the coolant, and acts on a mechanical valve, that regulates the coolant flow.

The tested structure lays on a thermally and electrically conductive copper plate, whose temperature is monitored via two flat Pt100 probes. The read-out electronics is connected, through the forward cylinder door, to the tested sensor. This electronics consist of a Canberra 2003BT charge preamplifier [117], that *integrates* the deposited charge coming from the sensed strip. This preamplifier is itself connected to a Canberra spectroscopy amplifier [118], providing both a measurable output signal and the preamplifier input power. The output signal is digitised in a Tektronix TDS 724A oscilloscope [123], with a maximal sampling rate of 1 GS/s.

The Pilas laser [119] wavelength peaks at 677 nm with a very narrow spectral width ($\sim$ 4 nm). The laser pulses last about 30 ps (FWHM). An external controller drives the laser head for the pulse repetition frequency (ranging from 1 Hz to 1 MHz). The beam spot extends up to $\sim$ 1 mm. The laser position is set via a knurl, on the rear of the cylinder, reaching a relative position precision of $\sim$ 100 μm. The second horizontal coordinate and the vertical positioning are tunable thanks to their corresponding screws, enclosed in the cylinder.

The tested silicon device is biased by a CAEN N470 high voltage source [121] and the current flowing through this power line is monitored via a IPC Current Digitiser module [122]. The high voltage provided by the CAEN module extends from -3 kV to 3 kV, for a maximal 3 mA current. The full setup is depicted in Fig. 5.4.

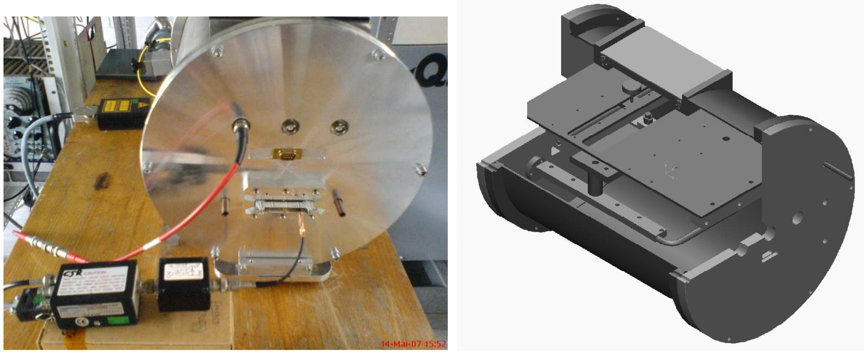

Figure 5.4: Picture (left) and exploded view (right) of the laser setup (Courtesy B. Florins). The feedthrough connections are visible on the front door, as well as on the preamplifier (left, in front) and the laser source (left, back).

5.4.3 Laser-cut silicon devices

The evaluation of laser-diced pads showed encouraging results, with respect to the edge sensitivity [96], motivating further R&D on laser-diced silicon microstrip sensors [97,98], operated at low temperature. CMS tracker silicon *baby sensors* were used for this evaluation. These devices are fabricated altogether (i.e. on the same wafer) with the final sensors for CMS tracker, and are usually meant to be testing structures, as for the production quality monitoring and studies of the evolution of detector properties after irradiation [114,115].

The initial $n^+/p/p^+$ single-sided Float Zone sensors were 320 μm thick, with 192 strips about 1.5 cm long, and a pitch of 120 μm. They were laser-diced in Brookhaven National Laboratory, and a subset of these underwent some chemical etching. Several cut geometries have been tested. All were straight cuts, but with different orientations with respect to the strip direction: parallel, perpendicular or with a slight angle (FIG. 5.5). After being diced, whether etched or not, the sensors shows as expected a large leakage current ($I_{\text{leak}} = \mathcal{O}(100)$ μA).

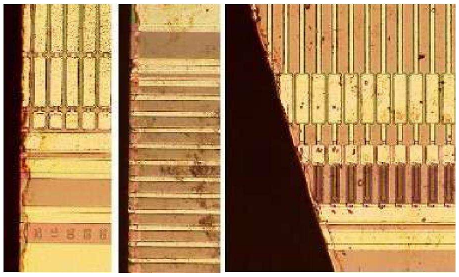

Figure 5.5: Picture of the laser cut sensors. Several cut geometries are shown: parallel to the strips (left), perpendicular (middle) and angular cut (right).

This total current decreases with the temperature (FIG. 5.6). However the decrease is not very steep and depends on the sensor: about 1 order of magnitude can be reasonably expected for good sensors, when operated around -30^oC. The experimental range $[240, 300]$ K is fixed by the lowest reachable temperature by the experimental setup. In general, a practical limitation for the use of such devices in a real experiment would be the availability of LN_2 as coolant, leading to even lower temperature operation.

Even if this current is overwhelming, only few channels are affected (FIG. 5.7). This emphasises the fact that cut-induced damages only have a local effect. These sets of measurements were performed thanks to the probe station, with needle contacts enabling to sense either the total current (from the bias ring) or single strip ones (from the corresponding pads). Depending on the studied structure, the total current could be decreased, within the measured temperature range, by at most one order of magnitude. Oppositely to mechanically cut devices [95], the chemical passivation of the diced edge did not help in improving this situation, but could be of interest for limiting the ageing of the device. Hopefully, most of the current is driven by the two closest channels (the ratio is $10^5 : 1$ compared to strips further from the diced edge). This fact could be used in some dedicated read-out design where the *signal* coming from these strips would be taken away from the read-out chips. Moreover, all other strips show a similar detector current, independently from their actual position, leading to a uniform distribution over the cut sensors. The I-V measurements of these sensors thus suggest that they could be successfully operated at moderately low temperatures, as $[180\ \mathrm{K}, 200\ \mathrm{K}]$.

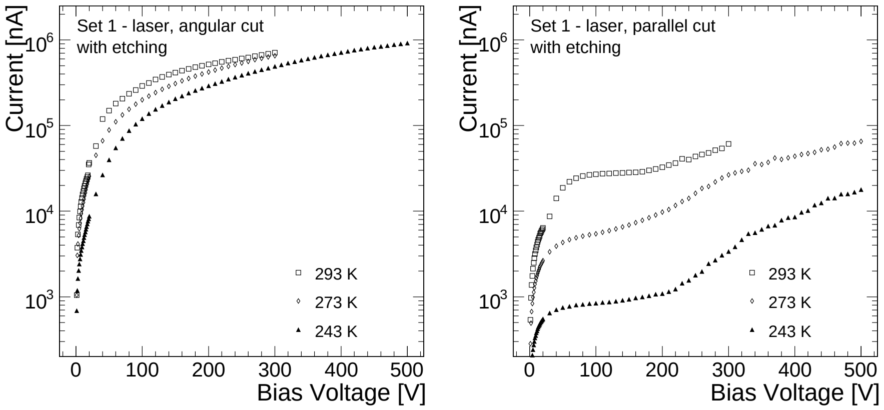

Figure 5.6: Temperature evolution of I-V for laser cut sensors [98]. Chemical etching has been applied.

In parallel, a first edgeless module prototype has been built (Fig. 5.8): two pairs of half sensors were glued on a silicon support plate for the cooling and the bias, with a glass CMS pitch adapter matching the pitch of the input pads of four APV25 read-out chips [126] mounted on a CMS tracker front-end hybrid. However, similar problems as the ones detailed in Section 5.5 prevented this module prototype to be fully exploited.

5.4.4 Plasma-cut silicon devices

As show in Fig. 5.5, the region touched by the laser during the cutting process has some extension (here of the order of a quarter of the strip pitch). The laser melts the silicon bulk and investigating a sharper cut technique is desirable in order to decrease the total leakage current of the structure.

A new cut technique, based on plasma etching, has been tested [99]. This plasma cut has been processed at the Helsinki Institute of Physics with Induction Coupled Plasma (ICP) at 260 K and a pressure between 10 and 20 mTorr. The ICP power is in [1 kW, 2 kW] and the Capacitively Coupled

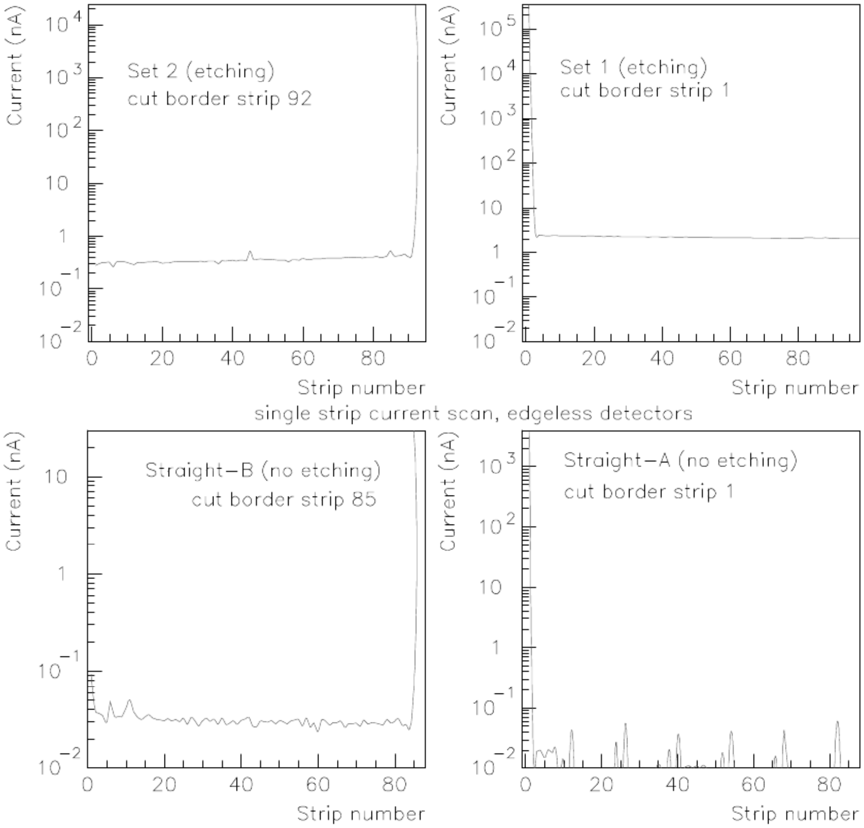

Figure 5.7: Strip-by-strip current measurement for laser cut sensors [98]. For all measured sensors, the total current is mainly driven by two or three strips, close to the cut edge.

Plasma power (CCP) from 1 to 3 W, with SF_6 flow of max. 100 sccm and O_2 flow of $12 - 20$ sccm. The plasma allowed an etch-rate up to 7.6 μm min^{-1}.

A set of sensors has been cut in the direction orthogonal to the strips, and others with the parallel geometry (Fig. 5.9). These baby-sensors correspond to the TIB[5] geometry: 300 μm thick, 192 strips with 80 μm pitch.

As expected, the current dramatically increases (from 10 to 10^5 nA) when comparing the measurement before and after the plasma cut (Fig. 5.10). As for non-cut and laser-cut sensors, the global shape of the I-V curve is not affected by the cut. However, the global increase is really dramatic. The temperature

---

[5] TIB = Tracker Inner Barrel. CMS tracker is divided into different regions. This corresponds to several position and orientation with respect to the interaction point. This implies several detector geometries, like TIB, TOB and TEC ones [104].

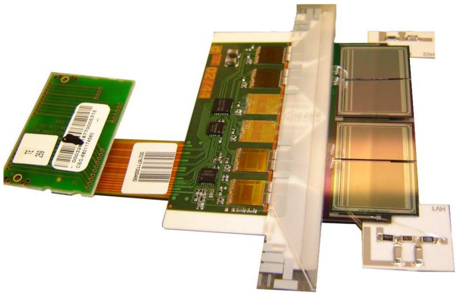

Figure 5.8: Laser-cut silicon microstrip detector module prototype.

evolution is also shown, from room temperature down to the setup lower limit, showing the expected decrease in current with decreasing temperature. Still, in the observed temperature range [240 K, 300 K], the temperature dependence of the total leakage current is in good approximation linear (Fig. 5.11). The overall effect of the temperature on the decrease of total leakage current is thus not as high as for classic sensors. An interpretation for this could be that the surface leakage current, with a smaller temperature dependence, is dominant in the case of cut-sensors, while volume leakage current drives the behaviour of classical sensors.

A deeper insight is possible with the single strip current measurements. Similarly to the laser cut sensors (Fig. 5.7), most of the leakage current is driven by the two closest strips to the cut border (Tab. 5.2). The current intensity, and its variable behaviour in terms of bias voltage and operation temperature, are such that these strips can in practice not be read-out safely by the electronics. For these particular sensors, the third strips seem useable and further ones are insensitive to the presence of a cut border. Further studies, involving acquisition electronics, are needed to understand whether the related noise is manageable on the third strips.

Strip	**Current (sensor 1) [nA]**	**Current (sensor 2) [nA]**
♯1	8.29×10^4	1.41×10^5
♯2	2.09×10^3	1.25×10^4
♯3	0.54	2.94×10^2
♯4	0.2	0.23
♯5	0.26	0.17

Table 5.2: Single strip leakage current, for plasma cut sensors with parallel geometry. The strip number is conventionally taken from the etched border [116].

The impact of the plasma cut technique and its usability for building edgeless detectors have been tested thanks to the *laser setup*. A red laser light is

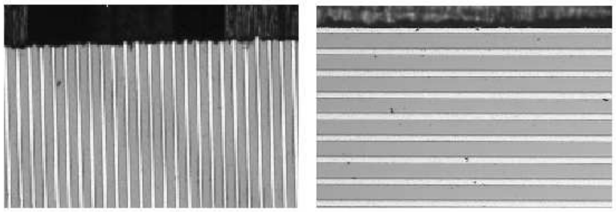

Figure 5.9: Picture of plasma cut sensors, with orthogonal (left) and parallel (right) cuts with respect to the strip direction.

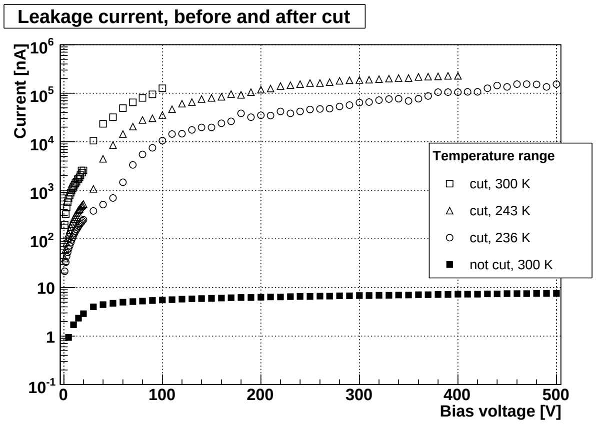

Figure 5.10: Temperature evolution of I-V for plasma cut sensors (perpendicular cut).

pointed to the strips, which are read-out by the setup. The detector response to a given calibrated injected signal is extracted from several strips. The measured output signal is the convolution of the detector sensitivity and response, and some geometrical factor due to the beam spot width.

As the laser setup is not equipped with precision needles, two half plasma-cut sensors with the parallel geometry have been glued on a copper plate and bounded to small gold pads. These pads are in turn connected to the pre-amplifier (see details in Section 5.4.2). Even if this assembly (Fig. 5.12) is not optimised in terms of noise handling (due to the wires carrying the strip signals), it is quite convenient: its design allows tests with either the probe station or the laser setup. Moreover, the observed noise was completely manageable.

In order to test the detector sensitivity close to the cut border (which could be expressed in terms of the charge collection efficiency), a scan in laser beam spot position is done on the sensor, while several strips close to the edge are

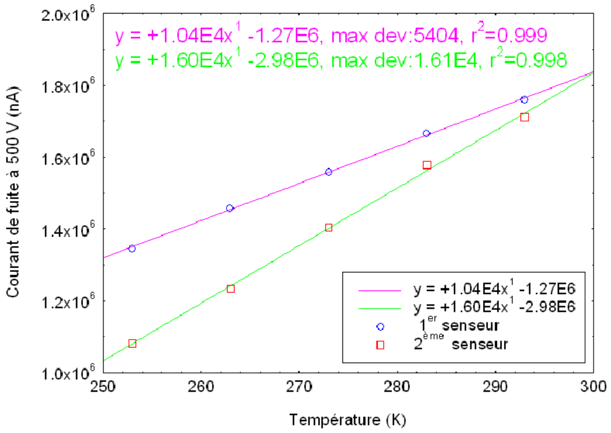

Figure 5.11: Temperature dependence of the total leakage current [116]. The evolution of cut sensors is in good approximation linear.

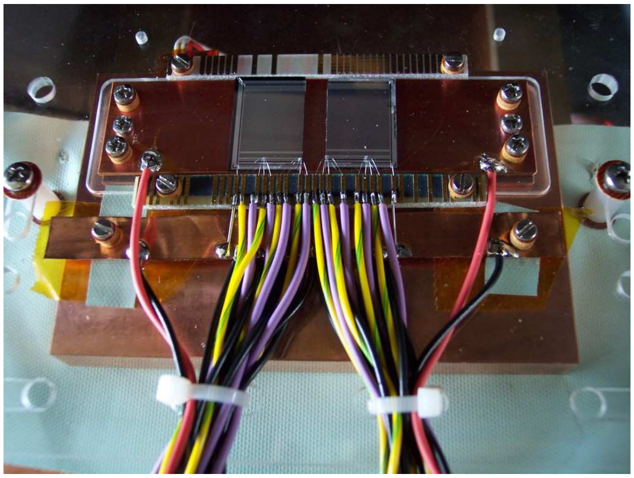

Figure 5.12: Picture of the testing board of plasma cut sensors.

read-out. As the spot radius is quite large (~ 1 mm), some energy is lost when approaching to the edge of the detector, as the light falls besides the sensor. On top of this, the expected signal could decrease due to a possible lack of CCE. A blind simulation of this situation has been performed. The free parameters of the simulation are the beam spot width, and the coupling between strips. Indeed, when a strip is illuminated, the non-zero coupling with the neighbouring strips leads to some activity on these latter ones. For the simulation, a bidimensional Gaussian profile shape is assumed for the beam spot. Fig. 5.13 and 5.14 report respectively the measurements and the simulation for the 4 closest strips to the cut edge.

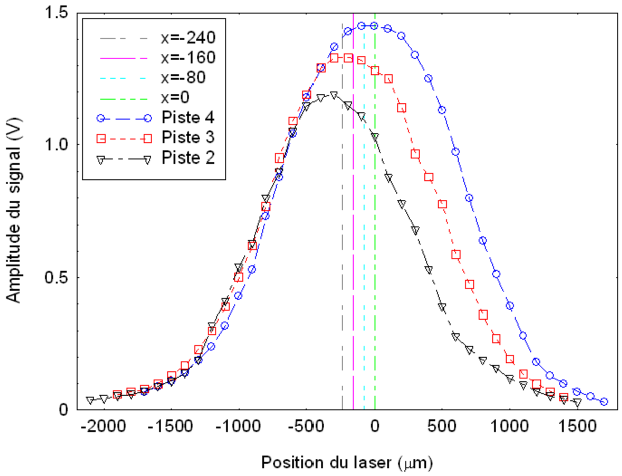

Figure 5.13: Strip signal measurements for a laser scan.

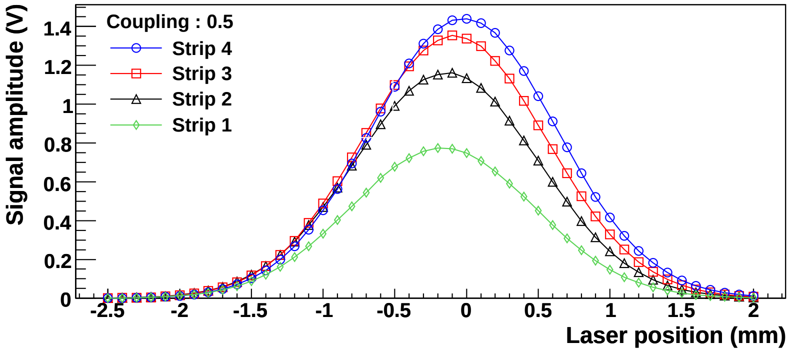

Figure 5.14: Strip signal simulation for a laser scan. The interstrip coupling is assumed to be 0.5 and the width of the bidimensional Gaussian distribution to $\sigma = 631\ \mu$m.

Meanwhile, other group have used ICP for the reduction of the border of silicon sensors [100, 101]. Their approach is albeit somewhat different: the edgeless side of the active area is enclosed by a terminating structure (current terminating ring, similar to the one in reference [106]). The inactive useless silicon width, behind the structure, has been removed via a plasma etching. Their cut geometry was perpendicular to the strips. As a consequence, single strips are not affected by the cut process. The effect of temperature on such devices have not been studied, as the leakage current values allow operation at room temperature. The achieved effective distance from the active area to the detector edge is 25 μm, for operational conditions like $I_{\text{leak}} \sim 100$ nA at full depletion voltage. These characteristics are preserved after a moderate (10^{14} n/cm^2) irradiation.

5.5 Cryogenic silicon detector module

While developing edgeless silicon detectors for the RD39 collaboration, a participation to the cryogenic silicon detector module project has been offered. The aim of this project was to study the feasibility of a detector module, based on cryogenic operation of a silicon sensor, equipped by read-out electronics similar to the CMS tracker one. These developments were following the work done by Blanca Perea Solano [124].

The cryogenic detector prototype design [98] is based on a 500 μm thick Float Zone (FZ) silicon detector [125]. It has a 32.5 cm^2 active area and 1024 strips with 50 μm pitch. The sensor, glued with all the module components on a silicon support plate uniforming the detector temperature distribution, is read-out through a silicon pitch-adaptor wire-bound to four APV25 chips [126]. These acquisition chips are 0.25 μm technology CMOS, with preamplifier and shaper abilities, and an internal pipeline for temporary data storage ($\sim 4\mu$s). They are clocked at 40 MHz and are mounted on a ceramic CMS tracker front-end hybrid [105], also glued on the support plate. This hybrid hosts also 3 other chips, dedicated to the CMS tracker environment: 1 PLL (for clock and timing), 1 DCU (for current and voltage monitoring) and 1 MUX (for channel multiplexing). The cooling of the cryogenic module is based on a two-phase flow of N_2 or argon inside a CuNi microtube (0.5 mm inner diameter). The two-phase flow has a higher heat transfer and a lower mass flow rate than single phase coolant. The microtube is itself embedded in a carbon fibre spacer which serves both as the module holder and as a compensation structure for the tube thickness in the assembly. The spacer is located under the pitch adapter, separating the sensor from the heat dissipated by the read-out electronics ($\sim$ 1.2 W). This design was assessed by a preliminary study of the thermoelasticity of the structure [124]. A cryostat for the two-phase flow cooling has also been developed in cryolab by the collaboration [127]. FIG. 5.15 shows the module prototype.

Two problems prevented from operating the cryogenic module as foreseen. The first small annoyance was the fluctuation of the test module working temperature, as provided by the cryostat. As the silicon properties depends on the temperature, the stability of operation temperature over long periods (i.e. more than a few hours) is required. The second, but major one, was the impossibility to run CMS tracker front end hybrid below $\sim$ 210 K, which is far above

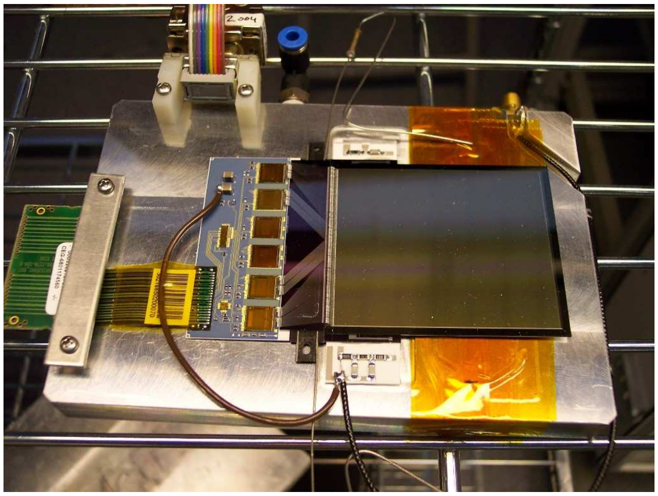

Figure 5.15: Prototype of the cryogenic detector module.

the temperature range achievable by the previously quoted cryostat. Several tests have been performed on a dozen of hybrids on a dedicated setup. This setup consist of a supporting chuck, whose temperature is controlled by two antagonist phenomenons: the chuck is cooled down by a direct contact to copper strings steeped in a bath of liquid nitrogen; at the same time, three heating resistors increase the temperature to a desired value, thanks to an external Yokogawa [120] temperature controller and a Pt100 probe for the monitoring (Fig. 5.16). The tested device (hybrids or module) is fixed on the holding plate via rows of vacuum lines sucking it during the measurements. The setup is partially enclosed in a dewar, with a dedicated closing plate. Feedthroughs allow for the hybrid read-out, for the temperature monitoring and control. A permanent flush of dry air prevents condensation on the silicon surface[6].

The setup is connected to an acquisition chain[7] made of small electronic boards, faking the CMS DAQ [128]: CCU-board, FED-PMC, FEC and VUTRI. An alternative setup, the ARC *system* [129], was also tried but did not suit to the needs. Thanks to this complete environment, the effect of *low* temperatures (i.e. above 200 K) has been studied on the cryogenic module prototype.

A first variable directly accessible for this study is the *pedestal*. This corresponds to the average activity output by the acquisition setup when no signal is present. This mean level obviously depends on the operation of the chips (APV25 operation modes, hybrid and sensor bias voltage, working temperature, etc.). One can easily distinguish between the four APV25 read-out chip signal

---

[6] This setup, designed and fabricated in UCL-Cyclotron Workshop, is inspired on a previous and simpler version, made in CERN cryolab.

[7] Commonly called *Lyon* DAQ.

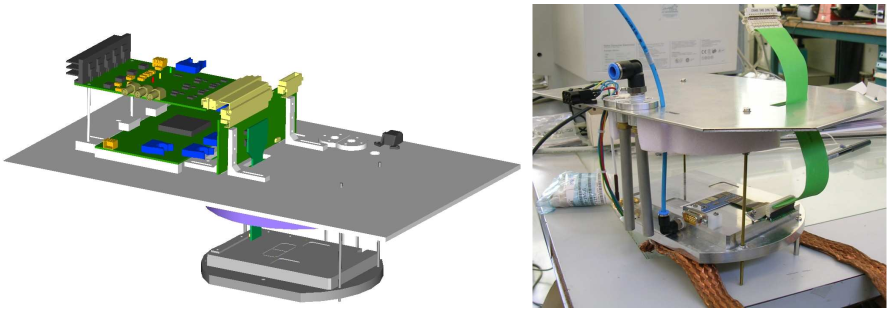

Figure 5.16: Testing setup for the study of the temperature influence on the operability of CMS tracker front-end hybrids.

when visualising the hybrid pedestal profile.

The expected pedestal mean level should decrease with the temperature, as previously observed with naked hybrids (i.e. with no sensor connected). This is normal thanks to a lower thermal activity and subsequent electronic noise, in particular at the input channels. In spite of this, one observes a slight increase of the pedestal height for the cryogenic detector prototype (Fig. 5.17). Reflecting a better sensitivity, an increase of the reverse bias voltage also leads to a higher pedestal. However, these values are completely under control, here in the range $[250, 320]$ ADC counts. The corresponding noise ranges from 0.5 to 1.2 ADC count, which is also completely satisfactory[8].

The pulse shape evolution, corresponding to the convolution of the detector response and the electronics operation mode, is also dependent on the temperature (Fig. 5.18). One sees the electronics acceleration due to the cooling, as the peak value occurs sooner for lower temperatures. In other terms, the signal is faster. The actual maximal signal height temperature dependence is not linear, but this is still controlable via the APV25. For these tests, the input signals are generated at the input stages of the APV25 read-out chips.

Even if the operability of APV25 chips was already proved at low temperatures [130], a stable and reproducible mode of operation of hybrids below ~ 250 K was not achieved. The lower bound around 207 K, with a large hybrid-to-hybrid variation, is the effect on the PLL chip of a non nominal operation temperature. This chip distributes the clock and trigger signals to the APV25s. When cooled down, the PLL does not deliver a stable signal, causing a complete loss of operability of the hybrid. This is yet recoverable if the temperature is increased enough. This behaviour is expected [131] and several approaches could solve this issue: on the one hand, an artificial increase of the temperature of the PLL; on the other hand, a tune of its working frequency[9]. The former

---

[8] Operational values of hybrid variables have been studied, for instance in [105].

[9] A PLL chip locks its phase on a specific frequency, belonging to a very narrow range of acceptable values. Still, this frequency can change with the operation temperature, if it

solution could be implemented by either locally warming up the chip – but this will increase the thermal stress on the sensor, which is not acceptable – or by removing the PLL from the cold volume. This would require a modification of the connections on the hybrid (via a long kapton cable for instance), that would bring signals from the warm lonely PLL chip to the cold hybrid. Still this solution was not investigated, for practical reasons. The tune of the working frequency of the PLL did not prove to be efficient during the preliminary tests. Finally, the re-allocation of acquisition systems, due to the late testing and assembly of CMS tracker, caused the contribution to this project to be stopped.

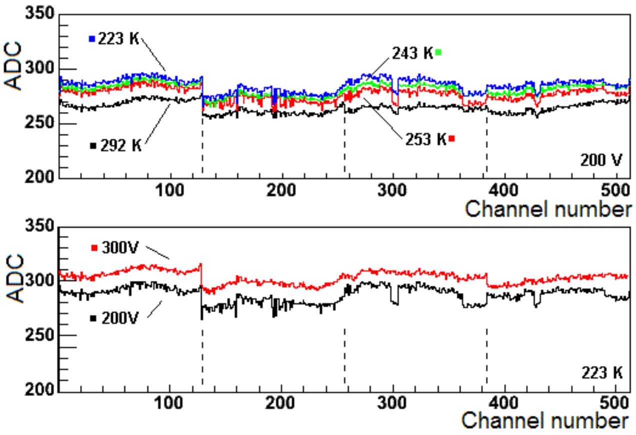

Figure 5.17: Pedestal evolution with respect to the temperature and the bias voltage, for the cryogenic detector module prototype.

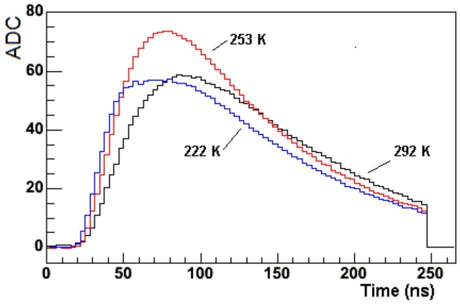

Figure 5.18: Pulse shape evolution with respect to the temperature, for the cryogenic detector module prototype.

---

becomes far from nominal specifications.

5.6 Conclusions and perspectives

Edgeless detectors are of interest in beam particle physics and other fields. Amongst several techniques, the cutting of CMS baby detectors, across their active area, has been tested. The cutting process was performed by either a laser light or a plasma. This leads to a very large increase of the total leakage current of the structure. This increase could be managed by an operation at low temperatures, even if the temperature dependence of this I_{leak} is linear. Most of the current is hopefully driven by the first two or three channels from the cut edge, leaving the opportunity for throwing away this excessive current while reading-out most of the strips.

The study could not be pushed as far as desired, and would be well-completed by an irradiation studies of these structure and the measurement in a test beam of the edge sensitivity (via the charge collection efficiency), when operated in reasonably low temperatures. The measurements could be extended to lower temperatures which was not possible here due to setup limitations. The laser setup would be improved with a more focused beam spot, a proper noise handling and the use of a linear amplifier for the study of the full signal shape (and not only its integral). Using the Current Transient Technique would also provide some usefull information. The CCE measurement could be taken from a source or a test beam, in relation to an external single track positioning system.

One of the goal was to evaluate the operability of such sensors in forward detectors for the LHC, like in the FP420 project. The short timescale and the operability difficulties (high I_{leak}, low T and the need for compatible read-out electronics) made such detectors not competitive compared to more advanced 3D technologies [102]. Moreover, the inactive border achieved with these designs (~ 200 μm) are not as remarkable as for some others (< 100 μm for scintillating fibres, ~ 50 μm for planar sensors with current terminating structure, ~ 30 μm for 3D pixels). And there is no evidence that reducing the strip pitch would allow to reduce this region.

However, the easiness of processing such laser- or plasma-cut devices made the corresponding R&D interesting for potential developments and applications in future collider experiments, like in the SLHC project, in medical detectors or even in technological industries using silicon detectors (like digital photography for instance). A big advantage of these two techniques is the ability to manufacture curved sensitive borders.

The cryogenic module needs the development of a dedicated electronics, for instance based on APV25 or any evolution, located on a silicon board (i.e. nor a kapton nor a ceramic one, for a better matching of thermo-elastic properties). The clock and timing synchronisation chip (PLL) would be external to avoid lock frequency drifts due to temperature changes. Finally, the radiation hardness of the detector would benefit from the current injection operation mode.

Part III

… to software: data acquisition and simulations

Chapter 6

Data selection and processing

Following the exhaustive list of detectors around the IP5 *in Chapter 4, this chapter introduces the main streams of* CMS *data acquisition, selection and processing [82,70]. The data processing chain is the connection of two successive links: the online and offline levels. The online selection consists in (1) the Level 1 Trigger which reduces the* 40 MHz *incoming rate to approximately* 100 kHz *with dedicated electronics; and (2) in the High Level Trigger, whose computers further filter the events down to a rate of* 100 Hz. *The analyses are performed offline, when the event is fully reconstructed.*

6.1 Introduction

Online Selection The final state particles from the collision of the proton beams generate signals in subdetectors, which are digitised and gathered in the front-end drivers (FED). A set of basic algorithms is then applied in order to identify the particles and estimate their properties (e.g., energy E and transverse momentum p_T) from the available data. Only events passing the predefined selection rules on these *reconstructed* properties are stored for later analyses, while those which are not selected are lost forever. This selection process, or *trigger*, is *online*, because it keeps pace with the collision rate. It is divided into two subsequent steps: called the *Level-1* (L1T) and *High-Level* triggers (HLT), for a global reduction of five orders of magnitude of the incoming flow. The triggers aim at selecting the remarkable events amongst the overwhelming majority of less interesting soft QCD events.

$$\underbrace{40\ \text{MHz}}_{\text{FED's}} \xrightarrow{L1T} \approx 100\ \text{kHz} \xrightarrow{HLT} \approx 100\ \text{Hz} \dashrightarrow \text{offline level}$$

The procedures for accepting an event have to cope with the high bunch crossing rate, and remain synchronous with the accelerator. After being evaluated, selected data are presented by the filter farm to the offline input stage, always using its full transfer capacity (*bandwidth*).

Offline processing The Event Filter feeds the input of the offline infrastructure, called *Tier-0* , where raw data are archived and handled into a common format. Event management becomes asynchronous with the LHC, i.e. *offline*. Events are sent to several *Tier-1* centres, where the reconstruction of hits and clusters, as well as more abstract physical objects (like tracks or particle candidates) follow in several steps. *Tier-2* and *Tier-3* centres interface the processed data to the end-user, e.g., for analysis, fulfilling their needs in storage and CPU's. The requirements on size and processing power, due to the impressive flow of incoming data, make the computing challenging in CMS. GRID technologies make the number of users, the processing needs and the data size manageable.

6.2 Considerations on the online selection

Low x strong interactions dominate by far the possible final state and thus constitute the major component of the event pile-up. On average, the sum of all signals from the CMS subdetectors amounts to 1.5 MB per event. At 40 MHz, this flow is not bearable, both in terms of processing and storage, even using state-of-the-art technologies [82].

On the other hand, such low energy events are *a priori* less interesting than others, looking at possible perspective beyond SM offered by the large c.m.s. energies of the LHC. Their study will not require all the statistics provided by CMS. It is a necessity to reject most of these data; small samples of these are still acquired with very low cut and after the application of a large reduction factor, called *prescale*. These application of the selection rules should be fast enough to cope with the high LHC rates, and occur at the very early stages of the data flow: selection is *online*. If an event complies with at least one rule, it *triggers* the acceptation procedure.

In CMS, the acceptable data flow is 225 MB/s and corresponds to a rate of events around[1] 150 Hz. Most of the events are produced uselessly. These selection procedures, or *triggers*, aim at selecting only a fraction of the events, in order to decrease the global data flow. Subsequently, interesting data can possibly be lost if the rules are inadequate. The CMS trigger is logically and physically divided into two steps (L1T and HLT) aiming at an efficient selection as the rejection power to achieve is large. The input data for the online selection are the partial raw data [DAQ-RAW] available from detector front-ends.

---

[1] These numbers actually includes a safety factor of 2, as the technical limit reaches approximately 300 Hz.

6.2.1 Level 1-Trigger

The level-1 trigger system is organised into three major subsystems: (i) the L1 calorimeter trigger, based on ECAL, HCAL and HF data; (ii) the L1 muon trigger, based on RPC, DT, and CSC hits; and (iii) the Global Trigger, which combines calorimetric and muon decisions to establish the final L1 decision. Fig. 6.1 illustrates these relations.

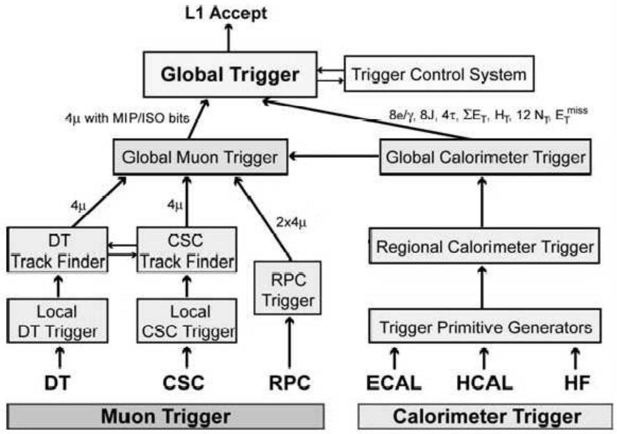

Figure 6.1: Level-1 trigger organisation. Data coming from the muon system (DT, CSC and RPC) are gathered into a Muon Trigger. Similarly, the Calorimeter Trigger is based on calorimeter components (ECAL, HCAL, HF). The Global Trigger, eventually producing a L1 Accept signal, mixed the information from the Muon and the Calorimeter Triggers. [70]

- Data from the calorimeters are locally processed; these values serve as primitives allowing the Regional Calorimeter Trigger to create candidates for electrons, photons, tau's, jets as well as to apply isolation criteria. The only available candidate properties are (E_T, η, ϕ). Based on this information, the Global Calorimeter Trigger (GCT) produces the several list of four particle candidates, for e/γ's[2], τ jets, central jets, forward jets, as well as the total transverse energy E_T and the transverse missing energy vector $\vec{\not{E}}_{\mathrm{T}}$.
- Muon detectors provide the L1 trigger with hits, which are being processed for track pattern recognition, and computation of the muon charge and transverse momentum. Muon candidates are already quite well-known, as the muon system provides $(\eta, p_T, E, \theta, \phi)$ for each candidate.

---

[2] It is worth noting that the lack of tracking data prevent from making the distinction between electrons and photons.

The Global Muon Trigger (GMT) performs these tasks and sends the four best candidates to the Global Trigger (GT).

- Gathering and synchronising data from GMT and GCT, the Global Trigger evaluates the candidates and takes the final decision, either to drop the event, or to release a Level-1 Accept (L1A) signal. In this case, L1A is sent to the TTC for distribution to subdetectors (tracker is waiting for L1A before sending their data to FED's.)

Each L1A needs about 75×10^6 channels, output by approximately 600 FED's. The available information is partial, in particular there is no inner tracking data, because of the relative slowness of the signal generation in silicon detectors[3]. There are six L1 object types: μ, isolated and non-isolated e/γ, central jet, τ jet, forward jet, total hadronic energy HTT and the missing transverse energy $\not{E}_T$.

In terms of hardware, detector channels are grouped into geometrically close regions and processed by programmable chips (FPGA's) that perform easy and fast logical tests – mostly comparing some measured levels to predefined thresholds located in RAM's. Once these tests are done, and the possible prescales applied, the output bit values (*true* or *false*) are logically combined into one unique and final Level 1 decision, which has to be propagated back to the detector front-ends in the CMS volume.

All the events which are not acknowledged by a L1A are lost forever. Moreover the hardware constraints in the tracker forces the L1 decision to take 3.2 μs. Changing this parameter would require a complete upgrade of the whole tracker.

The typical output rate by the L1 trigger bits is between 0.1 and 10 kHz. It sums up to about 12 kHz for the initial low luminosity[4] $\mathcal{L} = 10^{32}$ cm^{-2}s^{-1} [70]. These values obviously depend on the predefined thresholds and prescales, and will evolve during the first months of the LHC, as the detector will be calibrated and in order to optimise the used bandwidth. The selection system should take care of both bandwidth and processing resources and to minimise dead time. This dead time should always be smaller than $1 + 1$ % for the L1T+HLT.

The studies for the L1T improvements for the need of the Forward Physics Group, and in particular γ physics, are presented in Section 8.1.2.

In total, 128 L1T paths are available for the CMS experiment. These will evolve in time, as data are accumulated, depending on the actual rates, the available bandwidth and the evolution of the collider luminosity.

Inclusion of forward detector data in the L1 trigger. The 3.2 μs latency heavily constrains the possibility to add the forward detector measurements in the L1T decision making.

---

[3] At full luminosity, the signal peaking time in silicon sensors is even longer than the 25 ns separation between two bunch crossings. Three subsequent data samples are then used in order to recompute the actual signal height [80].

[4] At the LHC start-up, the expected available bandwidth is 50 kHz.

Beam protons are highly relativistic: any information takes 1 μs to cover 300 m. Any detector located at a distance d from the IP do not provide the L1T with its data before a time Δt:

$$\Delta t = \frac{d}{c} + \delta_{\text{det}} + (d+\epsilon)(\lambda + \frac{1}{c}) + \delta_{\text{TTC}} \leq 3.2\ \mu s. \tag{6.1}$$

The first term corresponds to the time needed by the scattered protons to reach the very forward detector; the VFD sensors and electronics generate a transportable signal (i.e. a low noise, shaped and amplified) within a δ_{det} latency; $(d+\epsilon)$ is the cable distance to be covered by the signal to reach the L1T decision chips; λ models the delay due to the cables and δ_{TTC} is the delay needed by TTC for the release of a possible L1 Accept signal.

This definitely excludes detectors beyond approximately 250 m (in particular FP420 detectors). TOTEM T1 and T2, CASTOR and ZDC can technically add their information to the L1T GT decision, thanks to their distance to the central detector, to their detection principle and their acquisition systems. The case of the TOTEM roman pots RP220 is not so obvious. Here is the time estimation for maximal electronics handling for detectors located at $d = 220$ m from the IP. Assuming $\epsilon = 50$ m as a safety margin on RP position and cable length, a cable delay of $\lambda = 5$ ns/m and a $\delta_{\text{TTC}} = 150$ ns, one gets [54]:

$$\delta_{\text{det}} = 150 \text{ ns} \tag{6.2}$$

In conclusion, the TOTEM roman pots located at 220 m should generate and shape their signal within 150 ns in order to be able to take part to the L1T.

6.2.2 High Level trigger

The HLT is the second and final step in the decision chain for the storage of events [70]. The needed reduction factor between input and output rates is also large ($\mathcal{O}(10^3)$). But for the HLT, the whole set of event data is available, even from the distant detectors. Moreover, the decision latency is longer and the data are now processed by a computing farm. This additional flexibility allows the use of unconstrained[5] algorithms designed to select the most numerous possibly interesting events while keeping the output rates stable. The HLT input stages are fed with incoming events arriving at a rate of about 100 kHz.

Each event is assigned, via the event building switch, to a processor (called a *node*); all processors are obviously running the same HLT code. For optimisation purposes, the HLT tests should discard bad event candidates as soon as possible; the tests are therefore based on partial information. As these check requirements are fulfilled, the event content is further reconstructed, and the full event information is only available towards the end of the selection process. At the same time, the information of which trigger path fired the event selection is added to its content. This allows for a quick sorting of the HLT selected events, into *primary datasets*.

---

[5] In terms of allowed operations, which is not the case for the L1T.

One entire event is sent to an HLT node to evaluate whether it passes the criteria (summarised into the HLT *trigger table*) for acceptance, or if it is discarded. The output is [RAW] data , classified into approximately 50 primary data sets. This *pre*-classification is only based on the fired L1T+HLT trigger paths[6], i.e. the ones that selected the event. These data sets are also organised into $\mathcal{O}(10)$ online streams with similar rates, for performance purposes. There is no replication of events in several streams but for priority events processed by the express line (like ones for calibration purposes, or with remarkable signatures, compatible with new physics) [82].

6.2.3 Reconstruction at trigger levels

This section summarises the reconstruction process during the trigger evaluation [70].

- **Muons**: Based on L1 muon candidates, the HLT reconstruction consists in so-called L2 and L3 evaluations of muon tracks before and after the addition of inner tracker data, alongwith a L2 condition requiring a minimal p_T. Optional *isolation* criteria, i.e. requesting no detector activity in the close vicinity to the muon candidate, can be applied from either the calorimeters or the tracker.

- **Electrons and Photons**: L1 e/γ candidates are based on ECAL towers, with no distinctions between electrons and photons, classified in isolated and relaxed particles. At the HLT, the following sequence is applied: the reconstruction of ECAL clusters, broaden in ϕ to include possible bremsstrahlungs; ECAL isolation; processing of HCAL data and isolation; looking at possible pixel hits for track seeding; reconstruction of the track. Tracking data obviously makes the difference between electrons and photons.

- **Jets and Missing Transverse Energy**: At L1, the candidates are selected by performing the transverse energy sum $\sum E_T$ on calorimeter trigger towers, using a sliding window than scans the (η, ϕ) grid. An iterative cone algorithm with $R = 0.5$, similar to what is performed offline, is applied at the HLT.

- **τ jets**: Being narrower than nominal jets, τ jets are identified if located in isolated 2×2 towers, passing a given E_T threshold. The HLT reconstruction is the succession of (i) a L2 level based on calorimetric information, with an interactive cone as for usual jets; (ii) a L2.5 level adding pixel data and (iii) a L3 level with full tracking, including strips and isolation.

- **b jets**: Whilst there is no specific identification of b jets at L1, the HLT looks in three steps for high p_T jets (L2), which have a displaced vertex

---

[6] as analyses are usually based only on a few numbers of trigger paths

according to the tracker pixels (namely, *b-tag* at L2.5) and the tracker microstrips (L3).

- **Combinations**: Other triggers, both at the L1T and the HLT, are based on combinations of high-level objects, like $e-\text{jet}$, $e-\mu$ or $\mu-\tau$, etc.

6.3 Offline processing

CMS online Data Acquisition System feeds the Tier-0, at CERN. The offline processing starts there. Tier-0 performs a first reconstruction [RECO], archives the [RAW] + [RECO] data into the so-called *full event* format [FEVT], and distributes the [RAW] and [RECO] to Tier-1 centres. In turn, the few ($\mathcal{O}(6)$), but large, Tier-1's will carry on data intensive analysis tasks: archiving, reconstruction and skimming[7]. A large ($\mathcal{O}(25)$) set of Tier-2 and even smaller Tier-3 centres will provide users with computing infrastructures for analyses or Monte-Carlo production.

6.3.1 Reconstruction algorithms

Reconstruction is the operation of constructing physics quantities from the raw data collected in the experiment [70]. The reconstruction process can be divided into three steps:

(i) a local reconstruction of a single detector module (from *digis* to *RecHits*);

(ii) a global reconstruction at the level of the whole detector (e.g., from tracker RecHits to full tracks), but inside a common sub-system. For instance, tracker hits are used for the construction of tracks or for the searches for displaced vertices. Calorimetric towers are created from same regions in ECAL and HCAL. Muon candidates arising from the only muon system (i.e. without using inner tracking information) are built. And eventually,

(iii) the production of higher-level objects (like electron candidates) as any combination of the "globally reconstructed" objects, like e/γ, μ, etc...

The (first) event reconstruction is performed in Tier-1, on [RAW] data. It consists in successive steps: first unpacking[8] the data, applying the detector calibration constants, reconstructing the detector hits. Then pattern recognition algorithms are applied on tracker data, to provide particle track candidates. Vertexing is the next step, i.e. finding primary and secondary vertices. The

---

[7] The *skimming* of data consists in reducing the event size by dropping intermediate algorithm byproducts and obsolete parts of the event content.

[8] In order to optimise the bandwidth use, the FED's output values whose format is not uniform, in terms of number of bits. For instance the value 2 can be expressed as 10 or 0010 but the former is more compact. The *unpacking* consists in assigning the same bit format for all the values.

final step is the identification of particle candidates, namely $e^{\pm}, \gamma, \mu^{\pm}, \not{E}_{\mathrm{T}}$, jets, heavy-quarks and τ decays. The output format of this whole process is [RECO] data. The reconstruction is very consuming in terms of processing time, which is dominated by the tracker data processing [82].

The offline reconstruction is very similar to the one applied online. The Analysis Object Data [AOD] are a subset of the reconstructed ones, meant for physics analysis. They correspond to the final reconstructed objects.

6.4 Efficiencies and resolutions of reconstruction for trigger and offline levels

The data from all subdetectors are collected to identify and reconstruct the particles produced by the interactions. This identification process should be as good as possible, but its real efficiency depends on several parameters related to the particle nature (e, γ, μ, ...), their kinematics (e.g., p_T or E) and trajectory (η, ϕ). Moreover, other effects decrease this efficiency, like the detector misalignment or the level of pile-up events. This section focuses only on muon identification, triggering and reconstruction, as an illustration. Further information is available elsewhere [70].

The efficiency to identify single muons at trigger level is illustrated in Fig. 6.2, as a function of η [70]. The average identification efficiency of muons by the Global Muon Trigger (GMT) is as high as 98.3% (flat distribution in $5 < p_T < 100$ GeV). The gaps between muon chambers explain the loss of efficiency in given $|\eta|$ regions. The contribution from several subsystems (DT: $|\eta| < 1.4$; RPC $|\eta| < 2.1$; CSC $1.04 < |\eta| < 2.4$) is also visible. Similarly, the ϕ dependence, shown in Fig. 6.3, indicates a very high average efficiency with local structures due to the subdetector geometry. Finally, the p_T dependence has a sharp activation region, between 3 and 6 GeV, followed by a plateau around 95% in both barrel and endcaps.

Similar results are obtained for the HLT and offline reconstructions, where tracking data are added. In particular, the p_T resolution is improved by a factor of 10, compared to the resolution based on the measurement of muon chambers only. The resolution of globally reconstructed muons (using $\mu-$chamber and silicon tracker data) is depicted in Fig. 6.4. It is worth noting that external causes, like the detector misalignment, decrease also the measurement resolutions; but these issues can partly be tackled by using accumulated data.

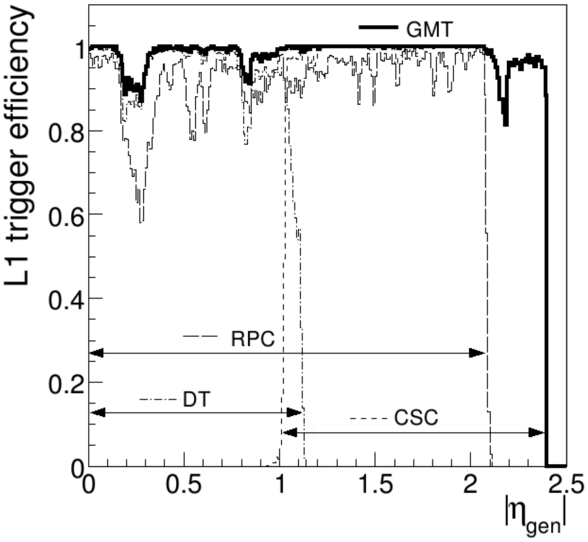

Figure 6.2: Efficiency to identify single muons, as a function of the muon pseudorapidity for the Global Muon Trigger (solid line), and for the DT, CSC and RPC trigger subsystems (dash-dotted, dotted and dashed lines, respectively). Generated sample muons have a flat distribution such that $5 < p_T < 100$ GeV and $|\eta| < 2.4$. No p_T and quality selection criteria are applied. Adapted from [70].

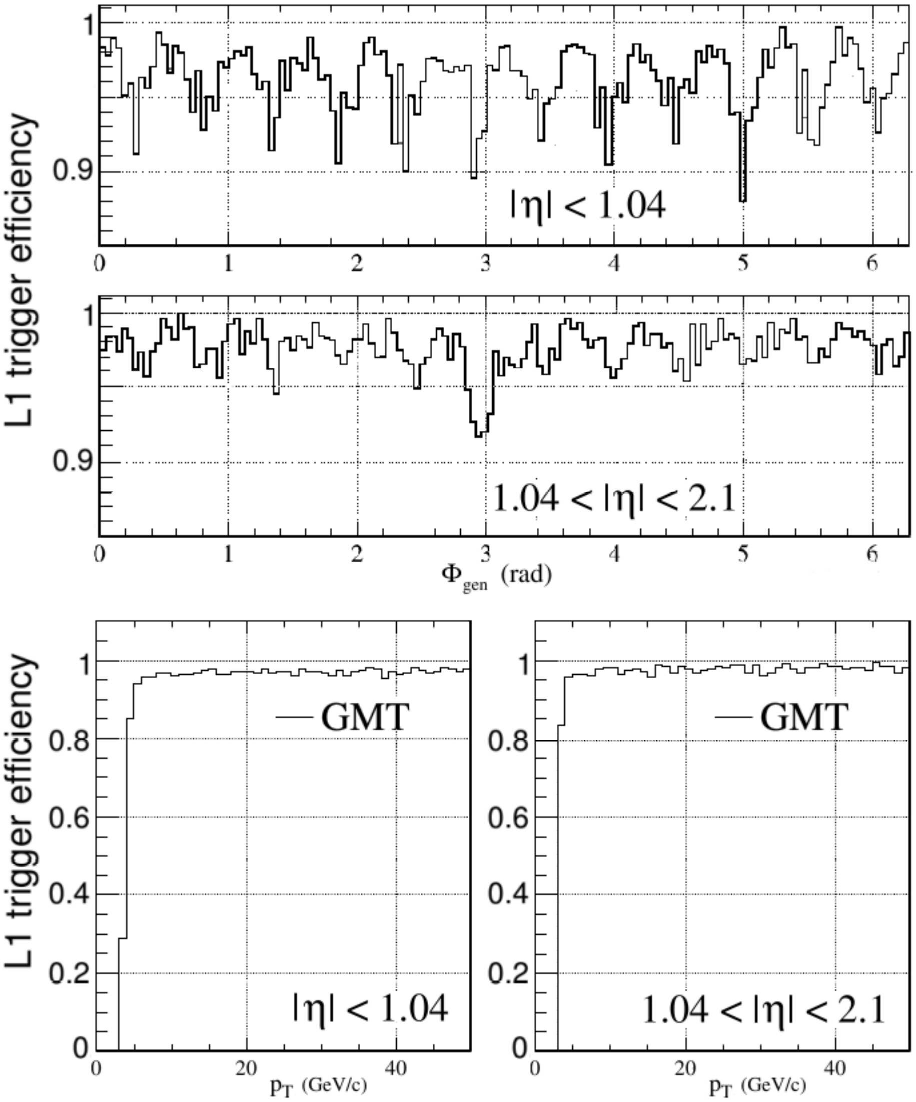

Figure 6.3: Efficiency to trigger on single muons, as a function of the muon ϕ coordinate (upper plots) and p_T (lower plots) for the Global Muon Trigger, in the barrel ($|\eta| < 1.04$) and part of the endcaps ($1.04 < |\eta| < 2.1$). Generated sample muons have a flat distribution such that $3 < p_T < 100$ GeV and $|\eta| < 2.4$. No p_T and quality selection criteria are applied. Adapted from [83].

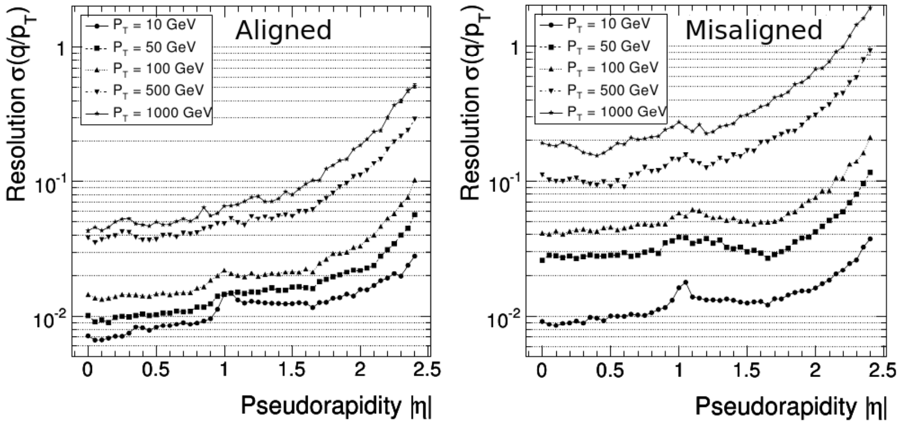

Figure 6.4: Resolution on q/p_T for globally reconstructed muons, as a function of pseudorapidity, for a perfectly aligned detector (left) and a misaligned detector after corrections corresponding to first data taking (right) [70].

Chapter 7

Particle transport to very forward detectors

Both simulation of the very forward detectors and the analysis of their data require a perfect knowledge of the mapping between the measurements of the forward particles and their kinematic properties at the interaction point. A new simulator of the particle transport in beamlines, called HECTOR*, has been developed [13, 132]. Many aspects of the forward physics can be studied, including the characterisation of the* VFD*s, and the reconstruction power of the kinematics of the measured protons. This software has been presented in various international workshops and has been integrated into the software of the CMS experiment.*

7.1 Principles and implementation

The basics of the forward detection rely on the difference of behaviour between nominal beam protons and the event final state particles, during their transport by the beamline optical elements. This is easily understood when considering that the characteristics, i.e. the magnetic field strength and length, of the optical elements are set for the beam protons. Changing the particle kinematics subsequently modifies the particle trajectory, compared to that of the nominal beam. The need for a good knowledge of the particle path in the forward region led to the creation of a new tool called[1] HECTOR [13, 132]. This software was written in common with Jérôme de Favereau (Université catholique de Louvain).

As explained in the following sections, this software computes the particle trajectory using the transfer matrix model. It includes the field strength correction due to non-nominal energies and is suitable for any particle, given its

---

[1] An homonymic program is used in the DIS community [133]

charge e and mass m. The limiting aperture check is performed at the entrance and the exit of the beamline elements. As an application, HECTOR uses this description for the evaluation of the forward detector acceptance as well as the reconstruction of kinematic variables at the interaction point. Several results have already been shown in previous chapters. This section details the physical principles, their implementation and some valuable information related to the main frame of this document.

7.1.1 Principles

The simulator relies on a linear approach to single particle propagation. A beamline consists of a set of optical elements, amongst dipoles, quadrupoles, drifts, collimators, kickers and VFDs. The optical elements are described by their magnetic field, their length and their aperture. In turn, a set of particles, with all possible smearings of initial positions, angles or energies, is propagated by HECTOR through the beamline, particle by particle. In classical electromagnetism, the influence of an external magnetic field $\vec{B}$ is given by the Lorentz force (EQ. 7.1).

$$\vec{F} = e\left(\vec{E} + \vec{v} \times \vec{B}\right) \tag{7.1}$$

The Taylor expansion of the vertical component of magnetic field B_y, around its central value is:

$$\frac{e}{p}B_y(x) = \frac{e}{p}B_y + \frac{e}{p}\frac{\partial B_y}{\partial x}x + \frac{1}{2}\frac{e}{p}\frac{\partial^2 B_y}{\partial x^2}x^2 + \dots \tag{7.2}$$

where p is the momentum of the particle and e its electric charge. The terms of this sum are interpreted as respectively dipolar ($\frac{1}{R} = \frac{e}{p}B_y$), quadrupolar ($k = \frac{e}{p}\frac{\partial B_y}{\partial x}$) and sextupolar fields. In the co-moving coordinate system, neglecting small deviations ($x \ll R$, $y \ll R$) and small momentum loss ($\Delta p \ll p$), this leads to the following equation of motions for a particle travelling along path length s through a magnetic element [134]:

$$\left\{ \begin{array}{l} x''(s) + \left(\frac{1}{R^2(s)} - k(s)\right)x(s) = \frac{1}{R(s)}\frac{\Delta p}{p} \\ y''(s) + k(s)y(s) = 0. \end{array} \right. \tag{7.3}$$

The solution $(x(s), x'(s), y(s), y'(s))$ to these equations can be expressed as a linear combination of the initial values (x_0, x'_0, y_0, y'_0), where the rotation matrices are defined by the properties of the optical element (length and magnetic field). The typical values $R \sim 200$ m and $x < 0.01$ m match the first assumption ($x \ll R$). As $\Delta p \ll p$ is not always verified, a further correction to the magnetic field of each optical element of the beamline is applied, as explained thereinafter.

In other words, for the simulation of the transport of a particle in a beamline, each beam particle is represented by a phase space vector and each optical element by a transfer matrix by which the vector is multiplied. The propagation of a single particle is thus the *rotation* of the phase space vector by the n optical element matrices.

$$X(s) = X(0)\,\underbrace{M_1 M_2 ... M_n}_{M_{\text{beamline}}}$$

The whole beamline is modeled as a single transport matrix acting on each particle phase space vector (no intrabeam interactions). The optical element description also refers to its physical aperture. When a particle is propagated through an optical element, two tests check whether its path is compatible with the element acceptance or not, at its entrance and exit. The fact that a bent path could hit a central part of the element is neglected[2]. A particle which does not pass through the element acceptance is flagged, allowing to know the stopping element for given particle parameters – for the computation of detector acceptance and irradiation doses for instance.

Energy	(GeV)	$\langle E \rangle = 7000$	$\sigma_E = 0.79$
Positions	(μm)	$\langle x \rangle = -500$	$\sigma_x = 16.63$
		$\langle y \rangle = 0$	$\sigma_y = 16.63$
Angles	(μrad)	$\langle \theta_x \rangle = 2 \times 142.5$	$\sigma_{\theta_x} = 30.23$
		$\langle \theta_y \rangle = 0$	$\sigma_{\theta_y} = 30.23$
Emittances	(μm)	$\epsilon_{x,y} \sim 500 \times 10^{-6}$	

Table 7.1: Nominal beam parameters, at the IP5 [64], in the so-called *low* β^* configuration (LHC optics version v6.500). These variables are similar for the IP1, excepted than the crossing plane is vertical (x, θ_x and y, θ_y variables are thus swapped).

The 7 TeV beam protons have a well-defined 4-momentum P^μ. However, the injection of the beams in the main LHC rings bring some uncertainties (or smearings) on the proton position, angle and energy (Tab. 7.1). These divergences increase the beam envelope and thus define the beam emittance ϵ. The emittance refers to the hypervolume covered by the beam particles in the phase space. Liouville's theorem quotes that this hypervolume keeps constant during the transport of the beamline, for a fixed energy. The projection of this hypervolume in a transverse plane (like (x, y) or (x, x') for instance) covers an ellipse. As the beam is transported along the beamline, the ellipse axes are rotated or rescaled, but with a preserved surface (Fig. 7.7).

The impact of these divergences is managed by a set of focussing lenses, i.e. quadrupole magnets, along the beamline. The beam amplitude in both transverse direction is represented by the β_x and β_y functions (Fig. 7.2). This provide one of the cross-check with the MAD-X simulator [139].

---

[2] This feature is available but not active by default, as it slows down the simulation.

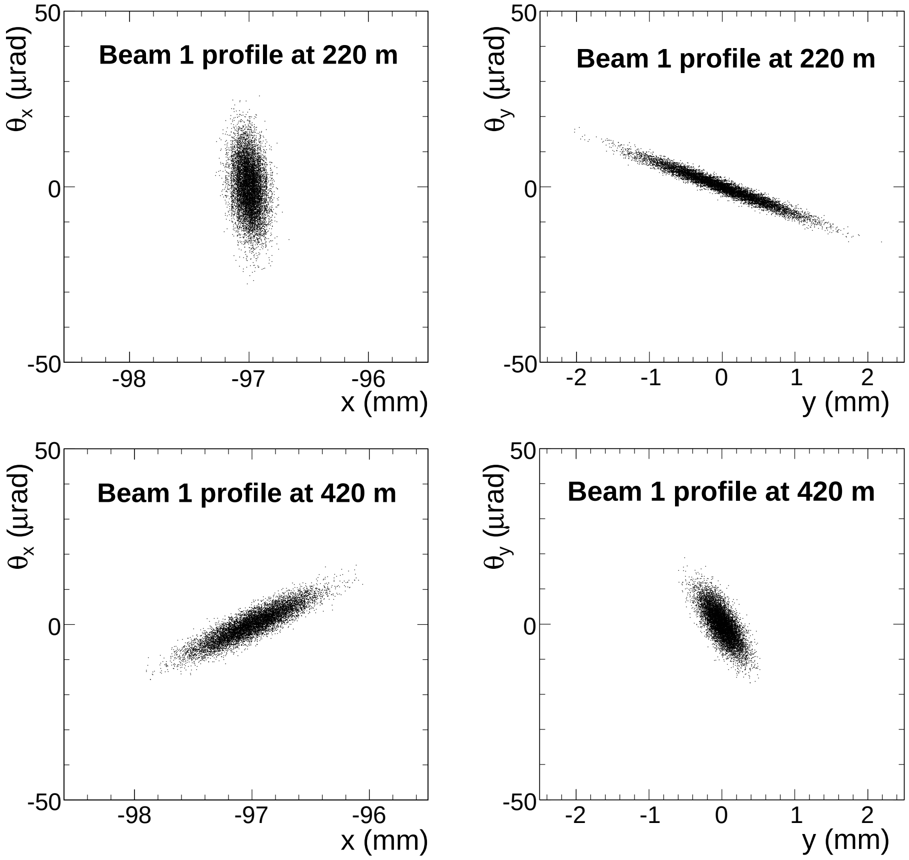

Figure 7.1: Illustration of the Liouville's theorem. LHC beam profiles in the transverse phase space at 220 m and 420 m from the IP5, for both beam 1. These graphs depict the horizontal (x, θ_x) and vertical (y, θ_y) distributions obtained by propagating $10,000$ protons through the LHC beamlines, in the forward direction from the IP5 (tunnel reference frame). The phase space area covered by the protons is conserved along the beamline, as expected from Liouville's theorem.

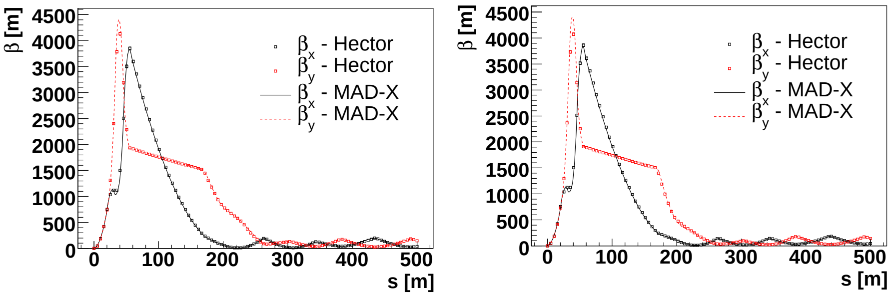

Figure 7.2: Beta functions β_x and β_y for beams 1 (*left*) and 2 (*right*) near the IP5, going forward: these functions depict the beam size variation and are computed from the beam emittance and the beam lateral profiles at successive positions. Indexes x and y are corresponding to the horizontal and vertical directions, respectively. The plain and dashed curves, coming from Mad-X, match exactly Hector's output (*squares*).

The beamline is a set of consecutive magnets. Around the IP5 (< 500 m), this list is restricted to dipolar and quadrupolar fields. The 4-momentum of non-proton particles or of protons that underwent an interaction deviates from the nominal P^μ. The bigger the difference, the larger the deviation of their path compared to the ideal trajectory (Fig. 7.3).

7.1.2 Implementation

The simulator has an object-oriented design, using the C++ Root framework [135], with dedicated classes describing:

- the beam particles. The 6-components phase space vector is

  $$X = (x, x', y, y', E, 1) \ ,$$

  with horizontal (x, x') and vertical (y, y') coordinates and angles; E is the particle energy. The sixth component is just a factor used to add an angular kick on the particle momentum direction.
- the optical elements (dipoles, drifts...) then inherit from a common class.

The 6x6 transport matrices can be decomposed into blocks

$$\mathbf{M} = \begin{pmatrix} \mathrm{A}_1 & \mathrm{A}_2 & 0 & 0 & 0 & 0 \\ \mathrm{A}_3 & \mathrm{A}_4 & 0 & 0 & 0 & 0 \\ 0 & 0 & \mathrm{B}_1 & \mathrm{B}_2 & 0 & 0 \\ 0 & 0 & \mathrm{B}_3 & \mathrm{B}_4 & 0 & 0 \\ \mathrm{D}_1 & \mathrm{D}_2 & 0 & 0 & 1 & 0 \\ K_1 & K_2 & K_3 & K_4 & 0 & 1 \end{pmatrix}$$

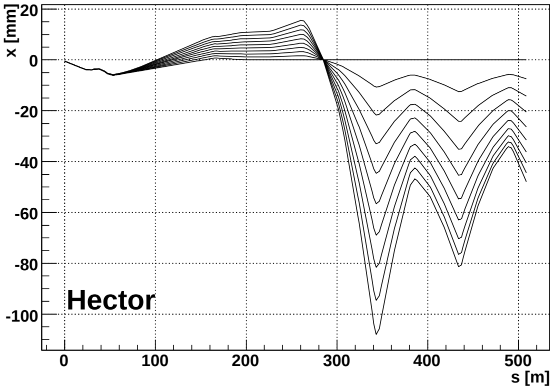

Figure 7.3: Protons with a different P^μ than nominal beam protons deviate from the ideal orbit. This figure shows a scan in energy for several protons without any divergence at the IP. Each curve corresponds to an energy loss of 50 GeV increment, from 0 to 500 GeV energy loss, with the optics of beam 1.

where

- A (and B) blocks refer to the action (focusing, defocusing, drift) on horizontal (and vertical, resp.) coordinate and angle.
- D$_i$ terms reflect the dispersion effects of the horizontal dipoles on off-momentum particles.
- K_i factors are the angular action of kickers.

A beamline is the implementation of a list of optical elements with such transport matrices. The introduction of dispersion terms allows a proper description of off-momentum particles ($\Delta p/p \neq 0$). The *dispersion function* can be defined from EQ. 7.3, for horizontal dipoles ($k = 0$), taking $\Delta p/p = 1$:

$$D''(s) + \frac{1}{R^2} D(s) = \frac{1}{R}. \tag{7.4}$$

Developing the solution of this equation leads to a correction term for the deflection of off-momentum particles in the dipoles:

$$x_{\mathrm{off-momentum}}(s) = x(s) + D(s)\frac{\Delta p}{p}. \tag{7.5}$$

Besides the dispersion correction which is valid for low Δp, the actual dependence of the particle deflection on its momentum is also taken into account. This is the *chromaticity*, or the energy dependence of the transport matrix, implemented by rescaling the magnetic field terms (R, k, K) with a factor $(\frac{p}{p-\Delta p})$. The propagation of particles different from protons is also possible by rescaling these magnetic field terms:

$$k_i(\Delta E, q_p) = k_i \frac{p_0}{p_0 - \Delta p} \frac{q_p}{q_{\text{proton}}} \quad , \qquad k_i = R, k, K; \tag{7.6}$$

where q_p is the particle charge. The ROOT framework easily interfaces HECTOR with the output of the high energy physics event generator PYTHIA [136]. Forward particles from the final state can be then propagated through the beamline via HECTOR, for example in photon interactions. Moreover, HECTOR is now used as an external library[3] in CMSSW (global software for CMS [137]) and FAMOS (the corresponding fast simulation software).

As HECTOR has been designed for the LHC beamlines, one class can parse the official LHC optics tables, interfacing them directly into the code at runtime. For a better compatibility with different table layouts, HECTOR can recognise column headers and is thus compliant with different table types.For the following analysis, LHC optics version 6.500 has been used, corresponding to $\beta^* = 0.55$ m at the IP1 and the IP5.

Limitations: sextupoles and magnets of higher order (multipoles) are neglected in HECTOR (reasonable the first 430 m after the IP). The energy dependence of the transfer matrices is taken into account, but neither beam-beam interactions, nor the field non-uniformities. The beam particle mass is also neglected with respect to its energy.

7.2 Validation and performances

As a part of the development phase of such a mid-scale computing project, the validation of the code and of its results plays a major role both for the quality of the software and time-wise. Several possibilities were investigated, like comparing HECTOR with exact calculation of single optical elements, or the equivalence with other transport programs, applied on the LHC beamlines. The results of these procedures are detailed thereinafter. In terms of the robustness, readability, accessibility and portability of the source code, traditional working tools have been exploited like `make`, `Doxygen`, `valgrind` and `CVS` [140].

7.2.1 Exact calculation for dipolar fields

The exact description of the path of a relativistic charged particle inside a dipole can be easily derived from classical electrodynamics [141]. Given a rectangular dipole, imposing a vertical and uniform magnetic field B_y on a single charge e. No border effect is taken into account, i.e. the field is either zero (outside the dipole) or maximal (inside) as depicted in FIG. 7.4. Knowing the coordinates

---

[3] HECTOR is integrated in CMSSW as an external library whose interface is the `SimTransport/Hector` package.

of the charge when it enters the dipolar field (x_0, y_0, z_0), its path inside the magnetic region is described by the following equations (Eq. 7.7).

$$\left\{ \begin{array}{l} x(t) = x_0 + \frac{v_{x0}}{\omega} \sin \omega t + \frac{v_{z0}}{\omega} \cos \omega t \\ y(t) = y_0 + v_{y0} t \\ z(t) = z_0 - \frac{v_{x0}}{\omega} \cos \omega t + \frac{v_{z0}}{\omega} \sin \omega t \end{array} \right. \tag{7.7}$$

where $\omega = \frac{ec}{E} B_y$, and e the particle charge and E its energy. This obvious helicoidal displacement is just the superposition of a vertical drift in the y direction and circular motion in the horizontal (x, z) plane. The corresponding radius is given by:

$$R = \frac{v_\perp}{\omega} = v_\perp \frac{E}{ecB_y} \quad \text{with} \quad v_\perp = \sqrt{v_x^2 + v_z^2}.$$

As expected, what matters is the component of the particle velocity which is transverse to the magnetic field, and the particle energy.

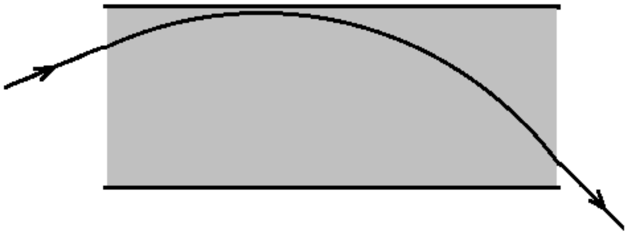

Figure 7.4: Comparison to classical electromagnetism: dipolar magnetic field profile and corresponding charged particle trajectory. No border effect is taken into account: the field is either zero (outside the dipole) or maximal (inside, in grey).

Assuming a particle travelling in the (x, z) plane, with a small angle θ_0 to the z axis. The dipole has a length l and a bending radius R. In the dipole frame, the deflection is then:

$$\left\{ \begin{array}{l} \Delta x = -R \cos \theta_0 + R \sqrt{1 - \left(\frac{l}{R} - \sin \theta_0 \right)^2} \\ l = R(\sin \theta_0 - \sin \theta_f) \end{array} \right. \tag{7.8}$$

The chromaticity effects are evaluated via a reference track for a given energy and no initial angle: Δx_0. This defines the 0-line in the beamframe, where the deflection Δx_* of an other particle, with less momentum and an initial angle is then given by Eq. 7.10 (Fig. 7.4):

$$\Delta x_* = \Delta x_0 + r\cos\theta_0 - r\sqrt{1-\left(\frac{l}{r}-\sin\theta_0\right)^2} \tag{7.9}$$

$$\text{with}\quad \Delta x_0 = -l\frac{l/R}{1+\sqrt{1-(l/R)^2}}. \tag{7.10}$$

The last term is rearranged to be numerically stable. As $r = \frac{1}{k}$ and $k(p) = k_0\frac{p_0}{p}$, $r = R\frac{p}{p_0}$. Assuming, for instance, $l = 10$ m and $R = 10^4$ m, this gives:

$\mathbf{p/p_0}$	$\mathbf{\Delta x_*}$
0.99	50.5 μm
0.9	555.6 μm

Hector results are in very good agreement with theory ($< 0.1\%$) at the level of this simple model. This test is still of importance, as Hector deals only with dipoles, quadrupoles and drifts. As their implementation into the matrix formalism do not need any simplification, the drift description does not bring further errors. Quadrupolar field have not been tested with this method.

7.2.2 Comparison to Mad-X

In order to validate Hector, cross-checks have been made with the output of mad-x [139], such as the beam beta functions (Fig. 7.2) and the beam relative positions (Fig. 7.5). For each point, the beta functions are computed from the beam emittance and the rms of its profile in the transverse plane. The beam beta functions, which describe the variation of the beam transverse dimension along the orbit, as output by Hector, match perfectly the results from Mad-X. The lateral beam position shown in Fig. 7.5 is relative to its ideal path, defined for disabled kickers (and no crossing angle). These graphs (Fig. 7.2 and 7.5), and their equivalents in backward direction, are the strongest tests for Hector, where smearings of position, angle and energy are applied as previously explained.

7.2.3 Comparison to FP-track

As the fp420 group is a unique collaboration between cms and atlas experiments, some tools are similar. Another transport code has been written in Fortran by P. Bussey (University of Glasgow), called FP-track. This code was initially dedicated to the study of the Double Pomeron Exchange production of Higgs boson (Central Exclusive Production). This provides some extra comparison plots, like the chromaticity grids. The parallel and independent development of both tools assessed their quality.

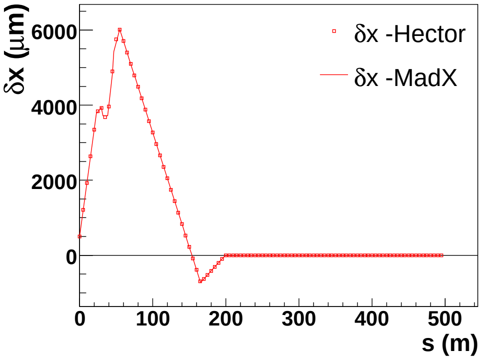

Figure 7.5: Relative horizontal position for beam 1, around the IP5, in the forward direction. The relative position is defined as the difference along the ideal orbit between the beam lateral positions with and without the crossing angle. This relative position graph (*squares*) matches MAD-X predictions (*plain line*). One clearly sees the crossing angle at the IP5 ($s = 0$ m) and the effects of the kickers that move the beam back to the ideal orbit.

7.2.4 Performances

HECTOR has been designed to be fast and light. All the code and its library altogether weight less than 2.5 MB for about 12,000 lines of code. FIG. 7.6 depicts its performance, leading for a first estimate to a CPU time of 4 μs per beam particle per beamline optical element at the LHC. As expected, the CPU time is linear with the number of optical elements and the number of protons.

7.3 Beamline simulation

By using the HECTOR classes and library, physics studies can be performed by means of the particle propagation inside the beamlines, away from the interaction point.

7.3.1 Trajectories

Knowing the optics tables for both LHC beams, their trajectories can be compared simultaneously, in both top and side views, for the two LHC beams aside (incoming beam 2 and outgoing beam 1, at the IP5 and the IP1: FIG. 3.3). The top view shows the beams on the horizontal plane, clearly depicting the crossing angle at the IP5, and the beam separation after 70 m away from the interaction point. The bending of the sector dipoles has been switched off in order to make the plot clearer – this is why both beams are straight and parallel after 250 m. However, the optical elements have been shifted (without tilt) in the horizontal plane by half of the beam separation distance, from 180 m

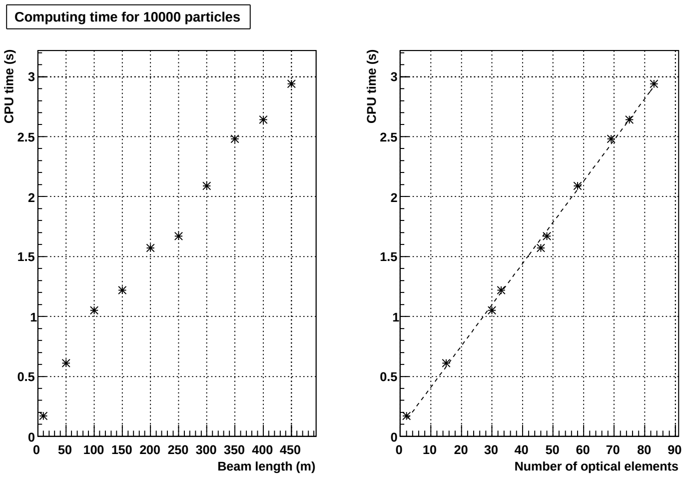

Figure 7.6: Hector speed performance: CPU time with respect to the propagation distance (*left*) and the number of optical elements (*right*) in the beamline, computed for a $10,000$ particle beam around the IR5. As the propagation of particles corresponds to the multiplication of matrices, the computation time is directly proportional to the amount of optical elements in the beamline, as well as to the number of beam particles. For a time estimate for large number of particles and long beamlines, a good approximation is 4 μs per optical element (including drifts) per particle. For this test (3.43 μs per element per particle), Hector is run on a regular laptop with 1.7 GHz Intel Pentium Centrino processor, Linux release Ubuntu.

away from the IP, in order to match the ideal beam path: a proton with nominal energy and on the ideal orbit should travel through optical elements in their geometrical centre. The side view shows the beams in the vertical plane, emphasising the difference between the IP1 and the IP5. Moreover, the major optical elements have been drawn: rectangular dipoles in red, sector dipoles in light green, and quadrupoles in yellow and blue.

7.3.2 Beam profiles

Lateral beam profiles along the beamline are of interest, for instance for studies of very forward detectors (Fig. 7.7). The beam size and shape are obtained after propagation of beam particles using initial dispersion in position, angle and energy at the interaction point. Assuming a Gaussian distribution for these variables, the evolution of both beams can be seen in the transverse plane at 220 m and 420 m away from the IP. As expected, the beam particles are distributed symmetrically on the vertical plane ($\bar{y} = 0$ mm), and are already separated in the horizontal plane ($\bar{x} = \pm 97$ mm). The symmetry between beam

1 and 2 is striking. The 3σ contours (red) guides the eye for the lateral beam extension. In the angular (θ_x, θ_y) plane, the beams evolve according to the focusings and the defocusings they undergo, even if the mean value of these angles remains effectively equal to 0 μrad. The evolution of the beams in the phase space has also been drawn (Fig. 7.1). Once again, the similitude between both beams is clear, even if they differ by slight details. All these profiles were obtained by simulation of $10,000$ beam protons (with $E = 7$ TeV).

7.3.3 Apertures

The physical aperture of the real optical elements has also to be taken into account. If a particle hits a collimator or a wall of the primary vacuum system, it is assumed lost. Each time a particle enters or leaves an optical element, a test is performed to determine if its position matches the element acceptance. This is illustrated in Fig. 7.8. Protons from the LHC beam 1, around the IP5 have lost some energy, which leads to a deflection with respect to the nominal beam position in $(0, 0)$ in the transverse plane. The aperture shape of the *MB.B9R5.B1* optical element is the *rectelliptical*[4] closed area. The proton energy has been chosen to 110 GeV, in order to match the element limiting energy acceptance. Due to the initial smearings, some protons (in black) still pass through the optical element without being stopped. On the other hand, some of them hit the limiting aperture shape and are tagged as stopped protons (in red). In such a case, the particles are considered as lost from the beam, and are not propagated any further.

7.4 Very Forward Detectors

This section will discuss two cases of VFDs, differing by their distance from the IP (s) and their minimal horizontal distance (x) from the nominal beam position. The assumed location of the first detector is ($s = 220 - 224$ m, $x = 2000$ μm), and of the second one at ($s = 420 - 428$ m, $x = 4000$ μm). No hypothesis is made on their detection efficiency or their resolution, unless quoted. VFDs providing 2D-measurement (x and y coordinates) are considered here, each consisting in fact of two stations separated by 4 and 8 m as a lever arm for the angle measurement, with no magnetic element in between. Several examples of studies performed using Hector are given.

7.4.1 Acceptance

Using Hector's aperture description, it is possible to identify the characteristics of the protons that will hit the VFD. The exchange of a photon or a pomeron, leaving the proton intact, results in a proton energy loss (E_{loss}) and a scattering angle, directly linked to the four-momentum transfer squared (t),

---

[4] The rectellipse is a superposition of a rectangle and an ellipse.

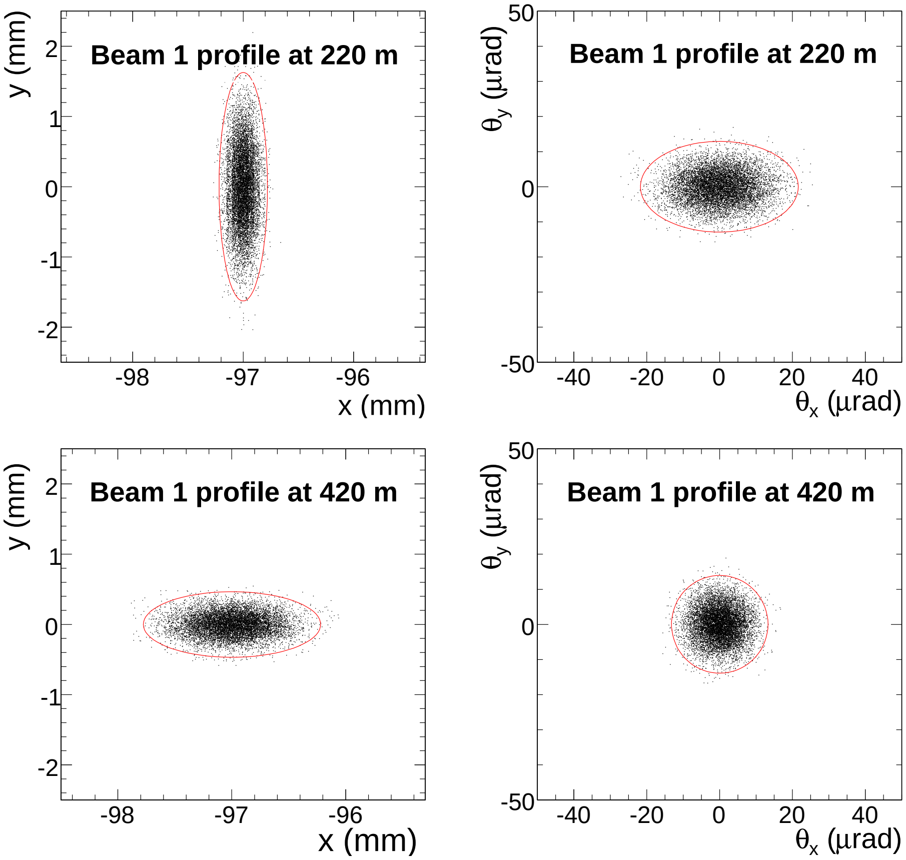

Figure 7.7: LHC beam profiles in the transverse plane at 220 m and 420 m from the IP5, for both beam 1. The graphs in the left column plot the horizontal and vertical position profiles. The graphs in the right column show the horizontal and vertical angular profiles. These plots are obtained by propagating ten thousand 7 TeV protons through the LHC beam 1, in the forward direction, from the IP5. The mean horizontal position $\bar{x} = -97$ mm matches the half of the separation distance between both beams (tunnel reference frame). The red ellipse delimits the 3σ contour for each plots.

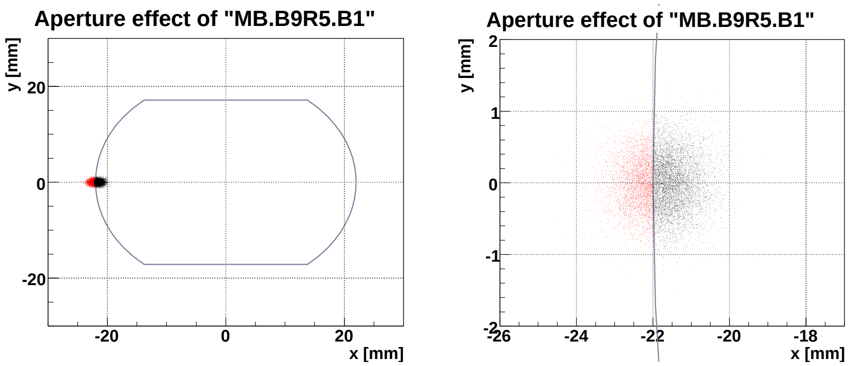

Figure 7.8: Example of aperture check for the *MB.B9R5.B1* dipole ($s = 338$ m), drawn in the (x, y) transverse plane, at the exit of this optical element. A set of protons, with a mean energy loss around 110 GeV, has been propagated from the IP5 to the *MB.B9R5.B1* dipole using the LHC beam 1 optics. The beam 1 is centred in $(0, 0)$ but is not shown. The closed area corresponds to the *rectellipse* aperture shape of the optical element. Protons that passed through the dipole are the black ones, while protons hitting the walls are tagged in red. The first graph is scaled for the full aperture shape, the second one has been zoomed in around the region of interest.

or equivalently to the virtuality (Q^2) of the exchanged particle. The acceptance windows of the VFDs can be computed by performing scans in (E_{loss}, t) and computing the probabilities of reaching the detectors. The Fig. 7.9 shows the contour plots of the detectors acceptance, in this (E_{loss}, t) plane. It is obvious from these graphs that the VFD acceptances mostly depend on E_{loss}, and have a very small sensitivity in t, within a large t range. For the VFD at 220 m, an area forbidden by kinematics is visible, for low $|t|$ and high E_{loss}. Corresponding profiles at fixed virtuality are shown at 220 m and 420 m (Fig. 7.10).

7.4.2 Irradiation levels

The total diffractive cross-section at the LHC is very large, resulting in a high rate of diffractive protons hitting the VFDs. As a result, it causes extremely high irradiation levels, requiring in turn the use of very radiation hard detectors. As an illustration, the number of hits and their respective map, due to the pp → pX processes has been investigated (Fig. 5.1). In this approach, other radiation sources are neglected, like beam halo or secondary particles coming from interactions in the beam pipe for instance.

The VFDs are located at $s = 220$ m (*above*) and $s = 420$ m (*below*) from the IP5. The horizontal position of the detector edge is respectively $x = 2$ mm and $x = 4$ mm from the nominal position of the centre of the corresponding beam. The fluence is given per square centimetre. The $pp \rightarrow pX$ processes are generated by Pythia [136] 6.2.10. The number of hits are normalised by square centimetre, assuming an integrated luminosity of $L = 20$ fb^{-1}. From the $1,000,000$ generated events, 17 % have been detected at 220 m, and about 12% at 420 m. This simulation shows that the hottest spots in the detectors are localised with areas of only a few squared mm, reaching proton fluences exceeding locally 1×10^{14} protons/cm^2.

7.4.3 Chromaticity grids

Once the acceptance windows of very forward tracking detectors are defined, it is interesting to see matching between the proton variables at the IP and those measured by VFDs. Depending on their energy and angle at the IP, forward protons will hit the VFDs at various positions. Drawing iso-energy and iso-angle curves for a set of sample protons produces a grid in the measurement related

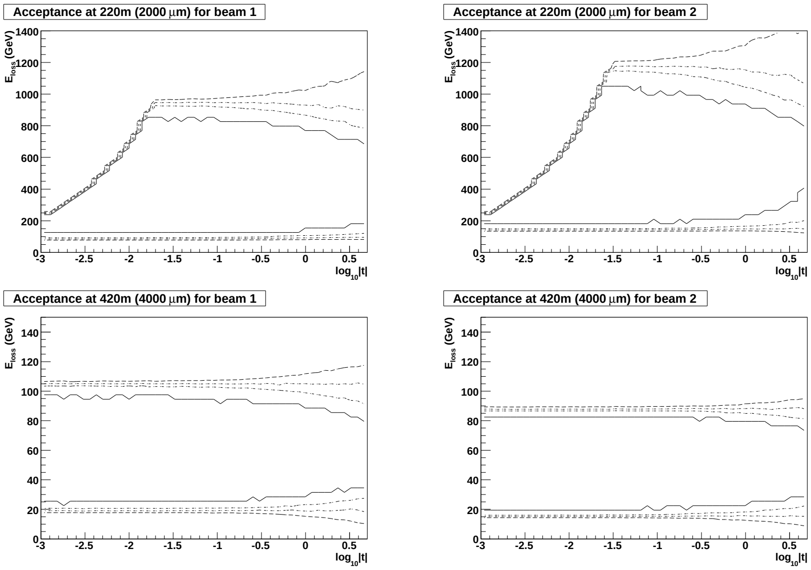

Figure 7.9: VFD proton acceptance for the LHC beam 1 (*left*) and 2 (*right*) around the IP5. These VFDs are located at ($s = 220$ m, $x = 2000$ μm horizontal position; *above*) and ($s = 420$ m, $x = 4000$ μm horizontal position; *below*). This map shows contours of 25%, 50%, 75% and (plain curve) 100% acceptance. The acceptance is roughly rectangular, i.e. independent of t. At 220 m, the missing triangle in the acceptance at low $|t|$ and high energy loss is prohibited by kinematics. This area corresponds to non-physical protons. The stair-stepping effect of the lower border of this triangle is only due the binning of the graph. At bottom right corner of each graph, the angular kick coming from the large momentum transfers leads to an increasing smearing of the graph lower edge.

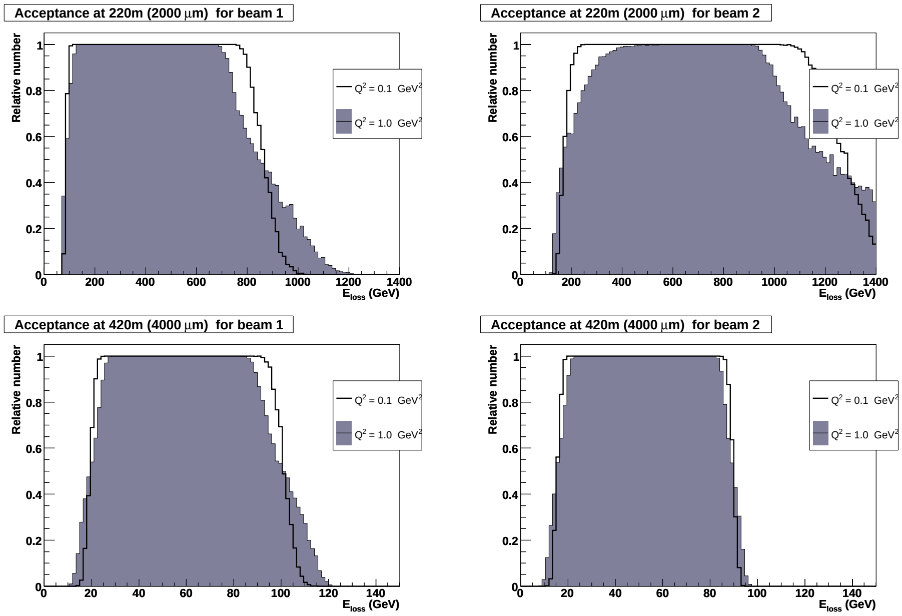

Figure 7.10: VFD acceptance as a function of energy loss, for two fixed virtualities. See previous figure for more details.

variables, (x_1, x_2) or (x_1, θ). Due to optics of the LHC beamlines, the grid unfolds itself in a much clearer way in the latter plane, and is almost invisible in the former one. The energy dependence of the transfer matrices implies a deformation of the grid – without such a dependence, the grid would be a parallelogram. One should note, that uncertainty of the transverse position of the proton vertex at the IP results effectively in smearing the chromaticity grids. Anyway, these chromaticity grids provide a straightforward tool for unfolding the energy and angle at the IP of the measured particle. The grids in Fig. 7.11 were calculated in the energy range accessible to the VFDs. Finally, the correlation between the vertical angle at the IP and the vertical coordinate measurement is shown in Fig. 7.12.

7.4.4 Reconstruction algorithms for the event kinematics

One of the main physical motivations for Hector is the reconstruction of the event kinematics. For instance, if a beam particle has exchanged a photon at the IP, one could reconstruct photon energy (E) and virtuality (Q^2). The particle energy at a given position in the beamline is obtained from the measured particle position and angle within the matrix formalism by solving these

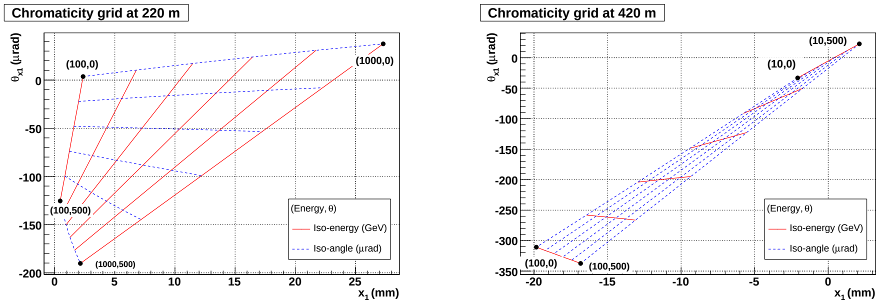

Figure 7.11: Chromaticity grids: iso-energy and iso-angle lines for the VFDs at 220 m (*left*) and 420 m (*right*) away from the IP5, for the LHC beam 1. The graphs show the position and angle x and x' of protons, given the energy loss $[0; 1000]$ GeV and $[0; 100]$ GeV, respectively, and the angular kick $[0; 500]$ μrad. The energy dependence of the transfer matrices induces a deformation of the grid, worsening the reconstruction power at higher angles.

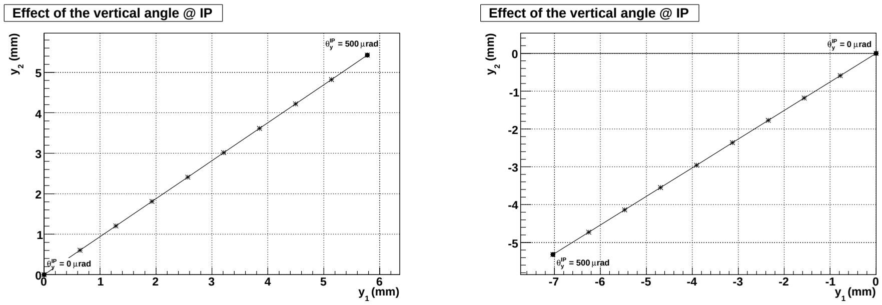

Figure 7.12: Shift in vertical coordinate (y_1 and y_2) for VFDs at 220 (left) and 420 m (right) from the IP5, due to the vertical angle θ_y^* at the IP.

equations:

$$\left\{ \begin{array}{l} x_s = a_s x_0 + b_s x'_0 + d_s E \\ x'_s = \alpha_s x_0 + \beta_s x'_0 + \gamma_s E \end{array} \right. \tag{7.11}$$

The transfer matrix of the beamline yields the coefficients a, b, etc. The introduction of an energy dependence on the strength of optical elements refines the transfer matrix, becoming a function of E: $a_s(E)$, $b_s(E)$, … This dependence introduces *non linearities* in the energy reconstruction.

Conclusion and perspectives

A new tool, called HECTOR, has been written for the LHC and is implemented in CMSSW and FAMOS. This fast simulator is generic and modular, and is able to do the particle transport in the beamline and to reconstruct the proton kinematics at the IP. It has been validated with MAD-X and classical electromagnetism. Several results for VFDs were obtained (acceptance, irradiation doses, reconstruction power, dependence on beamline misalignment). Finally, its use will be evaluated for RHIC (Relativistic Heavy Ion Collider, Brookhave National Laboratory, U.S.A) and CRC (Centre de Recherche du Cyclotron, Université catholique de Louvain, Belgium)

Part IV

Online selections and offline analyses

Chapter 8

Selection of exclusive dileptons in $\gamma\gamma$ collisions

$\gamma\gamma \to e^+e^-$ and $\gamma\gamma \to \mu^+\mu^-$ processes are favoured by a high cross-section and a very clean event topology. Event kinematics is characterised by a steep p_T dependence of the cross-section, and by back-to-back leptons in the transverse plane. The production of two same-flavour leptons exclusively in the final state is tested by requirements on the number of tracks and of calorimetric deposits. Online and offline selections are detailed in this chapter, as well as studies on background events. This analysis has been approved by the CMS *collaboration [5].*

8.1 Introduction

The exclusive production of pairs of same-flavour leptons is characterised by a large cross-section and a clean event topology. The studied samples of $\gamma\gamma \to \mu^+\mu^-$ and $\gamma\gamma \to e^+e^-$ events were produced by the LPAIR generator [47]. This elastic production has very little theoretical uncertainty, being a nearly pure QED process and as the proton form factor are well-known. Beyond their study in e^+e^-colliders, dilepton production has also been studied in ep, $p\bar{p}$ and heavy ion collisions (Section 8.1.3).

8.1.1 Event kinematics

FIG. 8.1 shows the exclusive dilepton production Feynman diagrams: the two interacting protons emit a virtual photon, which in turn interact via a fermionic line of muons or electrons. Full cross-sections are $\sigma_{pp(\gamma\gamma\to\mu^+\mu^-)pp} = 0.15$ μb and $\sigma_{pp(\gamma\gamma\to e^+e^-)pp} = 7.1$ mb, at the c.m.s. energy of $\sqrt{s} = 14$ TeV. These are extremely dependent on lepton p_T, as depicted in FIG. 8.2. For reference, a set of precise numbers is given in TAB. 8.1.

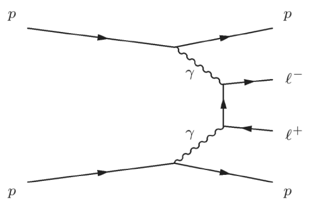

Figure 8.1: Exclusive production of a lepton pair via a two-photon exchange. Each incoming proton emits a photon and is scattered. The photons couple to the charged leptons.

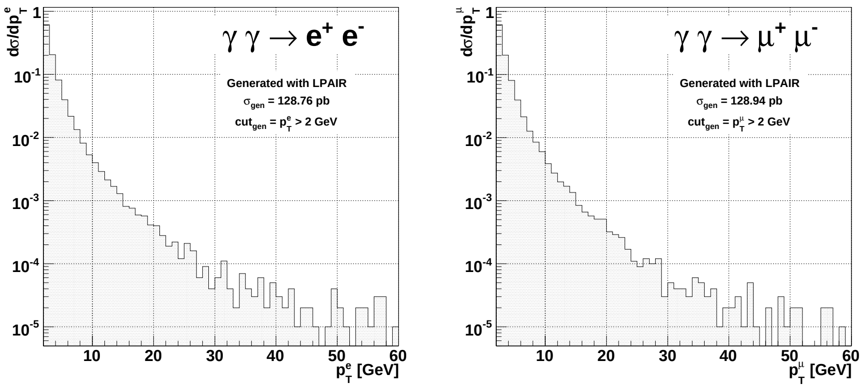

Figure 8.2: Distribution of the lepton transverse momentum p_T for $pp(\gamma\gamma \to e^+e^-)pp$ (left) and $pp(\gamma\gamma \to \mu^+\mu^-)pp$ (right), for leptons with $p_T > 2$ GeV. The protons are scattered elastically after the photon exchanges, at a c.m.s. energy of $\sqrt{s} = 14$ TeV. The distributions are normalised to unity. Two entries per event.

$\mathbf{p_T^\ell}$ **cut (GeV)**	no cut	1.0	2.0	2.5	5.5
$\sigma[\mathbf{pp}(\gamma\gamma \to \mathbf{e^+e^-})\mathbf{pp}]$ **(pb)**	7.06×10^9	682	129	74.7	10.4
$\sigma[\mathbf{pp}(\gamma\gamma \to \mu^+\mu^-)\mathbf{pp}]$ **(pb)**	147×10^3	677	129	74.7	10.3

Table 8.1: Dependence in p_T of the cross-section for $pp(\gamma\gamma \to \ell^+\ell^-)pp$ processes. Cross-sections in pb, for a c.m.s. energy of $\sqrt{s} = 14$ TeV. For reference, L1 trigger levels at $\mathcal{L} = 1 \times 10^{32}$ cm^{-2}s^{-1} are 3 GeV for dimuons and 8 GeV (6 GeV) per inclusive (exclusive) pairs of isolated electrons.

Event kinematics is a characteristic for exclusive lepton pairs, and looks similar in both cases (e^+e^-or $\mu^+\mu^-$). First, leptons are balanced in transverse momentum p_T (Fig. 8.3) and acoplanarity $\Delta\phi$ (Fig. 8.4). Whilst each of these variables is strongly correlated between the two leptons, no such link exists for the pseudorapidities, which hence cover a large range without a strong relation between the leptons (Fig. 8.5 and 8.6).

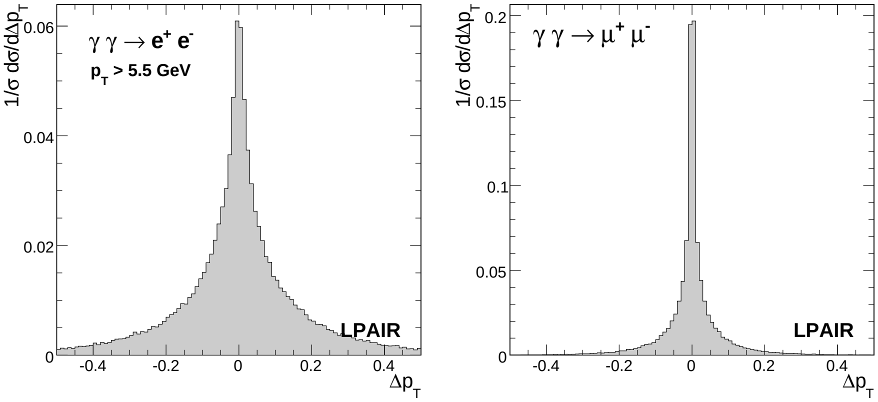

Figure 8.3: Distribution of $\Delta p_T = p_T(\ell^+) - p_T(\ell^-)$ for $\gamma\gamma \to e^+e^-$ (left) and $\gamma\gamma \to \mu^+\mu^-$ (right), at generator level ($\sqrt{s} = 14$ TeV). The electron sample requires $p_T(e) > 5.5$ GeV. The distributions are normalised to unity.

The present results are based on $2 \times 100,000$ events, for electron pairs ($p_T^e > 5.5$ GeV) and muon pairs ($p_T^\mu > 2.5$ GeV). The key elements are: (i) the exclusivity of these events, with only two leptons and no other particle in the central detector[1]; and (ii) the leptons are back-to-back in the transverse plane, with balanced transverse momenta. These clear kinematic constraints provide efficient means for the selection of such events, both at trigger level and during the offline data analysis. This document does not cover the $\gamma\gamma \to \tau^+\tau^-$ production, as the short τ lifetime makes the final states completely different. τ's can decay hadronically or into leptons, but with different kinematic distributions due to the presence of neutrinos.

8.1.2 Trigger concerns for exclusive dilepton events

Due to the relatively low average energy scale for photon-induced events, the default triggering schemes are not optimised for these events. As previously

---

[1] Event pile-up is neglected. This condition is valid at low luminosities or if extra final state particles coming from pile-up events can be rejected via techniques like, for instance, vertexing.

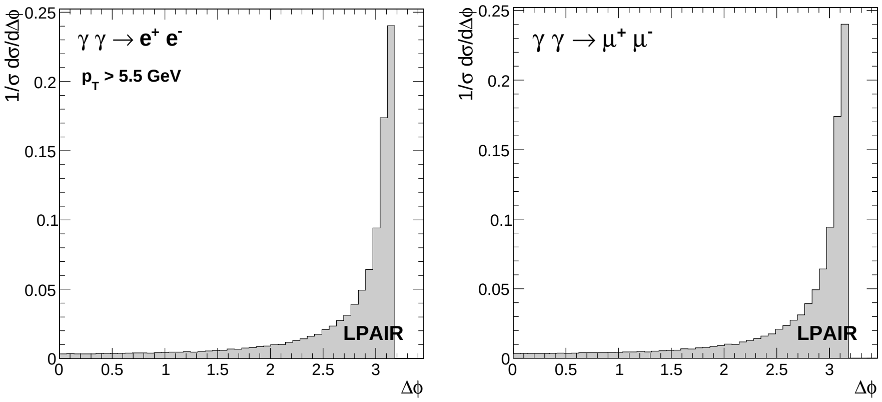

Figure 8.4: Distribution of $\Delta\phi = \phi(\ell^+) - \phi(\ell^-)$ for $\gamma\gamma \rightarrow e^+e^-$ (left) and $\gamma\gamma \rightarrow \mu^+\mu^-$ (right), at generator level ($\sqrt{s} = 14$ TeV). The electron sample requires $p_T(e) > 5.5$ GeV. The distributions are normalised to unity.

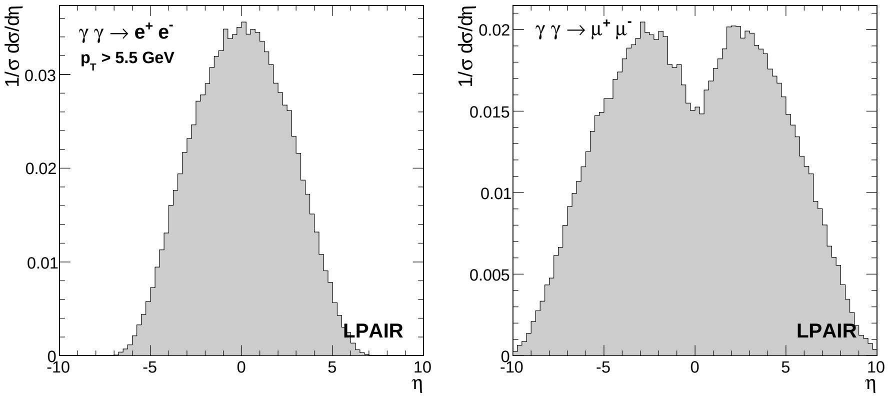

Figure 8.5: Distribution of lepton pseudorapidity η for $\gamma\gamma \rightarrow e^+e^-$ (left) and $\gamma\gamma \rightarrow \mu^+\mu^-$ (right), at generator level ($\sqrt{s} = 14$ TeV). The electron sample requires $p_T(e) > 5.5$ GeV. Two entries per event. The distributions are normalised to unity.

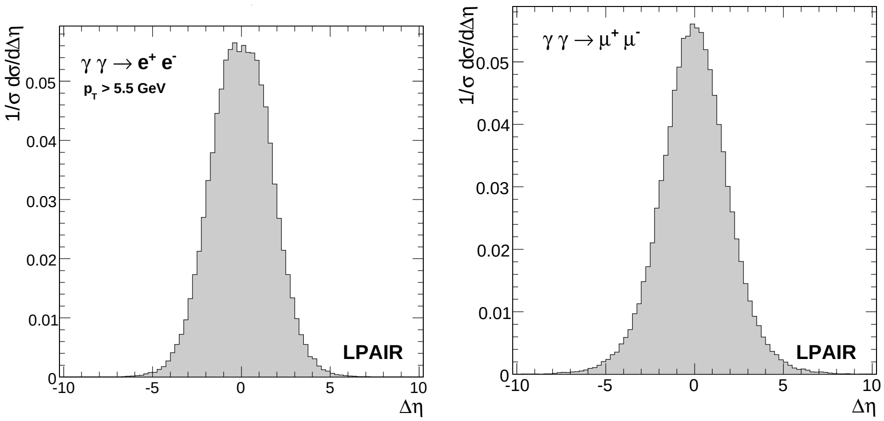

Figure 8.6: Distribution of $\Delta\eta = \eta(\ell^+) - \eta(\ell^-)$ for $\gamma\gamma \to e^+e^-$ (left) and $\gamma\gamma \to \mu^+\mu^-$ (right), at generator level ($\sqrt{s} = 14$ TeV). The electron sample requires $p_T(e) > 5.5$ GeV. Two entries per event. The distributions are normalised to unity.

shown in FIG. 8.2, dilepton production cross-sections are characterised by a very narrow peak at low p_T, followed by a steep slope towards higher values.

Unfortunately, $E_T \approx p_T$ is precisely the variable on which a lower threshold is applied at L1 trigger to reduce the selection output rate. Hence, a key element of the dilepton studies is to define dedicated L1 trigger algorithms to retain a larger fraction of these events. Subsequently, the corresponding HLT paths have to be optimised for a proper handling of the whole selection chain. Only data from the central detector are used here for these triggers[2].

8.1.3 Hera and Tevatron

The exclusive production of $\mu^+\mu^-$ and e^+e^- has been studied in other colliders, like in *ee*, *ep* [30, 31, 32], $p\bar{p}$ [35] and heavy ions [33, 34] collisions.

The dimuon invariant mass $M_{\mu\mu}$ and transverse momentum p_T^μ distributions, as observed in *ep* collisions at HERA by H1, are depicted in FIG. 8.7 ($\sqrt{s} = 319$ GeV). All electroweak processes are included at leading order, dominated by γ and Z exchanges.

For $p\bar{p}$ collisions at TEVATRON ($\sqrt{s} = 1.96$ TeV), the measurement by the CDF experiment of exclusive dielectrons gives:

$$\sigma_{e^+e^-} = 1.6^{+0.5}_{-0.3}(\text{stat}) \pm 0.3(syst) \text{ pb} ,$$

---

[2] New L1+HLT trigger paths have similarly been investigated for γp processes, using this time the presence of a forward rapidity gap in addition to one electron and at least one jet as a signature. This trigger work, which is not in relation with exclusive dileptons, is reported in Reference [142].

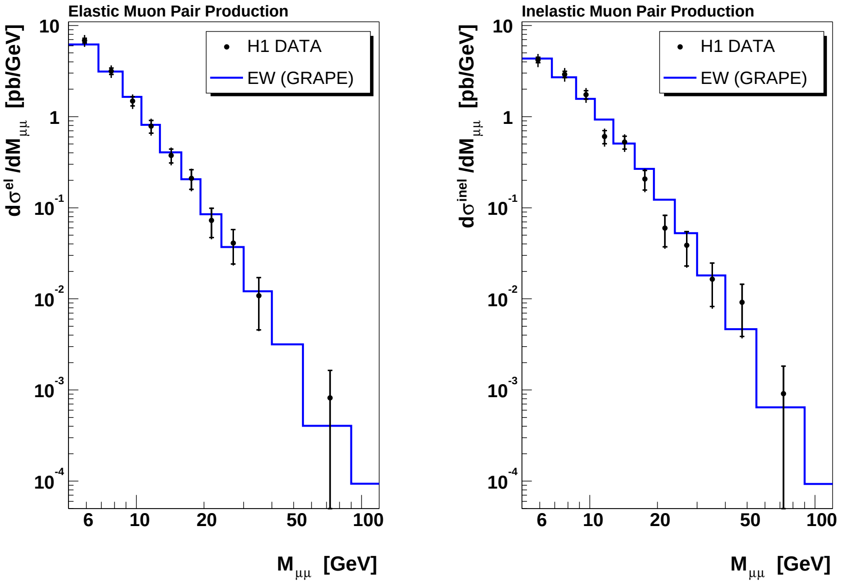

Figure 8.7: Cross-section for the production of two muons in *ep* interactions, as a function of the dimuon mass $M_{\mu\mu}$ [32]. Both elastic and inelastic case are shown, and compared to the GRAPE generator. Data from the H1 experiment in *ep* collisions at HERA, for $L = 70.9$ pb^{-1} and $\sqrt{s} = 319$ GeV.

which corresponds to 16 exclusive e^+e^-candidate events with an estimated background of $2.1^{+0.7}_{-0.3}$, corresponding to an integrated luminosity of 532 pb^{-1} [36]. The measured cross-section is consistent with the predicted one, including elastic and inelastic components (FIG. 8.8).

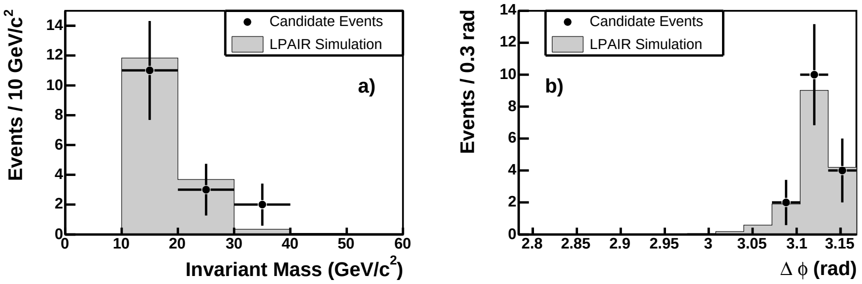

Figure 8.8: Invariant mass M_{ee} and acoplanarity $\Delta\phi$ distributions of exclusive e^+e^- productions in $p\bar{p}$ collisions in TEVATRON, at $\sqrt{s} = 1.96$ TeV and corresponding to an integrated luminosity of 532 pb^{-1}. Data from the CDF experiment [35].

Photon physics from heavy ion collisions will not be discussed here. It is important to note that for heavy ions, the incoming photon flux is strongly increased, by a factor of Z^2, as the number of charges Z is much larger than for protons.

8.2 Simulation and reconstruction of signal and background

This section describes the simulation of the observation of exclusive lepton pairs in the CMS detector. This study [5] is a common work with S. Ovyn (UCL) and J.J. Hollar (LLBL), and has been approved by the CMS collaboration.

8.2.1 Lepton pair signal

The photon-photon interaction, producing a pair of leptons, is simulated by the LPAIR program [47], run in proton-proton mode. This generator uses a particular numerically stable formula for the matrix element of the two-photon production of a fermion pair. Moreover, at low p_T the EPA approximation does not hold anymore. These differences explain the discrepancy with standard MadGraph/MadEvent or CalcHEP computation for the exclusive production of low mass pairs (e^+e^- and $\mu^+\mu^-$), while this difference vanishes for higher masses ($\tau^+\tau^-$). TAB. 8.2 summarises the characteristics of the signal samples employed for this analysis.

Topology		**Size (events)**	σ_{prod} **(pb)**
$\gamma\gamma \to \mu^+\mu^-$ with $p_T^\mu > 2.5$ GeV	elastic	100 k	74.7 ± 0.07
	inelastic	20 k	76.2 ± 15.2
$\gamma\gamma \to e^+e^-$ with $p_T^e > 5.5$ GeV	elastic	100 k	10.4 ± 0.01
	inelastic	20 k	13.6 ± 2.7

Table 8.2: Signal samples from the LPAIR Monte Carlo, for elastic $pp(\gamma\gamma \to \ell^+\ell^-)pp$ and singly inelastic $pp(\gamma\gamma \to \ell^+\ell^-)pX$ exclusive dilepton productions. The sample sizes, and minimal p_T cuts at generator levels are given, with the corresponding cross-section ($\sqrt{s} = 14$ TeV).

As the lepton transverse momentum distribution is very steep, the p_T cuts at generator level have been selected to be quite close to the corresponding minimal Level-1 trigger threshold. This is in order to retain as many events as possible for the analysis. While the elastic contribution $pp(\gamma\gamma \to \ell^+\ell^-)pp$ has been assessed by the comparison to data or to other generators, the inelastic part is more delicate. In the CDF analysis [35], the difference between GRAPE and LPAIR is underlined. In the present analysis, the inelastic samples refer to singly inelastic processes, using LUND fragmentation routines with the CTEQ5M structure function.

All these events are provided as an input to CMSSW, corresponding to the *generation* level. The *simulation* step, dealing with the interactions of the event particles with the central detector and its response, were performed in `CMSSW_1_4_5`. `CMSSW_1_5_4` was used for *digitisation* of the detector response and the application of the *reconstruction* algorithms. Finally[3], `CMSSW_1_6_0` emulated the trigger tables and the data selection.

8.2.2 Background samples

Irreducible and reducible backgrounds

As their detected final state is similar to the signal one (as far as the central detector is concerned), inelastic events are *irreducible* backgrounds: the only difference with the elastic signal is the dissociation of one or both incoming protons. The classification of these events as background is due to the large theoretical uncertainty on their cross-section (approximately 20 %, TAB. 8.2). However, in our simulation, only the singly inelastic processes could be generated. Fully inelastic events, where both incoming protons dissociate are thus neglected.

The diffractive photoproduction of Υ mesons ($b\bar{b}$ bound state), decaying into a pair of same-flavour leptons, gives also irreducible backgrounds: $\gamma p \to \Upsilon p \to$

---

[3] This sequence of versions was the correct one required for the steps detailed in the text, at the time of the analysis. For a faster evolution of the code, gathering hundreds of contributors, the software versions were specialised for given tasks.

$\mu^+\mu^- p$. The cross-section of this process is 62 pb with a large uncertainty ($\mathcal{O}(25\%)$).

In particular these events with large theoretical uncertainty on the cross-section are considered as backgrounds for the luminosity measurement (Chapter 9).

Other backgrounds, like Drell-Yan processes ($q\bar{q} \rightarrow \ell^+\ell^-$), WW decays, $\tau\tau$ and quarkonia decays, do have more particles in the final state. These events are thus considered as *reducible* backgrounds.

Generated samples

The Monte Carlo samples for background events were taken from CMS CSA07 production (so-called "130M CSA07 Cocktail", with 1.3×10^8 events), where various types of events were mixed according to their respective cross-sections. These included amongst other things Drell-Yan (DY) processes (6M, for e, μ, τ), Charmonium and Bottomonium (4M), inclusive electrons and muons (40M) and minimum bias events (20M) [146].

Additional contributions come from private productions of exclusive W pairs, decaying into leptons (e, μ, τ) and of DY events. These events were separated in three regions of dilepton invariant mass: $\text{DY}_1 \equiv 6 < M_{\ell\ell} < 10$ GeV, $\text{DY}_2 \equiv 10 < M_{\ell\ell} < 40$ GeV and $\text{DY}_3 \equiv 40 < M_{\ell\ell}$, while the CSA07 samples contain only the two higher mass bins (DY_2 and DY_3).

8.3 Exclusive dimuon analysis

Before any analysis, all events should first pass the Level-1 and High Level Triggers (*online* selection). Then, the process of signal offline selection extracts the signal from the backgrounds as much as possible.

8.3.1 Online selection of $\gamma\gamma \rightarrow \mu^+\mu^-$

The photon fusion producing two muons is characterised by the presence of only two muons, with opposite charges, in the central detector. The protons, whether dissociated or not, do not leave any signal but possibly in forward regions.

As CMS is designed and optimised for the muon measurement, its default L1 *double muon trigger* is based on a p_T threshold as low as possible: `L1_DoubleMu3` requires at least two muons with $p_T \geq 3$ GeV. Similarly, the default path called `HLT2MuonNonIso` is applied at HLT, which has the same 3 GeV p_T threshold, for an η coverage extending from -2.5 to 2.5. No isolation criteria are applied.

The signal online selection is as high as 12.0 pb after L1 and 7.5 pb after L1+HLT ($\sqrt{s} = 14$ TeV). As the p_T threshold almost corresponds to the minimal value achievable for the muon reconstruction itself [70], it cannot be decreased. In other terms, the dimuon trigger is already optimised for the

Trigger name		**Package**
L1	`L1_DoubleMu3`	`L1Menu2007.xml`
	At least two muons with $p_T^{\mu} \geq 3$ GeV	
HLT	`HLT2MuonNonIso`	`PathDiMuon_1032_NoIso.cff`
	$p_T^{\mu} \geq 3$ GeV, $\lvert\eta\rvert \leq 2.5$, no isolation	

Table 8.3: L1+HLT trigger path for dimuon events, with the corresponding package name in CMSSW and the set of conditions defining the triggers.

$\gamma\gamma \to \mu^+\mu^-$ events with two central muons at low luminosity. It is worth noting that the kinematics of inelastic events corresponds to a slightly flatter p_T distribution. A larger fraction is then selected with $13.9 \pm 2.6(th)$ pb after L1+HLT.

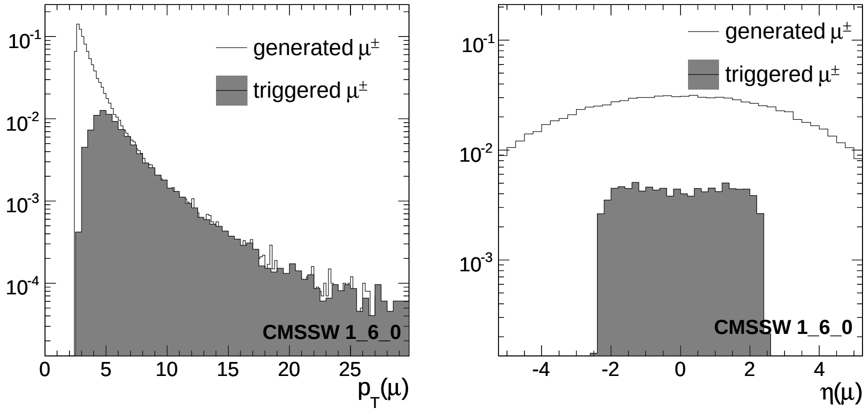

Figure 8.9: Reduction due to the application of trigger levels on the muon signal samples. p_T (left) and η (right) spectra for $\gamma\gamma \to \mu^+\mu^-$ and the reducible backgrounds [5]. The restriction in η coverage and the p_T trigger threshold are clearly visible. Two entries per event. Generator-level histograms are normalised to unity.

The signal events passing the L1+HLT triggers are shown in Fig. 8.9 and are compared to the generated sample (LPAIR). The triggers are applied in `CMSSW_1_6_0`. The reduction due to the $p_T > 3$ GeV cut and the η coverage is clearly visible.

8.3.2 Offline selection

Including the trigger selection efficiency, about 7.5 pb of data from elastic processes is available for analysis. On these, the offline selection criteria are applied. These criteria are divided into two categories in this analysis: *kinematic requirements* and *exclusivity conditions*.

Kinematic constraints The balanced kinematics between both muons has already been mentioned several times. Cuts on the transverse momenta and on the acoplanarity should be recalled at analysis level, on the required two muons. The rejection power is high for inclusive muon samples, exclusive W pairs and minimum bias, while Drell-Yan and resonant states (i.e. quarkonia) are preserved. This balance is shown for muons, after reconstruction, in FIG. 8.10. The exact requirements are loose cuts of $|\Delta\phi| > 2.9$ and $|\Delta p_T| < 2.0$ GeV, which retain most of the signal events.

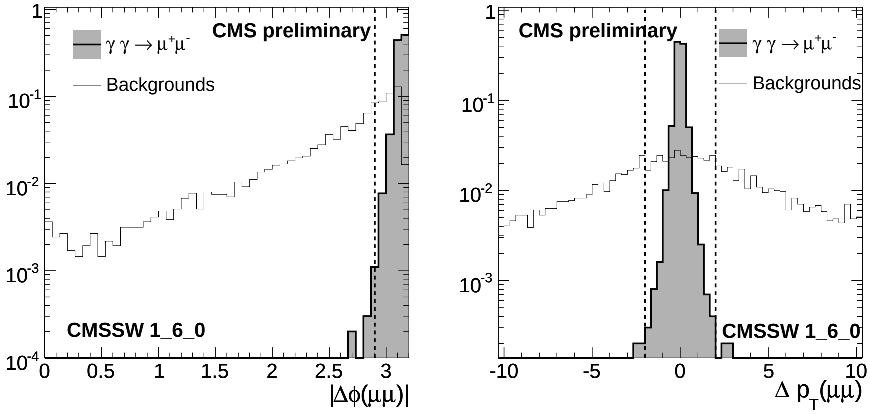

Figure 8.10: Distributions of $|\Delta\phi|$ and Δp_T for elastic $\gamma\gamma \rightarrow \mu^+\mu^-$ signal and reducible background. The corresponding cut applied for the analysis is symbolised by the vertical dashed line. This illustrates the reduction power on background events. All histograms are normalised to unity.

Exclusivity from tracking and calorimetry No exclusivity requirement is applied on the muon pairs at trigger level. After full event reconstruction, the exclusivity is tested from tracking and calorimetric data.

The *calorimetric exclusivity* criterion is based on the calorimetric tower multiplicity in the event. The towers should be away from any muon by $\Delta R > 0.3$ (muon isolation). Their energy should also be such that $E > 5$ GeV, in order to overpass the calorimeter noise (the threshold value is mainly due to the simulated noise in both HF). The event is selected if there are less that 5 of these extra calorimetric towers. The selection power of this cut is shown in FIG. 8.11 (left).

The *tracking exclusivity* condition is based on tracker, with a smaller coverage $(0 < |\eta| < 2.5)$ but a higher granularity than the calorimeters. The signal events are expected to have only two tracks. However, the track reconstruction can be delicate, as the p_T of muons can be very small. The requirement is that a selected event has less than three tracks, including those associated to the muons (Fig. 8.11 right).

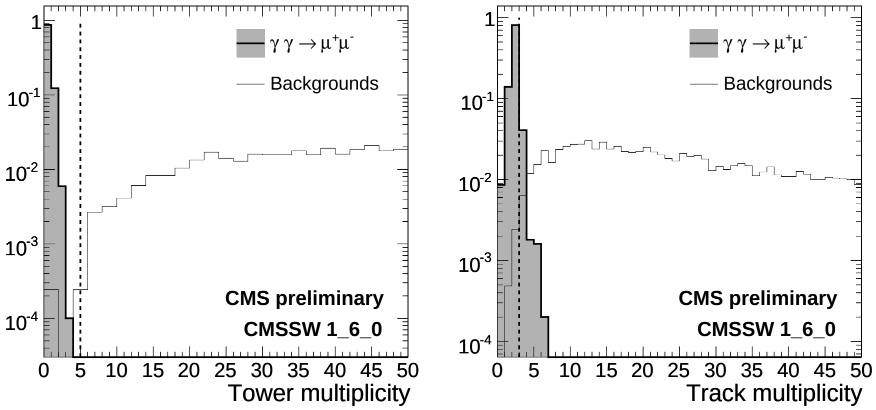

Figure 8.11: Application of the exclusivity conditions (*left:* calorimetric, *right:* tracker) on the signal and the reducible backgrounds [5]. Each histogram is normalised to unity over its full range.

With the default tracking algorithm (`pixelTrack`), the signal is sharply peaked for two identified tracks, while the background events extend to high track multiplicities. However, this algorithm is not optimal for tracks associated to a very low p_T. Another tracking algorithm, dedicated to low p_T tracks, is presented in [147]. This algorithm was not applied during the standard reconstruction of the CSA 07 samples. Eventhough it was not practically possible to rerun all samples with it, a large improvement of the background rejection is expected using this algorithm.

A generator level study has been done, based on the results of this tracking algorithm dedicated to low-p_T objects. The default `PixelTracks` algorithm is simulated by applying a reconstruction efficiency slowly reaching 90% for tracks of charged particles with $p_T > 1.5$ GeV. The `low` p_T `track` algorithm efficiency rapidly reaches 90%, for tracks of charged particles with $p_T > 0.3$ GeV. For comparison, tracks with a p_T of 2.5 GeV are reconstructed with an efficiency of 10% (`PixelTracks`) or 80% (`low` p_T `track`).

The application of this simple model to Drell-Yan events (generated with Pythia, $M_{\mu\mu} > 6$ GeV) is shown in Fig. 8.12. The improved low p_T algorithm (dashed line) is much closer to the generator level data (dotted line) than the default `PixelTracks` algorithm. The tracking exclusivity condition is more efficient for dedicated algorithm, as the tracks are reconstructed with a p_T closer to the reality: better background rejection is achieved.

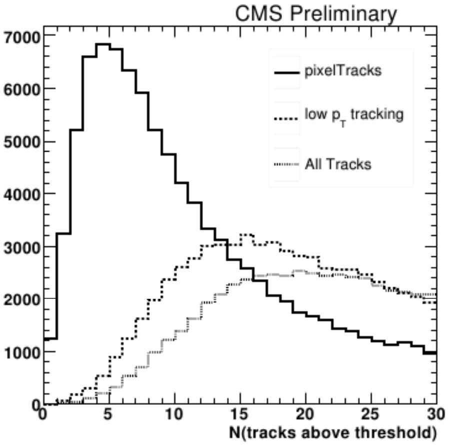

Figure 8.12: Number of tracks above threshold for Drell-Yan events at generator-level (dotted line) and after reconstruction with two different track algorithms [5]. The figure compares the default (`PixelTrack`, full line) and the dedicated (`low` p_T `Track`, dashed line) algorithms. The number of reconstructed tracks yielded by the `low` p_T `Track` algorithm is closer to the true number, leading to a better background rejection.

8.3.3 Results for signal, reducible and irreducible backgrounds

Tab.8.4 summarises the cumulative efficiency of all the cuts on $\gamma\gamma \to \mu^+\mu^-$ signal events, on major reducible backgrounds and irreducible singly inelastic $\mu^+\mu^-$ final states.

After all the cuts, no event from the reducible background remains from the large sample available. An upper limit is computed at 95% CL for the selection efficiency on these reducible backgrounds. The rejection is very high for all of them. As the DY events from the large CSA07 sample are lower-bounded at $M_{\ell^+\ell^-} > 10$ GeV, the statistics for the DY$_1$ sample ($6 < M_{\ell^+\ell^-} < 10$) is only based on private productions and is much smaller. Subsequently, the upper limit on this mass bin is by far larger. However, a similar reduction as for the other DY samples is expected, keeping all reducible backgrounds to negligible values.

With respect to the number of events passing the triggers, 95.4% of the signal and 45.8% of the singly inelastic events are selected. Taking into account the triggers and the selection, the *visible cross-section* for those samples are summarised in Tab. 8.5.

	$\mu\mu$	**inel**	**DY$_1$**	**DY$_2$**	**DY$_3$**
$\|\Delta\phi\| >$ 2.9	99.9	57.8	10.1	23.9	53.5
$\|\Delta p_T\| <$ 2.0 GeV	99.8	49.4	7.9	10.9	10.6
N(towers) $<$ 5	99.8	47.6	< 7.0	< 0.26	< 0.14
N(tracks) $<$ 3	95.4	45.8	< 3.5	< 0.16	< 0.14

Table 8.4: Cumulative efficiency of the analysis cuts for dimuon signal ($\gamma\gamma \to \mu^+\mu^-$ elastic), for major reducible (DY) and irreducible backgrounds ($\gamma\gamma \to \mu^+\mu^-$ inelastic), after trigger. The upper limits comply with a 95% CL limit, and are due to the lack of statistics. The three Drell-Yan event samples covers the following invariant mass ranges (in GeV): DY$_1$: $6 < M_{\ell^+\ell^-} < 10$, DY$_2$: $10 < M_{\ell^+\ell^-} < 40$ and DY$_3$: $40 < M_{\ell^+\ell^-}$. The two DY samples with the highest invariant mass bins (DY$_2$ and DY$_3$) have far more statistics than the first sample, explaining the difference on limit. Finally, the single inelastic cross-section carries a theoretical uncertainty of 20 %.

	$\mu\mu$	**inel**	**DY$_1$**	**DY$_2$**	**DY$_3$**	$\boldsymbol{\Upsilon}$
σ (pb)	74.7	76.2	$18,910$	2976	899	62
N (events)	100k	20k	96.6k	3M	3M	16k
ϵ_{trig} (%)	10.0	18.3	0.1	4.8	9.7	8.5
ϵ_{sel} (%)	95.4	45.8	< 3.5	< 0.16	< 0.14	95.0
σ_{vis} (pb)	7.09	6.38	< 0.59	< 0.003	< 0.001	5.02

Table 8.5: Summary of the dimuon analysis, for signal and major backgrounds: production cross-section (σ), number of generated events (N), efficiencies for triggers (L1+HLT, ϵ_{trig}) and selection (ϵ_{sel}), and visible cross-section (σ_{vis}). Samples labelled as $\mu^+\mu^-$ and "inel" refers to elastic and inelastic $\gamma\gamma \to \mu^+\mu^-$ processes, respectively. The three Drell-Yan event samples covers the following invariant mass ranges (in GeV): DY$_1$: $6 < M_{\ell^+\ell^-} < 10$, DY$_2$: $10 < M_{\ell^+\ell^-} < 40$ and DY$_3$: $40 < M_{\ell^+\ell^-}$. The Υ sample gathers all the numbers for $\Upsilon(1S + 2S + 3S)$ events. Other background events are negligible. The upper limits comply with a 95% CL limit.

8.3.4 Systematic uncertainties on dimuon selection

The main sources of systematic uncertainties are expected to come from the lepton reconstruction efficiency, the amount of inelastic background events and the calorimetric exclusivity.

Calorimetric exclusivity

The calorimetric exclusivity condition is affected by both the energy scale, related to the detector calibration, and the inherent detector noise. Similarly to studies on the missing transverse energy reconstruction in CMS [148], the impact of dead and noisy calorimetric channels (ECAL and HCAL) has been investigated, using the `CaloMiscalibTooks` package in CMSSW.

Dead channels are defined as channels with no output signal. The output of *noisy channels* is enhanced by a factor of 5. Several scenarios have been tested, with 1%, 3%, 5% of dead channels, 1%, 3%, 5% of noisy channels, and 2.5% + 2.5% of both in a mixed case. These channels are selected randomly. Tab. 8.6 and 8.7 summarise this study.

Scenario		**ECAL barrel**	**ECAL endcap**	**HCAL**
dead	1%	610	200	81
	3%	1845	590	266
	5%	2992	1025	484
hot	1%	588	184	100
	3%	1882	603	251
	5%	3039	962	424
mix 2.5 + 2.5%		3073	1019	429

Table 8.6: Number of affected calorimeter channels, corresponding to the assumed scenario, for the study of the detector effects, on signal samples. These channels are selected randomly.

Affected channels	**dead**	**noisy**
1%	−0%	−2%
3%	−0%	−30%
5%	−0%	−70%
2.5% + 2.5%	−30%	

Table 8.7: Systematic errors on $\mu^+\mu^-$ analysis from calorimeter exclusivity. Signal loss in percent for several scenarios of disabled (dead) or enhanced (noisy) calorimetric cells. Channels masking prevents in real conditions from having a scenario as extreme as 5% of noisy calorimetric cells.

As expected, adding dead channels in the calorimeter reinforces the exclusivity condition and has no impact on the signal selection. On the other hand, this condition is highly sensitive to the presence of unmasked noisy channels in the calorimeters.

Adding few enhanced channels directly increases the number of reconstructed towers in the event, preventing the signal events from being selected, as it effectively breaks the calorimetric exclusivity requirements (Fig. 8.13). The impact on signal selection can be large. However, from the detector experience and pedestal measurements during *empty* events, some channels can be identified as *noisy*, and be masked accordingly.

Tracking data could also serve to discriminate the noisy calorimetric channels, or at worse, be used as the only exclusivity requirement for $|\eta| < 2.5$. Similarly, additional tracking data are provided by TOTEM T1 in the $3 \leq |\eta| \leq 5$ range.

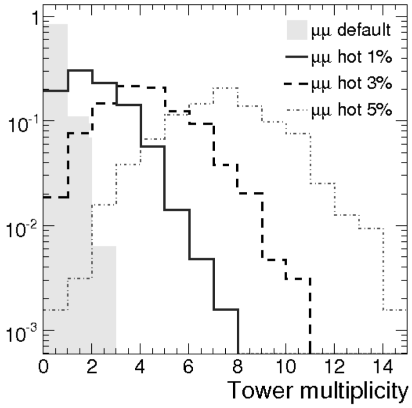

Figure 8.13: Impact on the dimuon selection on signal events of the presence of noisy channels in the calorimeters. The number of calotowers increases significantly above the threshold, leading to a major signal loss. This graph is normalised to unity.

Sensitivity on muon p_T

The strong dependence of the cross-section on muon p_T makes the final selection sensitive to any contribution that would decrease the real efficiency for low p_T. In order to model this possible inefficiency at trigger level, muons with a transverse momentum below 10 GeV are tempered by a moderation function depicted in Fig. 8.14. This function ranges from 85% to 100%, for p_T from 2.5 to 10 GeV. The impact on online selection is a loss of 3% of the signal, which can not be prevented by adding on a repetition of the p_T cut at the analysis level.

This extra offline cut ($p_T > 3$ GeV or higher) is still desirable to be safe with respect to the p_T reconstruction inaccuracy of the trigger. This requirement hardly changes the overall selection efficiency ($\epsilon_{\text{sel}}^{\mu\mu} = 94.7\%$) but makes explicit the dependence on the miscalibration of p_T scales. This systematic error has an expected effect on final selection as weak as 0.25%, for a 1% scale error[4] on p_T:

p_T rescale factor	0.95	0.99	1.01	1.05
Signal variation (%)	-1.47	-0.23	$+0.26$	$+0.88$

Singly inelastic background selection efficiency also remains within 1%. Moreover, it is possible to set an absolute p_T calibration for on low p_T muons by measuring the dimuon decay of an Υ meson.

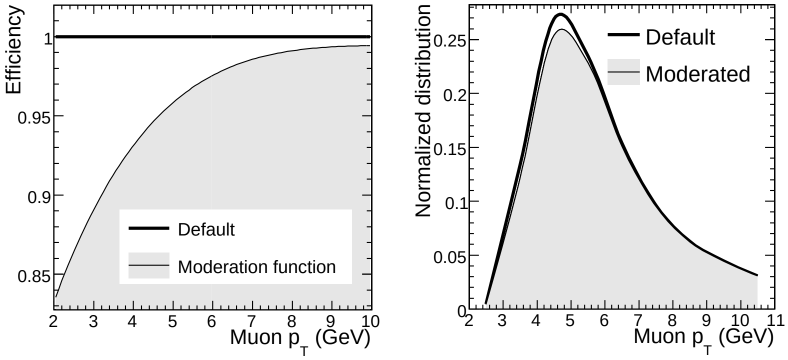

Figure 8.14: Impact of an additional selection inefficiency for p_T below 10 GeV. Left: Moderation function (grey area), ranging from $p_T = 2$ GeV to $p_T = 10$ GeV. Right: Impact of the application of this function to the trigger, leading to a loss of 3% of the signal. These graphs are normalised to unity.

Other sources of systematic errors

Besides these sources of systematic uncertainties, the relative misalignment of subdetectors could also broaden the distributions of p_T and ϕ, leading to a less effective selection than simulated.

The impact of the theoretical uncertainty on the fragmentation of protons in inelastic events could also be important, as quoted earlier. Solutions for the reduction of the inelastic content of the observed sample are presented in the next chapter.

The errors coming from the tracking exclusivity are already negligible with the default tracking algorithm. The application of the algorithm dedicated to low-p_T tracks would decrease these systematic errors even more.

---

[4] This assumption is conservative according to [71].

Finally, double dissociative events has not been taken into account in this study. From the experience of singly inelastic events, it is expected that a large fraction of double dissociative events pass the triggers (mainly due to the p_T cut), but that the analysis selection efficiency is significantly lower than for elastic events. The Δp_T and $\Delta\phi$ distribution are expected to be much flatter than for the elastic case.

8.4 Exclusive dielectron analysis

The dielectron analysis is in many points similar to the dimuon one, with kinematic cuts and exclusivity requirements. On the other hand, the $pp(\gamma\gamma \to e^+e^-)pp$ events are selected by a dedicated exclusive dielectron Level-1 trigger and a corresponding HLT path (Fig. 8.17).

8.4.1 Online selection of $\gamma\gamma \to e^+e^-$

The production of an electron-positron pair via photon-photon interaction, $\gamma\gamma \to e^+e^-$, is quite different from the corresponding $\mu^+\mu^-$ production, from the experimental point of view. Whilst muons leave a very clear signature in the detector, electrons require a more advanced reconstruction for their identification. The kinematics of these events, as shown in Fig. 8.2, is also driven by the E_T dependence of the cross-section, as the transverse energy is the limiting variable for the trigger definition. The default double isolated electron-gamma (in short, di-iso e/γ) L1 trigger has a E_T threshold at 8 GeV, and let pass only 1.47 pb of the events of interest.

The strategy to improve the selection at L1 is then to decrease the E_T cut on electron candidates. But then, the HLT input stage could face an overwhelming flow of data if no new rejection mechanism is introduced[5]. The solution is to introduce new requirements on the selected events, in this case in terms of *exclusivity*. The ideal $\gamma\gamma \to e^+e^-$ event has only two electrons in the central detector, and possibly the scattered protons p seen in the VFDs. Similarly to muon pairs, the electron pairs are balanced in ϕ and p_T (Fig. 8.3 and 8.4). Hence, the trigger scheme could rely on the exclusivity (i.e. the fact that only two electrons are present in the central detector), on the tight equality of their transverse momentum, and on their perfect alignment in the transverse plane. The improvements in selection efficiency obtained by the definition of a new *Exclusive Double Isolated EGamma* Level-1 trigger bit are detailed here below.

Level-1 trigger At L1, the exclusivity condition is precisely used in unison with a lower E_T threshold, in order to keep the trigger bit output rate to reasonable values, and to improve the signal selection efficiency. The approach

---

[5] One should remember that collisions produce most of the time soft QCD interactions, with a lot of low energy and low E_T particles. Lowering the trigger thresholds leads to increasing the trigger output rate.

relies on counting the number of electron candidates in the event, which is naively equal to two. At L1, electrons and photons can not be distinguished from each other. Moreover, it is required here that the candidate are separated from other detected particles, making them *isolated*. These are referred here to iso-e/γ candidates. Here are the key elements leading to the definition of a new L1 trigger bit for $\gamma\gamma \rightarrow e^+e^-$ events.

- **From e/γ counter to jet counter.** The use of dedicated electronics for Level-1 trigger forces to use only a predefined set of quantities for the definition of trigger bits. In particular, there is no e/γ counter available at L1, but only jet counters. Fortunately, the Global Calorimeter Trigger identifies e/γ candidates as jets, i.e. the e/γ objects always correspond to some jet candidates in the same (η, ϕ) direction. These jets will be called e/γ-jets from here onwards. e/γ candidates and e/γ-jets are matched if $\Delta R = \sqrt{\Delta\eta^2 + \Delta\phi^2} < 0.3$.

- **Jet energy correction** The definition of jet counters depends on the lowest achievable jet E_T, which is 10 GeV. Even the electrons considered here have E_T cuts below 8 GeV, the jet E_T cut is not problematic, thanks to the jet energy correction factors. These factors calibrate the jet energy scale at L1, via look-up tables. They are obviously meant for true jets, and the look-up tables are established accordingly. A consequence of the application of these calibration constants on e/γ-jets is that their reconstructed value is approximately twice their true value (FIG. 8.15). In other terms, an e/γ-jet with a true E_T of 6 GeV at generator level is reconstructed with 12 GeV, which is above the $E_T = 10$ GeV threshold of the jet counter. In conclusion, e/γ-jet E_T is systematically over-estimated at L1, allowing a safe use of jet counters for the exclusivity requirement.

- **Two e/γ candidates, or more.** Once the exclusivity is set to prevent rates from exploding, the E_T cut on e/γ candidate can be lowered. A transverse energy E_T of 5 or 6 GeV reaches the minimal achievable values for e/γ observation and reconstruction in CMS. However, for the new trigger definition, it is not safe to stick to an additional "only two e/γ candidates above 6 GeV" requirement. Indeed, due to the intense magnetic field in CMS, the probability for a bremsstrahlung emission is quite large, and the reconstruction of e/γ candidates at L1 does not take this effect into account. A consequence is that dielectrons often have additional photons in the final state. So the requirement on e/γ candidates is to count at least two of them.

- **Final algorithm.** In summary, the new L1 trigger bit dedicated to $\gamma\gamma \rightarrow e^+e^-$ processes should require an exclusivity condition, in terms of jet counters, and a E_T threshold applied on e/γ candidates:

  `L1_ExclusiveDoubleIsoEG6` : (`JetCounts`$=2$) AND `DoubleIsoEG6` where `JetCounts` is the number of jets seen with $|\eta| < 5$ and $E_T \geq 10$ GeV, and `DoubleIsoEG6` requires to have at least two isolated e/γ candidates passing a $E_T = 6$ GeV threshold.

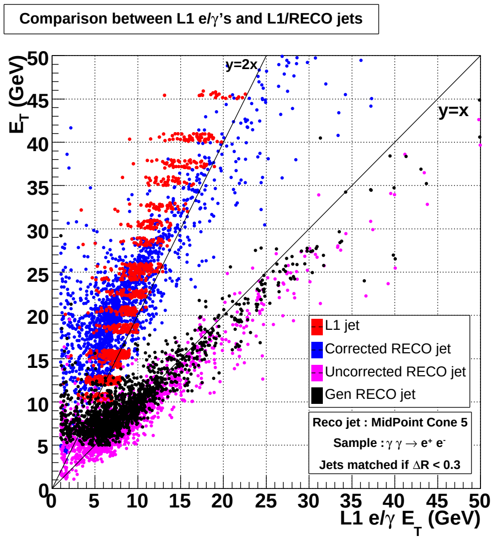

Figure 8.15: Effects of the energy correction factors of L1 jet algorithms on the reconstructed transverse energy E_T. The reconstructed jets at L1 should be rescaled with calibration constants, which make the E_T of corrected RECO jets more similar to the real E_T than uncorrected ones. This recalibration takes into account the losses in the energy measurement due for instance to the fragmentation (high multiplicity of low energy particles in the jet). However, the reconstruction of fake jets originating in e/γ, called here e/γ-jets, is already quite good before correction (*uncorrected* RECO *jet*, pink dots), compared to the particles at generator level (*Gen* RECO *jet*, black dots). The application of the calibration factors makes the E_T of *corrected* RECO e/γ*-jets* (red dots) twice bigger as it really is. The visible steps unveil the application of the look-up tables. Based on $\gamma\gamma \to e^+e^-$ events. Jets are matched with the e/γ if at a distance of $\Delta R < 0.3$. The reconstruction is based on MidPoint Cone jet algorithm, with a radius $R = 5$.

To be satisfactory, the new trigger bit should (i) increase the signal selection efficiency at L1 and (ii) have a low additional rate. The additional rate is evaluated by running on 3.2×10^6 minimum bias events (mostly soft QCD). This was the standard procedure for the trigger validation in CMSSW_1_6_0. The corresponding rate study is depicted in FIG. 8.16 and summarised in TAB. 8.8. The new trigger bit complies with both rate and efficiency requirements.

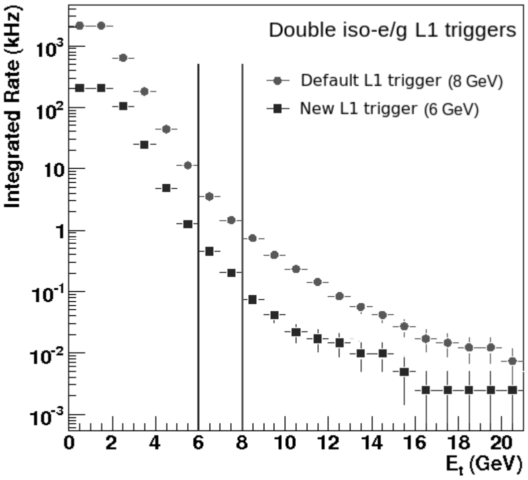

Figure 8.16: Rate study for L1 dilepton trigger. The new exclusive di-e/γ trigger (squares) has a rate at $E_T > 6$ GeV similar to the default di-e/γ trigger (circles), with $E_T > 8$ GeV.

Trigger bit name	$E_T^{\mathbf{thr}}$	**Rate (kHz)**	**Signal eff.**
`L1_DoubleIsoEG8` (default)	8 GeV	0.732 ± 0.042	1.47 pb
`L1_ExclusiveDoubleIsoEG6`	6 GeV	0.448 ± 0.033	2.39 pb

Table 8.8: Rates and selection for double e/γ L1 triggers. The trigger output rate is based on 3.2×10^6 minimum bias events and the signal selection efficiency on $10,000$ $\gamma\gamma \to e^+e^-$ processes.

High Level trigger Correspondingly to the new L1 trigger bit, a new HLT path has been written (`CandHLT2ElectronExclusive`).

First, this path collects the two L1 isolated e/γ candidates, repeats the transverse energy cut ($E_T > 6.0$ GeV), checks their balance $|\Delta E_T| \leq 10.0$ GeV and performs a filtering based on the acoplanarity ($|\Delta\phi| \leq 0.6$).

Secondly, the isolation based on HCAL data is checked, for both HB and HE, asking for the energy sum within a cone ($\Delta R < 0.15$) to be less than 9 GeV. Tracking data are exploited by requiring first two reconstructed tracks of electrons in the pixels; and the isolation of each electron based on tracking data – i.e. there should not be any track with a $p_T > 0.4$ GeV too close from each e candidates (2-sided cone $0.02 < \Delta R < 0.2$). Tab. 8.9 summarises the two trigger selection for the selection of $\gamma\gamma \to e^+e^-$ events.

Level	**Name**	**Package**
L1	`L1_ExclusiveDoubleIsoEG6`	`L1Menu2007.xml`
	Exactly two jets and at least two electrons with $p_T^e \geq 6$ GeV	
HLT	`CandHLT2ElectronExclusive`	`DoubleExclusiveElectronL1Isolated`
	E_T and ϕ balance, HCAL isolation, pixel matching and track isolation	

Table 8.9: L1+HLT trigger path for dimuon events, with the corresponding package name in CMSSW and the set of conditions defining the triggers.

8.4.2 Offline analysis

From all the events, only 0.738 pb will be available for the offline analysis, in spite of the very large production cross-section (7.1 mb without cuts). Most of this reduction is due to the 6 GeV p_T cut applied at Level-1, which already hits the lowest reasonable value for electron reconstruction in CMS. An analysis similar to the dimuon one is developed here for the selection of elastic dielectrons.

The electron candidates are selected using the `pixelMatchGSFElectrons` list. The candidates are seeded by pixel hits and matched to a super cluster in the ECAL. The electron track is fit with a Gaussian Sum Filter, designed to take into account the possible bremsstrahlung. From the triggered events, 94.7% comply with the extra requirement of exactly two opposite sign electrons. On this preselected sample, kinematics cuts and exclusivity conditions, similar to those for the muon analysis, are applied. As low p_T electrons are not as well-reconstructed as the muons, the kinematic cuts are looser. The distribution of the number of calotowers and of the tracks is similar to the dimuon case. The impact of all selection cuts is visible in Fig. 8.18 and 8.19, and summarised in Tab. 8.10 and 8.11.

The acoplanarity between both electron candidates ($\Delta\phi(ee)$) should be higher than 2.7, transverse energy balance ΔE_T better than 5 GeV. For the

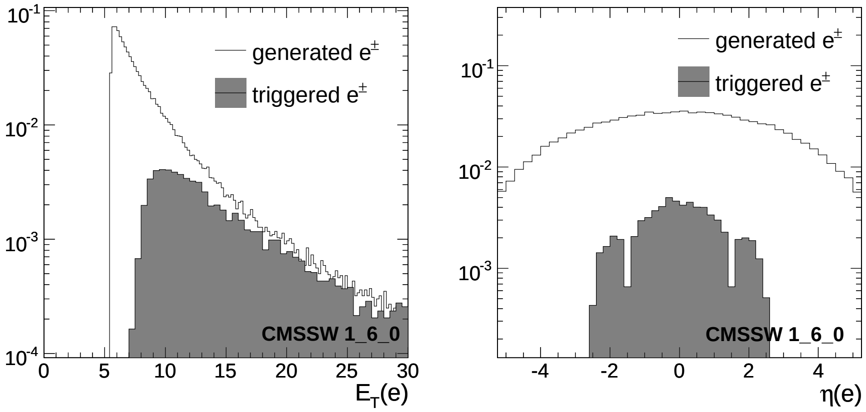

Figure 8.17: Reduction due to the application of trigger conditions on the electron signal samples. p_T (left) and η (right) spectra for $\gamma\gamma \to e^+e^-$ and the reducible backgrounds [5]. The reduction is due to both the p_T cut of the trigger and the η coverage of the tracker. The selection inefficiency around $|\eta| \approx 1.5$ corresponds to the transitions between the barrel and the endcaps. Two entries per event. Generator-level histograms are normalised to unity.

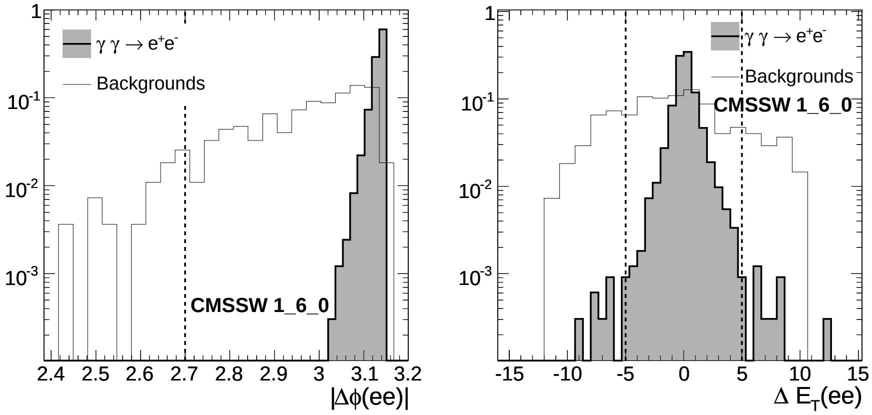

Figure 8.18: Distributions of $|\Delta\phi|$ and $|\Delta E_T|$ for elastic $\gamma\gamma \to e^+e^-$ signal and reducible background. The reduction power is illustrated by the vertical dashed line, symbolising the cut value. All histograms are normalised to unity.

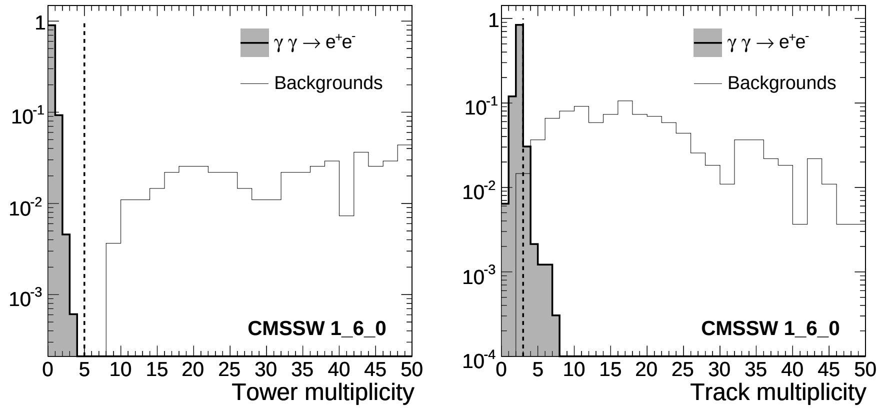

Figure 8.19: Application of the exclusivity conditions (*left:* calorimetric, *right:* tracker) on the elastic $\gamma\gamma \to e^+e^-$ signal and the reducible backgrounds [5].

	e^+e^-	**inel**	$\mathbf{DY}_2$	$\mathbf{DY}_3$
$\lvert\Delta\phi\rvert > 2.7$	99.9	97.5	87.2	93.6
$\lvert\Delta E_T\rvert < 5.0$ GeV	99.3	91.3	71.8	60.3
N(towers)< 5	99.3	91.2	33.3	27.4
N(tracks)< 3	95.7	86.9	< 7.6	< 1.2

Table 8.10: Cumulative efficiency of the analysis cuts for dielectron signal ($\gamma\gamma \to e^+e^-$ elastic), for major reducible (DY) and irreducible backgrounds ($\gamma\gamma \to e^+e^-$ inelastic), after trigger. The upper limits comply with a 95% CL limit, and are due to the lack of statistics as none of these events survives from the selection. The two DY samples with the highest invariant mass bins (DY_2 and DY_3) have far more statistics than the first sample, for which no event is selected by the trigger.

	$\mathbf{e^+e^-}$	**inel**	$\mathbf{DY_1}$	$\mathbf{DY_2}$	$\mathbf{DY_3}$
σ (pb)	10.4	13.6	$18,910$	2976	899
N (events)	100k	20k	96.6k	3M	3M
ϵ_{trig} (%)	7.1	7.3	< 0.003	0.1	1.1
ϵ_{sel} (%)	90.7	82.4	–	< 7.3	< 1.2
σ_{vis} (pb)	0.67	0.82	< 0.59	< 0.003	< 0.001

Table 8.11: Summary of the dielectron analysis, for signal and major backgrounds, with the production cross-section (σ), the number of generated events (N), the efficiencies for triggers (L1+HLT, ϵ_{trig}) and selection (ϵ_{sel}, including the preselection step), and finally the corresponding visible cross-section (σ_{vis}). Samples labelled as e^+e^- and "inel" refers to elastic and inelastic $\gamma\gamma \to \mu^+\mu^-$ processes, respectively. The three Drell-Yan event samples covers the following invariant mass ranges (in GeV): $\text{DY}_1 : 6 < M_{\ell^+\ell^-} < 10$, $\text{DY}_2 : 10 < M_{\ell^+\ell^-} < 40$ and $\text{DY}_3 : 40 < M_{\ell^+\ell^-}$. The upper limits comply with a 95% CL limit.

exclusivity, the number of extra calorimetric towers should be smaller than 5 (rejecting towers closer than 0.3 in $R = \sqrt{\Delta\eta^2 + \Delta\phi^2}$ from any of the two leptons, or with an energy below 5 GeV); it is also required that the number of tracks in the event should be less than 3.

The systematic uncertainties are similar to those in the dimuon channels. However, the impact of dead channels now decreases also the signal selection (Tab. 8.12). This effect is understandable, as the electron reconstruction is based on calorimetric data, while it is not the case for muons. A scenario with 5% of dead cells leads to a signal loss up to 4.7% and noisy channels have a similar impact as for muon selection.

Affected channels	**dead**
1%	−1.3%
3%	−4.0%
5%	−4.7%
2.5% + 2.5%	−30%

Table 8.12: Systematic errors on e^+e^- analysis from calorimeter exclusivity. Signal loss in percent for several scenarios of disabled (dead) calorimetric cells. Noisy scenarios provide the same results as for dimuons, as illustrated for the mixed (2.5% + 2.5%) case.

8.5 Conclusion and discussion

The observation of exclusive dimuons and dielectrons are considered here, via a two-photon exchange. Event kinematics is characterised by the exclusive presence of two back-to-back leptons in the final state. Leptons have opposite charges and same flavour.

Dimuons are easily selected at low luminosity by the default trigger paths. An efficient selection of the dielectron final states required the development of a new L1+HLT path.

The offline selection of these exclusive lepton pairs relies on two types of requirements: (1) kinematic constraints, testing the balance in transverse momentum and in acoplanarity; (2) exclusivity requirements, vetoing events with too large activities in the tracker or the calorimeters. Several sources of systematic uncertainties are investigated, mainly concerning the calorimetric noisy and dead channels, and the inefficiency of low p_T measurements.

Exclusive dileptons have several applications, as detailed in the next chapter: they provide an efficient way to measure the integrated luminosity in a low pile-up environment, i.e. at the LHC start-up. Calibration of forward detectors is also possible. As the luminosity increases, the level of pile-up also reaches higher values. The exclusivity requirements have to be updated, for instance by looking at the association between calorimetric towers and tracks pointing to a secondary vertex.

Chapter 9

Luminosity measurement and other applications

The accurate cross-section for exclusive production of dileptons make these events ideal for a precise measurement of the absolute luminosity, already for the early LHC *data. This is a major application of the dilepton analyses. The precise reconstruction of the final state lepton pair, coupled to a forward proton tagging, allows a calibration of the very forward detectors, against effects like the beamline misalignment. The exclusive dilepton analysis has been approved by the* CMS *collaboration [5] and the corresponding results are labelled accordingly. The beamline misalignment studies [13] have been presented in several international workshops [12]. The study of the calibration of the* VFDs *with exclusive dileptons is an update with full simulation of preliminary generator-level results [21].*

9.1 Exclusive dileptons at low luminosity

9.1.1 Results for the dimuons

The significant yield of exclusive muon pairs, the simple selection and the good theoretical knowledge of their cross-section make them a good candidate for absolute luminosity normalisation. They bring data complementary to the luminosity measurement using the inclusive productions of W and Z bosons [145].

On the one hand, the theoretical uncertainty on the production of exclusive dileptons is low ($\mathcal{O}(1\%)$ [10]), but their online selection needs some precautions, due to their low transverse energy/momentum.

On the other hand, the less known inclusive production of Z and W yields easily triggered final states. Exclusive dileptons are especially good candidates for luminosity normalisation in an environment with low event pile-up.

The integrated luminosity measurement depends on the number of observed events (N_{obs}), and on the estimated number of remaining background events (N_{bkg}).

TAB. 8.4 summarises the cumulative efficiency of all the cuts on $\gamma\gamma \to \mu^+\mu^-$ signal events, on reducible backgrounds and irreducible singly inelastic $\mu^+\mu^-$ final states. After all the cuts, no event from the reducible background remains from the large sample available. 95.4% of the signal and 45.8% of the singly inelastic events passing the trigger are selected. As an illustration, after an integrated luminosity of L = 100 pb^{-1}, the numbers of observed events for elastic and inelastic production of dimuons are expected to be the following ones:

$$\begin{aligned} N_{elastic}(\gamma\gamma \to \mu^+\mu^-) &= 709 \pm 27(stat) \pm 7(th) \\ N_{elastic}(\gamma p \to \Upsilon p \to \mu^+\mu^- p) &= 502 \pm 22(stat)^{+20}_{-150}(model) \\ N_{inelastic}(\gamma\gamma \to \mu^+\mu^-) &= 636 \pm 25(stat) \pm 121(model) \end{aligned} \tag{9.1}$$

The statistical errors are given by variance of the Poisson distribution ($\sqrt{N}$). Precision measurement of the integrated luminosity relies on a good theoretical understanding, making only elastic $\gamma\gamma \to \mu^+\mu^-$ events suitable for such an application. On the contrary, models for Υ photoproduction and inelastic $\gamma\gamma \to \mu^+\mu^-$ processes predict cross-sections with large uncertainties (referred to as *model errors*). In conclusion, these have to be removed from the observed sample for a precise determination of the absolute luminosity L, based on exclusive muon pairs.

Diffractive photoproduction of Υ mesons. First of all, the Υ dimuon decays are easily handled as the narrowness of the resonances allows a simple cut on the dimuon invariant mass to reject all these events. The application of an additional cut on the selected events, referred to as the $\Upsilon -$ *veto*, allows a rejection of almost 100% of these events:

$$\Upsilon - \text{veto}: \quad M_{\mu\mu} < 9 \text{ GeV } \texttt{OR } M_{\mu\mu} > 11 \text{ GeV}. \tag{9.2}$$

This [9 GeV; 11 GeV] interval covers the range of masses for the Υ ($1S$), ($2S$) and ($3S$) (with M_Υ from 9.4 to 10.3 GeV), including some detector effects.

Inelastic events. Secondly, the contamination of the final selected sample by the two-photon inelastic events is high. The cross-section for singly inelastic events is similar to the elastics one (σ_{inel} = 76.2 pb and σ_{el} = 74.7 pb, for $p_T > 2.5$ GeV at $\sqrt{s} = 14$ TeV), but is poorly known ($\Delta\sigma/\sigma \approx 20\%$). The cross-section prediction depends on the parton density function, the fragmentation function and the assumed cut on the mass of the dissociative system (M_Y). Following the example of TEVATRON measurement [35], a 19% correction is applied on the final number as a model error.

The rejection of inelastic dimuon events by the exclusivity requirements is not efficient, as the dissociative system of the proton is very forward according to the simulations.

Two possibilities are available to disentangle this irreducible background from signal: (1) fitting the shape of the acoplanarity and transverse momentum distributions, and (2) using the forward detector information. Solution (1) is illustrated in Fig. 9.1 (and 9.3 for dielectrons): the inelastic component is much broader than the elastic contribution, which is peaked to the most balanced values. The potential of solution (2) is depicted in Fig. 1.7: the η distribution of the most central particle of a proton dissociative system is superimposed on the acceptance of the CASTOR and ZDC forward calorimeters. It shows that many dissociative systems from inelastic events lead to particles visible in the forward calorimeters. This requirement is referred to as the *forward calorimeter veto*. Both solutions (1) and (2) are discussed in detail later in this chapter.

Distributions for signal and background events. The final invariant mass distribution for dimuons after all selection cuts is shown in Fig. 9.2. The different components (elastics, inelastics, Υ) are visible, as well as the impact of the forward calorimeter veto.

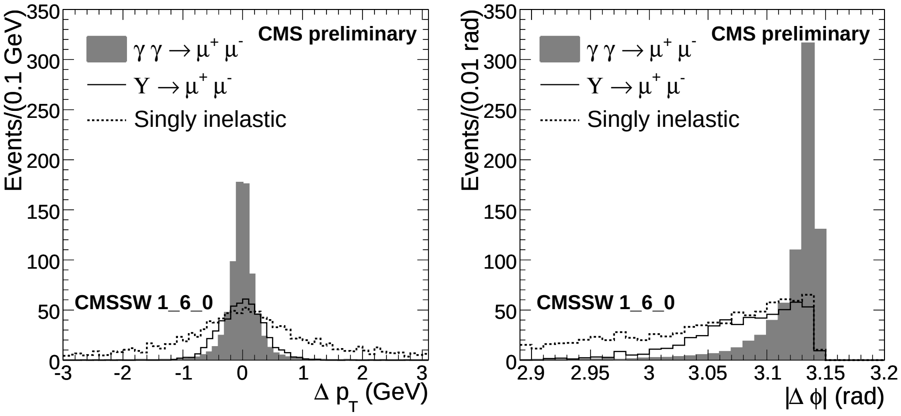

Figure 9.1: Δp_T and $\Delta\phi$ for events passing all the selection requirements, including the $\gamma\gamma \to \mu^+\mu^-$ signal (elastic events, grey area), the singly inelastic backgrounds (dashed line) and the Υ dimuon decay (plain line). Results of the full analysis in `CMSSW_1_6_0` after $\mathrm{L} = 100\ \mathrm{pb}^{-1}$ at $\sqrt{s} = 14$ TeV [5].

9.1.2 Results for the dielectrons

Trigger and offline selection of dielectrons lead to a very large reduction of the electron sample (Tab. 8.10 and 8.11), where most of the reduction comes from

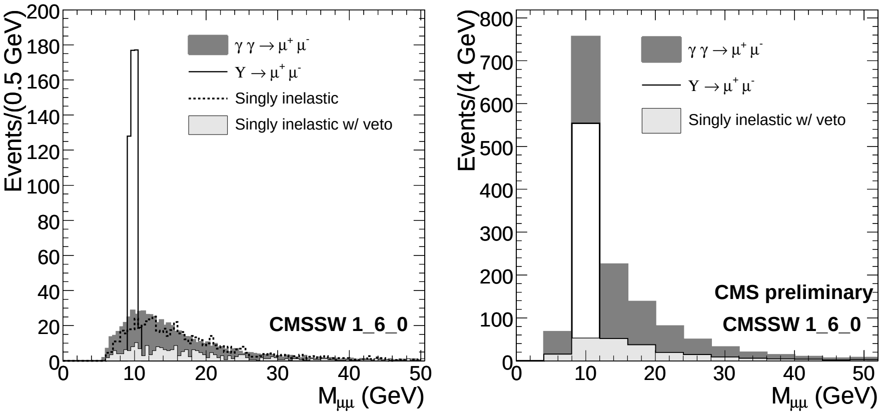

Figure 9.2: Dimuon invariant mass $M_{\mu\mu}$ for events passing all the selection requirements, at $\sqrt{s}$ = 14 TeV [5]. Left: histograms showing the number of expected events after L = 100 pb^{-1}, per 0.5 GeV. The inelastic events are shown both before and after the application of the veto. The grey histogram corresponds to elastic $\gamma\gamma \to \mu^+\mu^-$ events, and the three Υ samples are merged into the black plain line. Right: cumulative histogram after the application of the veto on inelastic events.

the $p_T \geq 6$ GeV cut at trigger level. For $L = 100$ pb^{-1}, the expected numbers of observed events are

$$\begin{aligned} N_{elastic}(\gamma\gamma \to e^+e^-) &= 67 \pm 8(stat) \pm 7(th) \\ N_{inelastic}(\gamma\gamma \to e^+e^-) &= 82 \pm 9(stat) \pm 15(model) \end{aligned} \tag{9.3}$$

The statistical errors are obtained by the Poisson distribution ($\sqrt{N}$). Similarly to dimuons, the theoretical uncertainty is less than 1% for elastic events. On the contrary, the model errors are large for the inelastic cross-section.

The p_T threshold is high enough to prevent any decay of Υ into electrons from being selected but, at the same time, the statistics left is very small. The extraction of inelastic content is similar to the dimuon analysis and the application of the veto based on the forward detectors gives a good reduction:

$$\begin{aligned} N^{w/oveto}_{inelastic}(\gamma\gamma \to e^+e^-) &= 82 \pm 9(stat) \pm 15(model) \\ N^{w/veto}_{inelastic}(\gamma\gamma \to e^+e^-) &= 31 \pm 6(stat) \pm 6(model) \end{aligned} \tag{9.4}$$

Finally, the invariant mass distribution for dielectrons after all selection cuts is shown in Fig. 9.4. The lack of statistics prevents any reasonable fit for inelastic events rejection. Moreover, the statistical error on luminosity is already higher than 10% for a background-free sample. Therefore, exclusive dielectrons can not provide an accurate normalisation of the integrated luminosity below 1 fb^{-1}. However, their measurement is already interesting as probes for low p_T electrons, for monitoring the trigger and to control the reconstruction efficiency.

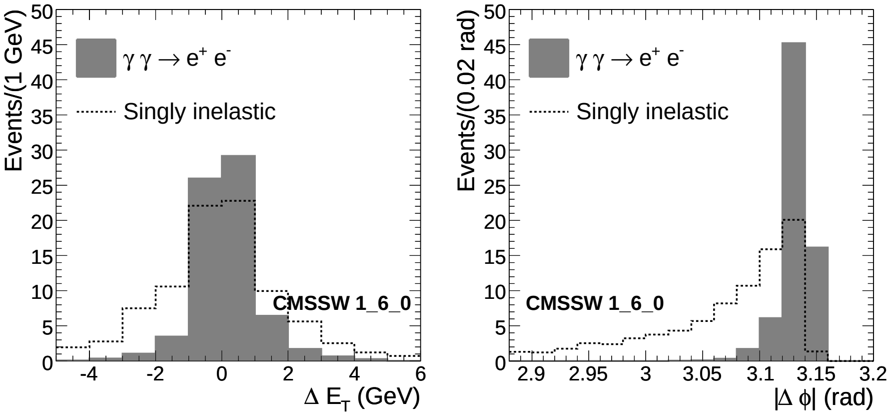

Figure 9.3: Δp_T and $\Delta\phi$ for events passing all the selection requirements, including the $\gamma\gamma \to e^+e^-$ signal (elastic events, grey area) and the singly inelastic backgrounds (dashed line). Results of the full analysis in `CMSSW_1_6_0` after L = 100 pb^{-1} at $\sqrt{s} = 14$ TeV [5].

9.1.3 Contribution from the reducible backgrounds

In spite of the large size of the simulated sample of reducible backgrounds, no such event remains after selection. It is still worth remembering that the tracking exclusivity requirement could be improved by the application of algorithms specific to low p_T tracks (Fig. 8.12). This would reject even more the non-exclusive final states, like those of the Drell-Yan processes, when dealing with real data.

In order to evaluate the impact of the reducible background after a given integrated luminosity, a method similar to the one for the CDF measurement [35] has been applied. A fit to the number of extra calorimeter towers is performed, as some events survive from the selection in the $N > 5$ sideband. This sideband sample is fitted to an exponential distribution $y = a + e^{-bx}$ (Fig. 9.5), in the range of [5; 25] towers. The extrapolation to $N \leq 5$ values gives an estimate of the background. For $L = 100$ pb^{-1}, this extrapolation gives $N_{\mathrm{bkg}} = 38.9 \pm 1.9$ [5]. This number will actually be decreased by the application of the tracking algorithm dedicated to low p_T tracks. Moreover, even if they are not simulated later on, their minor contribution will be taken into account by the fitting technique explained here below.

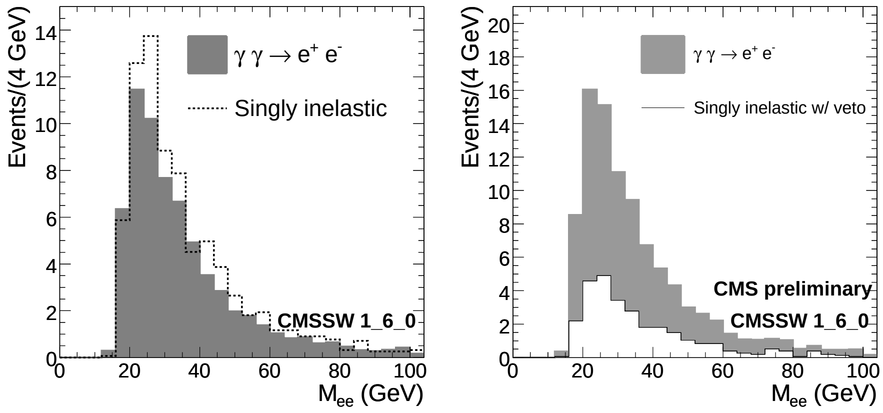

Figure 9.4: Dielectron invariant mass M_{ee} for events passing all the selection requirements, at $\sqrt{s} = 14$ TeV. [5]. Left: histograms showing the number of expected events after L = 100 pb^{-1}, per 4 GeV bin, before the application of the veto on inelastic events. The grey histogram corresponds to elastic $\gamma\gamma \rightarrow e^+e^-$ events. Right: cumulative histogram after the application of the veto on inelastic events.

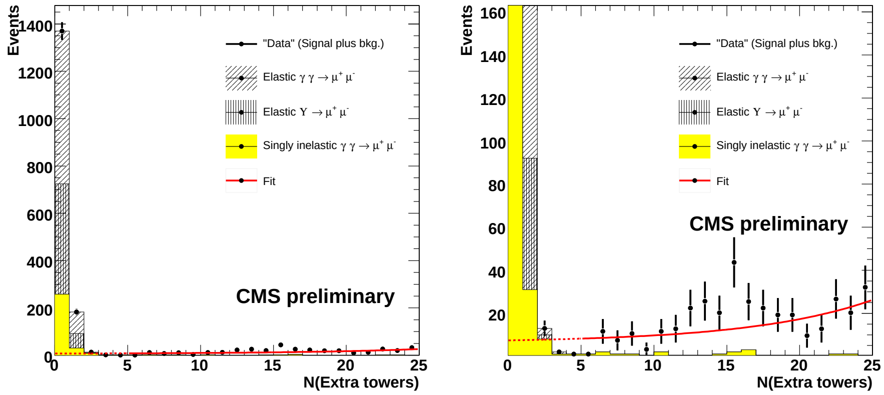

Figure 9.5: Fit to the number of extra calorimetric towers in the side band for the selected events, including all contributions. Numbers are expectation after L = 100 pb^{-1} at $\sqrt{s} = 14$ TeV, after kinematic requirements on Δp_T and $\Delta\phi$ and after tracking exclusivity. Full range (left) and magnified sideband region (right) are shown. Signal and irreducible backgrounds are localised in the lower edge of the distribution, while reducible background events (mostly Drell-Yan) extend to the whole range [5].

9.2 Absolute luminosity measurement using dimuons

The measurement of integrated luminosity with a high precision is possible with exclusive dimuon events [9], using Eq. 9.5:

$$\mathrm{L} = \frac{N_{\mathrm{obs}} - N_{\mathrm{bkg}}}{\epsilon\ \sigma} \tag{9.5}$$

where σ is the signal cross-section and ϵ the corresponding measurement acceptance, which is related to both trigger and selection efficiencies ($\epsilon = \epsilon_{trig} \times \epsilon_{sel}$).

In order to restrict to the region where the reconstruction efficiency is well known, it is required that each muon has a transverse momentum $p_T > 5$ GeV and a pseudorapidity $|\eta| < 2.4$ corresponding to the fiducial region of the muon chambers. It will be shown later that these cuts reduce the systematic uncertainties on L coming from the acceptance term ϵ. The Υ dimuon decays are completely rejected by the application of the Υ-veto. This reduces the number of background events N_{bkg}.

After applying these additional cuts, one expects after $L = 100$ pb^{-1}:

$$\begin{aligned} N_{elastic}(\gamma\gamma \to \mu^+\mu^-) &= 426 \pm 21(stat) \pm 4(th) \\ N_{inelastic}(\gamma\gamma \to \mu^+\mu^-) &= 407 \pm 20(stat) \pm 77(model) \end{aligned} \tag{9.6}$$

The only remaining background events are inelastic ones, while all other sources are negligible.

The major concern in the luminosity measurement (Eq. 9.5) is the proper estimate of the number of background events N_{bkg}, amongst the total number of observed events N_{obs}. Two possibilities are available to disentangle this irreducible background from the signal: (1) fitting the shape of the acoplanarity distribution and (2) using the forward detector information, for stronger vetoing of the inelastic, dissociative events.

9.2.1 Shape analysis

The acoplanarity definition chosen here is $\Delta|\phi| = |\phi_1| - |\phi_2|$. The observed $\Delta\phi$ distribution is the sum of the elastic and inelastic contributions, each with significantly different width. The $dN_{sig}/d\Delta|\phi|$ distribution is well described by a Breit-Wigner function[1], if both muons are detected either in the barrel ($|\eta| < 1.04$) or in the end-caps ($1.04 < |\eta| < 2.4$). Subsequently, as in general the muons are located in either parts of the central detector, the signal fitting function is chosen as a sum of two Breit-Wigner distributions. The use of two Breit-Wigner distributions for the signal reflects the fact that the quality of the muon measurement is better in the detector barrel than in the end-caps [70].

---

[1] Several fitting function were tried, like combination of Gaussian distributions. The solution presented here gives the best results.

Finally, the distribution of all events is described by a sum of three Breit-Wigner terms:

$$\begin{aligned} &\text{Fit (signal term):} \quad S_{fit} = \frac{A_1}{x^2 + (\Gamma_1)^2/4} + \frac{A_2}{x^2 + (\Gamma_2)^2/4} \\ &\text{Fit (all events):} \quad (S+B)_{fit} = A \times S_{fit} + \frac{B}{x^2 + \Gamma^2/4} \end{aligned} \qquad (9.7)$$

The A_i parameters are scaling the distributions vertically while Γ_i control their width. The choice of S_{fit} is justified by a preliminary test on the signal only (Fig. 9.6). For completeness, the distribution is also tested on simulated inelastic samples (Fig. 9.7).

The $\chi^2 -$ fit parameters are shown on the figure, for the reduced $\chi^2/n = 1.339$, in the range $-0.016\pi < \Delta|\phi| < 0.016\pi$. The small number of events implies relatively large bins in the histograms.

In order to extract the number of selected background events N_{bkg}, the fit on all events (signal + background) is adjusted by requiring a sum of three Breit-Wigner distribution $(S+B)_{fit}$, where the parameters of the first two are fixed to the result of S_{fit}; the relative normalisation A is determined by the $(S+B)_{fit}$ (Eq. 9.7). The normalisation of S_{fit} is determined by the fit. This fit, in the $-0.1\pi < \Delta|\phi| < 0.1\pi$ range, is shown in Fig. 9.8, and yields the Γ, A and B parameters ($\chi^2/n = 1.030$). The number of selected background events in the $[-0.016\pi; 0.016\pi]$ range is given by the integral of the second Breit-Wigner distribution B_{fit}:

$$B_{fit} = \frac{B}{x^2 + \Gamma^2/4} \qquad N_{\text{bkg}} = \int_{-0.016\pi}^{+0.016\pi} B_{fit} \times \frac{dw_{bin}}{d|\phi|}\, d|\phi|. \qquad (9.8)$$

with bin width $dw_{bin}/d|\phi| = \text{events}/(0.0025\pi)$.

9.2.2 Forward detector veto

Besides this study, the subtraction of inelastic events could also be partially improved by adding some information from forward calorimeters. Even if a large fraction of the inelastic events have their dissociated proton remnant outside the central detector acceptance ($> 65\%$, Fig. 1.7), a veto could be applied from the forward calorimeters, namely CASTOR and ZDC. The acceptance of these detectors is defined in Chapter 4. Assuming that their detection efficiency is 100% in their η coverage and that, for ZDC, photons with $E > 20$ GeV and neutrons with $E > 50$ GeV are seen, a large fraction of the remaining inelastic events can be rejected:

- 47% of the remaining singly inelastic events shows an activity in ZDC
- adding one CASTOR calorimeter on one side of CMS, this fraction increases up to 58%

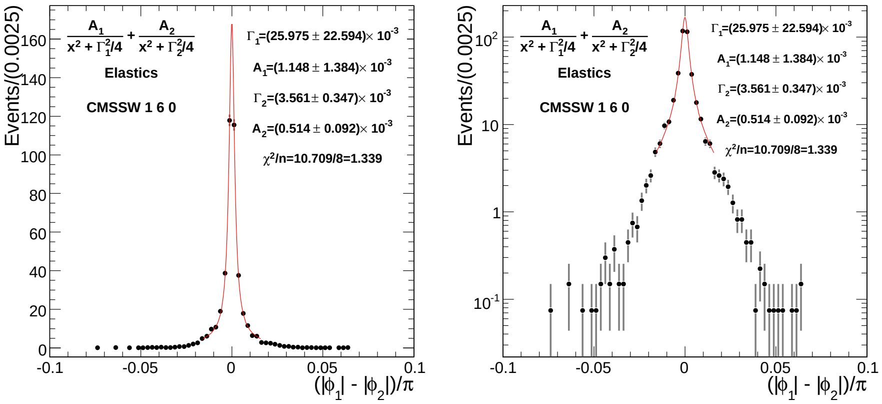

Figure 9.6: Fit of the dimuon acoplanarity $\Delta|\phi|$, for the $\gamma\gamma \to \mu^+\mu^-$ elastic sample, in linear (left) and logarithmic (right) scales. The events are analysed in `CMSSW_1_6_0`. The simulated sample is rescaled to the yield after L = 100 pb^{-1}, after a full offline selection and the application of the Υ veto. Additional kinematic cuts are required at the offline level: $p_T > 5$ GeV and $|\eta| < 2.4$. The χ^2 – fit function S_{fit} in $[-0.016\pi; 0.016\pi]$ has a reduced χ^2 of 1.339. This fit fixes the A_1, A_2, Γ_1 and Γ_2 parameters, used in the fit $(S+B)_{fit}$ of the total number of observed events.

- 68% for two CASTOR calorimeters

The application of such a condition is powerful and could also be complemented by the data from TOTEM detectors, as T1 and T2 are located in front of HF and CASTOR. For $L = 100$ pb^{-1}, the expected numbers of events before and after the application of the second veto (namely, 1 CASTOR + 2 ZDCs) are:

$$\begin{aligned} N^{w/o\ veto}_{inelastic}(\gamma\gamma \to \mu^+\mu^-) &= 407 \pm 20(stat) \pm 77(model) \\ N^{w/\ veto}_{inelastic}(\gamma\gamma \to \mu^+\mu^-) &= 141 \pm 12(stat) \pm 27(model) \quad , \end{aligned} \tag{9.9}$$

assuming, as above, $p_T > 5$ GeV, $|\eta| < 2.4$ and the $\Upsilon - veto$. The fitting procedure described above is also applied to the sample obtained after the forward detector veto.

9.2.3 Systematic errors on luminosity measurement

Several contributions are investigated to estimate the systematic uncertainties on the absolute luminosity measurement:

- **Evaluation of the acceptance term**. The acceptance parameter ϵ is deduced from the simulation and includes the selection efficiencies of the

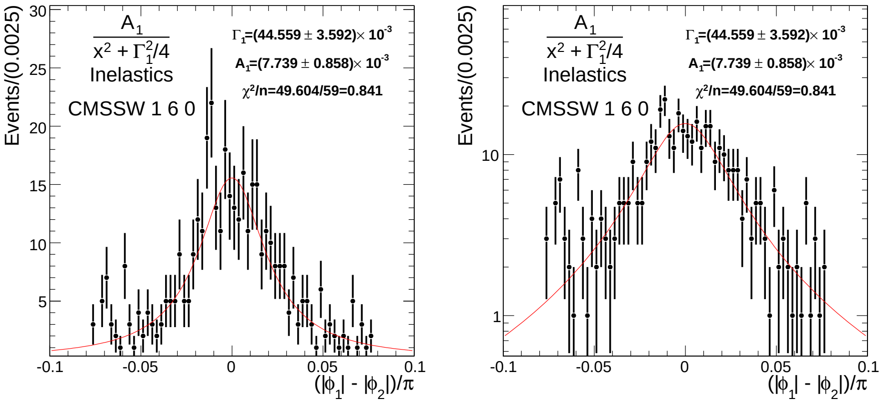

Figure 9.7: Fit of the dimuon acoplanarity $\Delta|\phi|$ for the simulated inelastic exclusive dimuon events, in linear (left) and logarithmic (right) scales. These events are analysed in `CMSSW_1_6_0` after $\mathrm{L} = 100\ \mathrm{pb}^{-1}$, a full offline selection and the application of the Υ veto. Additional kinematic cuts are required at the offline level: $p_T > 5$ GeV and $|\eta| < 2.4$. The χ^2 − fit function $(B)_{fit}$ in $[-0.1\pi; 0.1\pi]$ yields a reduced χ^2 of 0.841. This fit yields the A_1 and Γ_1 parameters, used for cross-checks.

triggers and the offline analysis. Both the trigger and the signal cross-section depend strongly on the muon p_T. The impact of a possible additional inefficiency affecting the muon p_T measurement below 10 GeV is estimated. Less signal (-3%) and inelastic background events (-2%) are triggered when the trigger efficiency curve is significantly modified close to threshold. Inelastic events are less affected as their p_T distribution is flatter than the one of elastic events. This yields an extra $\Delta\epsilon/\epsilon = 3\%$ systematic error to the luminosity measurement. The application of the tighter p_T and η cuts on each muon candidate reduces such errors from the trigger-level reconstruction inefficiencies down to 1.5%. The *in situ* control of this uncertainty can be provided for instance by use of a prescaled sample of single muon triggers at low p_T. Given enough statistics this would allow for determination of the actual trigger efficiency curve. A possibility investigated by the CMS collaboration is to use samples containing inclusively J/Ψ or Υ mesons, decaying into a muon pair. Such events have to be selected by any trigger path, due to other characteristics of the event. Then the real dependence on muon p_T of the muon trigger efficiency can be measured, *a posteriori*. If the integrated luminosity is large enough another solution is to simply apply a higher offline p_T thresholds.

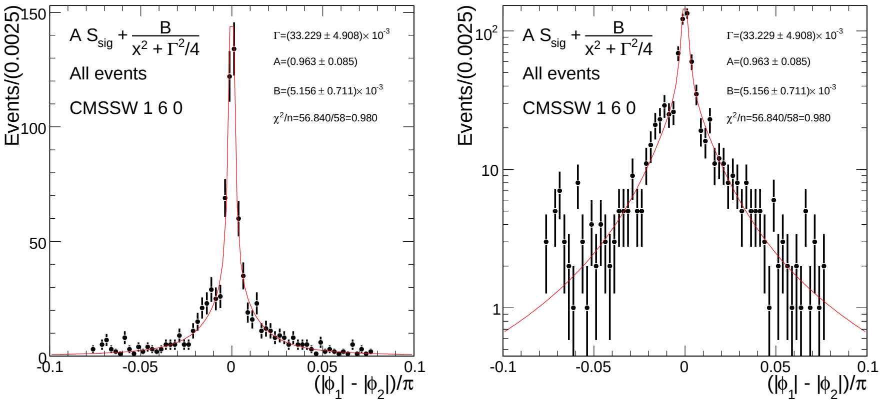

Figure 9.8: Fit of the dimuon acoplanarity $\Delta|\phi|$ for all observed exclusive dimuon events, in linear (left) and logarithmic (right) scales. These events are analysed in `CMSSW_1_6_0` after L = 100 pb^{-1}, a full offline selection and the application of the Υ veto. Additional kinematic cuts are required at the offline level: $p_T > 5$ GeV and $|\eta| < 2.4$. The χ^2-fit function $(S+B)_{fit}$ in $[-0.1\pi; 0.1\pi]$ yields a reduced χ^2 of 0.980. This fit yields the A, B and Γ parameters, used for the estimation of the number of observed background events. The integral of B_{fit} in the $[-0.016\pi; 0.016\pi]$ range gives $N_{\mathrm{bkg}} = 190.0 \pm 23.5$ events.

- **Scale of the transverse momentum** The dependence of the various steps of the event reconstruction depends on the muon transverse momentum p_T. A reasonable systematic error of 1% on the p_T scale changes the signal selection by approximately 0.25%. The muon transverse momentum measurement is also affected by the misalignment of the detector. The dimuon decay of exclusive Υ brings an absolute reference for the p_T scale dependence of the selection, as the dimuon invariant mass $M_{\mu\mu}$ is then very well known [5]. In addition, the reconstructed Upsilon resonance widths give direct information on actual resolution of the muon p_T.

- **Calorimetric exclusivity**. The amount of noisy channels in electromagnetic and hadronic calorimeters could imply that signal events do not satisfy the calorimetric exclusivity condition. However, these will be monitored during zero-bias triggers and abort gaps in the LHC bunch trains. Once identified, the contribution from these cells could be *masked* to avoid to take them into account. In the following, it is assumed that the number of unmasked noisy calorimetric channels do not exceed 1%. According to the study presented in the previous chapter (Tab. 8.7), a 2% uncertainty on the selected events could be expected. In case these assumptions are not valid, the exclusivity requirements could be modified by requiring (1) a tracking exclusivity and (2) rapidity gaps in the HF calorimeters. Such a rapidity gap condition can be set by cutting on the total energy in each HF, for instance [1]. The advantage is that this is less dependent on the number of noisy calorimetric cells.

- **Tracking exclusivity**. The tracking exclusivity requires an upper value for the number of reconstructed tracks in the event. Fake tracks could lead to a rejection of the signal events, but are negligible: the rate of fake tracks with a $p_T > 1$ GeV is at the permille level if a tracking algorithm dedicated to low p_T particles is used [147]. Subsequently, the contribution of tracking exclusivity to the systematic uncertainties on the absolute measurement of luminosity is supposed to be negligible.

- **Acoplanarity fit** In order to evaluate the effects of the uncertainties in the acoplanarity fit, the shape of the fitting function has been varied. Adding a constant term to the fit does not bring any significant change. On the other hand, varying the Γ, B parameters in the $(B+S)_{fit}$ gives some numbers for this kind of uncertainty. Increasing or decreasing the scale factor B by 10% leads to an $\Delta L/L$ relative error below 2%. The width parameter Γ is more sensitive to changes (10% increase or decrease leading to $\Delta L/L = 2.7\%$ or 1.2%). However, the parameters can not vary so much without yielding to an inconsistent reduced χ^2. Subsequently, 1.5% as an estimate for the measurement error from the fit is conservative. The major impact of a bad fit is the presence of a bias in the luminosity measurement. In general, if the acoplanarity fit is not satisfactory, it is still possible to try to fit separately the Δp_T distribution.

The various contributions to the systematic uncertainties are summarised in Tab. 9.1. The quadratic combination of these numbers gives an estimate of the total systematic errors at the level of 2.9%.

Acceptance	1.5%	Calibration using inclusive low p_T muon
Muon p_T scale	$< 0.3\%$	Use $\gamma p \rightarrow \Upsilon p \rightarrow \mu^+\mu^- p$
Calorimetric excl.	2%	Monitoring and masking the noisy calotowers and/or forward rap gap without calorimeter excl.
Tracking excl.	–	Use tracking algorithm dedicated to low p_T track reconstruction
Acoplanarity fit	1.5%	More data and/or other types of fit.

Table 9.1: Summary of the systematics on the luminosity measurement with muon pairs, and possible solutions to tackle them. The quadratic sum results in 2.9% systematic errors

When pile-up is increasing, the calorimeter exclusivity have to be removed. All the exclusivity then relies on the tracking, for which the error has to be evaluated and taken into account. It could be expected that the rise of the uncertainty from tracking exclusivity will not be as high as the decrease due to the removal of the calorimetric exclusivity. However, the contamination of the observed sample by background events will be larger. But these reducible background events will bring a clear constant term in the acoplanarity distribution. A proper fit can help in removing this new component, at higher luminosities.

9.2.4 Absolute luminosity measurement

The absolute measurement of the integrated luminosity with exclusive muon pairs is based on Eq. 9.5. Tab. 9.2 collects all the variables for this evaluation. The exhaustive list of cuts applied offline on the samples is:

- **Kinematic cuts:** $p_T > 5$ GeV and $|\eta| < 2.4$ for each muon
- **Acoplanarity cut:** $|\Delta\phi| > 2.9$ rad
- **Transverse momentum cut:** $|\Delta p_T| < 2$ GeV
- **Tracking exclusivity:** $N_{tracks} < 3$
- **Calorimetric exclusivity:** $N_{towers} < 5$, for towers with $E > 5$ GeV and isolated from the muon candidates ($\Delta R > 0.3$)
- **Upsilon veto:** $M_{\mu\mu} < 9$ GeV `or` $M_{\mu\mu} > 11$ GeV.

The simulated signal is fitted in the following range: $\Delta|\phi| \in [-0.016\pi; 0.016\pi]$, for the extraction of the Γ_1, A_1, Γ_2 and A_2 parameters. The distribution of the observed events is fitted in $\Delta|\phi| \in [-0.072\pi; 0.072\pi]$, and the integral of the background assumed distribution B_{fit} covers $\Delta|\phi| \in [-0.016\pi; 0.016\pi]$.

The statistical errors on N_{obs} come from the Poisson distribution and varies with the scenario. For the theoretical error on the cross-section, $\Delta\sigma/\sigma = 1\%$ is conservative. The errors on the acceptance ($\epsilon = \epsilon_{trig} \times \epsilon_{sel}$) are included in the systematic uncertainties (Tab. 9.1), and estimated to be 2.9%.

Measurement after 100 pb^{-1}

From Eq. 9.5 and Tab. 9.2, one obtain the results of a simulated luminosity measurement after $L_{true} = 100$ pb^{-1}, using the exclusive dimuon simulated sample is:

$$\text{Scenario (i): } \mathrm{L}_{true} = 100 \text{ pb}^{-1} \tag{9.10}$$

$$\mathrm{L}_{meas} = 96.8 \pm 6.1(stat) \pm 1.0(th) \pm 2.9(syst) \text{ pb}^{-1}. \tag{9.11}$$

The statistical errors dominates the total uncertainty on the measurement (7.0%), assuming that the understanding of the systematic effect is properly

L (pb^{-1})	σ (pb)	ϵ_{trig} (%)	Variant	N_{obs}	N_{bkg}	ϵ_{sel} (%)
100	74.7	10.0		578 ± 24	190.0	53.7
100	′	′	$w/veto$	455 ± 21	56.3	53.7
1000	′	′		5788 ± 76	1865	53.7
1000	′	′	$p_T > 8$ GeV	2382 ± 49	832	20.3

Table 9.2: Summary of the variables for the luminosity measurement with muon pairs: true luminosity L; process cross-section σ assuming $p_T > 2.5$ GeV and $\sqrt{s} = 14$ TeV; L1+HLT trigger selection efficiency ϵ_{trig}; number of observed events $N_{obs} \pm \sqrt{N_{obs}}$; estimated number of background events in the observed sample N_{bkg}; overall offline selection efficiency ϵ_{sel} including all cuts. Four scenarios are investigated: (i) $L_{int} = 100$ pb^{-1} with the default set of cuts, detailed in this section; (ii) $L_{int} = 100$ pb^{-1} with the application of the forward calorimeter veto; (iii) $L_{int} = 1$ fb^{-1} with the default set of cuts; (iv) $L_{int} =$ 1 fb^{-1} where the p_T cut is risen to 8 GeV.

evaluated. Here, the inelastic component of the simulated data is only rejected by the fit of the acoplanarity distribution. Provided that the forward calorimeters CASTOR and ZDC are installed and ready for acquisition, the inelastic events can be rejected by a veto using them, as discussed previously. The number of observed events, after L = 100 pb^{-1}, becomes:

$$\text{Scenario (ii): } \text{L}_{true} = 100 \text{ pb}^{-1} \text{ with forward calorimeter veto} \tag{9.12}$$

$$\text{L}_{meas} = 99.4 \pm 5.3(stat) \pm 1.0(th) \pm 2.9(syst) \text{ pb}^{-1}. \tag{9.13}$$

The effect of the background reduction is a better fit of the observed data. The estimate of the number of remaining background events is improved. As long as the accumulated data sample remains small, the total uncertainty of 6.2% is dominated by the statistical errors $\sqrt{N_{obs}}/(N_{obs} - N_{bkg})$. The determined luminosity agrees within statistical errors with true value. This term should improve with the size of the observed sample. A large part of the error comes from the statistics ($\sqrt{N_{\text{obs}}}$). As an estimate, a background-free sample would contain $N_{\text{obs}} = 601$ dimuon events, leading to a 4.1% accuracy from Poisson statistics, which is consistent with earlier generator-level studies [21]. However here, the range of the signal fit is narrower, which decreases the available statistics.

Measurement after 1 fb^{-1}

If more data are accumulated, the statistical errors decrease. On the other hand, pile-up events could become a problem and should be dealt with care. Two scenarios at higher luminosity are presented here, assuming a pile-up free environment. A true integrated luminosity of $\text{L}_{true} = 1$ fb^{-1} is assumed. The forward calorimeter veto is not considered as it is sensitive to the pile-up. The two scenarios differ on the kinematic cut on p_T. Indeed, as the luminosity increases, the p_T trigger thresholds will increase.

$$\text{Scenario (iii): } \mathrm{L}_{true} = 1 \text{ fb}^{-1} \tag{9.14}$$

$$\mathrm{L}_{meas} = 978 \pm 19(stat) \pm 10(th) \pm 28(syst) \text{ pb}^{-1}. \tag{9.15}$$

Under these assumptions, the total uncertainty reaches 3.6% and is now dominated by the systematic errors. These are supposed here to remain similar as at low luminosity, or even to decrease. The statistical errors drop to 1.9% but rely on a $p_T > 5$ GeV cut. The following scenario may be more realistic with that respect

$$\text{Scenario (iv): } \mathrm{L}_{true} = 1 \text{ fb}^{-1} \text{ with } p_T > 8 \text{ GeV} \tag{9.16}$$

$$\mathrm{L}_{meas} = 1023 \pm 32(stat) \pm 10(th) \pm 30(syst) \text{ pb}^{-1}. \tag{9.17}$$

The increase of the muon p_T threshold is consistent with the luminosity increase, as the trigger algorithms have to be adjusted to avoid too high output rates. First effect of this higher p_T threshold is larger statistical errors (3.1%), which become similar to the systematic ones. However, it could be expected that the systematical errors actually decrease with a higher p_T cut. The total uncertainty on the measurement is then 4.4% in this simulation.

In both high luminosity scenarios ($L_{true} = 1$ fb^{-1}), the bias stays small and is below the total uncertainty. The accumulated data bring the statistical errors at least at the level of the systematic ones, if not better. Very low values, at the order of 3%, are achieved, while they dominate by far the total uncertainty at $L_{true} = 100$ pb^{-1}.

Perspectives

A precise description of the pile-up rejection at high luminosity is not given in this document. Several techniques can be used in real conditions. In particular, vertexing is a possible tool for the rejection of observed particles coming from pile-up events.

In the previous section, the signal shape is determined from the simulated samples. With real data, for consistency, the A_1 and A_2 parameters could also be extracted from the data. For instance, if stronger cuts and the forward detector veto are applied, the content of the observed sample will be mostly made of elastic events, but with less statistics. Moreover, upsilon events will in principle provide a lot of checks for systematics. These events will help in tuning the monte carlo software and serve as a reference.

Processes with a double inelastic photon exchange, i.e. events where both protons dissociate, are not taken into account here. Full simulation has not been done but generator-level studies showed that: (1) the cross-section is lower, even if the uncertainty is larger; (2) the acoplanarity distribution is much flatter, contributing as a constant term in the corresponding distribution of observed events. This contribution seems very small and will be handled as any other contribution in the fit: it will be included in the estimate of N_{bkg}.

Conclusions

The total uncertainty on the measured integrated luminosity is will be at the order of 6%, for approximately 100 pb^{-1} and is driven by the statistical errors. This result is well below the expected 10% accuracy using inclusive W and Z boson productions at the LHC start-up [70]. At larger luminosity, a total uncertainty at the order of 3% or better could be achieved assuming high statistics, a good understanding of the systematic errors and a well-controlled pile-up subtraction. The absolute luminosity determination is a major application of the measurement of the exclusive muon pairs in the CMS experiment.

9.3 Effects of the misalignment of beamline elements on VFD detectors

In *forward physics*, a good knowledge of the whole beamline is critical. A displacement of the order of a few hundreds of micrometers is tolerated, provided that the beam characteristics remain identical at the interaction points. This tolerance has to be compared to the typical length of the magnets, which is of a few meters. Even if it looks negligible, the element displacement with respect to beamline maps is not harmless: while a vertical dipolar field is insensitive to a horizontal shift or tilt, such displacements could have a major impact when dealing with quadrupoles or collimators. This section discusses this impact for quadrupoles, and possible corrections being applied on the particle energy reconstruction from measurements by VFDs in a misaligned beamline [13].

The misalignment of the LHC optical elements could have a significant impact on the measurements with very forward detectors. As the deflection of the particle paths depends on their positions in quadrupoles, a misplacement of these optical elements implies a change in the nominal beam position. In turn, as the accurate position measurement with the forward tracking detectors (as well as the information inferred from the segmentation of forward calorimeters) is referred to the ideal beam location, changing this reference results in a biased reconstruction of the measured particles.

Fig. 9.9 shows the impact of possible shifts (0.5 mm) and tilts (0.1 mrad) of the beamline quadrupoles on the energy reconstruction with VFDs at 420 m. The reconstruction assumes ideal beamline in which only one quadrupole at a time is separately moved. Effects higher than 10 % could be expected. Even a perfect knowledge of the actual beam position at the VFD, using beam position monitors, does not entirely correct for this error, that depends on the quadrupole position. The further from the VFD, the more insensitive the correction. Better results are obtained using a physics calibration process like the exclusive dimuon production.

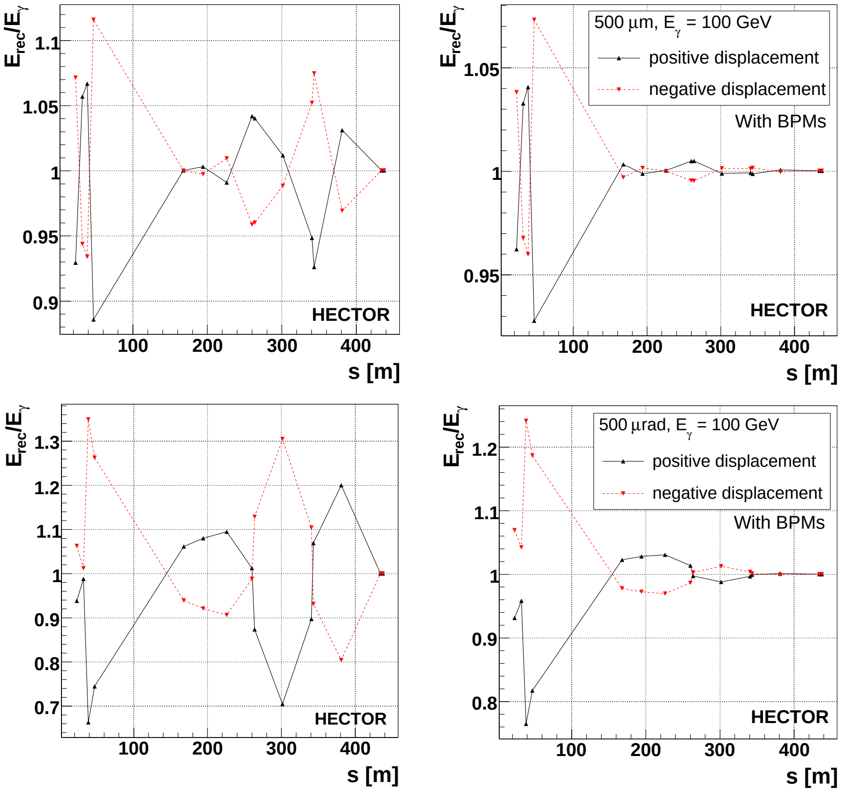

Figure 9.9: Ratio of the proton energy loss, reconstructed with the VFDs (E_{rec}), to the true energy loss (E_γ) in a beamline with one misaligned quadrupole. The graphs show the bias for the reconstruction of a 100 GeV energy loss assuming the misaligned quadrupole at various positions. Each element is separately shifted (500 μm, upper plots) or tilted (100 μrad, lower plots), assuming a perfect alignment for the rest of the beamline. The impact of the misalignment can be as high as 10% (left). Even a perfect knowledge of the actual beam position at the VFD (right), using Beam Position Monitors, does not compensate for this bias, depending on the position of the misplaced quadrupole. Simulation with HECTOR [13].

These results have been included in the recent design reports of the FP420 project [12].

9.4 Calibration of the VFDs from the exclusive dimuon data

Calibration of the reconstructed variables at forward detectors can be well-maintained using the physics processes and the central detectors. At HERA, the elastic ρ meson photoproduction was used where the momentum of the scattered proton could be deduced from the decay in two charged pions using the central tracking. At the LHC, the two-photon exclusive production of dimuon pairs seems a good calibration process, with large accumulated statistics for the detectors at 420 m. The visible cross-section is large ($\sigma \approx 7$ pb), including the acceptance of central detectors. This could even allow for a run-by-run calibration of the scattered proton energy scale within a full acceptance range. Moreover, the expected reconstruction power of central detectors is excellent for such dimuon events. Earlier studies quote a proton energy uncertainty of about 10^{-4} per event [21]. These results are updated here using a full detector simulation.

The CMS detector provides an accurate measurement of muons, and in particular of the dimuon invariant mass $M_{\mu\mu}$ and of the longitudinal momentum P_z. Assuming collinear photons, these quantities are given by:

$$M_{\mu\mu} = \sqrt{2E_{\gamma 1}E_{\gamma 2}} \tag{9.18}$$

$$P_z = E_{\gamma 1} - E_{\gamma 2}. \tag{9.19}$$

These equations provide an estimate of the photon energies ($E_{\gamma 1}$ and $E_{\gamma 2}$), or equivalently, of the proton energy loss:

$$E_{\gamma i} = \pm\frac{P_z}{2} + \frac{\sqrt{(M_{\mu\mu})^2 + (P_z)^2}}{2}, \quad i = 1, 2. \tag{9.20}$$

As far as the approximation holds, namely for low photon p_T, the measurement of the dimuon system provides a means to calibrate the VFDs. In the following, the proton relative energy loss

$$x = E_\gamma / E_{\text{beam}} \tag{9.21}$$

can be expressed in terms of (1) the true value obtained from MC protons (x^p_{true}), of (2) the value computed from the MC muons (x^μ_{true}) and of (3) the value calculated from the measured muons (x^μ_{reco}). The power of these calibration technique depends on the accuracy of the energy loss reconstruction. Fig. 9.10a shows the expected spectrum of the proton relative energy loss x for the selected $\gamma\gamma \to \mu^+\mu^-$ elastic events and the FP420 acceptance in this variable. The accuracy of the reconstruction algorithms for muons is assessed using Fig. 9.10b, where no bias is visible when comparing the x values for generator level muons and reconstructed muons (x^μ_{true} and x^μ_{reco}, respectively). A Gaussian shape gives an estimate of the RMS of the peak, of the order of 10^{-6}. In reality, reconstructed muons will be used for the estimate of the proton relative energy loss x and should be compared to the true value x^p_{true}. The difference is given for elastic and inelastic dimuon samples (FIG. 9.10c and 9.10d). Very good resolution is expected ($< 10^{-5}$), for a negligible bias, even though the sample of inelastic events show a broader peak. The possible bias is studied as a function of the x values. Four different x bins are selected:

(1) below 1×10^{-3}, i.e. below the FP420 acceptance

(2) $[0.001; 0.003]$, i.e. in the lower edge of FP420 acceptance, which depends on the distance between the detector active area and the beam

(3) $[0.003; 0.010]$, i.e. in the upper edge of FP420 acceptance. The upper limit of the FP420 acceptance depends on the actual position of RP220 detectors, that could possible screen the FP420 sensors.

(4) above 1×10^{-2}, i.e. in the region accessible to VFDs at 220 m or 420 m, depending on their distance to the beam.

FIG. 9.11 shows that the bias and the RMS increase with increasing x values. In particular, the uncertainty reaches 10^{-4} for the highest energy losses.

Samples	$\gamma\gamma \to \mu^+\mu^-$	$\gamma\gamma \to e^+e^-$
All events	709	67
≤ 1 proton tag at 420 m	280	39
≤ 1 proton tag at 220 m	5	4

Table 9.3: Number of selected dilepton events with at least one proton tag in the very forward detectors, after an integrated luminosity of 100 pb^{-1}.

The estimated number of selected dileptons, which are tagged in very forward detectors, is collected in TAB. 9.3. This method has much more limited statistics within acceptance of the detectors at 220 m. The high-energy bremsstrahlung $pp \to pp\gamma$ is a possible candidate for the energy scale calibration of the VFDs at 220 m [13]. It has relatively large cross-section, about 10 nb for $E_\gamma > 100$ GeV, and photons are emitted into a very forward cone, so could be detected in the zero-degree calorimeters (ZDCs). A simultaneous measurement of the scattered proton in the VFD and of the bremsstrahlung photon in the ZDC would then allow for cross-calibration of these two devices.

In this study, the misalignment of the muon system has not been taken into account.

Central Exclusive Production The misalignment effects and their corrections are illustrated (FIG. 9.12) by the study of two-photon exclusive production of the SM Higgs boson ($pp(\gamma\gamma \to H)pp$) with $\text{M}_H = 115$ GeV. The measurement of the energy of the two scattered protons yields the boson mass, by means

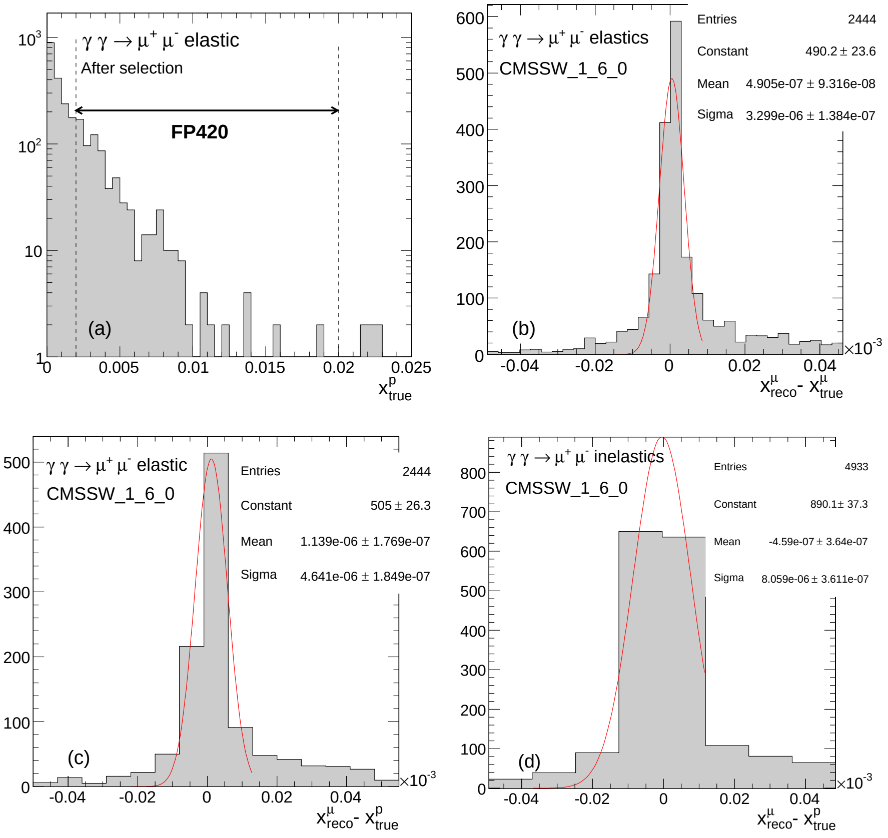

Figure 9.10: (a) Distribution of the relative energy loss of the protons $x = E_\gamma/E_p$, computed from the proton generator level data (LPAIR), for the elastic $\gamma\gamma \to \mu^+\mu^-$ process, after the offline selection of the dimuons in `CMSSW_1_6_0`. (b) Comparison of the x value computed from the muon generator level data x^μ_{true} and the value reconstructed from the muon measurement x^μ_{reco}. Very good resolution and no bias are achieved from the muon reconstruction algorithms. Comparison of the true relative energy loss x^p_{true} and the value reconstructed from the muon measurement x^μ_{reco} for elastic (c) and inelastic (d) processes.

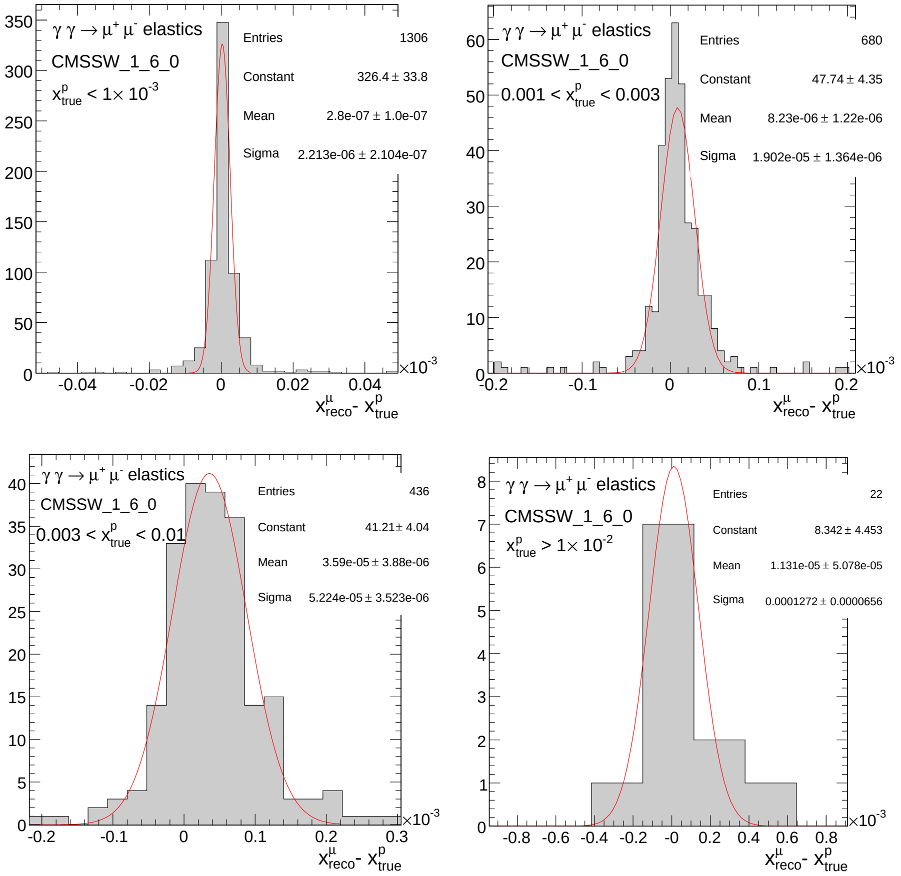

Figure 9.11: Reconstruction power on the relative energy loss of the proton x from the muon measurement, in four different bins in x, after selection, using `CMSSW_1_6_0`. Gaussian shapes give an estimate of the peak widths and offsets, which increase with higher x values. Misalignment of the muon system has not been taken into account.

of the missing mass method (Eq. 4.2). As a consequence, an uncorrected measurement with misalignment leads to a bad mass computation. A quadrupole (`MQM9R5`, $s = 347$ m) close to the detector has been shifted by 100 μm, and another quadrupole (`MQXA1R5`, $s = 29$ m) close to the IP by 500 μm; in the latter case, the misalignment-induced change in the VFD acceptance is visible, with a loss of signal. The limitations of the beam-position-based corrections are clearly visible ($\approx 3\%$), even assuming no systematic errors, while the muon-calibration stays unbiased (though only a relatively small sample of 700 dimuon events was used to get the correction factors).

9.5 Direct observation of lepton pairs in forward detectors

The measurement of both leptons by CMS, for pseudorapidities up to 2.5 gives some prediction power on the energy of the scattered protons. Very forward detectors – namely, RP220 and FP420 – can subsequently be calibrated by means of a physics process, as explained in the previous section.

But events with only one lepton from the pair detected in CMS could also be useful. From the η and $\Delta\eta = \eta_{\mu^+} - \eta_{\mu^-}$ distributions (Fig. 8.5 and 8.6), it is remarkable that (i) many muons will be produced out of the $[-2.5; 2.5]$ pseudorapidity window; (ii) many events can have a first muon in the central detector and the second one in a forward region. If we only focus on triggers based on central detector data, the only possibility left is when one muon is central ($|\eta| < 2.5$) and fires the *1 isolated muon* trigger, and the other muon is sent within the acceptance of some forward detector (Fig. 9.13). It should be noted that the single muon trigger is dependent on the real coverage of RPC detectors. In other terms, the single muon trigger works only in $-2.1 \leq \eta \leq 2.1$, while dimuon triggers could accept the second candidate to be in the $[2.1; 2.5]$ region, using the central tracking data. Both HF and CASTOR have been operated in muon test beams [76], with sensitivity starting at 50 GeV.

In the ideal case, the event signature is then 1 muon in the central detector, 1 muon in one of the forward detector (namely T1+HF or T2+CASTOR); in addition the forward protons p can be detected independently in RP220 or FP420. Moreover, it should be requested that the central muon has a transverse momentum large enough to be reconstructed (independently of the trigger lower threshold), i.e. $p_T \geq 3$ GeV. Two constraints arise: (i) no pile-up event should happen during this bunch crossing. Therefore, a (very) low luminosity is required. (ii) No fake signal is visible in the forward detectors. However the tight correlation in ϕ for both muons (Fig 8.4)[2] can be used to discriminate the single muon signal from some background events.

A simple study at generator level leads to the following figures: single muons from $\gamma\gamma \to \mu^+\mu^-$, with $p_T \geq 1$ GeV and a total production cross-

---

[2] i.e. muons are back-to-back in the transverse plane

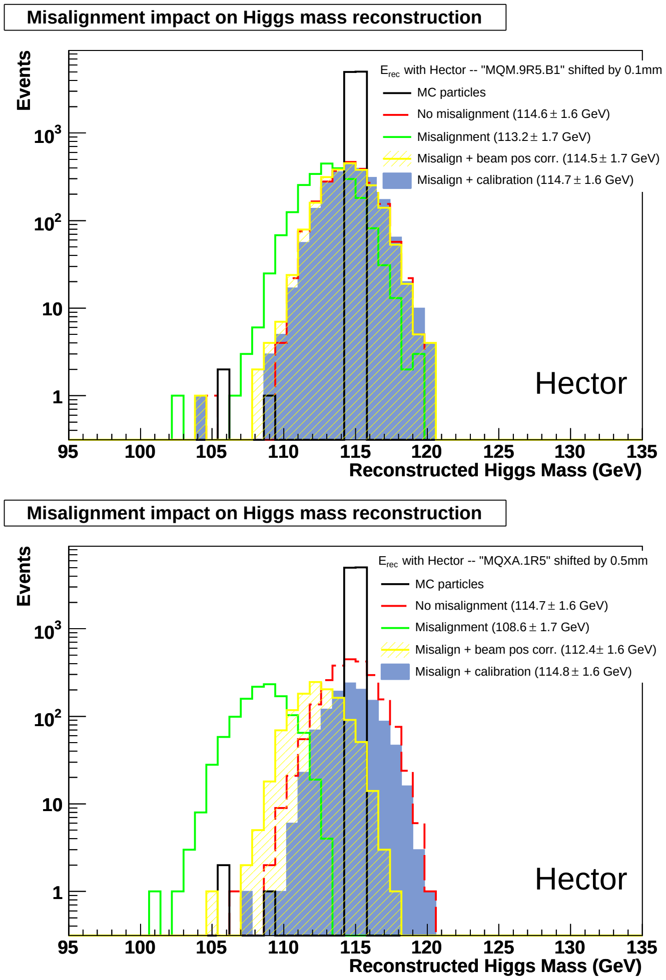

Figure 9.12: Illustration of the effects in the energy reconstruction due to the misalignment of the LHC quadrupoles. The graphs show the reconstructed Higgs boson mass in the two-photon exclusive production, using the energy of two forward scattered protons. In the upper plot, a quadrupole (`MQM9R5`, s = 347 m) close to the detector has been shifted by 100 μm. Misaligning an optical element (`MQXA1R5`, s = 29 m) close to the IP leads to a loss of acceptance (lower plot). The reconstructed values including the correction due to the dimuon calibration is also plotted. The average reconstructed mass and its resolution are given, without including the beam energy dispersion.

section of 0.676 nb, have a 48 % probability not to be central. Events with one centrally detected muon ($|\eta| \leq 2.5$ and $p_T \geq 3$ GeV) and one non-central muon ($|\eta| \geq 2.5$) will happen with 2 % chance, i.e. with 14.15 pb. Even at $\mathcal{L} = 10^{32}$ cm^{-2}s^{-1}, this corresponds to $N_\mu \approx 5$ per hour. The very narrow ϕ and p_T balance between both muons should serve for the identification of the forward muon, and possibly to the calibration (using p_T) or alignment (using ϕ) of the corresponding forward detector. But for such purposes, the development of a new *exclusive single muon*, possibly *isolated*, would be required, in order to decrease the p_T threshold. Indeed, the trigger efficiency ϵ would drop from $\epsilon(p_T \geq 3) = 2.0$ % to $\epsilon(p_T \geq 7.0) = 0.25$ % at L1. Tab. 9.4 summarises these numbers for HF and CASTOR. Similar considerations apply for dielectrons, with higher p_T thresholds in CMS (Tab. 9.5): 6.0 is the minimum for reconstruction and 12.0 is the threshold of default single electron Level-1 trigger. Rates left at this level emphasise the need for a definition of dedicated trigger paths.

In this generator level study, with no assumed reconstruction efficiency, 100, 000 LPAIR events were used. The effect of CMS magnetic field is not taken into account[3].

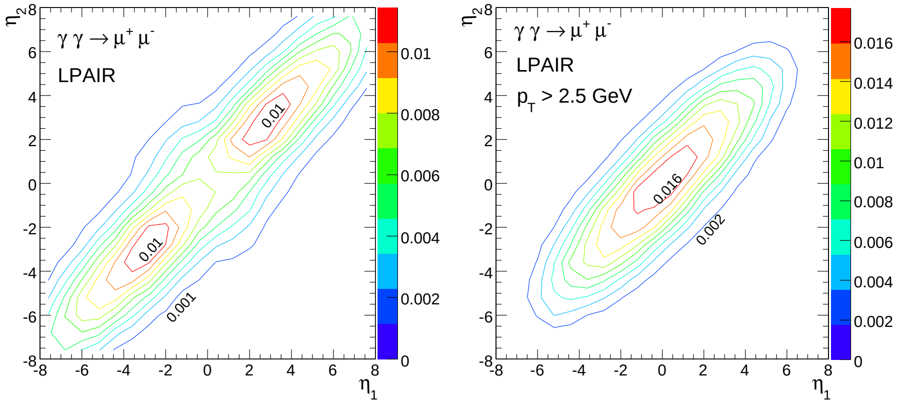

Figure 9.13: η distribution of muons from $\gamma\gamma \to \mu^+\mu^-$. Left: no cut on p_T. Right: $p_T > 2.5$ GeV.

9.6 Extending exclusive dilepton observation to higher luminosities

Driving the LHC to higher luminosities leads to a more numerous pile-up events. The exclusive productions will be *a priori* hidden by a large background of low energy particles coming from the pile-up. Moreover, in order to handle the data

---

[3] Which is in first approximation not important, as the considered transverse momenta are small.

$\mathbf{pp(\gamma\gamma \to \mu^+\mu^-)pp}$		$\sigma_{\mathbf{acc}}$ **(pb)**	**Rate** $(\mathbf{h^{-1}})$	$\mathbf{E_{peak}}$ **(GeV)**
$\mathbf{p_T \geq 3}$ **GeV**	HF	6.21	2.2	50
	CASTOR	0.34	0.12	300
$\mathbf{p_T \geq 7}$ **GeV**	HF	0.72	0.26	120
	CASTOR	0.034	7.6×10^{-3}	700

Table 9.4: Rates for dimuons detected simultaneously by CMS and a forward detector. It is assumed that one muon is within CMS acceptance ($|\eta| \leq 2.1$ and $p_T \geq 3$ or 7 GeV) and the second muon is within a forward detector acceptance. Cross-sections in pb are shown for the geometrical acceptances of T1+HF and T2+CASTOR. The rates in number of events per hour assume a luminosity of $\mathcal{L} = 10^{32}$ cm^{-2}s^{-1} = 0.36 pb^{-1}h^{-1}. The most probable muon energy E_{peak} is given (Fig. 9.14).

$\mathbf{pp(\gamma\gamma \to e^+e^-)pp}$		$\sigma_{\mathbf{acc}}$ **(pb)**	**Rate** $(\mathbf{h^{-1}})$	$\mathbf{E_{peak}}$ **(GeV)**
$\mathbf{p_T \geq 6}$ **GeV**	HF	1.06	0.38	100
	CASTOR	37×10^{-3}	13×10^{-3}	600
$\mathbf{p_T \geq 12}$ **GeV**	HF	0.16	58×10^{-3}	120
	CASTOR	2.5×10^{-3}	0.9×10^{-3}	1400

Table 9.5: Rates for dielectrons detected simultaneously by CMS and a forward detector. It is assumed that one electron is within CMS acceptance ($|\eta| \leq 2.1$ and $p_T \geq 6$ or 12 GeV) and the second electron is within a forward detector acceptance. Cross-sections in pb are shown for the geometrical acceptances of T1+HF and T2+CASTOR. The rates in number of events per hour assume an instant luminosity of $\mathcal{L} = 10^{32}$ cm^{-2}s^{-1} = 0.36 pb^{-1}h^{-1}. The most probable muon energy E_{peak} is given (Fig. 9.15).

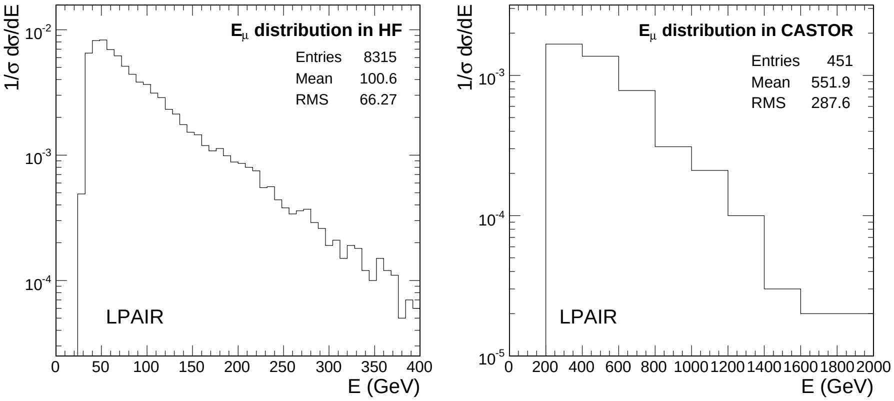

Figure 9.14: Energy distributions for muons detected in HF (left) and CASTOR (right), when requiring that the second muon is seen by CMS (i.e. $|\eta(\mu_2)| \leq 2.1$ and $p_T(\mu_2) \geq 3$ GeV).

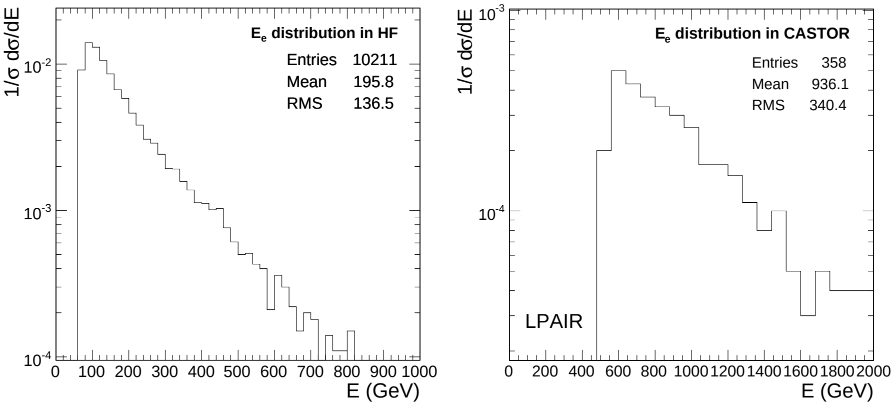

Figure 9.15: Energy distributions for electrons detected in HF (left) and CASTOR (right), when requiring that the second electron is seen by CMS (i.e. $|\eta(e_2)| \leq 2.1$ and $p_T(e_2) \geq 6$ GeV).

flow, the trigger thresholds are risen to higher p_T values. As a first estimate, it is conservative[4] to assume a dimuon (inclusive) trigger around 10 GeV at $\mathcal{L} = 10^3$ cm^{-2}s^{-1}.

Higher thresholds will largely reduce the signal selection; however, the achievable integrated luminosity could compensate for this. Larger statistics means also the extension of the dimuon invariant mass reach. At 10 fb^{-1}, assuming the abovementioned 10 GeV p_T threshold and an offline selection efficiency of 90%, one event is expected from SM exclusive dimuons for $M_{\mu\mu} \approx$ 800 GeV.

The major issue for high luminosity is the pile-up, which prevents from using bare exclusivity. The analysis at low luminosity showed that the tracking exclusivity was very powerful. Vertexing could bring further important constraints, as one could require to drop all tracks pointing to another vertex than the one from which both muons originate. Then, the exclusivity would be expressed as a cut on the number of tracks pointing to the dimuon vertex. Such a method would still suffer from pile-up events with a z coordinate similar to the one of the dimuon vertex. For signal selection, acoplanarity and p_T balance will remain usuable, even if the background will increase. However, systematic errors are expected to be much larger and will have to be understood with care. The use of prescaled samples of low p_T muons will allow for checking trigger efficiencies for instance. Similarly, the large production of Υ mesons will be helpful for the detector calibration.

The observation of exclusive dielectrons could be improved with larger statistics, as long as the increase of the trigger p_T thresholds is not too strong. Dimuons at higher luminosities could bring an alternative way to look for physics beyond the Standard Model, with similar final states. These searches would benefit from the stable and controlled environment using exclusive dileptons.

---

[4] Earlier studies [83] delivered a pair of asymmetric thresholds $(8, 5)$ for a dimuon L1 trigger bit.

Chapter 10

Υ diffractive photoproduction

Amongst the selected $\gamma\gamma \to \mu^+\mu^-$ events, the resonance peaks of the heavy Υ meson are visible. This chapter summarises the status of diffractive photoproduction of Υ mesons at high energy colliders, and brings prospects for the observation of the $(1S)$, $(2S)$ and $(3S)$ resonances via the exclusive dimuon analysis. This study assumes no pile-up events. Part of the results presented here has been approved by the CMS *collaboration.*

10.1 Introduction

Complementarily to $\gamma\gamma$ fusion, exclusive dilepton final states can be produced via leptonic decay modes of the J/Ψ and the Υ mesons. While the dimuon decays of Υ mesons are considered as a background to the exclusive dimuon two-photon production, their detection is very interesting in itself as detailed in this chapter. The diffractive photoproduction of these narrow $b\bar{b}$ resonances has been studied in the past, at HERA and TEVATRON. The Υ mass, around 10 GeV, is very well-known with a precision of the order of 10^{-5} (TAB. 10.1), from other production modes. In diffractive photoproduction, the mesons are produced at low p_T, therefore, the p_T of their decay muons is limited to 5 GeV. Subsequently, in the dimuon decay mode, only Υ mesons are visible in CMS in exclusive diffractive photoproduction, while lighter mesons will not be triggered. Due to the higher trigger threshold, the Υ dielectron decay is also not visible[1].

The Υ diffractive photoproduction corresponds to a $\gamma p \to \Upsilon p$ process and the only decay mode considered here is $\Upsilon \to \mu^+\mu^-$. The corresponding diagram

---

[1] Due to higher trigger thresholds in ATLAS, this experiment will not be able to measure these photoproduced quarkonia resonances, as they will not be triggered.

Resonance	**PDG mass (GeV)**	**BR($\mu^+\mu^-$) (%)**	
Υ (1S)	9.4603 ± 0.0003	2.48 ± 0.05	
Υ (2S)	10.0233 ± 0.0003	1.93 ± 0.17	
Υ (3S)	10.3552 ± 0.0005	2.18 ± 0.21	
Υ (4S)	10.5794 ± 0.0012	$(1.57 \pm 0.08) \times 10^{-3}$	
Υ(10860)	10.865 ± 0.0008	$(2.8 \pm 0.7) \times 10^{-6}$	(e^+e^-)
Υ(11020)	10.865 ± 0.0008	$(1.6 \pm 0.5) \times 10^{-6}$	(e^+e^-)

Table 10.1: Characterisation of the Υ resonances in terms of mass and dimuon branching ratio [153]. For the two heaviest states, dimuon decay is not observed and the dielectron is put as a reference.

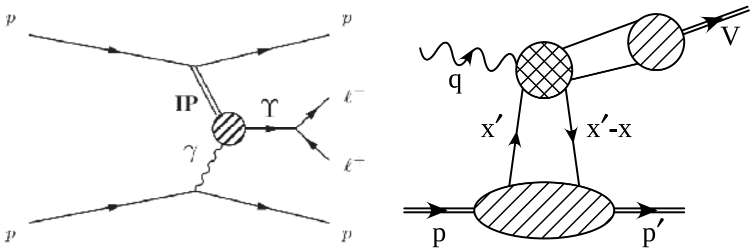

Figure 10.1: (Left) Diagram for Υ diffractive photoproduction. On one side, the interaction is driven by the exchange of a photon from one incoming proton. The photon fluctuates into a $b\bar{b}$ pair. On the other side, a pair of gluon, carrying no net colour, makes the connection between the $b\bar{b}$ and the second proton. Once produced, this $b\bar{b}$ pair evolves into an Υ meson. Finally, this meson decays into two muons.
(Right): Illustration of the model for the calculation of the $\gamma p \to \Upsilon p$ amplitude [149]. The three dashed areas correspond to the terms computed in the process amplitude: (1) the exchange of two gluons from one proton; (2) the photon fluctuates into a $b\bar{b}$ pair, which interacts via a two-gluon exchange; (3) the transition of a $b\bar{b}$ pair to a Υ resonance.

is shown in Fig. 10.1 (left). This process can be described by the fluctuation into a $b\bar{b}$ pair of a quasi-real photon, emitted by an incoming proton. This pair in turn interacts diffractively with a proton, i.e. via a colourless exchange carrying the same quantum numbers as the vacuum. Thanks to the large mass of the b quarks which provides a hard scale in the process, the use of perturbative QCD factorisation (pQCD) is allowed [149]. The factorisation is illustrated in Fig. 10.1 (right) and allows for the process amplitude $\mathcal{M}$ to be decomposed into three parts: (1) the exchange of two gluons from one proton; (2) the interaction between the incoming proton and the gluons, yielding a $b\bar{b}$ quark pair; (3) the transition of the quark pair into a Υ bound state.

In part (1), the amplitude $\mathcal{M}$ is expressed in terms of the *Generalised Parton Distributions*[2] (GPDs) for the gluons [151], which deal with the exchange of two gluons carrying different momentum fractions x. The Υ diffractive photoproduction is then sensitive to correlations between gluon-pairs within the proton. Approximately, the process cross-section is then proportional to the square of the gluon distribution of the proton $xg(x, \mu^2)$, where μ^2 is the chosen energy scale [150, 151] (e.g. $\mu^2 = M_\Upsilon$):

$$\sigma \sim \left(xg(x, \mu^2)\right)^2 \tag{10.1}$$

According to this two-gluon exchange, calculations show that the cross-section should increase with the γp collision energy W, which is confirmed by the measurements (Fig. 10.2). Since $W^2 \sim 1/x$ and provided that $xg(x, \mu^2)$ increases at low x, the rise of the cross-section with W corresponds to the rise of $xg(x, \mu^2)$ with decreasing x.

The second part (2) of the amplitude $\mathcal{M}$ is the hard process, computable with perturbative QCD. The last component (3) of the amplitude is the transition of the $b\bar{b}$ pair into a Υ bound state, which is not well-known theoretically. The overall uncertainty on the normalisation of the process cross-section comes mostly from the poor theoretical description of the meson wave function [152]. For the photon exchange, the Equivalent Photon Approximation is used. Finally, the experimental signature of interest here requires the meson to decay exclusively into a pair of muons.

The observation at the LHC of photoproduced Υ mesons, at a γp c.m.s. W about ten times higher than at HERA, probes the GPDs at low x values, down to 10^{-4} [151]. The distribution of the four-momentum transfer squared t at the $p I\!\!P$ vertex is sensitive to the distributions of the gluons and has never been measured for the Υ. Moreover, a measurement could provide an estimate of the cross-section, which could constrain the theory and improve the understanding of the Υ wave function.

---

[2] Also called *skewed parton distributions*.

10.2 Measurements at HERA and Tevatron

Diffractive photoproduction of Υ has been observed in ep collisions in HERA with low statistics. In addition, the diffractive photoproduction of ρ, ω, ϕ and J/Ψ has been investigated. Fig. 10.2 shows the evolution of the cross-sections with the γp c.m.s. energy W for these mesons. All cross-sections increase with increasing W, as expected from the models. The process model depends on the meson mass: lighter mesons are described by the Vector Dominance Model and heavier mesons by the model introduced before [40]. Fig. 10.3 is identical to Fig. 10.2, but magnified in the region of Υ, for W ranging from 100 GeV to 180 GeV. Results of several pQCD are also given for comparison. Finally, Fig. 10.4 shows the Υ peak over the Bethe-Heitler background events.

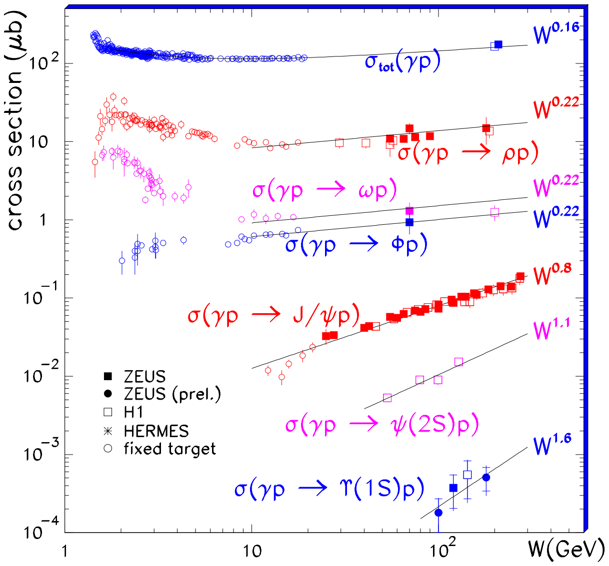

Figure 10.2: Diffractive vector meson photoproduction at HERA [40], including ρ, ω, ϕ, J/Ψ and Υ resonances (from the lightest to the heaviest). The cross-sections are fitted for high photon-proton centre of mass energy W, with a power law W^{δ}. The exponent δ increases with the meson mass. Various theoretical descriptions hold for these processes: The Vector Dominance Model is suitable for the light mesons, while the perturbative calculations work for the heaviest states.

Tevatron has similar data in $p\bar{p}$ collisions at $\sqrt{s} = 1.96$ TeV for lighter mesons, J/Ψ and Ψ' (Fig. 10.5) and has recently reported the observation of Υ (Fig. 10.6) [154]. The invariant mass $M_{\mu\mu}$ of exclusive dimuon final states

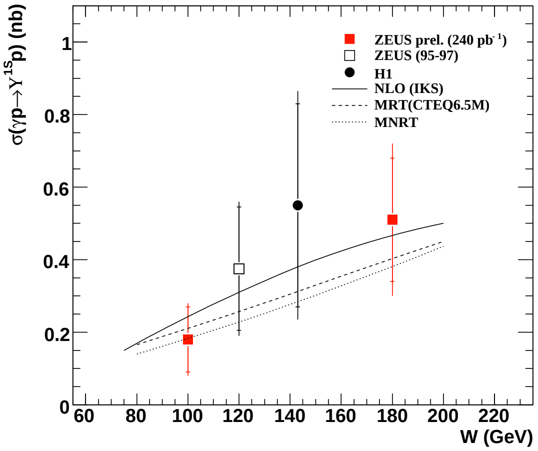

Figure 10.3: Υ diffractive photoproduction at HERA [39]. The cross-section as a function of the γp c.m.s. energy W is plotted. It can be fitted with a power law W^{δ}, which is used for predictions at the LHC energy ranges. Best fit gives $\delta = 1.6 \pm 0.7$. Measurements are compared to NLO predictions.

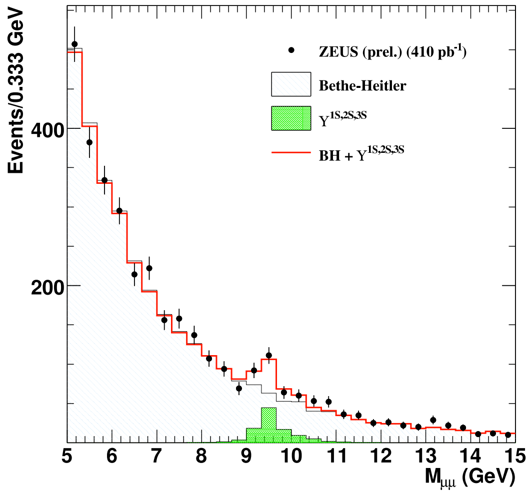

Figure 10.4: Υ diffractive photoproduction at HERA [39]. Number of observed events as a function of the invariant mass of the dimuon system. A broad peak in the Υ region is visible. This Υ signal is extracted after subtraction of the Bethe-Heitler background, and a correction for the dissociative one. Data from 1998-2007, for ep collision with $L = 410$ pb^{-1}.

is shown, with clear peaks at the mass of J/Ψ and Ψ' mesons, in a hadron collider. Similar techniques as those used at TEVATRON will be applied in this analysis.

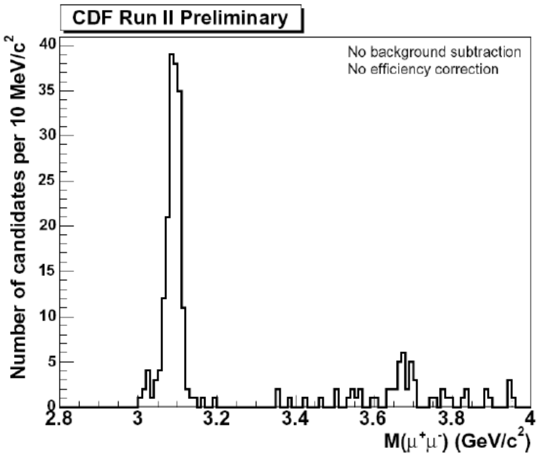

Figure 10.5: Invariant mass of exclusive $\mu^+\mu^-$ productions in $p\bar{p}$ collisions, in the [2.8 GeV; 4 GeV] range. The distribution indicates the observation of J/Ψ (left peak) and Ψ' (right peak) over some $\gamma\gamma \to \mu^+\mu^-$ events [37]. Measurements at $\sqrt{s} = 1.96$ TeV and for $L = 1.48$ pb^{-1}.

10.3 From generation to reconstruction

The following analysis has been done in collaboration with J.J. Hollar (LLNL) and S. Ovyn (UCL).

Due to the large uncertainty on the theoretical cross-section, the Monte Carlo simulations for diffractive photoproduction of Υ mesons have to rely on fitting the current data and on extrapolating the desired c.m.s. energy values. As for other exclusively photoproduced mesons, the measured Υ cross-sections scale with a power law:

$$\sigma \sim W^\delta. \tag{10.2}$$

where W is the photon-proton c.m.s. energy. As quoted earlier, the bigger the meson mass, the larger the exponent δ.

At HERA energy, but only four experimental points with large error bars are available for the fit and the extrapolation to the LHC energies. The best current fit is $\sigma \sim W^{1.6\pm0.6}$ [40].

For the production of the Monte-Carlo samples, STARLIGHT [42] has been used. This software uses such a fit, with $\delta = 1.7$, and extrapolates [40, 48] it to the corresponding W range at the LHC. This photon-proton c.m.s. energy is

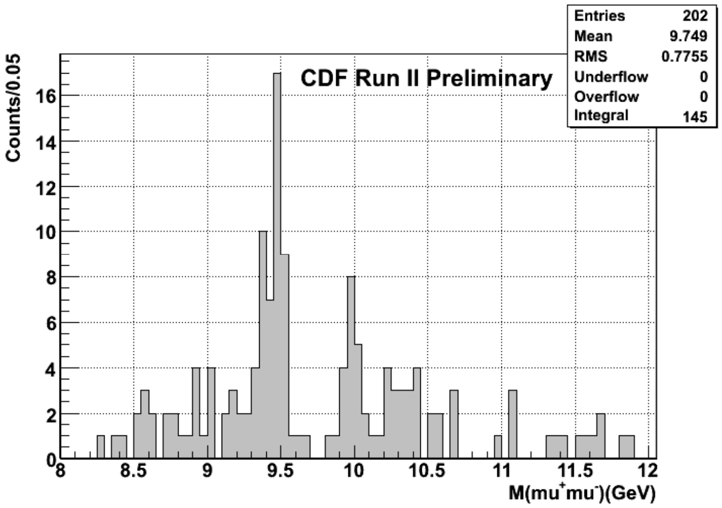

Figure 10.6: Invariant mass of exclusive $\mu^+\mu^-$ productions in $p\bar{p}$ collisions, in the [8 GeV; 12 GeV] range. The distribution indicates the observation of $\Upsilon(1S)$ and $\Upsilon(2S)$ over some $\gamma\gamma \to \mu^+\mu^-$ events [154]. Measurements at $\sqrt{s} = 1.96$ TeV and for $L = 890$ pb^{-1}.

obtained after the application of the EPA for the photon spectrum[3]. TAB. 10.2 summarises the corresponding cross-sections and the samples used in this study.

The $\Upsilon(1S)$, $(2S)$ and $(3S)$ have a non favourable branching ratio to $\mu^+\mu^-$, as shown in TAB. 10.1. However, when produced, such events yield a final state with exclusively two opposite-charge muons, as from $\gamma\gamma \to \mu^+\mu^-$. The dimuons from the Υ decay only differ from the invariant mass and have a $p_T^\mu \approx 5$ GeV. From the previous chapters, it is clear that photoproduced Υ mesons have a high efficiency for trigger and for offline selection.

$\Upsilon \to \mu^+\mu^-$	**N (events)**	$\sigma \times$ **BR(pb)**
Υ (1S)	10k	39
Υ (2S)	3.3k	13
Υ (3S)	2.6k	10

Table 10.2: Monte Carlo samples for Υ diffractive photoproduction. Simulated sample sizes, cross-section σ at $\sqrt{s} = 14$ TeV are shown. The STARLIGHT generator assumes $\delta = 1.7$.

Similarly to photon-photon dimuon production, STARLIGHT generator output files are provided as an HEPMC input to CMSSW. Simulation is performed

---

[3] For comparisons, another software, called PHITI, is used for cross-checks, with the extreme case of $\delta = 1$ [41].

in `CMSSW_1_4_5`. Digitisation and reconstruction in `CMSSW_1_5_4` and finally triggering and skimming in `CMSSW_1_6_0`.

10.4 Detection of $\gamma p \rightarrow \Upsilon p$

A measurement of Υ diffractive photoproduction at LHC would extend the coverage in the effective γp centre-of-mass energy W by approximately one order of magnitude [5]. Their well-known mass also makes them suitable as a benchmark for detector calibration, as it provides an absolute p_T scale, and a means for detector alignment. Their observation can also yield some information for modelling the transition from $b\bar{b} \rightarrow \Upsilon$, and constraining the theoretical expression of the Υ wave function.

The events are triggered via the default dimuon trigger, requiring at least two muons with a $p_T > 3$ GeV and with $|\eta| < 2.4$. This trigger will be available from the LHC start-up luminosity (10^{32} cm^{-2}s^{-1}). Once triggered, the events are selected using the same analysis as detailed in the dimuon part of the analysis chapter. The offline analysis relies on: (1) a kinematic cut on the difference of acoplanarities $\Delta\phi$ of the two muons; (2) a kinematic cut on the difference of transverse momentum Δp_T of the two muons; (3) an exclusivity cut on the number of calotowers N_{towers} in the event, and (4) an exclusivity cut on the number of tracks N_{tracks} in the event. The cumulative efficiency of each cut is reported in Tab. 10.3. The results of this analysis are summarised in Tab. 10.4.

Cumulative eff (%)	$\Upsilon(1S)$	$\Upsilon(2S)$	$\Upsilon(3S)$
$\lvert\Delta\phi\rvert > 2.9$ rad	99.7	100	100
$\lvert\Delta p_T\rvert < 2.0$ GeV	99.7	100	100
N(towers)< 5	99.7	100	100
N(tracks)< 3	94.2	95.9	96.2
8 GeV $< M_{\mu\mu} <$ 12 GeV	94.2	95.9	96.2

Table 10.3: Cumulative efficiency for Υ diffractive photoproduction ($\Upsilon \rightarrow \mu^+\mu^-$) of the analysis cuts: kinematic and exclusivity requirements are similar to those of the exclusive dimuon analysis. Υ resonances are selected by the additional cut on the dimuon invariant mass $M_{\mu\mu}$.

For $L = 100$ pb^{-1}, the expected number of events is

$$\begin{aligned} N_{elastic}(\gamma p \rightarrow \Upsilon(1S)p \rightarrow \mu^+\mu^- p) &= 294 \pm 17(stat) \\ N_{elastic}(\gamma p \rightarrow \Upsilon(2S)p \rightarrow \mu^+\mu^- p) &= 123 \pm 11(stat) \\ N_{elastic}(\gamma p \rightarrow \Upsilon(3S)p \rightarrow \mu^+\mu^- p) &= 110 \pm 10(stat) \end{aligned} \tag{10.3}$$

As the mesons present a very narrow width, the dimuon invariant mass $M_{\mu\mu}$ is also strongly peaked around each Υ mass, for $(1S)$, $(2S)$ and $(3S)$ states. No

	Υ(1S)	**Υ(2S)**	**Υ(3S)**	**$\gamma\gamma$ (el)**	**$\gamma\gamma$ (inel)**
$\sigma \times BR$ (pb)	39	13	10	74.7	76.2
N (events)	10k	3.3k	2.6k	100k	20k
ϵ_{trig} (%)	8.0	10.0	11.5	10.0	18.3
ϵ_{sel} (%)	93.8	95.0	95.5	30.0	12.4
σ_{vis} (pb)	2.94	1.23	1.10	2.24	1.73

Table 10.4: Summary of the Υ analysis, for signal, $\gamma\gamma \to \mu^+\mu^-$ elastic and inelastic backgrounds, with the production cross-section (σ), the number of generated events (N), the efficiencies for triggers (L1+HLT, ϵ_{trig}) and selection (ϵ_{sel}, including the extra $8 \leq M_{\mu\mu} \leq 12$ GeV requirement), and finally the corresponding visible cross-section (σ_{vis}).

results are available for heavier Υ, but the very low expected branching ratio (Tab. 10.1) to dimuons seems to suppress strongly their observability.

Backgrounds to the exclusive Υ measurement are the elastic and inelastic two-photon exchange $\gamma\gamma \to \mu^+\mu^-$. The maximum likelihood fit in the dimuon invariant mass range $8 < M_{\mu\mu} < 12$ GeV is presented (Fig. 10.7). The three Υ resonances ($1S$, $2S$ and $3S$) are fit as Gaussian curves and the elastic and inelastic photon-photon contributions scale like a second order polynomial. The input numbers are those obtained after reconstruction and selection, for an integrated luminosity of $L = 100$ pb^{-1}. The fit results are shown in Tab. 10.5 For all resonances, the fit mass is over-estimated by 0.05 GeV, but this is within the width of the peak. The peak widths, at the order of 0.1 GeV, are dominated by the detector effects (the experimental value of Υ widths are at the order of 20 keV). The number of expected events is also provided by the fit (Tab. 10.6).

Resonance	**PDG mass**	**Fit mass**	**Fit width**
Υ (1S)	9.4603 ± 0.0003	9.514 ± 0.007	0.099 ± 0.007
Υ (2S)	10.0233 ± 0.0003	10.059 ± 0.011	0.072 ± 0.011
Υ (3S)	10.3552 ± 0.0005	10.392 ± 0.017	0.114 ± 0.024

Table 10.5: Reconstruction of Υ from the dimuon measurement. Comparison between the current experimental limits on the Υ masses and the fit results. All numbers are expressed in GeV [5].

For the selected events, the average values of the photon-proton c.m.s. energy $< W >$ and of the exchanged photon virtuality $< Q^2 >$ are

$$< W >= 2398 \text{ GeV} \quad \text{and} \quad < Q^2 >= 0.046 \text{ GeV}^2. \tag{10.4}$$

Maximal Q^2 is approximately 1.2 GeV^2. The inelastic diffractive photoproduction has not been studied here but similar techniques as for the exclusive

Process	N_{data}	N_{Fit}
$\Upsilon(1S) \rightarrow \mu^+\mu^-$	294	300 ± 19
$\Upsilon(2S) \rightarrow \mu^+\mu^-$	123	116 ± 16
$\Upsilon(3S) \rightarrow \mu^+\mu^-$	110	129 ± 19
$\gamma\gamma \rightarrow \mu^+\mu^-$ (el+inel)	397	339 ± 24

Table 10.6: Fit yields for the 8 GeV $< M_{\mu\mu} <$ 12 GeV range [5].

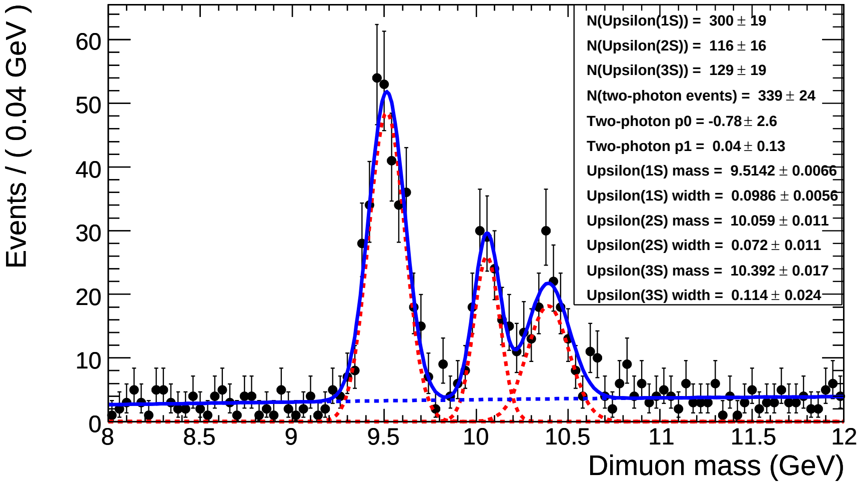

Figure 10.7: Dimuon invariant mass $M_{\mu\mu}$ for events passing all the selection requirements, close to the Υ resonances ($1S$,$2S$,$3S$) [5]. The production corresponds to an integrated luminosity of 100 pb^{-1}, at $\sqrt{s} = 14$ TeV.

dimuons could be applied to separate the elastic and inelastic components (fitting the Δp_T and/or $\Delta\phi$ distributions).

As mentioned earlier, the measurement of the 4-momentum transfer squared t of the diffractively interacting proton (i.e. the one that does not emit the photon) is sensitive to gluon correlations in the proton: the slope b of this variable is related to the interaction impact parameter, which in turn is related to the size of the proton-$b\bar{b}$ system. The measurement of this distribution at HERA is limited by low statistics. The t variable is not directly measurable at the LHC, but the Υ transverse momentum squared $p_T^2 = \left(p_T(\mu^+) - p_T(\mu^+)\right)^2$ is approximately equal to t, as long as the photon virtuality Q^2 is negligible. Fig. 10.8 shows the distribution of the p_T^2 of the Υ, at generator level (Starlight) and after reconstruction in `CMSSW_1_6_0`. A fit on this variable shows a good agreement with the fit of the t variable [5].

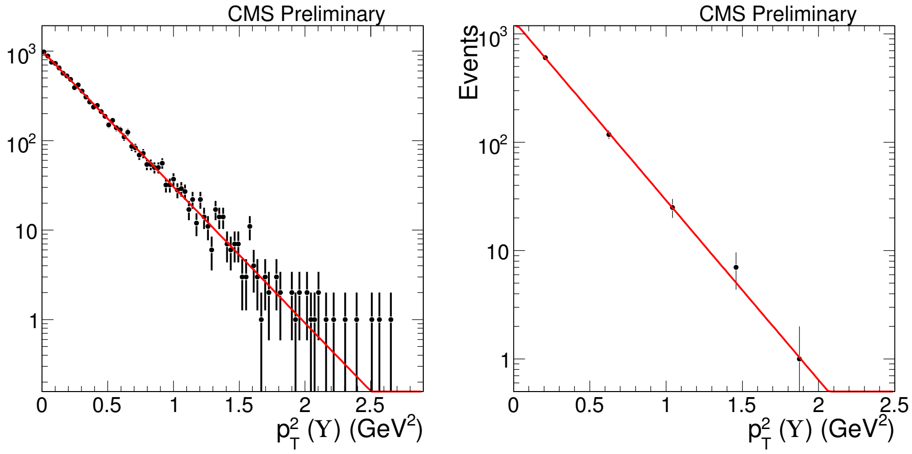

Figure 10.8: Distributions of the p_T^2 of the Υ at Generator level (left, Starlight) and after reconstruction (right, `CMSSW_1_6_0`). The production corresponds to an integrated luminosity of 100 pb^{-1}, at $\sqrt{s} = 14$ TeV.

Finally an important application of Υ events is the calibration of the energy scale of low p_T muons. This is of crucial importance as it allows for decreasing the systematic uncertainties in the absolute luminosity measurement and as it provides a mean for calibrating the VFDs. For instance, the bias in the proton energy loss reconstruction can be monitored using the Υ sample. As it can be seen in Fig. 10.9, the bias in x^{μ}_{reco} can be traced by means of the bias of the reconstructed Υ mass.

10.5 Conclusions

The Υ diffractive photoproduction is a theoretically attractive process, the measurement of which will give an additional experimental cross-section value

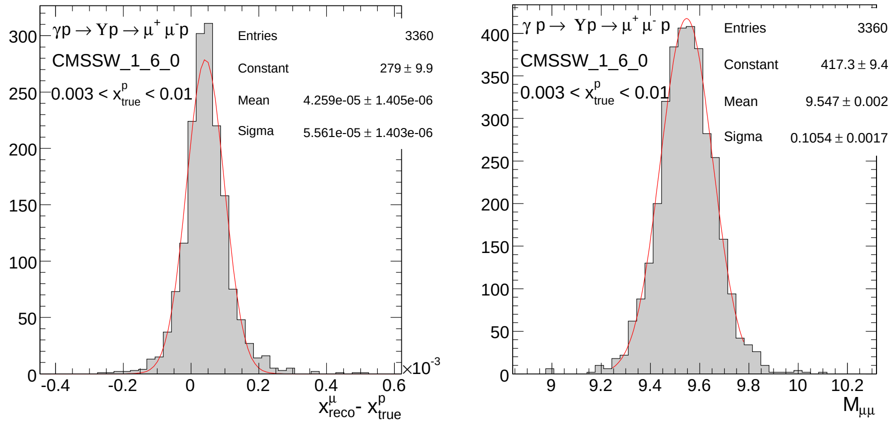

Figure 10.9: Distributions for the $\gamma p \rightarrow \Upsilon(1S)p \rightarrow \mu^+\mu^- p$ sample, in the $0.003 < x^p_{\text{true}} < 0.01$ bin, after offline selection of the muon pairs. Left: comparison of the true relative energy loss x^p_{true} and the value reconstructed from the muon measurement x^μ_{reco} Right: Invariant mass of the dimuon system ($M_\Upsilon = 9.4603$ GeV).

and will probe the generalised parton distributions. Its detection relies on a similar set of analysis cuts as the one applied for the exclusive dimuon selection. It is expected to be observable in the very first data sample at CMS. Moreover, thanks to the very small width of the Υ resonances, the dimuon decays can serve as an ideal calibration for low p_T muons.

Overall conclusions, summary and perspectives

Photon interactions at the LHC have a high relative luminosity and significant cross-sections leading to considerable event rates of high energy processes, above the electroweak scale. This offers an interesting possibility of a novel research domain. The photon-induced processes are theoretically well-understood and are characterised by clean experimental signatures, in particular by the presence of very forward scattered protons.

In a couple of months, the LHC will start colliding proton beams at 900 GeV, 10 TeV and then 14 TeV with luminosities up to 10^{34} cm^{-2}s^{-1}. Its fifth interaction point is instrumented by the CMS and TOTEM experiments, with a set of detectors reaching the widest pseudorapidity coverage ever in collider physics. This includes a central detector and a set of near-beam calorimeters, tracking detectors and timing devices. However, TOTEM very forward detectors will not be able to run at high luminosities due to the radiation damages.

In the context of the design of the near-beam very forward tracking detectors, research and development of cold edgeless silicon microstrip sensors has been carried out. It aimed at producing prototypes of radiation hard detectors by cutting silicon microstrip sensors through their sensitive area, with laser or plasma beams. The sensors are operated at very low temperatures to guarantee good detector performance. This technique offers a promising alternative to the advanced 3D-pixels or dedicated designs for applications at the highest LHC luminosities.

The link between the measurement by the very forward detectors and the kinematic properties of the scattered particle at the interaction point is provided by a custom-written software, called Hector. This simulator has been developed to describe the particle transport in beamlines. It plays a key role in the preparation of the measurement of very forward protons at the LHC. Hector has been integrated in the official software of the CMS experiment.

The two-photon exclusive production of dileptons is characterised by high cross-section and a very clean event topology. The selection and the measurement of these events have been studied with the full simulation of the CMS experiment. In particular, the exclusive dimuons will provide a sample for precision measurement of the absolute luminosity at the LHC. Other applications, like the calibration of the very forward detectors are also possible. The diffractive photoproduction of Υ meson, decaying into a muon pair, will be detected using the same selection as in the two-photon exclusive dimuon analysis. Υ detection is interesting from the theoretical point-of-view, as it could constrain the current models, and from the experimental one, as it provides a sample of low p_T muons, which is crucial for detector calibration. Part of the results of this analysis work has been approved by the CMS collaboration and was presented on behalf of CMS at several international conferences.

This thesis has established the technical framework (including detector developments), simulation techniques and event analysis, for the measurements of the two-photon interactions at the LHC right from the start of its operation.

Bibliography

[1] J. de Favereau *et al.*, *High energy photon interactions at the LHC*, CP3-08-04, June 2008.

[2] K. Piotrzkowski, *Tagging two-photon production at the CERN Large Hadron Collider*, Phys. Rev D63 (2001) 071502 *www*, hep-ex/0201027 *www*.

[3] K. Piotrzkowski, *As an Introduction: Quest for New Physics in Photon-Photon Interactions at the LHC*, arXiv:0807.1624 [hep-ph] *www*, Nucl. Phys. B (Proc. Suppl.) 179-180 (2008) 2-6 *www*.

[4] X. Rouby, *Tagging photon interactions at the LHC*, arXiv:0806.4941 [hep-ex] *www*, Nucl. Phys. B (Proc. Suppl.) 179-180 (2008) 202âĂŞ210 *www*.

[5] J. J. Hollar, S. Ovyn, X. Rouby, *Exclusive* $\gamma\gamma \to \ell\ell$ *production*, CMS AN-2007/032 *www*; The CMS Collaboration, $\gamma\gamma \to \ell^+\ell^-$ *and* $\gamma p \to \Upsilon \to \ell^+\ell^-$ *production*, CMS PAS DIF-07-001 *www*.

[6] T. Pierzchala and K. Piotrzkowski, *Sensitivity to anomalous quartic gauge couplings in photon-photon interactions at the LHC*, arXiv:0807.1121 [hep-ph] *www*, Nucl. Phys. B (Proc. Suppl.) 179-180 (2008) 257-264 *www*.

[7] J. Ohnemus, T. F. Walsch, P. M. Zerwas, $\gamma\gamma$ *production of non-strongly interacting* SUSY *particles at hadron colliders*, hep-ph/9402302 *www*.

[8] N. Schul and K. Piotrzkowski, *Detection of two-photon exclusive production of supersymmetric pairs at the LHC*, arXiv:0806.1097[hep-ph] *www*, Nucl. Phys. B (Proc. Suppl.) 179-180 (2008) 289-297 *www*.

[9] X. Rouby and K. Piotrzkowski, *Luminosity determination by CMS using exclusive muon pairs with early data*, CMS AN 2008/061 *www*.

[10] A. G. Shamov, V. I. Telnov, *Precision luminosity measurement at LHC using two-photon production of* $\mu^+\mu^-$*pairs*, Nucl. Inst. & Meth. A 494 (2002) 51-56, *www*.

[11] M. W. Krasny, J. Chwastowski and K. Slowikowski, *Luminosity measurement method for LHC: The theoretical precision and the experimental challenges*, Nucl. Inst. & Meth. A 584 (2008) 42-52, *www*.

[12] M. G. Albrow *et al.*, *The FP420 R&D Project*, CERN-LHCC-2005-025 *www*; M. G. Albrow *et al.*, *The FP420 R&D project*, arXiv:0806.0302 [hep-ex] *www*.

[13] X. Rouby, J. de Favereau, K. Piotrzkowski, *HECTOR, a fast simulator for the transport of particles in beamlines*, JINST 2 P09005, *www*.

[14] I. F. Ginzburg, A. Schiller, *Search for heavy magnetic monopole at the Tevatron and LHC*, Phys. Rev. D57(1998)6599, hep-ph/9802310 *www*.

[15] Dougall, S. D. Wick, *Dirac Magnetic Monopole Production form Photon Fusion in Proton Collisions*, arXiv:0706.1042 [hep-ph] *www*.

[16] See for example: The OPAL Collaboration, *Inclusive Jet Production in Photon-Photon Collisions at* $\sqrt{s_{ee}}$ *from* 189 *to* 209 *GeV*, arXiv:0706.4382 [hep-ex] *www*; The ALEPH Collaboration, *Measurement of the Cross Section for open b-Quark Production in Two-Photon Interactions at LEP*, arXiv:0706.3150 [hep-ex] *www*; The LEP Collaborations, *A Combination of Preliminary Electroweak Measurements and Constraints on the Standard Model*, arXiv:0612034 [hep-ex] *www*. The OPAL Collaboration, Phys. Rev. D 70 (2004) 032005, arXiv:0402021 [hep-ex] *www*.

[17] S. Ovyn, *Associated W and Higgs boson photoproduction and other electroweak photon induced processes at the LHC*, arXiv:0806.1157 [hep-ph] *www*, Nucl. Phys. B (Proc. Suppl.) 179-180 (2008) 269-276 *www*.

[18] S. Ovyn *et al.*, *High energy photoproduction at the LHC, proceedings of the International Conference on the Structure and Interactions of the Photon (Paris, 2007)*.

[19] J. de Favereau de Jeneret, S. Ovyn, *Single top quark photoproduction at the LHC*, arXiv:0806.4886 [hep-ph] *www*, Nucl. Phys. B (Proc. Suppl.) 179-180 (2008) 277-284 *www*.

[20] H1 Collaboration, proceedings of the DIS conference, May 2008, London.

[21] The CMS and TOTEM diffractive and forward physics working group, *Prospects for Diffractive and Forward Physics at the LHC*, CERN/LHCC 2006-039/G-124 *www*.

[22] G. Baur , D. d'Enterria, S. Klein, J. Nystrand, M. Strikman *et al.*, *Photoproduction at collider energies: from RHIC and HERA to the LHC*, hep-ph/0702212 *www*.

[23] See for example: ZEUS Collaboration, *Three- and four-jet final states in photoproduction at HERA*, arXiv:0707.3749[hep-ex] *www*; N. Coppola, *High p_T jets in DIS and γp at HERA*, arXiv:0711.4540 [hep-ex] *www*.

[24] V. P. Gonçalves and M. V. T. Machado, *Diffractive photoproduction of heavy quarks in hadronic collisions*, hep-ph/0612265v2 *www*.

[25] S. Klein and J. Nystrand, *Photoproduction of J/Ψ and Υ in pp and $p\bar{p}$ Collisions*, hep-ph/0310223 *www*.

[26] V. P. Gonçalves and M. V. T. Machado, *Diffractive photoproduction of Z^0 bosons in coherent interactions at CERN-LHC*, arXiv:0710.4287v3 *www*

[27] See for example: ZEUS Collaboration, *Diffractive photoproduction of dijets in ep collisions at HERA*, arXiv:0710.1498 [hep-ex] *www*; A. Baltz *et al.*, *Photoproduction at collider energies: from RHIC and HERA to the LHC*, arXiv:0702212 [hep-ph] *www*.

[28] V. M. Budnev, I. F. Ginzburg, G. V. Meledin and V. G. Serbo, *Equivalent Photon Approximation*, Phys. Rept. 15 (1974) 181.

[29] See for example: K. Passek-Kumericki, G. Peters, *Nucleon Form Factors to Next-to-Leading Order with Light-Cone Sum Rules*, arXiv:0805.1758v1 [hep-ph] *www*.

[30] ZEUS Collaboration, *Measurement of elastic Upsilon photoproduction at HERA*, Phys. Lett. B 437(1998), 432-444 *www*.

[31] H1 Collaboration, *Elastic photoproduction of J / psi and Upsilon mesons at HERA*, Phys. Lett. B 483(2000), 23-35 *www*.

[32] H1 Collaboration, *Muon pair production in ep Collisions at HERA*,Phys. Lett. B 583(2004), 28-40; arXiv:0311015 [hep-ex] *www*.

[33] J. Adams *et al.*, Phys. Rev. C0 (2004) 031902.

[34] D. d'Enterria *et al.*, *Coherent photoproduction of J/Psi and high-mass e+e- pairs in ultra-peripheral Au+Au collisions at* $\sqrt(s_{NN}) = 200\ GeV$, nucl-ex/0601001 *www*.

[35] CDF Collaboration, *Observation of Exclusive Electron-Positron Production in Hadron-Hadron Collisions*, Phys. Rev. Lett. 98, 112001 (2007).

[36] A. Hamilton, *Exclusive Interactions in $p\bar{p}$ collisions at $s = 1.96\ TeV$*, Ph. D. Thesis, University of Albera 2006; arXiv:0611040 [hep-ex] *www*

[37] K. Terashi, talk in Moriond QCD 2007, arXiv:0705.3804 [hep-ex] *www*; A. Hamilton, talk in ECT Trento Workshop on Photoproduction, January 2007.

[38] DELPHI Collaboration, *Study of double-tagged $\gamma\gamma$ events at LEPII*, hep-ex/0604039 *www*.

[39] I. Rubinskiy, *Exclusive processes in ep Collisions at HERA*, EPS07.

[40] A. Levy, *Exclusive vector meson electroproduction at HERA*, arXiv:0711.0737 *www*.

[41] J. de Favereau, PHITI*: a generator for upsilon photoproduction with dimuon final state*, unpublished 2007.

[42] S. R. Klein and J. Nystrand, *Photoproduction of quarkonium in proton proton and nucleus nucleus collisions*, Phys. Rev. Lett. 92 (2004) 142003 *www*, arXiv:hep-ph/0311164 *www*; J. Nystrand, *Electromagnetic interactions in nucleus nucleus and proton proton collisions*, Nucl. Phys. A752 (2005) 470-479, arXiv:hep-ph/0412096 *www*.

[43] M. Arneodo, M. Diehl, *Diffraction for non believers*, hep-ph/0511047 *www*.

[44] D. d'Enterria, *Forward Physics at the LHC*, arXiv:0708.0551v3 [hep-ex] *www*.

[45] A. Pukhov, *Batch calculations in CalcHEP*, Nucl. Inst. Meth A502, (2003) 596-598 *www*.

[46] F. Maltoni and T. Stelzer, JHEP0302, (2003) 027 *www*; T. Stelzer and W.F. Long, Phys.Commun.81, (1994) 357-371; J. Alwall *et al.*, *MadGraph/MadEvent v4: The New Web Generation*, JHEP09 (2007) 028, *www*

[47] J. Vermaseren, LPAIR, Nucl. Phys. B 229, 347 (1983).

[48] V. A. Khoze, A.D. Martin, and M. G. Ryskin, *Photon-exchange processes at hadron colliders as a probeof the dynamics of diffraction*, Eur. Phys. J. C24 (2002) 459, hep-ph/0201301v2 *www*.

[49] V. A. Khoze, A.D. Martin and M. G. Ryskin, Eur. Phys. J. C26, (2002) 229.

[50] V. A. Khoze, A.D. Martin and M. G. Ryskin, Eur. Phys. J. C23, (2002) 311, hep-ph/0111078 *www*.

[51] W. Herr, B. Muratori, *CERN Accelerator School: the concept of luminosity*, Zeuthen 2003, Intermediate accelerator physics 361-377 *www*.

[52] D. Bocian, *Luminosity measurement of pp colisions with the two-photon process*, Ph. D. Thesis, Polish Academy of Sciences, Kraków (2004).

[53] https://twiki.cern.ch/twiki/bin/view/CMS/LumiWikiHome *www*.

[54] TOTEM Collaboration, TOTEM *Technical Design Report*, CERN-LHCC-2004-002.

[55] V. Avati *et al.*, *The* TOTEM *experiment*, EPJdirect A1, 1-11 (2003) *www*.

[56] ATLAS Collaboration, ATLAS *Technical Design Report*, volume I.

[57] X. Rouby, *Forward Physics at the LHC*, CMS CR 2008-020, arXiv:0805.4406[hep-ex] *www*.

[58] M. Deile *et al.*, *Diffraction and Total Cross-Section at the Tevatron and the LHC*, hep-ex/0602021 *www*.

[59] TOTEM Collaboration, *The TOTEM experiment: Total cross-section measurement and soft diffraction at LHC*, J. Phys.: Conf. Ser. 110 (2008) 022037 *www* ; G. Latino, *The TOTEM experiment at the LHC*, arXiv:0805.3968 [hep-ex] *www*.

[60] ATLAS Collaboration, *ATLAS Forward Detectors for Measurement of Elastic Scattering and Luminosity*, CERN-LHCC 2008-004 *www*.

[61] S. Ask, *Luminosity Measurement at ATLAS with a Scintillating Fiber Tracker*, Nucl. Sc. Symp. Conf. Record, 2006. IEEE 2, (2006) 929-934 *www*.

[62] COMPETE Collaboration, *Benchmarks for the Forward Observables at RHIC, the Tevatron-Run II, and the LHC*, PRL 89, (2002) 201801. *www*.

[63] UA4 Collaboration, Phys. Lett. B198 (1987) 583-589.

[64] O. S. Brüning, P. Collier, P. Lebrun, S. Myers, R. Ostojic, J. Poole, P. Proudlock, *LHC Design Report, v.1: the LHC Main Ring*, CERN-2004-003-V-1 Geneve (2004) *www*.

[65] M. Benedikt, P. Collier, V. Mertens, J. Poole, K. Schindl *et al.*, *LHC Design Report, v.3: the LHC Injector Chain*, CERN-2004-003-V-3 Geneve (2004) *www*.

[66] P. V. Landshoff, *The total cross-section at the LHC*, arXiv:0709.0395v1 [hep-ph] *www*.

[67] Zeus experiment, Online documentation : luminosity values, *www*.

[68] J. F. Grivaz, *The Run II of the Tevatron*, Europhysics News (2003) Vol. 34 No. 1 *www*.

[69] S. Van der Meer, *Calibration of the effective beam height in the ISR*, CERN-ISR-PO/68-31 (1968) *www*.

[70] M. Della Negra *et al.*, CMS physics Technical Design Report, CERN-LHCC-2006-001 *www*.

[71] M. Della Negra *et al.*, CMS physics Technical Design Report, CERN-LHCC-2006-021 *www*.

[72] Quartz G. Mavromanolakis, *fiber calorimetry and calorimeters*, arXiv:physics/0412123 *www*.

[73] CMS Collaboration, *The Electromagnetic Calorimeter Project - Technical Design Report*, (1997) CERN/LHCC 97-33.

[74] CMS Collaboration, *The Magnet Project - Technical Design Report*, (1997) CERN/LHCC 97-10.

[75] G. Ruggiero, *Planar edgeless silicon detectors for the TOTEM experiment*, IEEE Volume 2, Issue , 16-22 Oct. 2004 Page(s): 922 - 924 *www*.

[76] X. Aslanoglou *et al.*, *Performance of Prototype II for CMS CASTOR forward calorimeter*, Eur. Phys. J. C 52 (2007) 495, arXiv:0706.2641 [physics.ins-det]

[77] X. Aslanoglou *et al.*, *First performance studies of a prototype for the* CASTOR *forward calotimeter at the CMS experiment*, arXiv:0706.2576 [physics.ins-det] *www*.

[78] L. Bonnet, T. Pierzchala, K. Piotrzkowski, P. Rodeghiero, *Ultra-fast ToF forward detector for exclusive processes at the LHC*, hep-ph/0703320v1 *www*.

[79] See for instance: G. Gustafson, *Multiple Scattering, Underlying Event, and Minimum Bias*, arXiv:0712.1941v1 [hep-ph], *www*.

[80] L. Jones *et al.*, *The APV25 deep submicron readout chip for CMS detectors, Proceedings of 5th workshop on electronics for LHC experiments*, CERN/LHCC/99-09,162-166.

[81] M. Taševský, *Proton tagging at high luminosities at LHC*, ATL-PHYS-CONF-2007-016.

[82] CMS Collaboration, *The computing project Technical Design Report*, CERN/LHCC 2005-023.

[83] CMS Collaboration, *The Trigger and Data Acquisition project, Volume I, The Level-1 Trigger, Technical Design Report*, CERN/LHCC 2000-038 *www*.

[84] A. Vasilescu and G. Lindström, *Displacement damage in silicon*, on-line compilation available at http://sesam.desy.de/members/gunnar/Si-dfuncs.html *www*.

[85] L. Fiore *et al.*, *Assembly of the Inner Tracker Silicon Microstrip Modules*, CMS NOTE 2008-004 *www*.

[86] See for instance, A.G. Clark *et al.*, *Design and test of a prototype silicon detector module for ATLAS Semiconductor Tracker endcaps*, Nucl. Inst. & Meth. A 538 (2005) 265 *www*.

[87] LHCb Collaboration, *LHCb VELO (VErtex LOcator) : Technical Design Report*, CERN/LHCC 2001-011 *www*.

[88] A. Bergamaschia *et al.*, *A detection system for clinical breast tomography with synchrotron radiation*, Nucl. Inst. & Meth. A 535 (2004) 88 *www*.

[89] See for instance: RD39 Collaboration, *RD39 Status Report*, CERN-LHCC-2006-034 *www*.

[90] See for instance: RD50 Collaboration, *RD50 Status Report*, CERN-LHCC-2005-037 *www*.

[91] B. Dezillie, V. Eremin, Z. Li, E. Verbitskaya, *Polarization of silicon detectors by minimum ionizing particles*, Nucl. Inst. & Meth. A 452 (2000) 440.

[92] E. Verbitskaya *et al.*, IEEE Trans. Nucl. Sci. NS-49 (1) (2002) 258.

[93] E. Verbitskaya *et al.*, *The effect of charge collection recovery in silicon pâĂŞn junction detectors irradiated by different particles*, Nucl. Inst. & Meth. A 514 (2003) 47.

[94] J. Härkönen *et al.*, *Recent results from the CERN RD39 Collaboration on super-radiation hard cryogenic silicon detectors for LHC and LHC upgrade*, Nucl. Inst. & Meth. A 535 (2004) 384 *www*.

[95] V. Avati *et al.*, *First test of cold edgeless silicon microstrip detectors*, Nucl. Inst. & Meth. A 518 (2004) 264 *www*.

[96] B. Perea Solano *et al.*, *Edgeless silicon pad detectors*, Nucl. Inst. & Meth. A 560 (2006) 135 *www*.

[97] RD39 Collaboration, *RD39 Status Report*, CERN-LHCC-2005-035 *www*.

[98] X. Rouby *et al.*, *Cryogenic detector modules and edgeless silicon sensors*, Nucl. Inst. & Meth. A 570 (2007) 308-311 (CP3-06-17) *www*.

[99] X. Rouby *et al.*, *Recent developments of CERN RD39 cryogenic tracking detectors collaboration CERN RD39 Collaboration*, Nucl. Inst. & Meth. A 583 (2007)99-103 *www*.

[100] G. Pellegrini *et al.*, *Edgeless detectors fabricated by dry etching process*, Nucl. Inst. & Meth. A 563 (2006) 70 *www*.

[101] G. Pellegrini *et al.*, *Characterization of edgeless detectors fabricated by dry etching process*, Nucl. Inst. & Meth. A 576 (2007) 95 *www*.

[102] See for instance: C. Da Via *et al.*, *Radiation hardness properties of full-3D active edge silicon sensors*, Nucl. Inst. & Meth. A 587, (2008) 243-249 *www*.

[103] See for instance: E. Fretwurst, *et al.*, *Radiation damage studies on MCz and standard and oxygen enriched epitaxial silicon devices*, Nucl. Inst. & Meth. A 583, (2007) 58-63 *www*.

[104] C. Civinini, *The CMS Silicon Strip Tracker*, Nucl. Inst. & Meth. A 579, (2007) 726-730 *www*.

[105] X. Rouby, *Caractérisation des circuits hybrides et des modules de détection pour le trajectoraphe de CMS*, Master Thesis, Université catholique de Louvain (2002) *www*; X. Rouby, *Testing and characterizing CMS tracker front-end hybrids*, Physicalia Magazine, 25-3 (2003) 149-158.

[106] T. Palviainen *et al.*, *Minimizing guard ring dead space in silicon detectors with an n-type guard ring at the edge of the detector*, Nucl. Inst. & Meth. A 573 (2007) 277-279 *www*.

[107] G. Ruggiero, V. Eremin, E. Noschis, *Planar edgeless silicon detectors for the TOTEM experiment*, Nucl. Inst. & Meth. A 582 (2007) 854-857 *www*.

[108] ATLAS Collaboration, *ATLAS Forward Detectors for Measurement of Elastic Scattering and Luminosity*, CERN/LHCC 2008-004, *www*.

[109] *Karl SüSS PA-200 semi-automatic Probe Station*, KARL SUSS KG GmbH & Co., Schleissheimer Strasse 90, D-85748 Garching b. München Âů Germany

[110] *Keithley Sourcemeter 2410*, Keithley Instruments, Inc., U.S.A.

[111] *Agilent DC power supply*, Agilent Technologies, Inc., 5301 Stevens Creek Blvd Santa Clara CA 95051, U.S.A.

[112] *Agilent LCR meter*, Agilent Technologies, Inc., 5301 Stevens Creek Blvd Santa Clara CA 95051, U.S.A.

[113] *Keithley 6514 Electrometer*, Keithley Instruments, Inc., U.S.A.

[114] E. Forton, *Radiation damage induced by neutrons in CMS silicon sensors*, Ph. D. Thesis, Université catholique de Louvain (2006).

[115] S. Assouak, *Les senseurs de CMS: Etude de leur résistance aux flux intenses de neutrons rapides*, Ph. D. Thesis, Université catholique de Louvain (2006).

[116] G. Pierre, *Tests et caractérisation de détecteurs au silicium sans bord*, Master Thesis, Université catholique de Louvain (2007).

[117] *Silicon Surface Barrier Detector Preamplifier, Canberra 2003 BT*, Canberra Industries, Inc. 800 Research Parkway, Meriden, CT 06450, U.S.A.

[118] *Spectroscopy Amplifier-Shaper, 2026 Canberra*, Canberra Industries, Inc. 800 Research Parkway, Meriden, CT 06450, U.S.A.

[119] *Pilas laser diode*, Advanced Photonic Systems GmbH, Schwarzschildstr 6, Photonic Center, Berlin, Germany.

[120] *Temperature controller*, Yokogawa Electric Corporation 9-32, Nakacho 2-chome, Musashino-shi, Tokyo 180-8750, Japan.

[121] *CAEN N470 High Voltage supply*, CAEN S.p.A., Via Vetraia, 11, 55049, Viareggio, Italy.

[122] *IPC Current measurement module* made by the electronics workshop in ULC-FYNU.

[123] *Tektronix TDS 724A 500MHz 1GS/s oscilloscope* Tektronix, Inc., U.S.A.

[124] B. Perea Solano, Ph. D. Thesis, CERN, Universitat Politecnica de Catalunya (2004) ISBN 84-688-8952-0.

[125] J. Härkönen *et al.*, *Processing and recombination lifetime characterization of silicon microstrip detectors*, Nucl. Inst. & Meth. A 485 (2002) 159 *www*.

[126] R. Turchetta *et al.*, *Design and results from the APV25, a deep sub-micron CMOS front-end chip for the CMS tracker*, Nucl. Inst. & Meth. A 466 (2001) 359 *www*.

[127] S. Grohmann, *Distributed cooling in cryogenics with miniaturized fluid circuits*, Ph. D. Thesis, Technischen, Universität Dresden, Fakultaät Maschinenwesen (2003).

[128] *CCU, FED-PMC, FEC, VUTRI*: unpublished.

[129] M. Axer *et al.*, *Test of CMS tracker silicon detector modules with the ARC readout system*, Nucl. Inst. & Meth. A 518 (2004) 321-323 *www*.

[130] H. Angerer *et al.*, *Present status of silicon detectors in COMPASS*, Nucl. Inst. & Meth. A 512 (2003) 229 *www*.

[131] A. Marchioro: private communication.

[132] J. de Favereau de Jeneret, X. Rouby, K. Piotrzkowski, HECTOR*, a fast simulator for the transport of particles in beamlines*, arXiv:0707.1198v2 [physics.acc-ph] *www*.

[133] A. Arbuzov, D.Y. Bardin, J. Bluemlein, L. Kalinovskaya, T. Riemann, HECTOR *1.00: A Program for the calculation of QED, QCD and electroweak corrections to e p and lepton+- N deep inelastic neutral and charged current scattering*, *Comput. Phys. Commun.* **94** (1996) 128-184 *www*.

[134] K. Wille, *The Physics of Particle Accelerators*, Oxford 2006.

[135] R. Brun and F. Rademakers, ROOT *An Object Oriented Data Analysis Framework*, *Nucl. Inst. & Meth. in Phys. Res* **A 389** (1997) 81-86.

[136] T. Sjöstrand, L. Lönnblad, S. Mrenna, PYTHIA *event generator* hep-ph/0603175 *www*.

[137] The CMS Collaboration, *CMS, The TriDAS Project, Technical Design Report, Volume 2: Data Acquisition and High-Level Trigger*, CERN LHCC 2002-36.

[138] K. L. Brown, F. Rothacker, D.C. Carey, F. C. Iselin, TRANSPORT*: a computer program for designing charged particle beam transport systems* CERN 80-04 *www*.

[139] F.C. Iselin, J.M. Jowett, J. Pancin, A. Adelmann, MAD, CERN-SL-2000-026 *www*.

[140] GNU make, www.gnu.org/software/make *www*;
Doxygen, www.doxygen.org *www*; Valgrind, valgrind.org *www*;
CVS, www.cvshome.org *www*.

[141] Classical Electrodynamics, J.D. Jackson, Wiley 1925, ISBN 0-471-30932-X.

[142] S. Ovyn, X. Rouby, J. J. Hollar, *Forward physics triggers*, CMS IN 2008-028.

[143] C. Foudas, private communication.

[144] David d'Enterria for the CMS Collaboration, *Small-x QCD studies with CMS at the LHC*, hep-ex/0703024 *www*.

[145] N. Adam *et al.*, CMS AN-2007/026 (42p) *www* and CMS AN-2007/031 *www* (37p).

[146] F. Moortgat *et al.*, Generator Group online documentation, https://twiki.cern.ch/twiki/bin/view/CMS/GeneratorProduction2007CSA07 *www*.

[147] F. Sikler, K. Krajczar, *Measurement of charged hadron spectra in proton-proton collisions at* $\sqrt{s} = 14\ TeV$, CMS AN-2007/021 ; F. Sikler, *Reconstruction of low* pT *charged particles with the pixel detector*, CMS AN-2006/100.

[148] S. Esen *et al.*, *Missing ET performance in CMS* CMS AN-2007/041.

[149] J.C. Collins, L. Frankfurt, M. Strikman, *Factorization for hard exclusive electroproduction of mesons in QCD* arXiv:9611433 [hep-ph] *www*.

[150] A. Rybarska, W. Schäfer, A. Szczurek, *Exclusive photoproduction of Υ: from HERA to Tevatron*, arXiv:0805.0717 [hep-ph] *www*.

[151] L. Motyka, G. Watt, *Exclusive photoproduction at the Tevatron and LHC within the dipole picture*, arXiv:0805.2113 [hep-ph] *www*.

[152] M. Diehl, *Generalized Parton Distributions*, DESY-THESIS-2003-018, arXiv:0307382 [hep-ph] *www*.

[153] W.-M. Yao *et al.*, 2006 Review of Particle Physics, J. Phys. G 33, 1 (2006).

[154] J. Pinfold, *CDF Results on Exclusive Leptonic and Photonic Final States*, Nucl. Phys. B (Proc. Suppl.) 179-180 (2008) 46-53 *www*.

List of Figures

List of Tables